UNIVERSIDADE DA CORUÑA

CICA | CENTRO DE INVESTIGACIONES
CIENTÍFICAS AVANZADAS

Max Planck Institute for
Biophysical Chemistry

DEPARTAMENTO DE QUÍMICA FUNDAMENTAL

Programa regulado por el RD 1393/2007: Química Ambiental y Fundamental

New Advances on Anisotropic NMR and Detection of Bioactive Marine Natural Products

Nuevos Avances en la RMN Anisotrópica y Detección de Productos Naturales Marinos Bioactivos

Memoria presentada por

Juan Carlos C. Fuente Monteverde

Directores:

Dr. Jaime Rodríguez González
Dr. Carlos Jiménez González

A Coruña 2018

Acta de Tesis

El tribunal, nombrado por el Excmo. Sr. Rector de la Universidade da Coruña para calificar la tesis doctoral titulada "**Nuevos Avances en la RMN Anisotrópica y Detección de Productos Naturales Marinos Bioactivos/New Advances on Anisotropic NMR and Detection of Bioactive Marine Natural Products**" dirigida por los Drs. Jaime Rodríguez González y Carlos Jiménez González, presentada por Don Juan Carlos de la Cruz Fuentes Monteverde y constituido en el día de la fecha por los miembros que subscriben la presente Acta, una vez efectuada la defensa por el doctorando y contestadas las objeciones y/o sugerencias que se le han formulado, ha otorgado por …………………………la calificación de:

En A Coruña, a……………… de ……………………………… de 2019

PRESIDENTE
Prof. Dr. Michael Reggelin
Organic Chemistry
Technische Universität Darmstadt

SECRETARIO
Pr. Dr. Marcos D. García Romero
Pr. Titular Química Orgánica

VOCAL
Pr. Dr. Victor Sanchez Pedregal
Pr. Titular de Química Orgánica

Firmado

Firmado

Firmado

Don Juan Carlos de la Cruz Fuentes Monteverde:

Presenta la memoria adjunta, titulada **"Nuevos Avances en la RMN Anisotrópica y Detección de Productos Naturales Marinos Bioactivos/New Advances on Anisotropic NMR and Detection of Bioactive Marine Natural Products"** para optar al grado de Doctor en Química que ha sido realizado bajo la dirección de los Doctores Jaime Rodríguez González y Carlos Jiménez González en los laboratorios del Centro de Investigaciones Científicas Avanzadas (CICA) de la Universidade da Coruña.

A Coruña, a 7 de diciembre de 2018.

Fdo. Juan Carlos de la Cruz Fuentes Monteverde

Fdo. Jaime Rodríguez González   Fdo. Carlos Jiménez González

D. **Jaime Rodríguez González** y D. **Carlos Jiménez González**, Catedráticos de Universidad, pertenecientes al Departamento de Química (Área de Química Orgánica) de la Facultad de Ciencias de la Universidade da Coruña,

Certifican:

Que la memoria adjunta, titulada "**Nuevos Avances en la RMN Anisotrópica y Detección de Productos Naturales Marinos Bioactivos/New Advances on Anisotropic NMR and Detection of Bioactive Marine Natural Products".** ha sido realizada bajo su dirección por el licenciado en Química Don **Juan Carlos de la Cruz Fuentes Monteverde**, en el Área de Química Orgánica dependiente del Departamento de Química.

Considerando que constituye trabajo de Tesis, autorizan su presentación en la Universidade da Coruña para optar al grado de Doctor en Química.

Y para que así conste, expiden el presente certificado en A Coruña, a 7 de diciembre de 2018.

Fdo. Jaime Rodríguez González   Fdo. Carlos Jiménez González

New Advances on Anisotropic NMR and Detection of Bioactive Marine Natural Products

x

ABREVIATURAS

λ	Longitud de onda
$[\alpha]_D$	Rotación óptica específica
A549	Línea celular de carcinoma humano
APCI	Ionización química a presión atmosférica
APT	Attached Proton Test Experimento de multiplicidad de ^{13}C
CC	Cromatografía en columna
CCF	Cromatografía en capa fina
COSY	Experimento de RMN bidimensional de correlación homonuclear protón-protón
δ**(ppm)**	Desplazamiento químico en partes por millón
d	Doblete
da	Doblete ancho
dd	Doble doblete
ddd	Doble doble doblete
DEPT	Distorsionless Enhacement by Polarization transfer. Amplificación sin distorsión por transferencia de polarización
DFT	Density Functional Theory.Teoría de Funcionales de Densidad
EMEA	Agencia Europea Medicamentos
ESI	Ionización por electrospray
FAB	Ionización por bombardeo con átomos acelerados
FD	Fracción de Diclorometano
FH	Fracción de hexano
FM	Fracción de acuosa-metanólica
FT-IR	Espectrometria de infrarrojo con transformada de Fourier
FT-MS	Espectrómetro de masas con transformada de Fourier
g	Gramo
HSQC-HECADE	(Heteronuclear Couplings from ASSCI-Domain Experiments with E.COSYtype crosspeaks) Experimento de correlación heteronuclear de medida de constante de acoplamiento mediante HSQC-TOCSY
HL-60	Línea celular de leucemia promielocítica humana
HMBC	(Heteronuclear Multiple-Bond Correlation).Experimento de correlación heteronuclear a larga distancia
HMQC	(Heteronuclear Multiple-Quantum Correlation).Experimento de correlación heteronuclear directo mediante cuanto múltiple
HPLC	Cromatografía líquida de alta eficacia
HRMS	Espectrometría de masas de alta resolución
HREIMS	Espectrometría de masas de alta resolución, técnica de impacto electrónico
Hz	Hercios
IC50	Concentración que inhibe el 50% del crecimiento celular
IR	Infrarrojo
J	Constante de acoplamiento
m	Multiplete

MS	Espectro de masas
m/z	Relación masa carga
mg	Milígramo
min	Minuto
mL	Mililitro
NOESY	Nuclear Overhauser Enhancement Spectroscopy. Experimento bidimensional homonuclear de correlación nOe
Ref.	Referencia
PM	Peso molecular
RMN	Resonancia Magnética Nuclear
RMN ^{13}C	Resonancia Magnética Nuclear de carbono-13
RMN ^{1}H	Resonancia Magnética Nuclear de protón
RP-HPLC	Cromatografía Líquida de Alta Eficacia en Fase Invertida
s	Singulete
sa	Singulete ancho
t	Triplete
ta	Triplete ancho
tR	Tiempo de retención
UV	Ultravioleta
WB	Fracción de *n*-BuOH
WW	Fracción acuosa

Resumen

A continuación, se presenta un breve resumen de cada capítulo:

Capítulo 1:

El uso de RMN anisotrópica en el análisis estructural de moléculas pequeñas quirales se ha expandido en los años recientes. En la actualidad, las Constantes Dipolares Residuales (CDR) pueden ser aplicadas como una herramienta estándar en el mejoramiento eficiente de la determinación de la configuración relativa de compuestos de pequeño tamaño mediante RMN estándar.

En la presente tesis doctoral hemos desarrollado otra metodología de *RMN anisotrópica basada en medidas de anisotropía de desplazamiento químico residual de protones (^1H RCSA)* que ha sido aplicada, primero a moléculas modelo, estricnina, estrona, retrorsina y a-santonina, y posteriormente a nuevos productos naturales: a un meroditerpeno aislado del alga parda *Sargassum muticum*, a las tricloromammindas A y B aisladas del hongo no comestible *Tricholoma equestre* y, finalmente a un briarano de origen marino aislado de la gorgonia Briareum asbestinum recolectada de la penísula de Yucatán.

estricnina   estrona   retrorsina α-santonina

tricholomaminda A   tricholomaminda B

meroditerpeno **1**   briarano-3
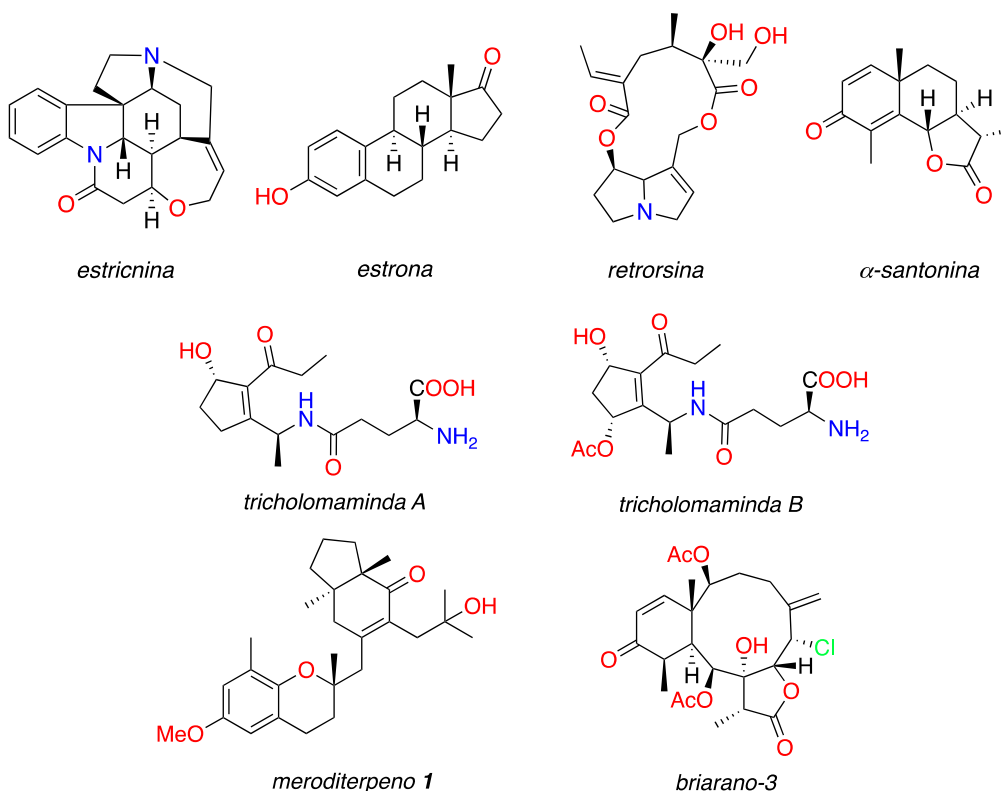
Toda esta nueva metodología se ha podido realizar a través de la mejora de nuevos dispositivos de compresión y extensión de geles aplicados a tubos de RMN de menos de 5 mm. Este desarrollo de este tipo de dispositivos es una herramienta adicional que puede ser utilizada en el futuro por espectroscopistas en el campo de RMN anisotrópica.

Por último, también hemos introducido un nuevo gel deuterado (PMMA-d_8) derivado de polimetilmetacrilato deuterado como medio alineante.

PMMA-d_8 EGDMA   PMMA-d_8
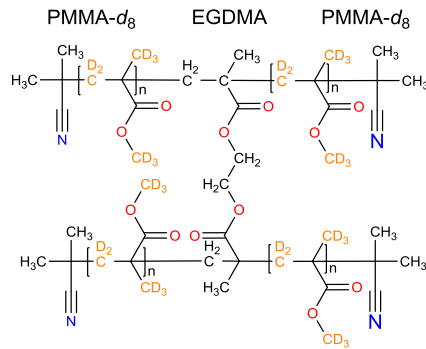
Capítulo 2:

La detección y cuantificación de productos naturales presentes en trazas en mezclas complejas es aún un campo de investigación activo para los químicos. Desde la introducción en el mercado del detector de masas Orbitrap® se iniciado una revolución en las técnicas analíticas de detección. En la presente Tesis Doctoral hemos aprovechado esta tecnología para la detección y, en algunos casos, el aislamiento y la cuantificación de algunos productos naturales de origen marino de interés biológico.

Las distintas aproximaciones en las técnicas de LC/HRMS empleadas fueron aplicadas a:

La detection y el aislamiento de la producción de sideróforos en varias bacteria marinas patógenas: tipo vancrobactina en tres especies de *Vibrio*, tipo piscibactina en una cepa mutante de *Vibrio alginolyticus*, el sideróforo producido por las bacterias *Edwardsiella tarda* y *Photobacterium damselae* subsp. *damselae*.

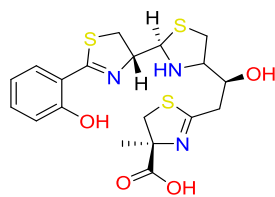Detección y cuantification de AHLs en tres especies patógenas de *Vibrio*.

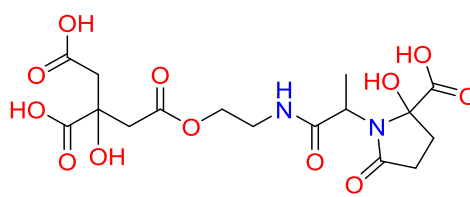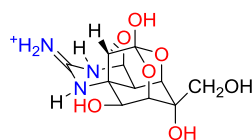Detección de (TTX) en el pez *Diodon hystrix* recolectado en El Salvador.
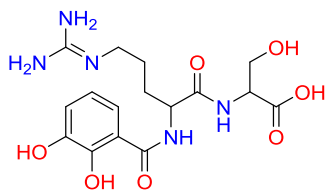
vancrobactina   *divancrobactina*
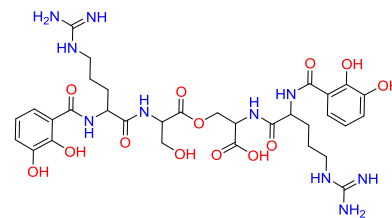
piscibactina   *vibrioferrina*


TTX

Resumo

A continuación amósase un resumo de cada capítulo.

Capítulo 1

O uso da RMN anisotrópica na análise estrutural de moléculas pequenas quiraies, expandiuse nos anos recentes. Na actualidade, as Constantes Dipolares Residuais (CDR) poden ser aplicadas como unha ferramenta estándar na millora eficiente da determinación da configuración relativa de compostos de pequeno tamaño mediante RMN estándar.

Na presente Tese Doutoral desenvolvemos outra metodoloxía de RMN anisotrópica baseada en medidas de anisotropía de desprazamento químico residual de protones (^{1}H RCSA) que foi aplicada, primeiro a moléculas modelo, estricnina, estrona, retrorsina e α-santonina, e posteriormente a novos produtos naturais: a un meroditerpeno illado do alga parda *Sargassum muticum*, ás tricloromammindas A e B illadas do fungo non comestible *Tricholoma equestre* e, finalmente a un briarano de orixe mariña illada da gorgonia Briareum asbestinum colleitada da penísula de Iucatán:

estricnina   *estrona*   *retrorsina*   *α-santonina*

tricholomaminda A   *tricholomaminda B*

meroditerpeno 1   *briarano-3*
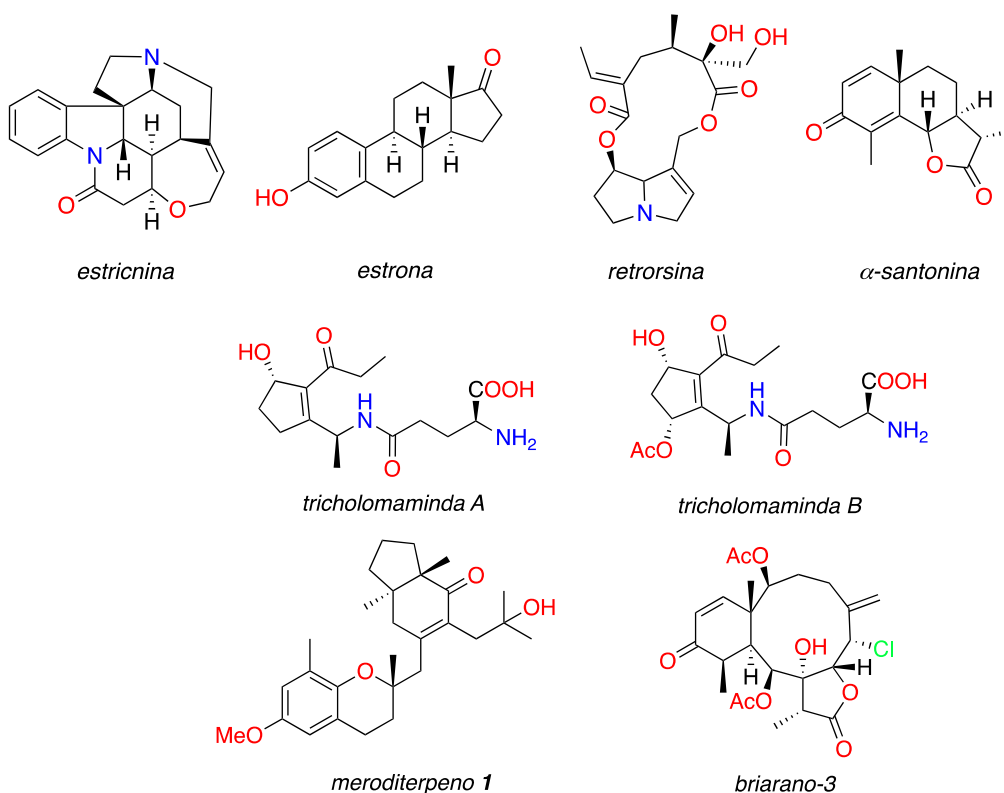
Toda esta nova metodoloxía púidose realizar a través da mellora de novos dispositivos de compresión e extensión de xeles aplicados a tubos de RMN de menos de 5 mm. Este desenvolvemento deste tipo de dispositivos é unha ferramenta adicional que pode ser utilizada no futuro por espectroscopistas no campo de RMN anisotrópica.

Por último, tamén introducimos un novo xel deuterado (PMMA-d8) derivado de polimetilmetacrilato deuterado como medio alineante.

PMMA-*d*₈   EGDMA   PMMA-*d*₈
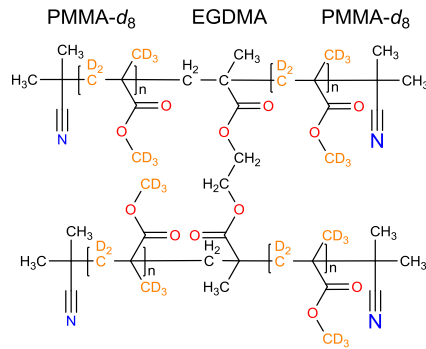
Capítulo 2

A detección e cuantificación de produtos naturais presentes en trazas en mesturas complexas é aínda un campo de investigación activo para os químicos. Desde a introdución no mercado do detector de masas Orbitrap® #iniciar unha revolución nas técnicas analíticas de detección. Na presente Tese Doutoral aproveitamos esta tecnoloxía para a detección e, nalgúns casos, o illamento e a cuantificación dalgúns produtos naturais de orixe mariña de interese biolóxico.

As distintas aproximacións nas técnicas de LC/HRMS empregadas foron aplicadas a:

A detection e o illamento da produción de sideróforos en varias bacteria mariñas patógenas: tipo vancrobactina en tres especies de *Vibrio*, tipo piscibactina nunha cepa mutante de *Vibrio alginolyticus*, o sideróforo producido polas bacterias *Edwardsiella tarda* e *Photobacterium damselae* subsp. *damselae*.

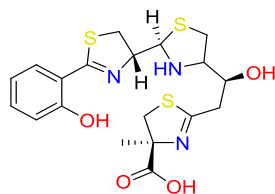Detección e cuantification de AHLs en tres especies patóxenas de *Vibrio*.

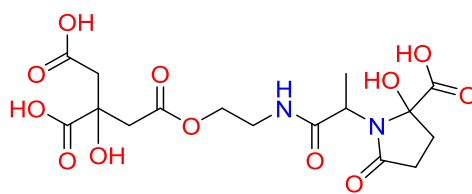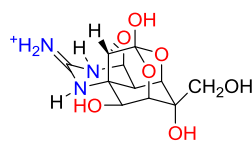Detección de (TTX) no peixe *Diodon hystrix* colleitado no Salvador.
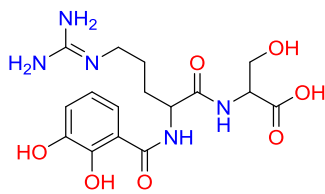
vancrobactina
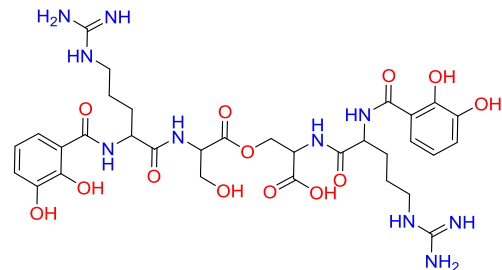
divancrobactina

*piscibactina*

vibrioferrina

TTX

ABSTRACT

A summary of each chapter shall be presented below.

Chapter 1:

The use of anisotropic NMR in the structural analysis of chiral small molecules has expanded in recent years. Currently, Residual Dipolar Constants (RDC) can be applied as a standard tool in the efficient improvement of the determination of the relative configuration of small-sized compounds by standard NMR.

In the present Thesis dissertation, we have developed another methodology of anisotropic NMR based on measures of anisotropy of residual chemical proton displacement (^{1}H RCSA) that has been applied, firstly to compound-models, strychnine, estrone, retrorsine and α-santonin, and subsequently to new natural products: to an isolated meroditerpene of the brown alga *Sargassum muticum*, the trichloromaminades A and B isolated from the non-edible fungus *Tricholoma equestre* and, finally to a briarane of marine origin isolated from the gorgonian *Briareum asbestinum* collected from the peninsula of Yucatan (México).

strychnine *estrone* *retrorsine* *α-santonin*

tricholomaminde A *tricholomaminde B*

*meroditerpene 1* *briarane-3*
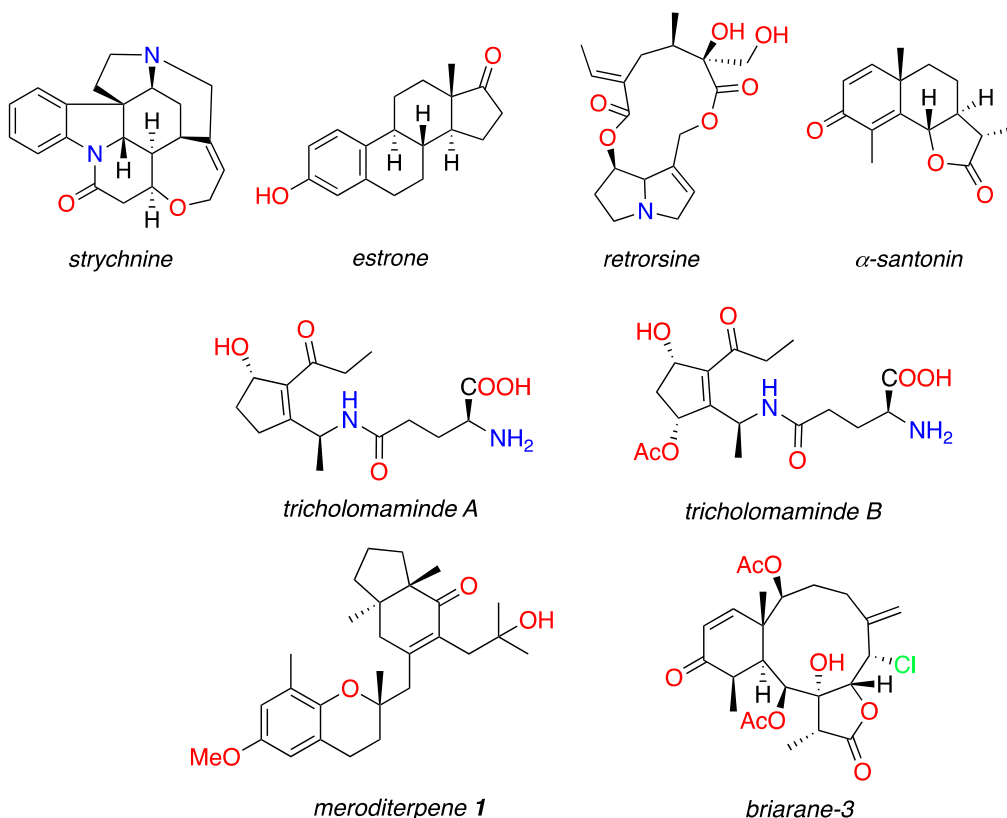
Chapter 2:

The detection and quantification of natural products present in traces in complex mixtures is still an active field of research for chemists. Since the introduction of the Orbitrap® mass detector into the market, a revolution in analytical detection techniques has begun. In this Doctoral Thesis we have taken advantage of this technology for the detection and, in some cases, the isolation and quantification of natural products of marine origin of biological interest.

The different approaches in the LC / HRMS techniques used were applied to:

Detection and isolation of siderophore production in several pathogenic marine bacteria: vanchrovatin type in three *Vibrio* species, piscibactin type in a mutant strain of *Vibrio alginolyticus*, the siderophore produced by the bacteria *Edwardsiella tarda* and *Photobacterium damselae* subsp. d*amselae*

Detection and quantification of AHLs in three pathogenic *Vibrio* species.
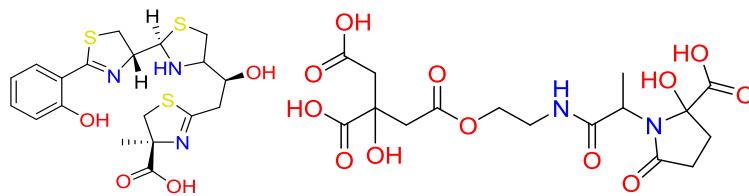
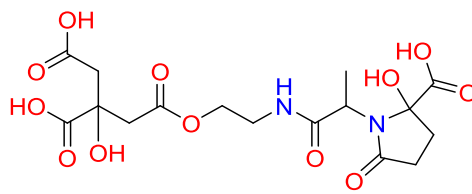Detection of TTX in the fish *Diodon hystrix* collected in El Salvador.
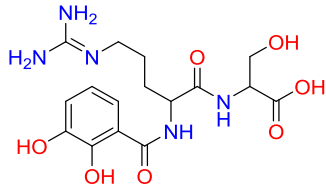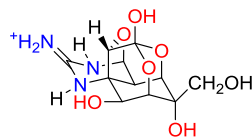

vanchrobactin
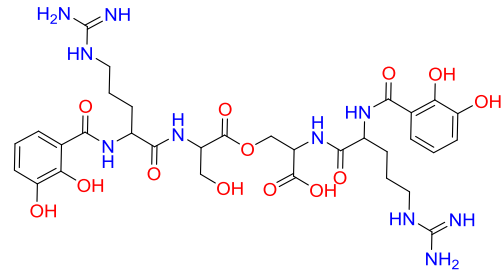
divanchrobactin

piscibactin

vibrioferrin

TTX

List of communications

2013:

MANAPRO. PISCIBACTIN, A SIDEROPHORE FROM Photobacterium damselae subsp. Piscicida, CAN BE PRODUCED BY Vibrio alginolyticus AFTER CONJUGATIVE GENE TRANSFER. Juan Carlos Fuentes-Monteverde, Carlos Jiménez, Jaime Rodríguez, Amable J. Rivas, Carlos R. Osorio, Manuel L. Lemos

XXIV Congreso de Microbiología SEM. SÍNTESIS DE SIDERÓFOROS DE TIPO VANCROBACTINA EN DIFERENTES ESPECIES DEL GÉNERO VIBRIO. Balado M, Fuentes-Monteverde JC, Vences A, Osorio CR, Rodríguez J, Jiménez C, Lemos ML

2015:

Congreso Nacional de Microbiología. Estudio de los sistemas de comunicación celular quorum sensing en bacterias patógenas marinas. José Carlos Reina, Marta Torres, Carlos Jiménez, Juan Carlos Fuentes, Jaime Rodríguez, Emilia Quesada, Inmaculada Llamas

Avances en Microbiología. Mecanismos de asimilación de hierro mediante sideróforos en *Photobacterium damselae* Subsp. *damselae*. Miguel Balado, Beatriz Puentes, Juan Carlos Fuentes, Jaime Rodríguez, Carlos Osorio, Carlos Jiménez, Manuel Lemos

XXXV Reunión Bienal. NUEVOS SIDERÓFOROS DE LA BACTERIA PATÓGENA DE PECES Photobacterium damselae subsp. damselae

17th International Conference on Diseases of Fish and Shellfish. Evidence that a citrate-derived siderophore is shared by *Photobacterium damselae* subsp *damselae* and subsp *piscicida*. M. Balado, B. Puentes, J.C. Fuentes, J. Rodríguez, C. Jiménez, M.L. Lemos

2016:

10th International Biometals Symposium. Citrate acts as siderophore for the marine pathogen *Photobacterium damselae* Subsp. *damselae*. M. Balado, B. Puentes, L. Couceiro, J.C. Fuentes-Monteverde, J. Rodríguez, C. Jiménez, M.L Lemos

2017:

7th Congress of european microbiologists. Identification of the siderophore piscibactin as a relevant virulence factor for vibrio anguillarum serotype O2. M. Balado Dacosta, J.C. Fuentes-Monteverde, J.M. Cabaleiro, J. Rodríguez, C. Jiménez, M.L. Lemos

2018:

59th Experimental Nuclear Magnetic Resonance Conference. Unequivocal determination of 3D molecular structures using proton residual chemical shift anisotropy. Nilamoni Nath; Juan Carlos Fuentes; Michael Reggelin; Christian Griesinger

EUROMAR. Determination of relative configuration of small molecules using proton residual chemical shift anisotropy at microgram levels. Juan C. Fuentes-Monteverde, Nilamoni Nath, Michael Reggelin, Christian Griesinger

List of Publications

2015:

Applied and Environmental Microbiology. A Transmissible Plasmid-Borne Pathogenicity Island Confers Piscibactin Biosynthesis in the Fish Pathogen *Photobacterium damselae* subsp. *piscicida*. Carlos R. Osorio, Amable J. Rivas, Miguel Balado, Juan Carlos Fuentes-Monteverde, Jaime Rodríguez, Carlos Jiménez, Manuel L. Lemos, Matthew K. Waldor

Journal of Fish Diseases. Insights into the virulence-related genes of Edwardsiella tarda isolated from turbot in Europe: genetic homogeneity and evidence for vibrioferrin production. N Castro, C R Osorio, N Buján, J C Fuentes, J Rodríguez, M Romero, C Jiménez, A E Toranzo and B Magariños

2017:

Frontiers in Cellular and Infection Microbiology. Secreted Citrate Serves as Iron Carrier for the Marine Pathogen *Photobacterium damselae* subsp *damselae*. Miguel Balado, Beatriz Puentes, Lucía Couceiro, Juan C. Fuentes-Monteverde, Jaime Rodríguez, Carlos R. Osorio, Carlos Jiménez and Manuel L. Lemos

PLOS ONE. AHL-lactonase expression in three marine emerging pathogenic *Vibrio* spp. Reduces virulence and mortality in brine shrimp (*Artemia salina*) and Manila clam (*Venerupis philippinarum*). Marta Torres, José Carlos Reina, Juan Carlos Fuentes-Monteverde, Gerardo Fernández, Jaime Rodríguez, Carlos Jiménez, Inmaculada Llamas

List of publications under progress

Hypalocrinins, Taurine Conjugated Anthraquinone and Biaryl Pigments from the Deep Sea Crinoid Hypalocrinus naresianus

Reaching Absolute stereochemistry of isolated stereoclusters combining ^{1}H-ΔRCSA and DFT methods: The case of the meroditerpenes from Brown alga *Sargassum muticum*

Unequivocal determination of 3D molecular structures including relative configuration using proton residual chemical shift anisotropy

Structure elucidation of a new toxic natural products (tricholomanmides A and B) with conformational flexibility isolated from *Tricholoma equestre* using anistropic NMR

Contenido/Table of contents

New Advances on Anisotropic NMR

and Detection of Bioactive Marine Natural Products

Chapter 1

New advances on Anisotropic NMR for
relative structure determination of chiral natural products

1.1 An introduction to basic concepts of Anisotropic NMR

NMR anisotropy have recently found a wide range of applications in high-resolution NMR of natural products. A nonisotropic orientational distribution of a molecule in a weak alignment media results in nonzero average dipolar coupling constants.

Residual dipolar couplings, chemical shift anisotropies and quadrupolar couplings provide information about the orientation of inter-spin vectors and the anisotropic contribution of the local environment to the chemical shifts of nuclei, respectively. Structural interpretation of these observables requires parameterization of their angular dependence in terms of an alignment tensor. Information can be used to refine local structure, it can make a unique contribution in determining the relative orientation of remote parts of molecules, which are locally well structured, but poorly connected based on NOE data. Analysis of dipolar couplings in terms of Saupe order matrices provides a concise description of both orientation and motional properties of locally structured fragments in these cases.

Both RDCs and RCSAs provide three-dimensional restraints relative to a global reference frame and, therefore are complementary to conventional, distance-constrained NMR measurements of NOE (or ROE) or J-couplings. In comparison to RDCs, RCSAs have the further advantage of providing placement information on quaternary carbons, which otherwise can only be reached through less sensitive long-range RDC measurements. The ability to address the orientation of quaternary carbons is especially important for proton-deficient, drug-like molecules where NOE, *J*-coupling, and one-bond RDC data may be insufficient.

1.1.1   An introduction to basic concepts of Anisotropic NMR

   Dipolar couplings through space are probably the most important interactions in NMR anisotropy. This interaction can be understood in a simplistic, classical picture if one considers spins as magnets with an inherent rotation at the Larmor frequency. Although spins are not oriented directly along the static magnetic field B_0, the integration over time of the fast rotating magnets yields a secular magnetic moment parallel or antiparallel to B_0. (See Figure 1, panel a and b)
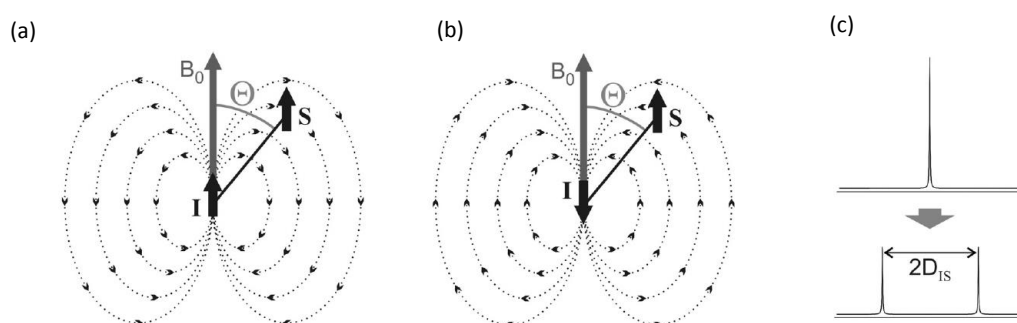
Figure 1. Dipolar interaction between to nucleus. The magnetic field induced by spin I adds up to the static magnetic field B_0 and leads to a shift of the resonance frequency of the close-by spin S. Since parallel spins (a) and antiparallel (b) to the magnetic field are about equally populated, a splitting with twice the dipolar coupling $2D_{IS}$ is observed (c).

The magnetic field produced by spin I now adds up to the static magnetic field felt by spin S and causes a shift of its resonance frequency, the so-called dipolar coupling. Since the spin I is almost equally populated parallel and antiparallel to B_0, a dipolar coupled signal shows a splitting as shown in Figure 1 (panel c).

As one can experience by playing with permanent magnets, the interaction between two dipoles depends on the distance and on the angle between them. If a north pole gets close to a south pole, one feels an attractive force and, similarly, when two identical poles come together, one feels a repelling force. Furthermore, with the right angle between two magnets, one can also find an arrangement without interaction (Figure *2*, panel a). Similar to a classical magnet, the magnetic moment of spin I results in a magnetic field with the typical r-3-dependence with respect to the distance r to the magnet and with the (3 cos² Θ - 1)-dependence with respect to the angle Θ relative to the axis of the magnetic moment (Figure *2*, panel b). Since the magnetic moment of the spin is oriented along the static magnetic field B_0, this angle is identical to the angle with respect to B_0.
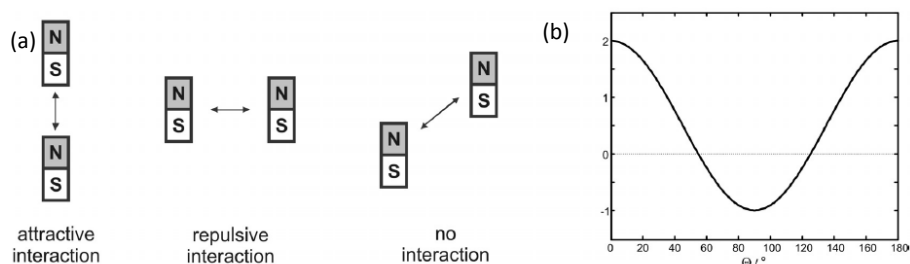
Figure 2 Angular dependence of the dipolar interaction. Depending on the arrangement of two classical magnets the dipolar interaction between them might be attractive, repulsive or no interaction might be present (a). Similarly, the dipolar coupling between the two spins is directly proportional to the (3 cos² Θ - 1)-function (b) and can be used as angular information relative to the static magnetic field B_0.

Therefore strength and sign of this additional magnetic field vary, depending on the distance *r* between the two spins I and S and the angle Θ of their internuclear vector relative to B_0. The exact formula for the resulting dipolar coupling D_{IS} between two spins in a defined orientation is showed in Figure 1

1.1.2 Residual dipolar couplings (RDC)

The measurement of residual dipolar couplings by solution state nuclear magnetic resonance (NMR) spectroscopy gives information about the alignment of the vectors linking pairs of nuclei with non-zero spin relative to the magnetic field. The measured RDC value D_k is a function of $<\cos^2(\theta(\mathbf{r}_k,\mathbf{r}_H))>$, where $\theta(\mathbf{r}_k,\mathbf{r}_H)$ is the angle between the inter-spin vector $\mathbf{r}_K$ and the magnetic field director $\mathbf{r}_H$. Specifically, D_k is given as

$$D_k(r_k,r_H) = -\frac{\gamma_{k1}\gamma_{k2}\mu_o h}{8\pi^3}\langle\frac{3cos^2\big(\theta(\mathbf{r}_k,\mathbf{r}_H)\big)-1}{2r_k^3}\rangle$$

Equation 1

Where Υ_{K1} and Υ_{K2} are the gyromagnetic ratios of the two spins, μ_o is the magnetic permittivity of vacuum, h is Planck's constant, and r_k is the distance between the two spins. The averaging in Equation 1 encompasses ensemble as well as time averaging. [1]
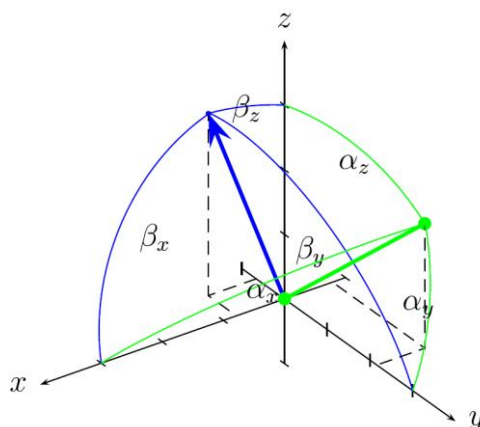
Figure 3. The inter-spin vector r_k (green) and magnetic field vector r_H (blue) with respect to the molecular frame; angles between the interspin vector and the axes of the molecular frame are denoted as $\alpha_{\{x,y,z\}}$; angles between the magnetic field vector and the axes of the molecular frame are denoted as $\beta_{\{x,y,z\}}$

1.1.3   Residual chemical shift anisotropy (RCSA)

RCSAs report on the orientation of the chemical shielding tensor of individual atoms in the molecule. [2] RCSA can be interpreted as a linear combination of two sphero-conics. [2] In order to develop a graphical intuition of CSA see Figure 4.
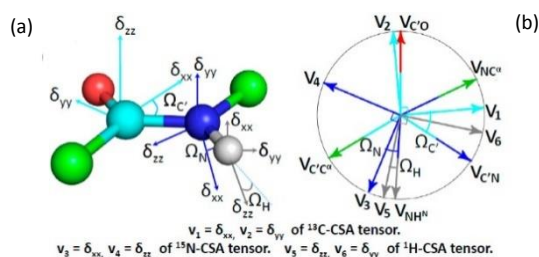
Figure 4. Orientations of the principal components of ^{13}C-, ^{15}N- and ^{1}H-CSA tensors with respect to a molecule, for instance a peptide, the plane are shown in cyan, blue and gray, respectively. δ_{zz} is the most- and δ_{xx} is the least-shielded component. For each tensor, one of the components is approximately perpendicular to the peptide plane; therefore, the other two components lie on the peptide plane, and are completely defined by the angle Ω (a) The wagon wheel shows the CSA tensor components on the peptide plane along with the bond vectors drawn using C′ atom as the origin. In principle, ^{13}C-, ^{15}N- and ^{1}H-CSA tensors can be used for structural elucidation. Nevertheless only ^{13}C and ^{1}H tensor are described.

RCSAs, since they are reflected in the chemical shift, are measured with high sensitivity, thus facilitating measurement of minute samples for which RDC measurement would either be much more challenging or impossible to detect. This type of NMR observables yields a valuable information about the global alignment of atoms and their local environment in a molecule relative to a magnetic field and, therefore, indirectly relative to each other. The measured

anisotropic contribution δ_k^{an} of the local environment to the chemical shift δ_k of a nucleus and the residual quadrupolar interaction of nuclei of angular momentum I > ½ with their electronic environment have the same angle dependence as RDCs, and can therefore be expressed by the same alignment tensor.

The practical challenge, however, is to reliably eliminate isotropic chemical shift changes during molecular alignment. Any viable method must be able to distinguish RCSA shifts due to weak alignment from isotropic shifts due to chemical environment variations between different alignment conditions. The key to accurately measuring RCSAs is to collect the data without altering environmental conditions.

Formulations of RCSAs In any arbitrary molecular frame, [3] the RCSA of any nuclei i is given by

$$RCSA^i(ppm) = \sum_{\alpha,\beta=x,y,z} A_{\alpha\beta} CSA_{\alpha\beta}^i \qquad \text{Equation 2}$$

Where $A_{\alpha\beta}$ (equals $\frac{2}{3} S_{\alpha\beta}$, representing the Saupe order matrix) are the molecular alignment tensor matrix elements. We annotated the chemical shift tensor elements as $CSA_{\alpha\beta}$ instead of δ. The RCSA of a nucleus i was determined as the difference in chemical shift measured under the "max" and "min" alignment conditions (Equation 3) with respect to a chosen reference nucleus (δ_{ref}); [4] which is conveniently chosen as the one with the lowest value of chemical shift anisotropy (CSA) taken from the DFT file. CSA tensors are calculated from density functional theory (DFT) combined with the gauge independent atomic orbital (GIAO) methodology. [5,6] For the stretched gel, we used tetramethylsilane (TMS) for internal chemical shift referencing. Referencing removes factors that impact all chemical shifts equally, including potential changes of the overall effective field due to susceptibility changes as well as misreferencing due to lock ambiguity associated with the split ^2H signal of $CDCl_3$. Due to the difference character of the measurement, RCSA is manifested as ΔRCSA between two alignment conditions as shown in Equation 3

$$\Delta RCSA_i = \left(\delta_i^{aniso} - \delta_{ref}^{aniso}\right)^{max} - \left(\delta_i^{aniso} - \delta_{ref}^{aniso}\right)^{min} \qquad \text{Equation 3}$$

$$= \sum_{\alpha,\beta=x,y,z} \left[\left(A_{\alpha\beta}^{max} - A_{\alpha\beta}^{min}\right)CSA_{i,\alpha\beta} - \left(A_{TMS,\alpha\beta}^{max} - A_{TMS,\alpha\beta}^{min}\right)CSA_{TMS,\alpha\beta}\right]$$

Because TMS is highly symmetric, it has negligible alignment under the conditions used here, and therefore, $\left(A_{TMS}^{\overline{max}} - A_{TMS}^{max}\right) \approx 0$. Furthermore, the carbon of TMS has small chemical shielding anisotropy, i.e., $\widehat{CSA_{TMS}} \approx 0$. Consequently, Equation 3 simplifies to the following form:

$$\Delta RCSA = \sum_{\alpha,\beta=x,y,z} \left(A_{\alpha\beta}^{max} - A_{\alpha\beta}^{min}\right)CSA_{i,\alpha\beta} = \Delta\delta \qquad \text{Equation 4}$$

Recently the carbon tetrachloride has been indicated as a valid option to replace the TMS.[7]

1.1.4   From anisotropic media to Residual Anisotropic Parameters

The desired additional structural information without significant loss, as in solid state, in chemical shift resolution, an intermediate state between solid and liquid has to be reached: the molecule should be partially aligned. This can be achieved with the help of so-called alignment media, which works as an orienting matrix as visualized in *Figure 5*. Within the alignment medium the molecule tumbles almost freely so that most of the anisotropic interactions are averaged out over time. However, the interaction with the oriented grid of the alignment medium prevents from complete averaging and a net orientation remains.
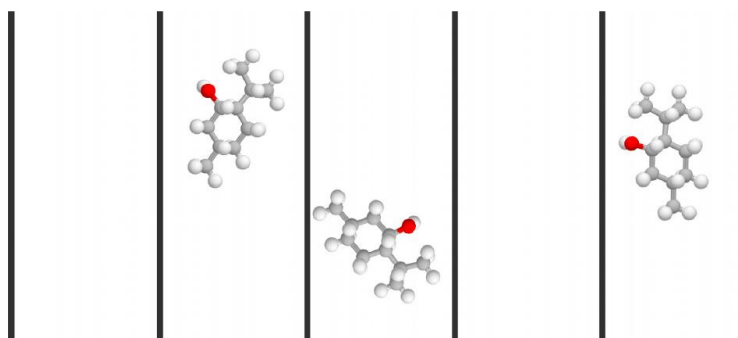
Figure 5. Alignment media as a molecular grid. It is badly assumed that solute molecules can tumble almost unhindered in the oriented matrix given by an alignment medium. Only a small fraction of time the molecule is oriented by the medium which leads to a time averaged net orientation. For practical purposes it is believed that el conformational equilibrium, if any exist, is not affect by the alignment medium net.

To use RDCs and RCSAs measured in partially aligned samples and obtain structural information, the partial averaging over time due to the tumbling of the molecule and its inherent flexibility has to be addressed by an adequate model. The description of the averaging is given in Equation 1 and Equation 4, respectively.

1.1.5   Description of alignment

In order to extract structural information from RDCs and RCSAs it is necessary to introduce a parametrization of the averaged angle dependence in Equation 1 and Equation 4. This is achieved by firstly defining a coordinate system (molecular frame), and then, relative to this, the orientation of the magnetic field vector r_H and the inter-spin vector rk. The alignment of the molecule relative to the magnetic field can be then described using an alignment tensor as it can be seen on Figure 3 and Figure 4, panel (a) for RDCs and RCSAs respectively.

The effect of the anisotropic distribution of molecular orientations is conveniently described by a set of order parameters which are known as the alignment tensor or the Saupe order matrix. The size of the residual tensorial interactions is a function of both the alignment tensor and of the orientation of the individual chemical groups with respect to the alignment tensor's principal axes system; hence, the content of intramolecular structural information. In order to extract this information from the measured interaction energies, some knowledge about the alignment tensor is a prerequisite. This tensor is characterized by five independent parameters, e.g. its largest principal value, the rhombicity, and the three Euler angles describing the orientation of the principal axes with respect to the molecular coordinates.

1.1.6   Algorithms

Two algorithms for generating the optimal alignment tensor for a given molecular structure and set of experimental data are commonly named in literature; Single Value Decomposition (SVD)[3] and the linear least squares algorithm.[8] By using singular value decomposition as a method for calculating the order matrices, principal frames and order parameters can be determined efficiently, even when a very limited set of experimental data is available.

1.1.7   Alignment Media

An intermediate state between the total alignment in a solid and the isotropic averaging in solution must be achieved in order to measure residual dipolar couplings. This partial alignment is obtained by a so-called alignment medium, which works as an oriented molecular grid capable to constrain the tumbling of the molecule in a way, that a time averaged net orientation remains.

Three different ways of partially aligning a molecule are known today: alignment in a liquid crystalline phase, alignment in a stretched gel, and the orientation via paramagnetic ions. The last one is beyond the scope of this thesis.

1.1.8   Data fitting

RDC and RCSA data do can be process and fitted by different software. Being the most prominent for small molecule analysis MSpin. [9] The software for the analysis of residual dipolar coupling an residual chemical shift anisotropy data. It is specially designed for small molecule analysis, can directly read many molecular-modeling and popular chemistry file formats and accept RDC/ RCSA values as a simple free-format table. Isotropic correction for RCSA analysis can be automatically done. [10] Alignment tensor can then be computed by SVD. Trial structures are then ranked according to their Cornilescu's quality factor (Q) values. Analysis of multiconformational problems and fitting of RDC data to relative populations can be accomplished using the single-tensor approximation. The only disadvantage that can be point out in MSpin is the lack of ability to fitting the alignment tensor when data includes long range RDC ($^nD_{CH}$). The software Relax [11] is the correct chose is that the case. The current research does not include any $^nD_{CH}$

1.1.9 Integrated methodology for solving natural products by NMR anisotropy

The overall approach can be divided in:

(a) **Conformers assembling.** To describe the molecule equilibrium, a computer assisted conformational search is indispensable. Those conformers should satisfy NOESs and dihedral angles from *J*-based couplings restrictions. It is assumed a restricted number of conformers to be present and one alignment tensor can be fit to all conformers jointly, significantly reducing the amount of linearly independence RCSAs required.[12–14]

(b) **Experimental anisotropic measurements (RDC and RCSA).** Data is completed mainly by two methodologies: (i) a stretching device originally used to measure RCSAs in proteins, which produces RCSA data free of isotropic shift interference, and (ii) a compression device which suffers from isotropic chemical shift interference and the RCSA data must be corrected before the fitting. Both devices are available by New Era Company. [15,16]

A crucial factor for a good anisotropic analysis is the *choice of the right solvent and alignment media.* The deuterated solvent should completely dissolve the sample, avoiding the formation of aggregates. On the other hand the alignment media must provide a degree of order that allows discrimination among the possible configurations. The choice for our analysis is a strain-induced alignment in a gel (SAG), where the degree of order is gel cross-linking dependent. In recent years, the influence of the background signal coming from the polymer as alignment media has been pointed out at microgram scales.[17] Using a device that reduces the mass of the gel-sticks is highly recommended. This is the case of the Hilgenberg's semi micro stretching device (2.4/1.8 mm) introduced in our study (see section 1.3.2.3). This device along with the micro/semi micro compression device (1.7 and 3 mm outside diameter respectably) are our recommendations over popular 5 mm New Era´s devices.

(c) **DFT-Chemical shift anisotropy tensor (CSA) computation**. DFT calculations gives enough degree of accuracy when the Gauge-Independent Atomic Orbital (GIAO) method is used. Nath *et al*. have recently demonstrated that the Continuous Set of Gauge Transformations (CSGT) approximation can be also used without detriment to the results.[18]

(d) **Calculation of the alignment tensor ($\hat{A}$).** This step fits all RCSAs to the DFT-computed CSA tensor through the singular value decomposition (SVD) method.[3]

(e) **Comparisons of the fitting Quality factor.** The fitting is expressed either by Cornilescu's (Q) or Q(CSA) quality factor.[19] The latter is computed by scaling both experimental and back-calculated ΔRCSA's by each corresponding atom's chemical shift anisotropies. Quality factors emerge from the formula given below in

(f) Figure 6, where $CSA_{i,ax}$ equals $\sigma_{33} - (\sigma_{22} + \sigma_{11})/2$ and the chemical shielding Eigenvalues σ_{11-33} are obtained from DFT.

(a)

$$RCSA^i(ppm) = \sum_{\alpha,\beta=x,y,z} A_{\alpha\beta} CSA^i_{\alpha\beta}$$

Single Value Decomposition (SVD)

$$D_k(r_k, r_H) = -\frac{\gamma_{k1}\gamma_{k2}\mu_o h}{8\pi^3} \langle \frac{3cos^2(\theta(r_k, r_H)) - 1}{2r_k^3} \rangle$$

Experimental RCSAs and RDCs

Ensemble of structures

(c)
$$\begin{pmatrix} \sigma_{xx} & \cdots & \sigma_{xz} \\ \vdots & \ddots & \vdots \\ \sigma_{zx} & \cdots & \sigma_{zz} \end{pmatrix}$$

CST (GIAO)

(d)

$\hat{A}$

$$Q_{CSA} = \sqrt{\frac{\left(\frac{RCSA^{exp}_{i,ax} - RCSA^{calc}_{i,ax}}{CSA_{i,ax}}\right)^2}{\Sigma\left(\frac{RCSA^{exp}_{i,ax}}{CSA_{i,ax}}\right)^2}}$$

Back-calculate RCSAs

$$Q = \sqrt{\frac{\left(RCSA_{exp} - RCSA_{cal}\right)^2}{RCSA^2_{exp}}}$$

$$Q = \sqrt{\frac{\left(RDC_{exp} - RDC_{cal}\right)^2}{RDC^2_{exp}}}$$

(e) Calculate $Q(Q_{CSA})$ for each configuration and compare them
Lowest $Q(Q_{CSA})$ will give the best fitting : **Correct Answer**

Figure 6. General strategy used in RDC and ^{13}C and ^{1}H RCSA analysis for resolving the relative configuration of flexible small molecules.

1.1.10 NMR Experiments for measurement of direct carbon-proton residual dipolar coupling $^1D_{CH}$

1.1.10.1   CLIP/CLAP-HSQC

Heteronuclear residual dipolar one-bond couplings of organic molecules at natural abundance are most easily measured using t2 coupled HSQC spectra. However, inevitably mismatched transfer delays result in phase distortions due to residual dispersive antiphase coherences in such experiments. CLIP/CLAP-HSQC experiment, slightly modified t^2 coupled HSQC experiments with clean inphase (CLIP) multiplets are introduced which also reduce the intensities of undesired long-range cross peaks. With the corresponding antiphase (CLAP) experiment,

situations where α and β components overlap can be resolved for all multiplicities in an IPAP manner.
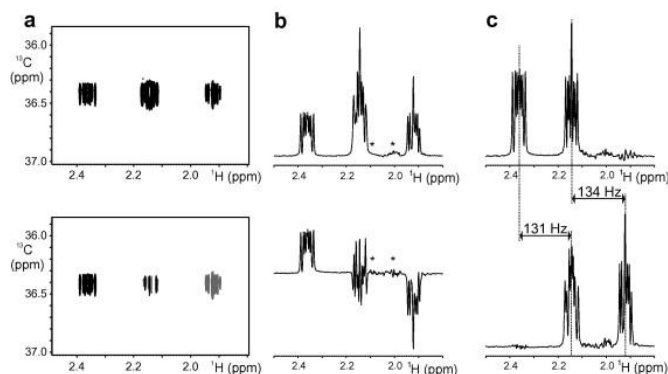
Figure 7 CLIP and CLAP-HSQC spectra of a methylene group of 6-methyl-2-phenyl-1-oxa-spiro[4,4]non-2-en-4-one dissolved in CDCl$_3$ and recorded at 600 MHz proton frequency (a). After combining the two spectra in IPAP manner (b), coupling constants of the overlapped signals can be determined from the corresponding α and β subspectra (c). Residual long-range signals are marked with asterisks in (b). [i]

It is worth mentioning, the recently development Real-time broadband proton-homodecoupled CLIP/CLAP-HSQC. [20] The new real-time pure shift CLIP/CLAP-HSQC experiments are designed to speed up coupling constant determination, to increase the sensitivity of measurement, and to simplify the extraction of accurate one-bond heteronuclear couplings from pure in- or anti-phase doublets using automatic peak picking.

1.1.10.2   J-Resolved HSQC

The accurate and precise measurement of one-bond scalar and residual dipolar coupling (RDC) constants is of prime importance to be able to use RDCs for structure determination.
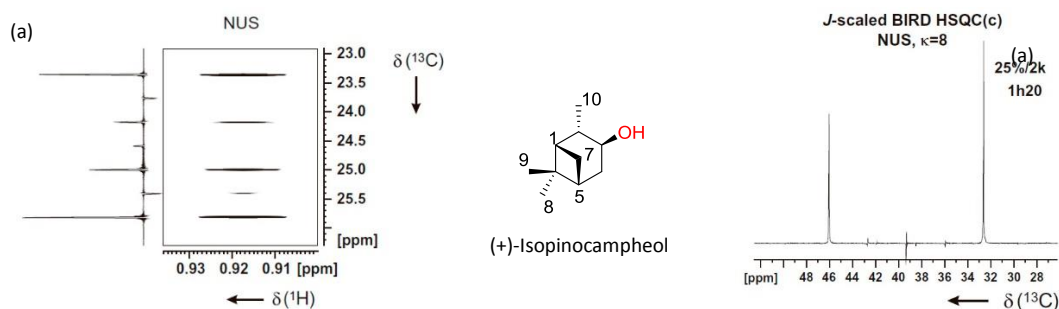
Figure 8 Section of the C9 methyl group of (+)-IPC in isotropic solution and corresponding extracted columns from x1-coupled HSQC (a and b) and BIRD-HSQC (c and d) spectra recorded under traditional sampling scheme (a and c) and using NUS with 30% of 4k (30%/4k/1228) complex points (b and d).

---

[i] Taken from Re. [112]

Coupling constants extraction from the indirect dimension of HSQC spectra has a significant saving of measurement time can be achieved by non-uniform sampling (NUS). [21] This is the approached used in the experiments used in this research

1.1.11 NMR Experiments for measurement of Residual Chemical Shift Anisotropy

1.1.11.1   Carbon de coupling

An appropriate and robust way to measured ^{13}C RCSA is thru an 1D sequence with decoupling using 30 degree flip angle.[4] In the recent methodology published by Nath *et al.* [22] is the experiment chosen to solve several molecules of increasing complexity. Its use is displayed in Figure 9
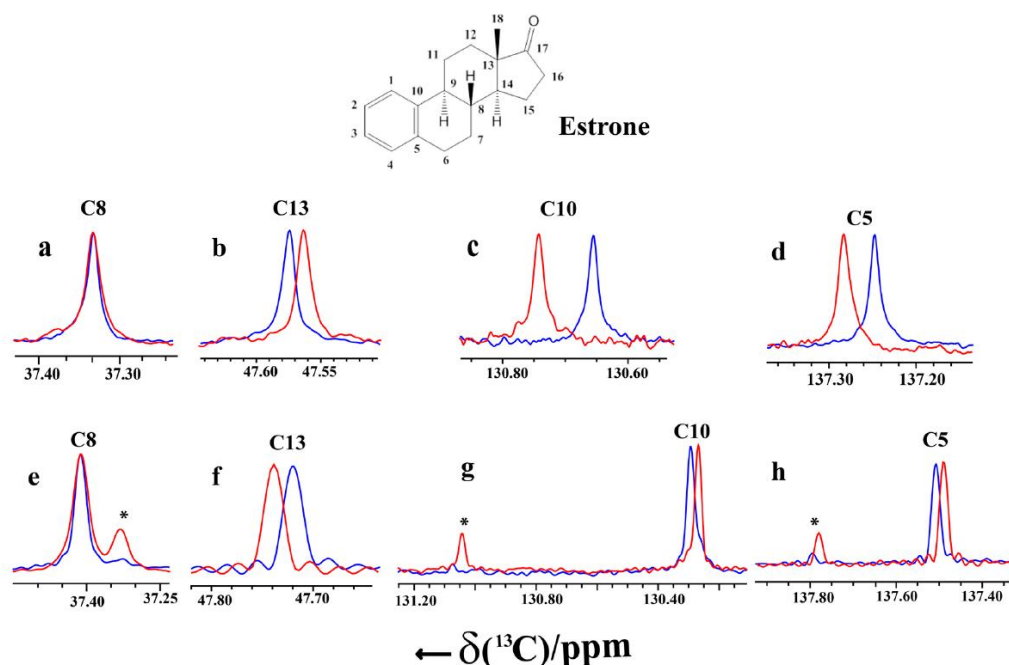
Figure 9 ^{13}C RCSAs obtained with stretching and compression devices. Stretching device: Panels a–d show resonances extracted from the ^{13}C-{^{1}H} 150 MHz NMR spectra of estrone in the narrow-bore (blue) and wide-bore (red) sections of the tube. *Compression device:* Panels e–h show resonances from the ^{13}C-{^{1}H} 225 MHz NMR spectra from estrone observed under minimum (red) and maximum (blue) compression. The C8 resonance shown in panel e was used as the reference resonance. Note the presence of both isotropic (marked with an asterisk) and anisotropic signals for some carbons. Spectra recorded with minimum alignment were recorded under almost complete relaxation of the PMMA gel had approximately 67% of the analyte in the gel. Maximum compression (ΔvQ = 48 Hz) increased the molar fraction of the gel residing population to 85%. *[ii]*

[ii] See Ref. 22

A recently published article from Márco *et al.*[23] applies an 1D Psyche, Carr-Purcell-Meiboom-Gill sequence (CPMG) in a pure shift HSQC experiment[24,25] during the measurement of residual chemical shift anisotropy (Figure 10).

In the present Thesis dissertation, the practical use of this sequence will be presented for the first time. Initially as proof of concept in a series of molecules and then in the resolution of a new natural products from marine and terrestrial origin.

Δδ('H)=	H4	H3	H1	H2	H22	H12	H23a	H23b	H16	H8
	9.7	5.8	<1.5	2.6	<1.5	4.7	3.3	3.3	1.5	<1-5
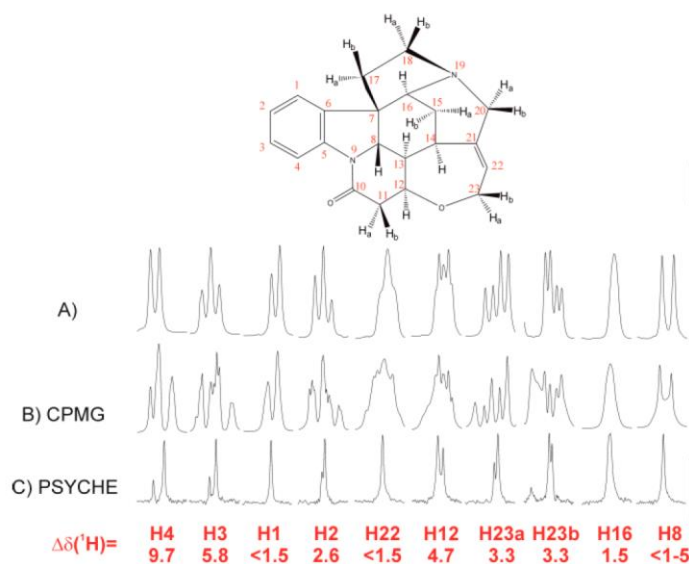
Figure 10 Expanded 1D multiplets corresponding to the 600.13 MHz (A) conventional ^{1}H spectrum of an isotropic sample of strychnine in CDCl$_3$, and (B) CPMG and (C) homodecoupled PSYCHE experiments of an anisotropic sample of strychnine dissolved in a compressed PMMA/CDCl$_3$ gel (^{2}H ΔδQ(CDCl3) = 33.6 Hz). Note that Δδ (1H) > 1.5 Hz can be determined for those resonances showing differentiated isotropic and anisotropic singlet signals in the homodecoupled spectrum.

1.1.11.2   1D Psyche pure shift

Broadband homodecoupling techniques in NMR, also known as "pure shift" methods, aim to enhance spectral resolution by suppressing the effects of homonuclear coupling interactions to turn multiplet signals into singlets. Such techniques typically work by selecting a subset of "active" nuclear spins to observe, and selectively inverting the remaining, "passive", spins to reverse the effects of coupling. [26] Pure Shift Yielded by Chirp Excitation (PSYCHE) is one such method; it is relatively recent, but has already been successfully implemented in a range of different NMR experiments. [25]
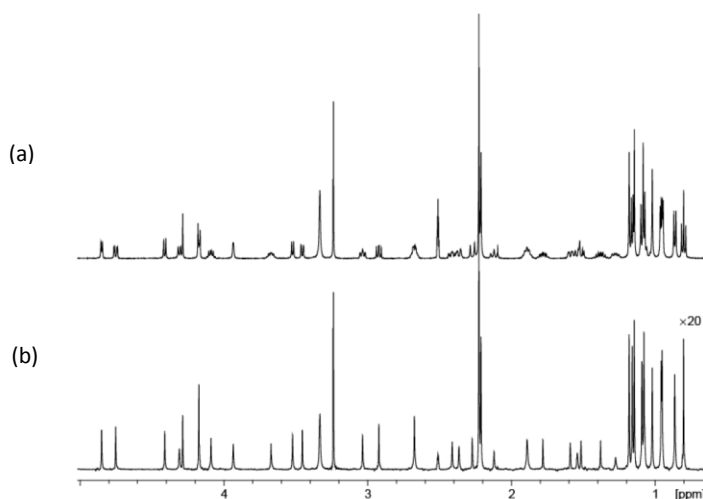
Figure 11 Normal 1H NMR (a) and PSYCHE (b) spectra of a 72 mM sample of azithromycin in DMSO-*d*6. Pure shift pulse-sequence greatly improve resolution, but often at a high cost in sensitivity. Here in new class of pure shift experiments (PSYCHE) was used; with superior sensitivity, spectral purity, and tolerance of strong coupling.[iii]

1.1.11.3   Real-time pure shift HSQC

Spectral resolution in proton NMR spectroscopy is reduced by the splitting of resonances into multiplets due to the effect of homonuclear scalar couplings. Although these effects are often hidden in NMR spectroscopy by low digital resolution and routine apodization, behind the scenes homonuclear scalar couplings increase spectral overcrowding (Figure *12*). [27] Pure Shift NMR Spectroscopy suppresses the effects of homonuclear coupling, allowing HSQC spectra to be produced that contain chemical shift only in both dimensions. Real-time pure shift acquisition provides a major improvement in resolution, and a modest sensitivity enhancement, compared to the conventional g-HSQC experiment. [24]
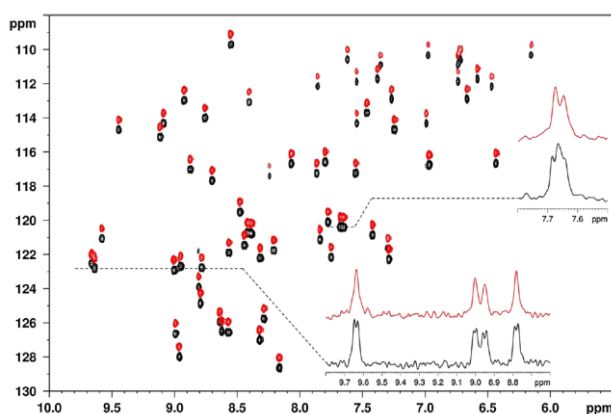
Figure 12 ^{1}H–^{15}N HSQC-SE spectra of unlabeled mutant PAFD55N (3) in 95 % H_2O/5 % D_2O without (black, lower) and with (red, upper) real-time pure shift gBIRD acquisition. The pure shift spectrum is shifted in the nitrogen dimension for easier comparison. The top right inset shows two overlapping peaks [iv]

[iii] See reference 26
[iv] See reference 27

1.2 Main Objectives

The use of anisotropic NMR in the analysis of the structure elucidation of chiral small molecules has been expanded in the recent years. Nowadays, Residual Dipolar Constants (RDC) can be applied as a standard tool for the efficient improvement in the elucidation of the relative configuration of small compounds determined by standard NMR data.

In this chapter 1, we want to further explore the use of another anisotropic NMR method based on residual chemical shift anisotropy (RCSA) measurements, as well as the utilization of a new compression and stretching NMR tubes to be applied also as an additional NMR tool available for spectroscopists.

To complete this main goal, we will address these new methodologies as follows:

- Development of the approach for the measurement of ^{1}H-RCSA. Demonstration as proof of concept with to known compounds: strychnine, estrone and retrorsine.
- Assembly of new alignment devices for the measurements of ^{13}C/^{1}H RDC and ^{13}C/^{1}H RCSA. Those include:
    1. A new device for shimming and locking to be used in anisotropic media
    2. A new universal compression device for 3 mm NMR tube. Application to a known terpene, α-santonin, and to a flexible compound with restricted rotation the meroditerpene **1**
    3. Application to the total resolution of new natural compounds with conformational flexibility with ^{1}H and ^{13}C RCSA and ^{13}C RDC using a HSQC pure shift and NUS: the case of the tricholomaminde A and B.
    4. A new 3 mm stretching device for the measurements of ^{13}C/^{1}H RCSA and RDC. Application to a known steroid, progesterone
- Application of the developed methodologies for the submicrograms structural elucidation with deuterated gels: the diterpene briarane-3.

1.3 Unequivocal determination of 3D molecular structures including relative configuration using proton residual chemical shift anisotropy (RCSA)

1.3.1 The proton Residual Chemical Shift Anisotropy (^{1}H RCSA)

1.3.1.1 State of the art

Given the enormous diversity of natural products, the elucidation of the relative and absolute configurations, is the main objective of exhaustive investigations by chemists and molecular structural biologysts.[28] It is well known that different stereoisomers (eg starch and cellulose) show different biological and pharmacological properties.

Currently, an increasing number of chiral drugs have been clinically approved as a single configuration, since one of the enantiomers is either less active or has side no desired effects.[29] This is one of the reasons why pharmaceutical research critically relies on the correct determination of the relative and absolute configurations of stereogenic centers in a molecule.

A latest SciFinder search under the keyword "structure revision" brings to light that there were more than 1200 wrong structural reports in the period 1991 and 2016, with ~~There are~~ even 39 wrong structural reported in 2016. It is important to notice that these are just the known incorrect structures not including the unknown ones. Therefore, once the molecular constitution is known, the determination of the relative configuration of the stereogenic centers in a natural product is essential.[28] However, so far any method is time-consuming and error-prone.[30] Total synthesis, probably the most laborious and time consume approach, is considered to be the gold standard to establish a final configuration.[28] Yet, total synthesis of mefloquine and ulapualide, for instance, provided a wrong absolute and relative configuration assignation, respectively, as it has been reported.[31–33] While X-ray crystallography is a standard technique for crystalline compounds, Nuclear Magnetic Resonance (NMR) is the method of choice to determine the relative configuration when a suitable crystal is not available.

Conventionally isotropic NMR restraints viz., Nuclear Overhauser effect (NOE)[34] and J-couplings[35] are used to establish 3D features of molecules. However, the combination of these two restraints proves to be insufficient for configuration determination in most cases, specifically when either stereoclusters of chiral centers are separated by several bonds or the molecule presents a highly degree of flexibility (Figure 13)
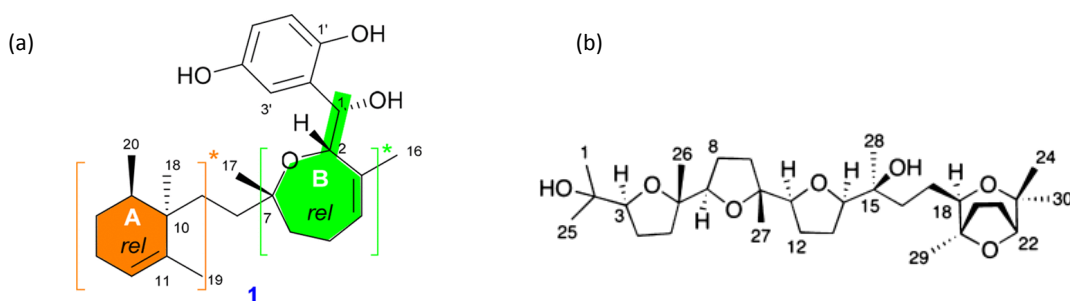
Figure 13 . Halioxepine was isolated from an Indonesian sponges of the genus Haliclona, represents an example of two separated stereoclusters (a). The pentacyclic polyether, Nivariol, isolated from Laurencia viridis a molecules with potential flexibility with a high number of quaternary carbon atoms that it contains make its configurational assignment very difficult (b)

Anisotropic NMR along restraints NOE[36] methods and J-based coupling analysis (JBCA)[37] have contributed in a crucial way how to resolve new chemical entities.[38,39] Residual dipolar coupling (RDCs)[14,40–44] and residual chemical shift anisotropy (RCSA) are two anisotropic NMR parameters employed specifically for nuclei with spin 1/2.[4,10,16,22,45,46] While, in the past decade, it has been found that RDCs, principally the one-bond $^1D_{CH}$, have become essential to determine the configuration of small molecules, ^{13}C RCSA can be robustly measured only since 2016.[22] Yet, ^1H RCSAs, that should be measurable even for minute quantities of compound because of the high natural abundance of ^1H, have not been introduced to determine the configuration of small molecules.

1.3.1.2 Alignment media

Measurement of anisotropic NMR parameters requires partial ordering of the molecules in alignment media such as aligning gels and liquid crystals.[38,47–53] Although RDC has become the most common anisotropic data, their sensitivity turn out to be problematic if the available amount of sample is below of few hundreds of micrograms.[54] On the other hand, to overcome the difficulty of RCSA measurements due to isotropic shift changes upon molecular alignment, robust ^{13}C RCSA data have been recently reported by using constrained PMMA (polymethylmethacrylate) gel either by compression or stretching.[10]
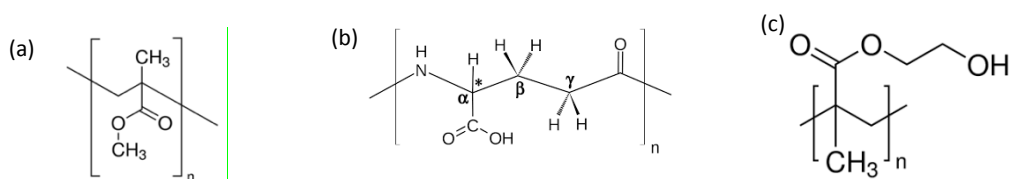
Figure 14. Alignment media has evolved so far until a point where almost solvents or any polarity can be used during anisotropy NMR. Polymethylmethacrylate gel (PMMA) is the It is the preferred choice for those molecules CHCl$_3$ compatibles (a) poly-Υ-(benzyl-L-glutamate) (PBLG) is another valid option for non-polar solvents, spatially those that yield small amount alignment as CH$_2$Cl$_2$. It is highly recommended in direct RDC measurement, due the high values of $^1D_{CH}$ found (b) DMSO-d6 is a valuable solvent, especially in drug design/development. Poly-HEMA offers compatibility with DMSO-d6: Moreover, RDCs and RCSAs can be measured by using it (c).

Same as RDCs, RCSAs allowed the determination of the relative configuration for molecules with several stereogenic centers from a pool of all possible other relative configurations. ^{13}C RCSAs were also extracted recently from PMMA gel with 3% cross linker density using another type of stretching device developed by Ad Bax and his coworkers for proteins. [7,55] Very recently, ^{13}C RCSA were also measured from the mesophase of a poly-Υ-(benzyl-L-glutamate) (PBLG) that involves three steps sample preparation.[56] However, ^{13}C RCSA measurement from ^1D ^{13}C-{^1H} spectra is a daunting task due to low sensitivity of carbon if the sample is available around 10 micrograms.

As mentioned above, ^1H RCSAs despite being the most sensitive anisotropic NMR parameter, have not been yet measured to determine the configuration of small molecules.

1.3.1.3 Specific objectives

Accurate ^{1}H RCSA measurement bears the promise to the spectroscopists that minute amounts will allow determination of relative configuration. In the section of this chapter, we will introduce two independent tools to robustly obtain ^{1}H RCSA data:

  a) In one implementation, RCSA will be collected on several rigid and flexible molecules by using stretchable PMMA and poly-HEMA (polyhydroxyethylmethacrylate) gels.

  b) In another implementation, ^{1}H RCSAs will be measured from polyacetylene based liquid crystal prepared in chloroform solvent.

Different alignment strategies by will be tested varying strength and temperature in order to achieve best gel performances. This methodology will not need any special tube or piston mediacy, therefore, the measurement will be performed in a 1.7 mm, 3 mm or in standard 5 mm NMR tubes unlike with the constrained gels that require special devices.[22] The measured RCSAs will be later employed in determining the relative configuration of several molecules.

It is noteworthy that polymer ^{1}H NMR resonances will dominate the spectrum and, very often, it will mask sample signals when the amount is less than 100 µg. This problem will be circumvented by the use of a deuterated gel (i.e. PMMA-d_8), as it will be demonstrated for 10 µg of strychnine.

1.3.1.4 Methodology: description

For a liquid crystalline sample, molecular alignment varies with the temperature. The dependency of the chemical shift is small and relatively constant over tens of degrees. Therefore, ^{1}H RCSAs can be measured by varying the alignment of the sample inside a 5 mm NMR tube at certain temperatures. One way to measure ^{1}H RCSAs is to record two different ^{1}H NMR spectra in anisotropic and isotropic phase, respectively. The ^{1}H chemical shift differences of both phases provide a set of uncorrected RCSAs, which can be corrected by calculating the *temperature-induced isotropic shift* using a second 1D ^{1}H NMR spectrum recorded at another temperature in the isotropic media. If the liquid crystal is anisotropic at 300K and isotropic at 305K and 310K, then the RCSA of nuclei "*i*" was determined from the following equation:

$$\Delta RCSA_i = \left(\delta_i^{300K} - \delta_i^{305K} \right) - \left(\delta_i^{305K} - \delta_i^{310K} \right) = \delta_i^{300K} - 2\delta_i^{305K} + \delta_i^{310K} \qquad \text{Equation 5}$$

where 'i' is ^{1}H and δ_i is the chemical shift of proton "i". This equation assumes that the temperature gradient for the isotropic shift behaves linearly between 300 and 310 K, such that the anisotropic shift can be separated from the temperature dependent isotropic shift.

In case that there are no two conditions yielding isotropic phases in the temperature range that is accessible in the spectrometer, the RCSA can be also measured correctly by measuring the anisotropic and isotropic spectra at two temperatures e.g., 300K and 315K using the following equations:

$$\mathrm{D}RCSA_i = [(\delta_i^{300K} - \delta_{ref}^{300K})_{aniso} - (\delta_i^{315K} - \delta_{ref}^{315K})_{iso}]$$

Equation 6

where, δ_{ref} is the chemical shift for any chosen reference nucleus. Reference nucleus is chosen in the bases of it CSA value, those with the lowest value are the best to be used as Reference.

For stretchable gels, the molecular alignment is induced by elongating the gel through a radial mechanical force. During this process, the concentration of analyte is kept constant and hence, no correction due to isotropic chemical shift changes is required. For such a gel, the RCSA of a nucleus "i" is derived from the following equation:[10]

$$\mathrm{D}RCSA_i = [(\delta_i - \delta_{ref})^{max} - (\delta_i - \delta_{ref})^{min}]$$

Equation 7

In this case, one of the nuclei is taken as reference atom, and RCSA's are measured as chemical shift differences between the maximum (Max) and minimum (Min) alignment conditions.

The anisotropic distribution of orientations of the compound under alignment conditions is described by the alignment tensor $\hat{A}$ that contains five independent parameters and therefore requires minimally five linearly independent RCSAs.[3,57] Furthermore, the chemical shift tensors necessary for RCSA analyses can be obtained at low computational cost by using density functional theory (DFT) calculations in Gaussian 09.[58,59] These DFT methods are very powerful and reliable in determining the various NMR parameters from optimized geometries. In practice, they can be calculated in parallel in a time frame that is usually chosen for the measurement of experimental data, thereby speeding up the structure elucidation process.

The proton chemical shifts can be calculated with appropriate accuracy by using DFT methods with a larger basis set or by using Møller-Plesset perturbation (for example MP2) theory. Contrarily to carbon chemical shifts theoretical calculations, which are marginally influenced by solvent, proton RCSAs are noticeably affected by the solvent. In view of this, we performed calculations in two steps:

- Firstly, proton chemical shifts were computed at different DFT functional models and MP2 level with various medium to larger size basis sets. This step enables the selection of the best theoretical model.
- The impact of the different solvent models on the CSA values were also tested on this model.

For methyl groups all three proton RCSA tensors are calculated and then an average tensor is estimated.

The experimentally measured RCSAs are fitted to an alignment tensor using a Singular Value Decomposition (SVD) model as is implemented in the MSpin program.[9] The quality of the fit is represented with the following Q factors; sometimes referred to as $Q_{UNSCALED}$.

$$Q = \sqrt{\frac{\sum (RCSA_{exp} - RCSA_{cal})^2}{\sum RCSA_{exp}^2}} \qquad \text{Equation 8}$$

and

$$Q_{CSA} = \sqrt{\frac{\sum [(RCSA_{exp} - RCSA_{cal})/CSA]^2}{\sum (RCSA_{exp}/CSA)^2}} \qquad \text{Equation 9}$$

in which, CSA, the axial anisotropy of the tensor equals $\sigma_{33}-(\sigma_{22}+\sigma_{11})/2$, and the chemical shielding Eigen-values σ_{ii} are obtained from DFT calculations.

1.3.1.5 ^{1}H RCSA to a rigid molecule: strychnine

Alignment media using a stretching gel

We measured ^{1}H RCSA's for a well-studied model system, strychnine. For alignment media we used separately a polyacetylene based liquid crystal and a stretched PMMA gel using formulae represented by Equation 6 and Equation 7, respectively and they are subsequently utilized for the configuration analysis.

Initially, 8 mg of strychnine were aligned in PMMA/CDCl$_3$ gel by using a special NMR tube that has an inner diameter of 3.2 mm for maximum alignment and of 4.2 mm for the minimum alignment. The measured RCSAs ranged from 2.1 to 8.4 Hz at 700 MHz. For the analysis, from the observed ^{1}H RCSAs and DFT determined CSA tensors an alignment tensor was determined through least-squares SVD fitting for different relative configurations by using the MSpin program. The quality of the fit is measured through Q factors. Ideally, for the correct

configuration, the Q factor should be 0. Only 13 out of 32 possible configurations are energetically feasible due to the multicyclic constitution of strychnine.

These 13 configurations were used in the analysis and their chemical shift tensors were computed by DFT at B3LYP/6-311+g(2d,p) level by using the ICF-PCM solvent continuum model with $CHCl_3$ as a solvent in Gaussian09.[58,59] The configurations were labelled via the *R* or *S* configuration of carbons C7, C8, C12, C13, C14, and C16 respectively, for example *RSSRRS* for the correct configuration.

We found for the correct configuration RSSRRS a Q factor 0.253 and for the configuration RSRRRS a similar Q factors 0.256. These two configurations also showed the best fittings based on ^{13}C RCSA with Q factors 0.050 and 0.100, respectively. [16] CSA tensors for protons, including the axial component, varied over a large range. For instance, the variation was from 10.2 ppm for H18b to 3.4 ppm for H8.

As an example, axial anisotropies for aromatic protons viz., H1, H2, H3 and H4 were 10.2, 4.9, 4.4 and 9.3 Hz, respectively, while those for the aliphatic protons 11Hb, 13H, 20Ha, 15Hb and 18Ha were 4.7, 2.9, 9.4, 10.2 and 11.0 Hz, respectively. It was also observed that the CSA of the diastereotopic proton H18 was 11.0 Hz while for the other pair was 5.7 Hz. This large variation for diastereotopic protons was also observed for other such pairs. Due to the large variation of CSA tensors (similar to the approach taken for the evaluation of carbon RCSAs) [22] Q_{CSA} (Equation 9) scales the RCSA errors of each nucleus with the axial value of the CSA. This makes the contribution of the RCSAs independent of their respective sizes and then it weighs each RCSA more equally. Indeed, the mentioned configurations RSSRRS with a Q_{CSA}=0.256 and RSRRRS with a Q_{CSA}=0.276 could be distinguished by this Q factor. Similarly to ^{13}C RCSAs, ^{1}H RCSAs furnished the lowest Q and Q_{CSA} factors for the correct configuration. The Q RCSA and Q_{CSA} factors computed for the thirteen energetically favorable configurations are listed with a bar diagram in Figure 15:
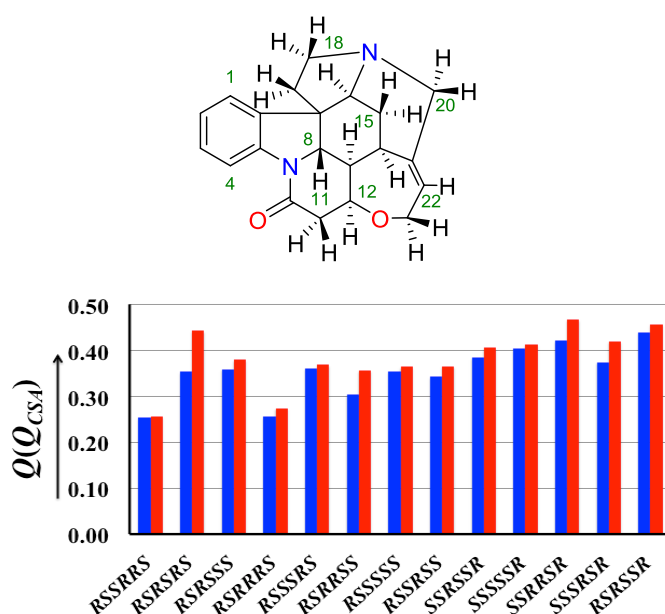
Figure 15. The Q_{CSA} factors (red bar) for the two closest configurations RSSRRS and RSRRRS are 0.256±0.03 and 0.274±0.03, respectively. The unscaled Q factors are reported with the blue bars. The two configurations RSSRRS and RSRRRS were also the two with the lowest Q factors in the ^{13}C RCSA analysis.

Alignment media using a liquid crystal

We explored the measurement of ^{1}H RCSA's of strychnine in a lyotropic liquid crystal made of L-valine derived polyacetylene and chloroform that uses different temperatures to induce dissimilar alignment conditions necessary for RCSA measurement. 12 mg of strychnine is aligned in the liquid crystal in 5 mm NMR tube. The sample provided maximum alignment at 300 K and minimum alignment at 315K. The RCSAs were measured by using Equation 7 and RCSAs have values in between -12 and 10.4 Hz. In this case, both ^{13}C and ^{1}H RCSA analysis furnished a slightly higher Q factors for the correct configuration (0.122 and 0.343) as compared to ^{1}H RCSA data collected in PMMA gel.[10] The Q (QCSA) factors are 0.343 (0.439) for RSSRRS and 0.414 (0.455) for the next best RSSSRS configuration. The results obtained for different configurations of strychnine in liquid crystal 1H RCSA data is represented in the bar diagram in Figure 16 below.
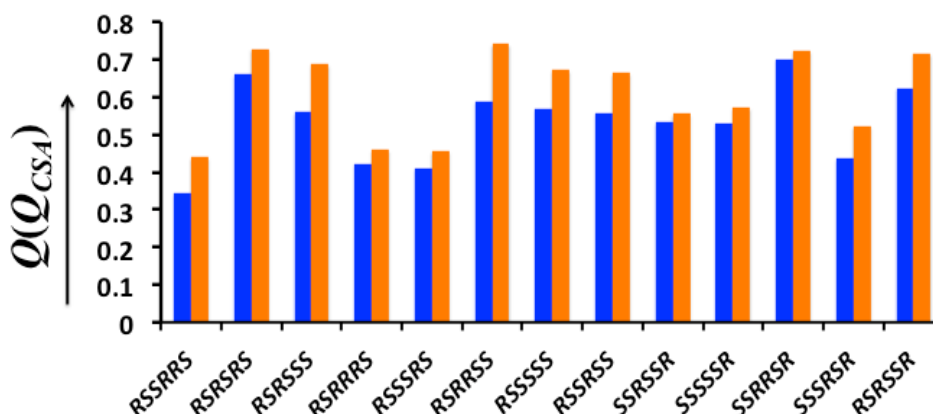
Figure 16. The unscaled Q factors (blue bar) and Q_{CSA} factors (red bar) are reported for thirteen configurations of strychnine aligned in polyacetylene liquid crystal.

1.3.1.5.1   Improving the method sensitivity using a deuterated gel

The sample for the above-discussed molecule contained 8 mg strychnine. Regarding high sensitivity of proton detection, ^{1}H RCSAs should be measurable down to a few micrograms of the sample embedded in a PMMA gel. However, the signals of the protons of the gel overshadow large regions in the spectrum to an extent that T_2 filters and solvent suppression do not work efficiently. The best way to exclude the solvent signal is using deuterated gels that can be made from commercially available deuterated monomers along with a protonated cross-linker, which unfortunately is more difficult to obtain in a deuterated form. However, the protonated cross-

linker does not pose a problem, as it constitutes only a very small fraction of the gel. The prominent signals that are usually observed in the protonated gels are efficiently suppressed in deuterated gels and is presented in the supplement material (see Figure 17)

Figure 17 compares the 1D ^{1}H NMR spectrum of 300 µg of strychnine, which was acquired by using a stretchable protonated PMMA gel (Figure 17, panel a), with that of 80 µg of strychnine aligned in deuterated PMMA gel (PMMA-d_8) (Figure 17, panel b). Note that in PMMA-d_8, the polymer signals are suppressed completely allowing the extraction of 20 ^{1}H RCSAs of strychnine. In contrast, in the protonated gel, only a few signals of strychnine are visible with low intensities and many of the ^{1}H resonances are masked by very intense polymer signals. It is noteworthy that significant suppression of polymer signal is possible from PMMA gels by using a 1.7 mm compression device (see the supplementary material). The preparation of each deuterated gel sample cost 16 USD more than that of a protonated gel (see supplementary material). The range of RCSA shifts of the resonances using the stretching device was approximately -0.8 to 3.4 Hz in a 800 MHz spectrometer. When the ^{1}H RCSAs were SVD-fitted into a single tensor, it furnishes a Q (Q_{CSA}) factor of 0.199 (0.220) for RSSRRS and 0.264 (0.299) for the next best RSRRRS configuration. The other 11 configurations have even higher Q (QCSA) factors (see Table S4 and S5 in the supplementary material)

(a)
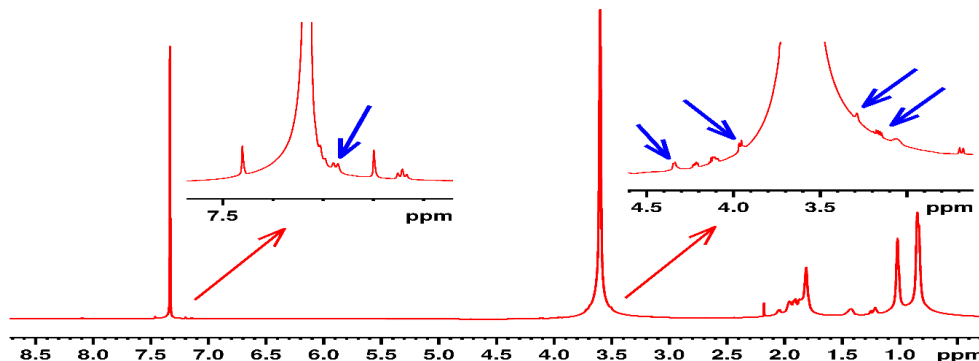
(b)
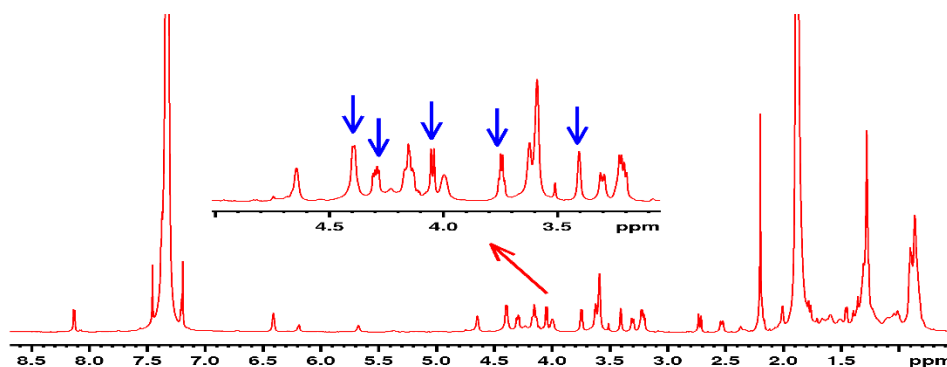
Figure 17. 1D ^{1}H NMR spectrum (128 scans) of 300 μg of strychnine in protonated gel. Note that few peaks are visible (indicated by the blue arrows) and many signals are masked by the polymer signals (a). 1D ^{1}H NMR spectrum (8 scans) of 80 μg of strychnine in deuterated PMMA gel (b). Both the spectra were recorded in a Bruker 800 MHz NMR spectrometer. Use of a stretching device that has an inner diameter of 4 mm for minimum and 3.2 mm for maximum alignments.

Encouraged by the above-mentioned results for 80 μg of sample, we decided to explore the limitation of the technology in terms of sample amount. Therefore, we aligned only 10 μg of strychnine in PMMA-d_8 gel. 1D ^{1}H NMR spectra were recorded for maximum and minimum alignment conditions using a stretching device with 4.2 and 3.2 mm inner diameters in a 800 MHz NMR spectrometer. 8192 scans were necessary to observe the signals with sufficient signal-to-noise ratios. 12 ^{1}H RCSAs were measured and compared to 20 RCSAs collected for 80 μg sample because of overlap with gel signals. When the ^{1}H RCSAs were SVD-fitted into a single tensor, it provided a Q (Q_{CSA}) factors of 0.092 (0.090) for the RSSRRS configuration and 0.116 (0.100) for the next best RSRRRS configuration, with other 11 configurations exhibiting higher Q (QCSA) factors.

1.3.1.6 Epimers discrimination by 1H-RCSA: estrone and 13-epi-estrone. Establishing the right functional in the DFT calculations

In order to find a DFT benchmarking in determining the effect of solvents in the computation of the anisotropy of CSA tensors, we were looking for the right combination of robust functional along with the basis set. CSA tensors were calculated in functionals such as B3LYP, MPW1PW91 and MP2 in different solvents.

3 mg of estrone were aligned in a poly-HEMA/DMSO-d_6 gel by using a special NMR tube with an inner diameter of 3.0 mm for maximum alignment and 4.2 mm for the minimum alignment. The measured RCSAs range from -1.6 to -6.4 Hz in an 800 MHz spectrometer. The analysis was made for two different configurations, estrone and 13-epi-estrone. While ^{13}C RCSA data collected in DMSO did not reach a correct configuration[45], ^{1}H-RCSAs proved to be most robust assigning the right epimer: the SVD-fitted ^{1}H RCSA data analysis provided the lowest Q / Q_{CSA} factors of 0.276/0.319 while for 13-*epi*-estrone, they were 0.396/0.419, respectively. The difference of 0.120 and 0.100 for Q and QCSA factors showed that the configuration differentiation is possible using just ^{1}H RCSA. It is worth mentioning that ^{13}C RCSA data acquired in PMMA gel gave Q factors of 0.09 and 0.13 for estrone and 13-*epi*-estrone, respectively.

The Q factors obtained for estrone and 13-epi-estrone are tabulated in Table 1. We find that the results are consistent in different theoretical models. It is noteworthy that proton CSA values for different models follow the identical trends (see supplementary material) with the exception of computation with smaller basis sets. The Q factors are provided in the bar diagram in Figure 18.

Table 1. Calculated Q factor for estrone and 13-*epi*-estrone in different theoretical combinations functionals-basis sets/solvents.

Method/basis set	Solvent	Q factor for estrone	Q factor for 18-*epi*-estrone
MPW1PW91/ 6-311+G(2d,p)	DMSO	0.279	0.444
B3LYP / 6-311+G(2d,p)	DMSO	0.280	0.430
B3LYP / 6-311+G(2d,p)	CHCl$_3$	0.309	0.430
MPW1PW91/ 6-31+G(2d,p)	DMSO	0.300	0.456
B3LYP / 6-311+G(2d,p)	Methanol	0.280	0.433
MPW1PW91/ 3-21+G(2d,p)	DMSO	0.303	0.435
MP2/ 6-311+G(2d,p)	CHCl$_3$	0.289	0.467
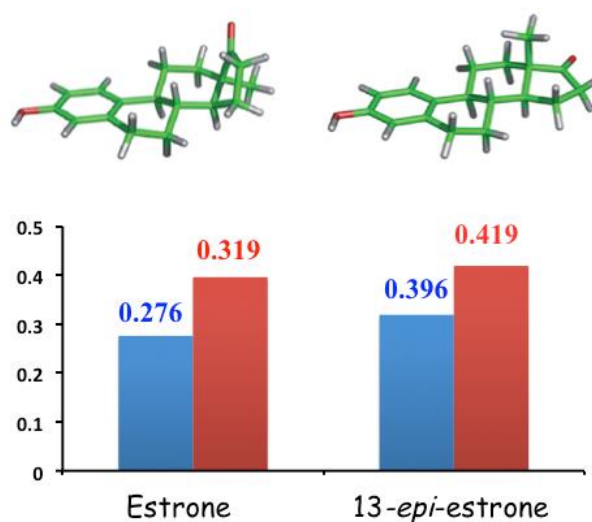
Figure 18. Unscaled Q factors (blue bar) and Q_{CSA} factors (red bar) for estrone and 13-*epi*-estrone

1.3.1.7 Retrorsine, a flexible molecule

Retrorsine is a good model to emphasize how complicate can be the structure elucidation of a molecule with several chiral centers, along with a high degree of flexibility in a fragment of the molecule. This compound has been also used in the past as a model for the total structure elucidation through RDC's. Authors observed that the methodology could not discriminate structures with different stereochemistry at the position C11 because the lack of information in this carbon with no hydrogens attached.[60] With the purpose to cover this experimental flaw, we would like to demonstrate that ¹H RCSA's extracted from a PMMA gel are able to discriminate even molecular situations with large flexibility.

For configuration analysis of retrorsine, the complete structural motifs that are compatible with the NMR data, need to be considered. In this way, all conformers that are energetically feasible were obtained by a conformational search in a molecular modeling calculations using the force field MMFF94 as is implemented in the Macromodel program.[61,62] Other type of programs, such as Maestro[61] of PCMODEL[63] can be also used for this purpose.

The four chiral carbons at C2, C3, C10, and C1, implies 8 diasteroisomers to be considered. All possible configurations were treated with a similar approach: conformational search, election of conformers, geometry and NMR properties DFT calculations followed by a final Q fitting using MSpin. The experimental RCSAs were fitted to a single tensor.

Therefore, 2 mg of retrorsine was aligned in the gel by using a stretching device and RCSAs were measured in an 800 MHz spectrometer. The RCSA analysis provided Q (QCSA) factors of 0.326 (0.408) and 0.406 (0.438) for configurations RRRS and RRRR, respectively. It may be notice, that these two configurations presented the lowest scores when ^{13}C RCSA analysis was performed with Q factors 0.184 and 0.216, respectively. At this point is easy to realize that the Q factor difference and ratio is larger, i.e. discrimination between the configurations is more obvious using ^{1}H RCSA (Figure 19).
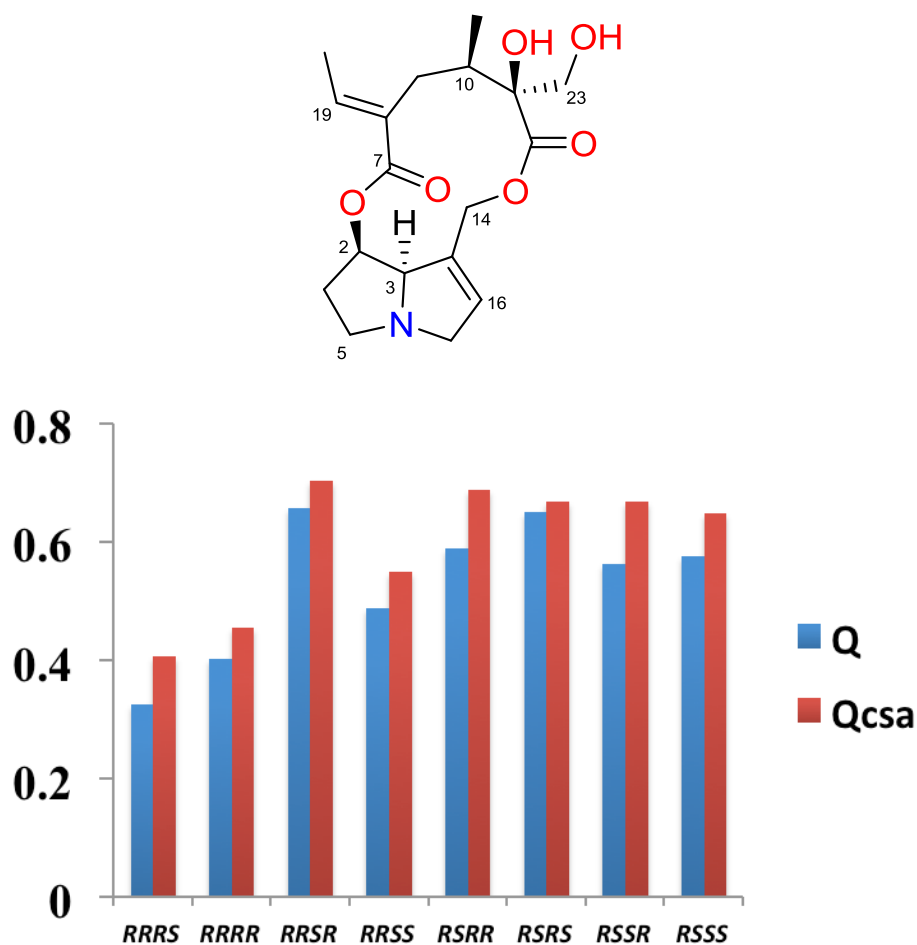
Figure 19. The unscaled Q factors (blue bar) and QCSA factors (red bar) for the eight possible relative configurations for the retrorsine.

We also wanted to investigate what was the minimum amount of sample required to reliably extract ^{1}H RCSA's, in PMMA gels and polyacetylene-based liquid crystal. To meet this goal we made all the measurements in a stretching device that has inner diameters of 4.2 and 3.2 mm to induce maximum and minimum alignment conditions. We were able to collect data to just 10 µg of strychnine in a PMMA-d_8 gel and 1.2 mg for a PMMA gel. However, for liquid crystal 1 mg of strychnine is required for a good RCSA measurement when a standard 5 mm NMR tube was used. However, by the combined use of a deuterated polyacetylene liquid crystal and 1.7 mm tubes, one might further reduce this amount. The minimum amount of sample, which is necessary for different types of aligning gels under various stretching conditions and also for liquid crystal, can be found in the supplementary material.

1.3.1.8 Partially deuterated gel obtained by radical polymerization of 2,2'-azobis(2-methylpropionitrile) and monomer methylmethacrylate-d8 to measure RCSA's and other anisotropic parameters

Deuterated gels used as anisotropic alignment media, have the best performance a concentration fixed of monomer set to 70 % v/v, meanwhile a molar concentration of the cross linker of either 0.04 or 0.05 mol % EGDMA is recommended. The radical polymerization process is suitable for both the New Era's stretching device (4.2/3.2; 3.0 mm) [16,22] and for the Hilgenberg's stretching device (2.4/1.8 mm).[18]

The radical initiated polymer reaction of methylmethacrylate (MMA) cross-linked with EGDMA is well described in literature.[64] Free radical polymerization of MMA-d_8 using 2,2'-azobis(2-methylpropionitrile) (AIBN) at high temperature mainly goes through a termination by disproportionation and a final incorporation of the butyl group of the initiator into the polymer chains.[65,66] The network of the cross-linked PMMA structure has been reported before,[67,68] We critically assume that in the case of deuterated monomer (MMA-d_8) the main network present in the polymer is the normal cross-linked (Figure 20), nevertheless other possibilities are also possible.[67]
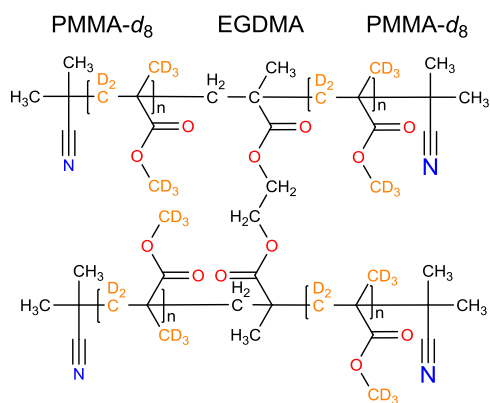
Figure 20. Normal cross-link chemical structure of EGDMA-cross-linked PMMA-d_8

Both ^{1}H and ^{13}C spectra of protonated PMMA (70/0.04) are given in Figure 21. The signal at 0.772 ppm corresponded to the methyl protons in alpha position to the carbonyl group, the two small peaks in the olefinic proton region at 6.086 and 5.569 ppm are assigned to the vinyl methylene protons at the chain formed through the disproportionation reaction (Figure 21 b). We did not find any evidence of the terminal olefinic methine proton (Figure 21 c), expected at 6.5-7.0 ppm, [69] yet we do not rule out its present, they can be overlapped with the broad peak with a chemical shift of 3.519 ppm correspond to the pending methoxy group in the side chain. ^{13}C spectrum (Figure 21 e) was assigned in basis of an HSQC experiment (SI) and matched with previous reported data.

Two versions of the stretchable PMMA-d_8 were prepared (70/0.04 and 70/0.05) and both showed suitable properties to be used as alignment media in the determination of ^{1}H RCSA. The 70/0.04 gel was prepared with a 5% of protonated MMA while the 70/0.05 one uses only MMA-d_8 leaving only as a source of protons those presents in the cross linker (EGDMA). This strategy allowed us to fully assign the signals in both polymers. a and b show both ^{1}H spectra on PMMA-d_8 70/0.04 and 70/0.05 respectably. In the two spectra we can observe signals corresponding to the methyl groups (1.47 -2.17 ppm) from the initiator (AIBN), while the gel PMMA-d_8 70/0.04 showed two signals with moderate intensity at 0.772 ppm and 1.198 ppm corresponding to the α–CH$_3$ and –CH$_2$- from the protonated MMA. As expected those signal are absents in the PMMA-d_8 70/0.05 gel (b). On c) and d), signals from 3.0 to 6.7 ppm due to the remaining protons in the monomeric units are present on both deuterapolymers.

On Figure 23 we can observe all the spectra overlapped for the described gels. We believe that it will allow to have stronger signals from analytes because the absence of protons from the gel, and therefore a most easy measurement of ^{1}H RCSA's. Another anisotropic parameters like long range ^{1}H-^{1}H RDC and direct RDCs will be also easier to extract from 1D spectra.

Relative hydrogen content of the synthesized PMMA gels was determined by integrating the relative intensity of the signal of interest to the signal due to the partially undeuterated chloroform present in the lock solvent (Table 2). Protonated gel shows the highest number of protons as the only source of deuterium derives from the interchangeable proton in CD$_3$OD, as a matter of fact is demonstrated that is included in the polymer network yet is meaning less in this case.[66,70] Both deuterated polymers showed –CH$_3$ groups from the mentioned disproportionation step, with similiar order of magnitude, while PMMA-d_8 the α-CH$_3$ and –CH$_2$-

moieties are present just in the PMMA-d_8 (70/0.04), which contains 5 % of MMA-H$_8$. No signs of these methyl or methylene groups are observed in the PMMA-d_8 (70/0.05).

Table 2. Relative proton contend in AIBN cross-linked methyl Methacrylate using protonated and deuterated monomer

Polymer	-CH$_2$- from protonated monomer	α-CH$_3$ from protonated monomer	-OMe from protonated monomer	-CH$_3$ from AIBN	-CH$_3$ from AIBN
PMMA-H$_8$ (70/0.04)	11.000	28.000	69.000	NR	NR
PMMA-d$_8$ (*) (70/0.04)	670	690	188	1300	2100
PMMA-d$_8$ (70/0.05)	-	-	123	1400	1350

(*) Contains 5 % of protonated monomer. We badly assigned a value of 3000 to the signal due to the partially undeuterated chloroform. NR not readable. (-) Not present

We would like to point out that the presence of those signals does not cause major inconveniences, even measuring samples at micrograms levels. Furthermore, the importance of using fully deuterated methanol as solvent on the polymer reaction; it has been reported the introduction of a proton from methanol as terminal methine that produces a singlet at 2.57, which is not present in any of our gels [65]

Spectra and assignment of all the chemicals used were done based on spectra measured in a Bruker 700 MHz equipped with a cryo-probe with CDCl$_3$ as locking solvent; ^{1}H, ^{13}C and HSQC were recorded using 32, 256 and 4 scans and an spectral with respectively. All the chemical were inside specified purity.
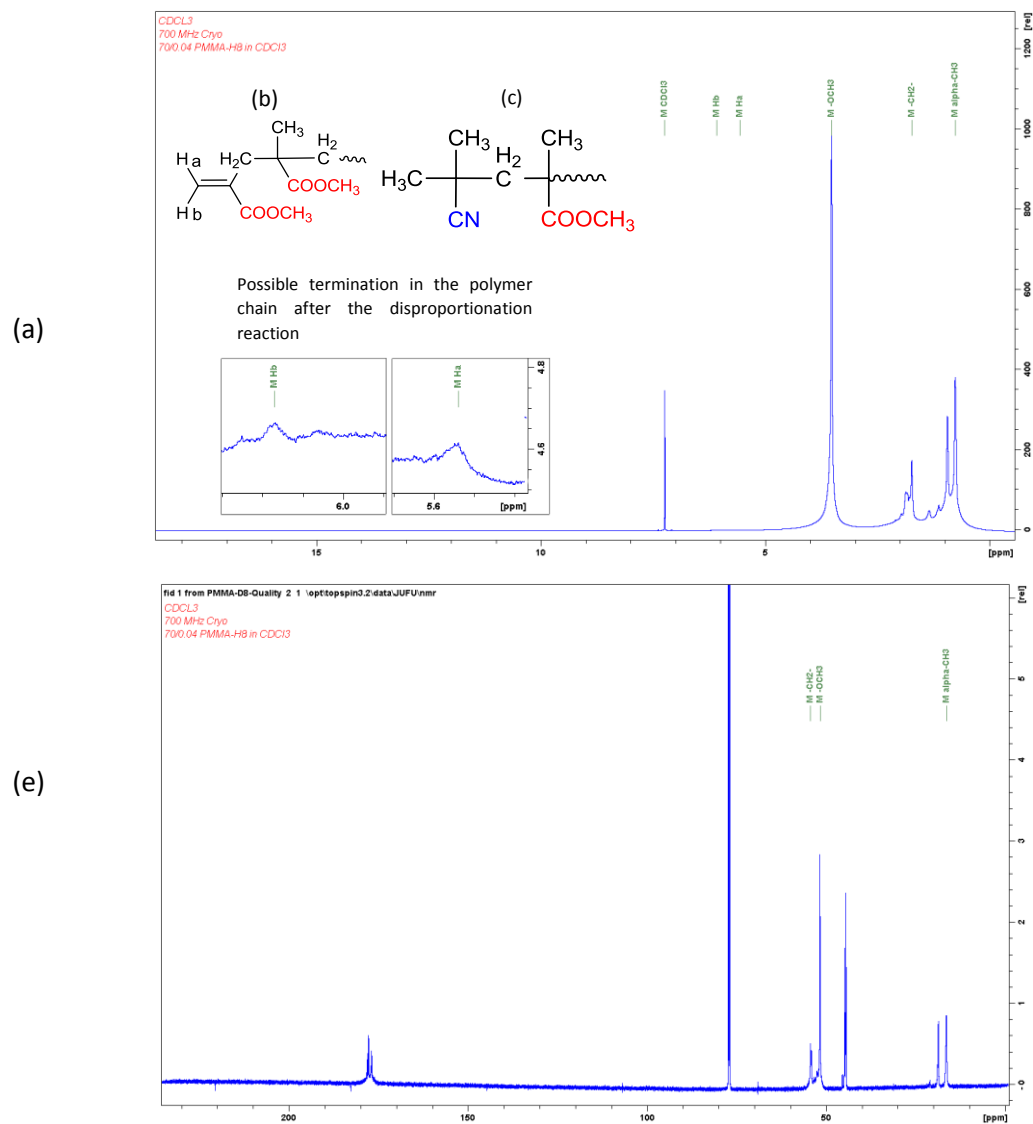
Figure 21. ^{1}H (a) NMR and ^{13}C (b) spectrum of protonated PMMA cross-linked with EGDMA prepared with AIBN (CDCl$_3$)
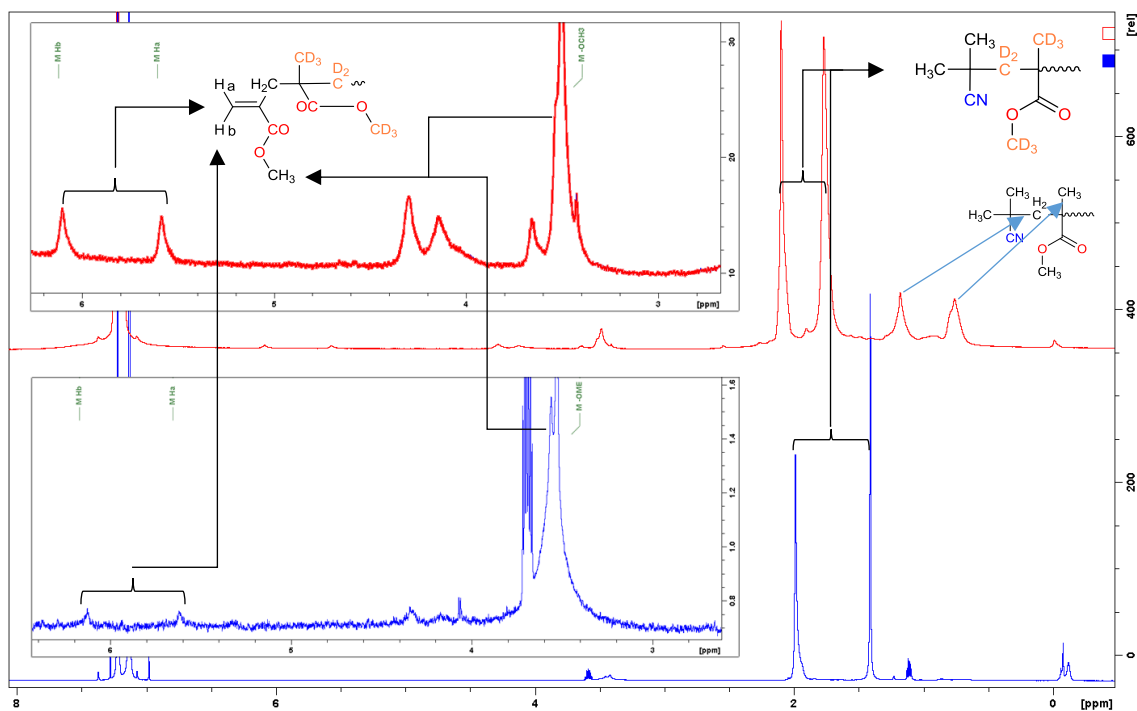
Figure 22. ^{1}H NMR spectrum of PMMA-d$_8$ (70/0.04) and PMMA-d$_8$ (70/0.05) cross-linked with EGDMA measured in a Bruker 700 MHz (CDCl$_3$).
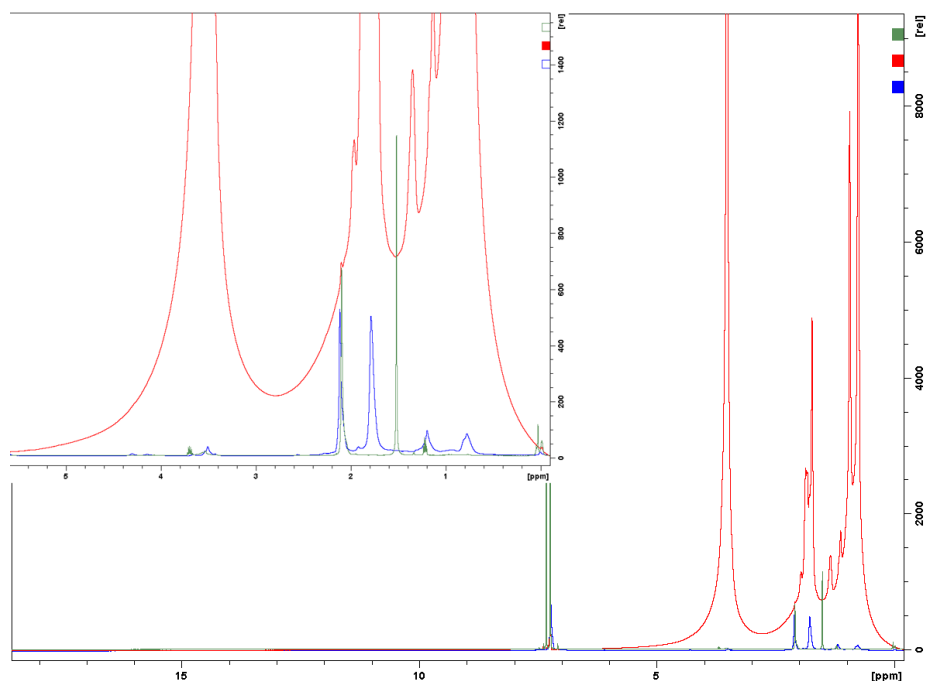
Figure 23. Overlapping of ^{1}H spectrum of stretching compatible protonated and deuterated PMMA (CDCl$_3$) measured in a Bruker spectrometer at 700 MHz. Protonated PMMA 70/0.04 (red line), PMMA-*d*$_8$ 70/0.04 (blue line) and PMMA-*d*$_8$ 70/0.05 (green line). First and second gel are suitable for the New Era's stretching device (4.2/3.2 mm) and the last one is compatible with the Hilgenberg's semi micro stretching device (2.4/1.8 mm). All measurements were done at relaxed state.

1.3.1.9 Conclusions

Determination of 3D molecular structure remains challenging for natural products or organic compounds available in minute amounts. While the constitution can be derived from proton/proton and proton/carbon correlations, J couplings and NOEs are used to determine the relative configuration oftentimes supported by one-bond ^1H-^{13}C RDCs or by ^{13}C RCSAs. However, these RDCs or carbon RCSAs rely on 1% natural abundance of ^{13}C preventing their use when only 10 μg of a compound are available. We introduce here the highly sensitive ^1H RCSA's measurements that provides spatial orientation of structural moieties within a molecule, yet with μg amounts required. In this thesis section, robust measurement of ^1H RCSAs is shown using constrained aligning gels or liquid crystals. 3D molecular structures of molecules with varying complexity are determined. Deuterated alignment media allows for observation of RCSAs of around 10 μg of analyte and determine a previously unknown relative configuration with this amount. Therefore we can cloncude:

a) The ^1H RCSA's, a highly sensitive NMR anisotropic observable, can be robustly measured in chloroform and DMSO swollen chemically cross-linked polymer gels and liquid crystals. ^1H RCSA's are very powerful parameters as they complement conventional J-couplings, and NOEs, without the necessity of using one bond and long range ^1H-^{13}C RDCs or ^{13}C RCSA's. For microgram amounts, we showed that deuterated gels provide clean spectra of the sample down to 10 microgram quantities.

b) Through three examples of rigid and flexible molecules, strychnine, estrone and retrorsine, we have demonstrated that ^1H RCSAs can be successfully employed to determine the correct relative configuration using Q or Q_{CSA} values. In addition, spectroscopists not well trained in NMR, may find it more appealing to use RCSAs than RDCs since RCSAs can be easily read from the 1D ^1H or ^{13}C-$\{^1H\}$ spectra while RDC measurements require some training with 2D spectroscopy.

c) The analysis tools are available in the Mestrelab software and CSA tensor calculation in Gaussian. Therefore, measurement of ^1H RCSA will open up new avenues for the structural analysis of synthetic and natural products that are hitherto not solvable due to their limited amount down to 1 digit microgram quantities.

1.3.2 Accurate Measurement of RDC and RCSA for Natural Product Configuration Analysis Using Semi micro Stretching and Compression Devices

1.3.2.1 Development of a shimming optimization device for the measurement of anisotropic parameters on micro compression device (1.7 mm OD)

Measurement of ^{13}C RCSA at minute amount was robustly achieved on 2016 by using a micro-compression device (MCD) in a highly sensitive 1.7 mm cryoprobe.[17] The MCD follows the same principle as in the commercially available 5 mm compression device from New Era Company, with different alignment conditions induced by moving a piston located in the device. Despite the fact that MCD is a valid option for the analysis of small molecules in minute amounts, it shows significant issues during the locking and shimming in the most common 5 mm cryoprobes. The space between the capillary tube and the shim coils contains a tiny amount of deuterated solvent inside the sample tube (40 µL) that is responsible for such drawbacks.

To avoid this situation, we introduce here a locking/shimming device that overcomes such mentioned difficulties. The locking/shimming device (LSD) can be described as a *3 mm tube coat containing deuterated solvent for calibration and to make the lock signal shaper and to guarantee a proper shimming*. The in-house device has been designed in Teflon® (Figure 24) and it is provided with two rubber bands which secures the fixation of the sample to the capillary tube and the outsider 3 mm tube.

Gels in our MCD are used to make the same reaction of polymerization explained on section 1.3.1.8 for stretched gels at 70/0.05 ratios (monomer v/v; molar % cross-linker concentration). After the reaction occurred, the PMMA crude gel was cut into 2.2 cm long sticks and used after solvent cleaning, showing the same mechanical properties as the gels prepared for a 3 mm NMR tube. Washing, pre-swelling and dialysis were done as before to prepare the gel for measurement[43], giving a maximum ^{2}H splitting (ΔH_Q) in the range of 4 to 4.8 Hz. For the final measurement, the compression was done by means of the dialyzed gel in 40 µL of chloroform inside a 1.7 mm NMR tube using a MCD. In this way, ^{1}H-RCSAs can be efficiently shimmied and measured at two different compressions, using the locking/shimming device in a 5 mm cryo probe.

On Figure 25, 70 µg of strychnine were aligned, shimmed and locked and a T2 filtered ^{1}H NMR spectrum was run to demonstrate that a very good signal to noise can be achieved.

(a)   (b)   (c)   (d)

(e)

Rubber band.
OD: 6.26 mm

15.6 mm

6.9 cm

Outside diameter (OD): 4.97 mm

Internal diameter (ID): 1.77 mm
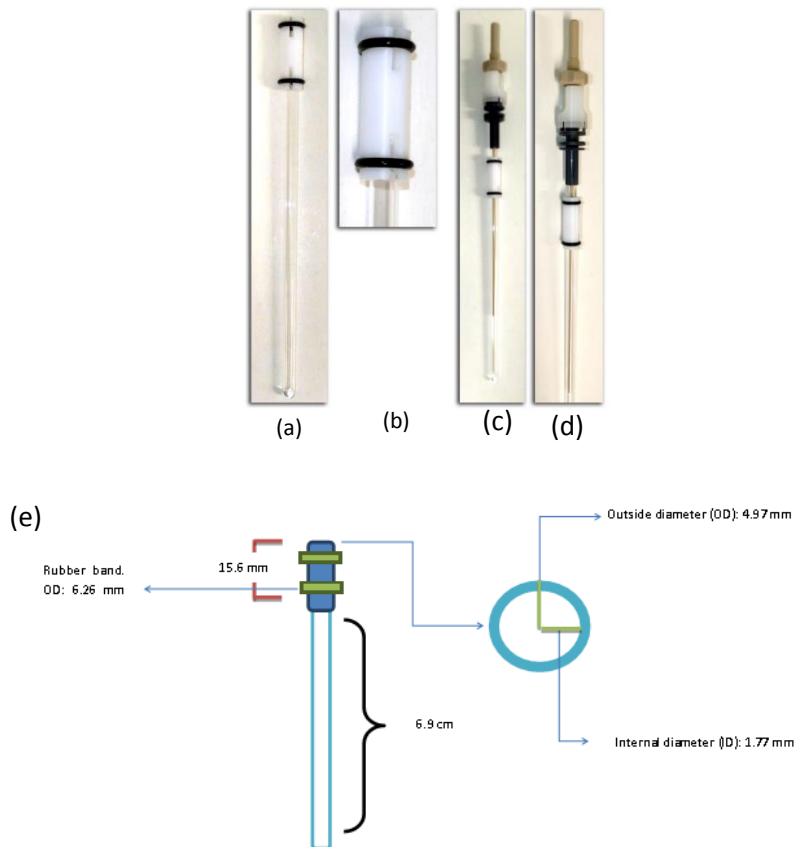
Figure 24. Locking/shimming device (LSD) (a) detail of the head of the LSD (b) Complete assemble as it was used during ^{1}H RCSA experiments (c and d). Plans and measurements of the Locking shimming device (e)
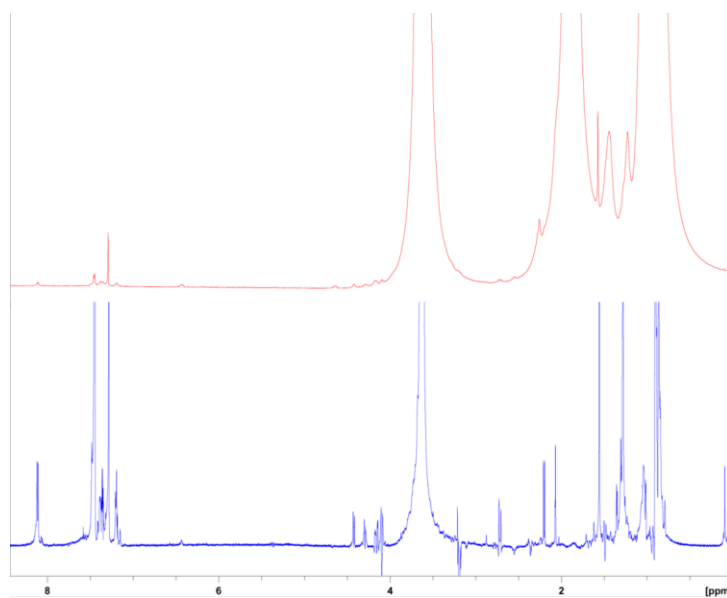
Figure 25. ^{1}H NMR spectra of 70 µg of strychnine sample in a micro compression device MCD (1.7 mm NMR tube) in a protonated PMMA gel (70/0.05) in which no polymer signal suppression was applied (red color). Signal suppression by using a T_2 filtered was also applied (blue color).

1.3.2.2 Development of a universal 3 mm compression device for measuring RDC and RCSA

In this section we will describe the use of a semi micro compression device (SMCD) for measuring any NMR anisotropy parameter in high concentrations of analyte. The USMCD is a 5 mm version of the New Era compression device, which operates following the same principles.[43,22] Therefore, it will efficiently align strain induced swollen gels, either in polar or nonpolar media, by mechanically compressing strengths. These approaches have been extensively used in the elucidation of natural product structure in the past decade.

In our hand, we have found that SMCD is suitable for a rapid and reversible gel compression to collect anisotropic NMR parameters such as RDCs, ^{1}H and ^{13}C RCSA's and subsequently use them for diastereoisomers stereo-discrimination. Additionally, besides the uses of the device in measuring ^{1}H RCSA in swollen PMMA-d_8 gel in CH_2Cl_2, we also describe its usage for other compatible gels in other organic solvents.

A Teflon® made plunger (outer diameter 2.0 mm) is placed inside the clamping head (see Figure 26), which is provided with two fastening screws that keep the system integrated and permits the accurate measurement of different anisotropic parameters with rapid and reversible variation of the alignment strength. It engages the well described stretched polyacrylamide gels (SAG) method, which mainly consists of swelling the gel until equilibration of 24 h. After the equilibration the sample is dissolved in the swelling solvent/gel media and then is allowed to diffuse into the gel during a period of approximately 5 minutes. Specific details in how to use this device are described in the Experimental Part.

Herein, we present a SAG approach that overcomes the principal experimental problems of the currently existing 1.7 and 5 mm devices as reduced mass of gel, improved capabilities of shimming and locking.
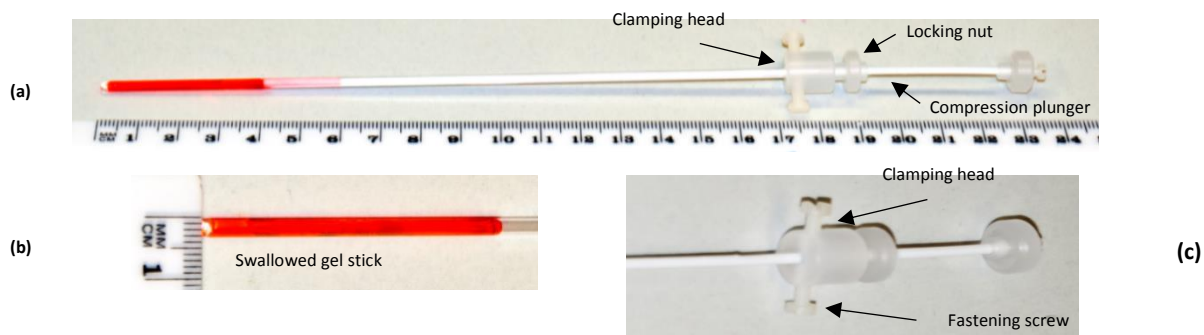
Figure 26. Experimental arrangement needed for the 3 mm semi-micro compression device. (a) Complete alignment system including the 3 mm NMR tube, a swallowed gel, and the SMCD. (b) Fully relaxed swallowed gel colored by a pigment. (c) Head detail of the SMCD; fastening screws allow the compression system to keep the tube attached to the 3 mm glass NMR tube. Pigment used is from a commercial maker from the German company Faber Castell Company.

The polymer sticks were cut into 22-mm-long pieces and placed into a 5-mm NMR tube, and then were allowed to swell in a suitable deuterated solvent (600 µL). After 24–48 h, the gel was carefully transferred to a 3-mm NMR tube. At this point the gel has almost reached the NMR tube walls (Figure 26 a), the SMCD was attached to the 3-mm NMR tube by adjusting the fastening screw. A fully relaxed gel of approximately 40 mm in length showed a quadrupolar splitting (ΔH_Q) 0 Hz, yet after compression in the vertical direction was applied it revealed a non-zero ΔH_Q. Several values of ΔH_Q (see Table 3) can be achieved by either changing the gel´s chemical composition or the amount of compression over the gel stick. The parameters showed in Table 3 are the result of optimizing critical parameters to guarantee the right flexibility and highest ΔH_Q. We anticipate that ΔH_Q was linearly scalable as a function of the degree of compression (ε), yet it hasn't been measured so far.

During the sample preparation, sample was dissolved in 75 µL of deuterated solvent and firstly added to the 3-mm NMR tube in which anisotropic data was collected. The swallow gel stick was then carefully pulled in by using the Teflon plunger. At this point, the gel behaves like a sponge and the compound to be analyzed is sucked inside the gel in a few minutes after repeated compression and decompressed maneuvers with a gentle pumping action of the plunger.

The methodology allowed the determination of several anisotropic parameters as RDCs and RCSA by tuning the alignment in easy and robust way. So far, we have successfully reused the PMMA-d_8 (70/0.27) at micro-gram scale to collect ^{1}H RCSA's for two different compounds over 3 weeks choosing CD_2Cl_2 as locking solvent. However, more tests must be done before establishing a rule of use.

The background signal in the protonated gel was less intense due the mass reduction in the alignment media from 42 mg to 22 mg, and it can be diminished by filtering with a Carr-Purcell-Meiboom-Gill sequence (CPMG). [23] Moreover, background can be almost completely nullified, not only in the 1D ^{1}H-NMR spectrum as well as in the ^{13}C and HSQC experiments with the introduction of PMMA-d_8.

Correction of the chemical shift anisotropy by compression

The use of the compression device for measuring RCSAs, implies that the polymer/solvent ratio changes upon compression. Thus, the change on the isotropic contribution to the chemical shift must be corrected. Equation 10, described by *Nath et al*[22], allows the calculation of corrected RCSAs. Extrapolating those conclusions regarding the CSA tensor of carbon atoms, we proposed here that the proportionality constant *c* (Equation 11), could be determined assuming a sufficiently large number of protons attached to sp^3 carbons, their associated CSA tensor principal frame equally span all the space, and as a consequence, their mean RCSA should be zero.

$$\Delta RCSA_i = \Delta\delta^i_{max} - \Delta\delta^i_{min} - c\left(\Delta\delta^i_{min} - \Delta\delta^i_{iso}\right)$$

$$c = \frac{\overline{\Delta\delta^i_{max} - \Delta\delta^i_{min}}\ sp^3}{\Delta\delta^i_{min} - \Delta\delta^i_{iso}\ sp^3}$$

However, the conditions are not always fulfilled in small molecules. The problem has been recently solved [10] and implemented in MSpin[9] in an automatic way. [28] The automatic isotropic correction method will be the one used in our study.

Device limitations

So far, we have solved three natural product using anisotropic parameters with the 3 mm compression device (at micro gram scale), yet the main drawback is the limited amount of pressure one can applies over the gel before the tube gets broken. We are currently developing a dedicated 3 mm compression device that allows to compress the gel even more, without the risk of the tube to collapses. It shall be available soon in   https://www.hilgenberg-gmbh.de

(a)

(c)

(b)
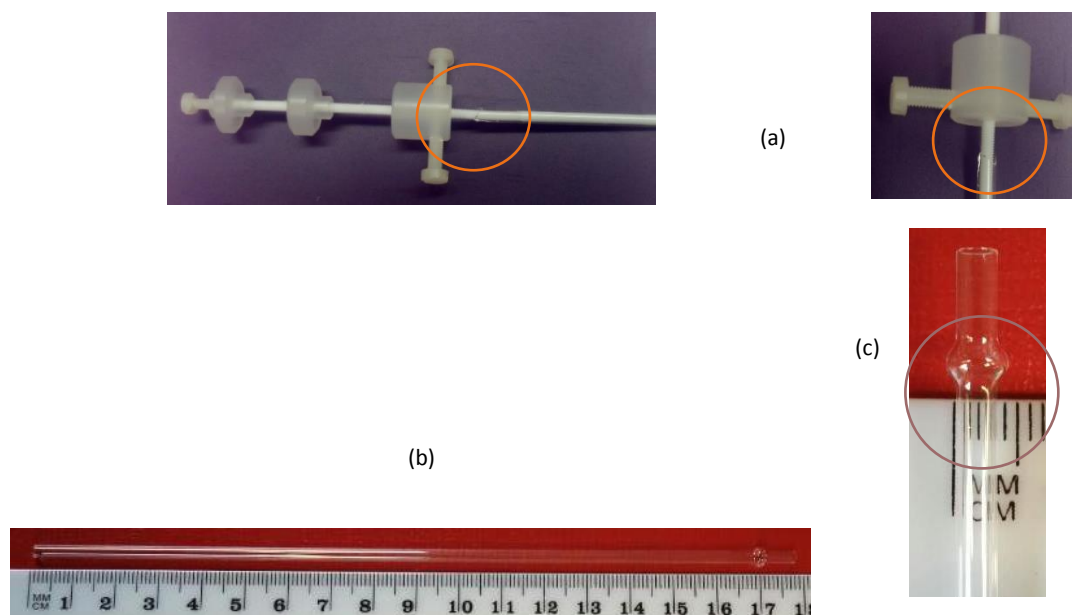
Figure 27. Hilgenberg´s 3 mm NMR tube shows suitable properties to be used in combination with the SMCD, nevertheless in extreme compression the tube can broke (a). Hilgenberg Company has recently manufactured a 3 mm compression tube (b), which should solve the situation as it includes a section in the top that can hold the press ion caused by the gel stick during the compression.

Conclusions

We have presented a version of the compression device to measure anisotropic NMR parameters of small organic molecules, mainly natural product at micro-gram scale:

a) Experimental arrangement does not require a complex device but just a compatible polymer gel stick of 1.6 mm diameter and 2.2 mm length, a regular 3-mm NMR tube, and the compression device described herein. A variety of gel for this device have been prepared so far, extending anisotropic measurement to other solvents as $CDCl_3$, CD_2Cl_2 and CD_3OD.

b) The device did not present any issues with shimming and locking at the spectrometer. Besides, when the methodology was combined with our recently introduced PMMA-d_8 gel, there was no interference of the background signal at microgram scale. [1]H RCSA's data collection as well as RDCs can be accurately measured at minute amount of approximately 550 μg.

c) Although deuterated gels preparation is worth nearly 16 $ more expensive for each stick, recycling is possible. The same gel can be reused, at least 2 times, as long as it is thoroughly washed after each experiment.

d) On other hand the SMCD has considerably facilitated the collection of RCSAs and RDCs at microgram level, and has been used to solve the structure of three natural products.

Table 3. Value of quadrupolar splitting (ΔH_Q) for several alignment media compatibles with the universal semi micro compression device (3 mm O.D).

Gel´s chemical composition	Solvent	Quadrupolar splitting (Hz)
PMMA 70/0.27	$CHCl_3$	40.7
PMMA-d_8 70/0.27	CH_2Cl_2	4.6
Poly-DEGMEMA 75/0.3	CD_3OD	4.4

SAG polymers are named usually as: PMMA 70/0.27. Where PMMA is the monomer´s name, 70 is the monomer concentration in v/v concentration and 0.27 is the cross linker concentration in %molar.

1.3.2.3 Application to a rigid molecule: α-Santonin

As a proof of concept of the utility of USMCD, we will study the α-Santonin, [71] which RDC [72] and ^{13}C RCSA[10] have been recently reported. α-Santonin (Figure 28), is a wide spread sesquiterpene lactone, found in plants from genus *Artemisia.* [73,74] Used in the past as an anthelminthic agent,[75] its use has been banned because of the side effects that have been found in humans.[76]
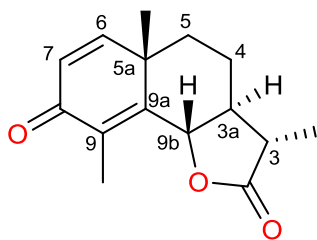
Figure 28 Structure of α-Santonin

Four stereocenters are present in the compound, therefore 8 diastereomers are possible. As usual, all the possible relative configurations were labelled via the *R* or *S* nomenclature at C3, C3a, C5a and C9b respectively. For instance (3S,3aS,5aS,9bS) for the correct configuration. A conformational search was performed for all relative configurations of α-Santonin by using the Discovery Studio – Accelrys package.[77] Structures were then refined at HSEH1PBE/CC-pvdz level, and chemical shift tensor were computed at PBE1PBE/aug-CC-pvdz (CSGT)[78–80] and the IEFPCM[81] solvation model with CH_2Cl_2 parameters. DFT calculation were carry on by using Gaussian09 suite software.[59]

4.0 mg of α-Santonin was aligned in PPMA-d_8 gel (70/0.27) swollen in CD_2Cl_2 using the compression/relaxation method[43] with our developed USMCD. Pure shift 1D-^{1}H NMR Psyche [23,25,82] were acquired with both fully relaxed and with the compressed gel at quadrupolar splitting of 4.6 Hz. ^{1}H RCSA's extraction was done after superimposing the 1D Psyche on the H7 signal (Figure 30).

Data were fitted in units of Hz to get reasonable weight[4] and ^{1}H RCSA from methyl groups were averaged as previously described. In order to yield minimum Q factor, [83] all fittings minimize the Q factors were computed both with the isotropic automatic compensation and without it, where are the RCSA fitting was done by SVD. [3] Quality of the fits was scored in terms of the Cornilescu quality factor (Q)[84] and Chemical Shift Anisotropic quality factor Q(Q_{CSA}).[22]

RCSAs analyzed data was obtained with ^{2}H Δv_Q of 4.6 Hz at maximum alignment. When RCSAs were used uncorrected as $\Delta\delta_{max}$-$\Delta\delta_{min}$ differences, fitting resulted in large quality factors and discrimination was dramatically reduced, nevertheless is still present (Figure 29, left panel).

The corrected values of RCSAs were in a range of -0.141 and 1.729 Hz (Table 4). Data were fitted to each configuration, and *c* factor optimized to its minimum in the software MSpin. When using the automatic isotropic correction procedure, the quality factors drops for all the configurations, and the correct diasteroisomer for α-Santonin (5aS,9bS,3aS,3S), presented the lowest Q(QCSA) = 0.154 (0.167) but with an small differences with (5aS,9bR,3aS,3S) Q(QCSA) = 0.200 (0.181) (Figure 29, right panel). Nevertheless, it increased the Q(Q_{CSA}) difference with the other six configurations, thus discrimination was improved.

When analyzing Cornilescu´s Q factor for the data ^{1}H RCSA, is worth mentioning that absolute difference between the two closest configurations is 0.046 where as in a recent study [10], where RDC and ^{13}C RCSA were combined, the two closest configurations is 0.023. This illustrates the potentialities of ^{1}H RCSA as a tool for stablish the relative configuration of small molecular systems with several diastereotopic protons.

In summary, we have stablished the suitability of our SMCD, which has been used to measure anisotropic RCSA's data using, for first time, a deuterated compressed compatible PMMA gel swallowed in CD_2Cl_2.

Table 4. Proton residual chemical shift anisotropies (Hz) data for α-Santonin

# H	^{1}H RCSA (exp. in Hz)	^{1}H RCSA (calc.in Hz)
H6	1.628	1.262
Me-C3	0.000	0.099
Me-C5a	1.528	1.321
H5b	0.342	0.202
Me-C9	0.000	0.100
H9b	1.186	1.331
H3	1.548	1.564
H4b	1.668	1.86
H5a	1.688	1.797
H3a	1.347	1.641
H7	Ref	Ref
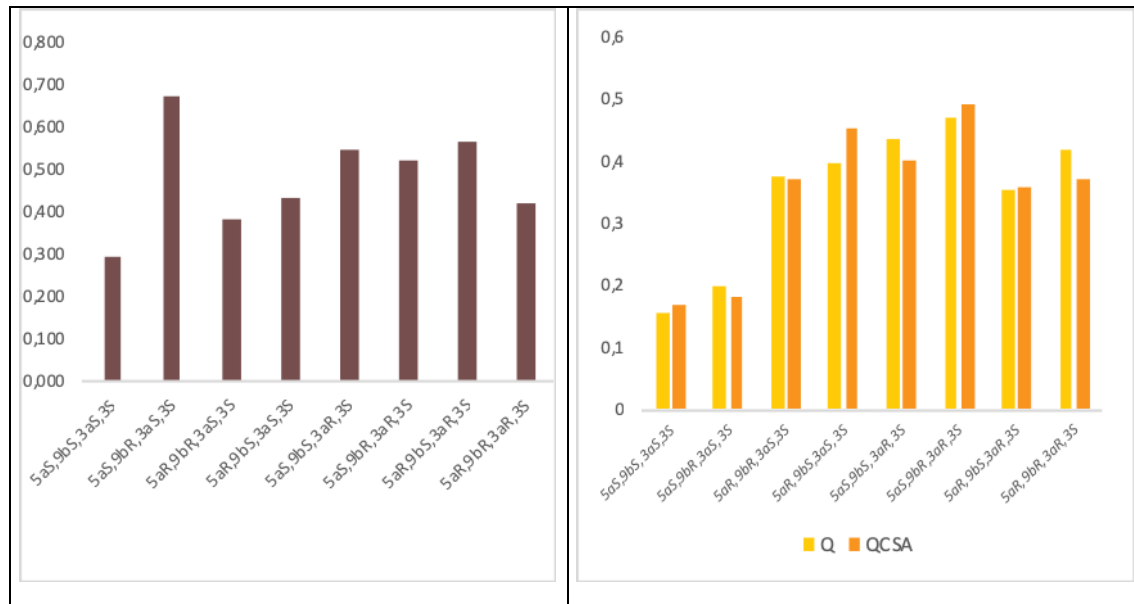
Figure 29 Proton Residual Chemical Shift Anisotropy (^{1}H RCSA) quality factors for the eight possible diastereomeric configurations of α-Santonin. Uncorrected ^{1}H RCSA data Q (left) and optimizing scale factor (right) Q(Q_{CSA}).
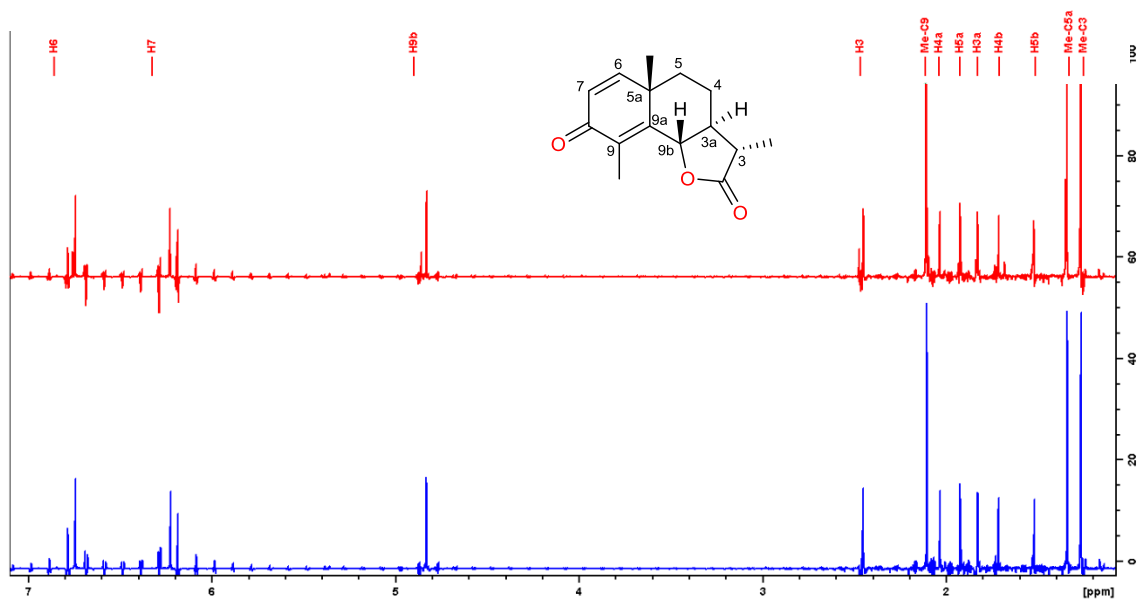
Figure 30. Pure shift ¹H NMR (1D Psyche experiment) of α-santonin measured in a 800 MHz Bruker spectrometer equipped with a 5 mm Cryo-Probe (blue line). Sample contained 4.0 mg of α-santonin in fully relaxed PMMA-d8 gel swallow in CD2Cl2 using the 3 mm compression device (red line). At milligram scale deuterated PMMA does not shows any background signals, although the use of 1D Psyche is need due the present of the isotropic signal.

1.3.3 Absolute stereochemistry of two isolated stereoclusters combining ¹H-RCSA and DFT methods: The case of a meroditerpene from the brown alga Sargassum muticum

The sea weed *Sargassum muticum*, collected in the southern coast of Galicia, yielded a new compound with a chemical structure of meroditerpene. The complete elucidation was made by using HRMS and NMR spectra, being the Proton Residual Chemical Shift Anisotropy (¹H RCSA) along with NOESY measurements, key tools to elucidate for first time the relative configuration of this natural compound.

1.3.3.1 Identification and structure elucidation of the plane structure of compound 1.

Compound **1**, was obtained as a greenish amorphous solid, HRESIMS *m/z* 441.2975 [M + H]⁺ (calcd for $C_{28}H_{41}O_4$, 441.3000 Δ *m/z* 5.7 ppm), and its plane structure was characterized on basis of standard 1D and 2D-NMR (HSQC, HMBC and COSY) experiments along with comparison of its spectroscopy data with reported values.[85,86] UV λ_{max} (CH₂Cl₂) nm (ε): 294 (6800), 250 (15000). The ECD spectrum of compound **1** recorded in CH₂Cl₂ (2.88×10^{-4} M) in the 225-470 nm range showed a positive Cotton Effect (CE) at 252 nm (Δε = 6.4×10^3) and two negative CE at 290 nm (Δε = -1.26×10^3) and 330 nm (Δε = -4.54×10^3) ESI(+)MS, 70 eV, *m/z* (rel. int.): 463 [M+Na]⁺ (100); 423 [M-H₂O+H]⁺ (72); 903 [2M+Na]⁺ (60); 441 [M+H]⁺ (13); (Figure 32) ¹³C and ¹H NMR (CD₂Cl₂) and Table 5.

As it is shown in Table 5 the chemical shift and relevant NOESY allowed us to assign all protons and carbons of this compound,[87] (see also Figure 39 to Figure 41). Therefore, **1** was identified as a tetraprenyltoluquinol chromane meroterpenoid as is presented on Figure 31. A diasteroisomer related to 1 was recently reported as an epimeric mixture, presumably at C3, and with both methyl groups attached to C7 and C11 in a *cis* relatioship.[85] Herein we want to report the isolation of this compound, in a pure form as is supported by integration of the ¹H spectrum (Figure 35) and by the fact that there is no duplication of signals in the 1D-pure shift and the ¹³C spectra (Figure 36 and Figure 38). Moreover, H8b and H9 were assignment using a pure shift ¹H NMR (Figure 37).
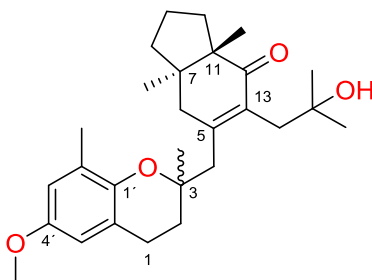
Figure 31. Chemical structure of the tetraprenyltoluquinol chromane meroterpenoid isolated from *Sargassum muticum*.

Table 5. ^{1}H, ^{13}C and NOESY correlations of Compound 1 (CD$_2$Cl$_2$)

Position	δ$_C$, mult. [a,b]	δ$_H$, mult. [c]	NOESY Correlations [d]
1	23.10 CH$_2$	2.780 (t, 6.9)	H3' (s)
2	34.10 CH$_2$	H2a: 1.864 (dt, 13.5, 6.9)	H4b
		H2b: 1.811 (dt, 13.5, 6.9)	H4b
3	76.83 qC		
4	45.21 CH$_2$	H4b: 2.518 (d, 13.7)	
		H4a: 2.710 (d, 13.7)	H1; H2a
5	155.05 qC		
6	44.82 CH$_2$	H6b: 3.035 (d, 18.7)	
		H6a: 2.227 (d, 18.7)	H4a
7	45.28 qC		
8	35.43 CH$_2$	H8a: 1.520 (m)	H6b
		H8b: 1.759 (m)	H6a
9	19.36 CH$_2$	1.744 (m)	
10	30.07 CH$_2$	H10a: 1.947 (td 12.0, 11.9, 6.8)	
		H10a: 1.448 (ddd, 13.1, 8.4, 3.1)	
11	55.46 qC	-	
12	209.30 qC	-	
13	133.52 qC	-	
14	40.43 CH$_2$	H14b: 2.572 (d, 14.3)	
		H14a: 2.514 (d, 14.3)	
15	71.17 qC		
Me16-	31.94 CH$_3$	1.241 (s)	H14a (s); Me16
Me17-	29.14 CH$_3$	1.046 (s)	H10b; H14b (s); H14a; H4b (s)
Me18-	21.55 CH$_3$	1.111 (s)	H10b; H6b (s); H8b
Me19-	22.75 CH$_3$	0.811 (s)	H10a; H6a; H8a (s)
Me20-	24.31 CH$_3$	1.231 (s)	H1 (s); H14b (s); H1b; H1a; H4b (s); H6b (w); H6a
1'	145.81 qC		
2'	121.19 qC		
3'	111.63 CH	6.456 (d, 3.0)	
4'	153.19 qC		
5'	115.68 CH	6.569 (d, 3.0)	
6'	127.47 qC		
MeO-4'	56.01 CH$_3$	3.707 (s)	H3' (s); H5' (s)
Me-6'	17.11 CH$_3$	2.172 (s)	H5' (s); H6b

[a] Multiplicities inferred from DEPT and HSQC experiments. Solvent as internal standard s: singlet d: doblet; dd: doble double; t: triplet; m: multiplet.
[b] Measured at 100 MHz. [c] Measured at 950 MHz. [d] Measured at 800 MHz.

1.3.3.2 Conformational study of compound 1.

Compound **1** (Figure 31) presented three chiral centers at C3, C7 and C11 resulting in 4 possible diasteroisomers. NOESY correlations (Figure 42) allowed us to rule out those configurations with a *cis* orientation between the methyl groups attached to carbons 7 and 11. Therefore two configurations as valid possibilities were considered, (*3S,7R,11S*)-**1** and (*3R,7R,11S*)-**1**. In our conformational study we used the assumption that both chromane and the bicyclo[4.3.0]nonane moieties are expected to be rigid, and chances on conformational equilibrium can arise just from staggered conformations of the bound between both sections C3 to C5 and the side chain attached to C13.

The bicyclo[4.3.0]nonane moiety relative configuration was clearly deduced by NOESY correlations: the absence of any correlation between Me18 (s, 1.111) and Me19 (s, 0.811) indicated a clear *trans* orientation. Besides correlations from both methyl groups to pairs of diastereotopic protons H6a/H6b, H8a/H8b, and H10a/H10b allowed us to unambiguously assign the alfa or beta sides of the molecule. At this point, it is important to notice that the *trans* configuration deduced in our compound, clearly is opposed to previous reported similar compounds, being compound **1** a new natural compound.

Correlations from MeO- (3.700 ppm) to both aromatic protons in the chromane moiety indicates a free rotation in the bound with to H3' (6.450 ppm), based on signal intensity. H2a and H2b presented medium and strong NOESY correlations, respectively with Me20, consequently H2b should be in the same plane that Me20, with the tetrahydropyran ring in an enveloped conformation. Besides, Me20 displayed NOESY correlations as well as to H6a (2.227), H4b (2.709) and H14a (2.5140), denoting that compound **1** adopts a preferred disposition. Nevertheless, H4b showed a NOESY correlation with both protons attached to C2 (1.864 and 1.811) and Me17 (1.045). On the other hand, Me17 presented NOESY correlation to both protons in C14, and Me16 only showed proximity with H14a, indicating a staged configuration with the side chain. Finally H10b presented a NOESY correlation with Me17 showing a spatial vicinity between the side chain and five member ring in the bicyclo[4.3.0]nonane moiety.

With all this NMR data, relative configuration of compound **1** by connecting all the stereocenters by 2D NMR clearly failed, therefore another approximation is needed. This fail is a opportunity in using anisotropic measurements to complete the structure elucidation of **1**. (Figure 33).
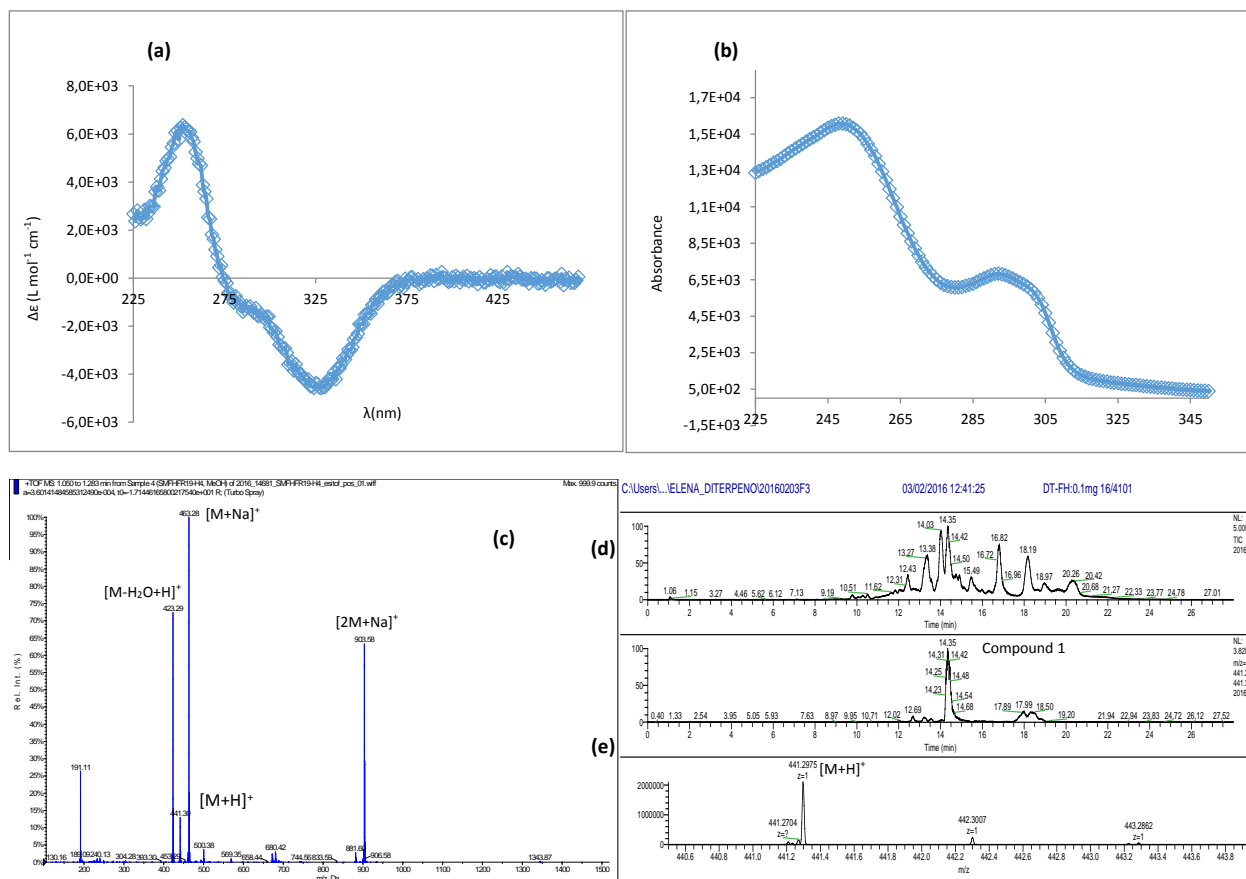
Figure 32. Experimental ECD (a) and UV (b) Spectrum of **1** in CH_2Cl_2 (0.000288 M). MS and ESI(+)HRMS Spectrum of **1**. MS: $[2M+Na]^+$ = 903; $[M+Na]^+$ = 463; $[M+H]^+$ = 441; $[M-H_2O+H]^+$ = 423 (c). Total ion chromatogram of FH in a RP-C_{18} column (d) Extracted mass chromatogram (*m/z* 441.20 to 441.38) showing a peak with retention time of 14.35 min (e) (+)-HRESIMS of the peak at t_R of 14.35 min identified as compound 1: m/z 441.2975 ($[M+H]^+$). Calc. for $C_{28}H_{40}O_4^+$, 441.3000 (Δ *m/z*: 6 ppm) (f) Chromatographic conditions: XTerra® column (3x100 mm, 5 μm) (Waters); 13 min gradient from 30 to 95% of MeOH in H2O (1 % TFA) and 7 min isoctratic with 95% MeOH; flow rate 350 ᵒL min⁻¹

.
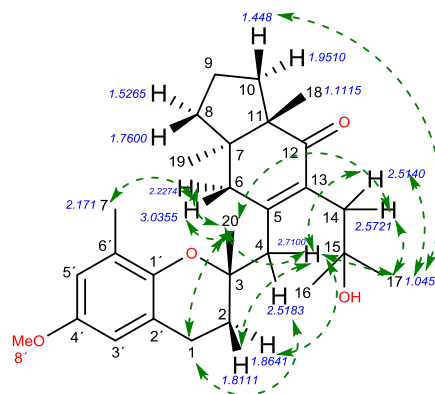
Figure 33. Relevant NOESY correlations observed in Compound 1 which evidence the rotation round C3-C5 and the side chain attached to C13. NOESY experiment was done in a Bruker Spectrometer running at 800 MHz

1.3.3.3 Establishing the relative configuration of the meroditerpene **1** by NMR anisotropy

1.3.3.3.1 Computational details: building a conformational space

As it was described before, NOESY analysis reduced the possibilities to two configurations for compound **1**, either (*3R,7R,11S*)-**1** or (*3S,7R,11S*)-**1**. However, we wanted to include an extra (*3R,7R,11R*)-**1** configuration because previous reports for this type of compounds also considered a *trans* disposition between Me18 and M19, and also with the purpose of definitively ruling out this possibility.
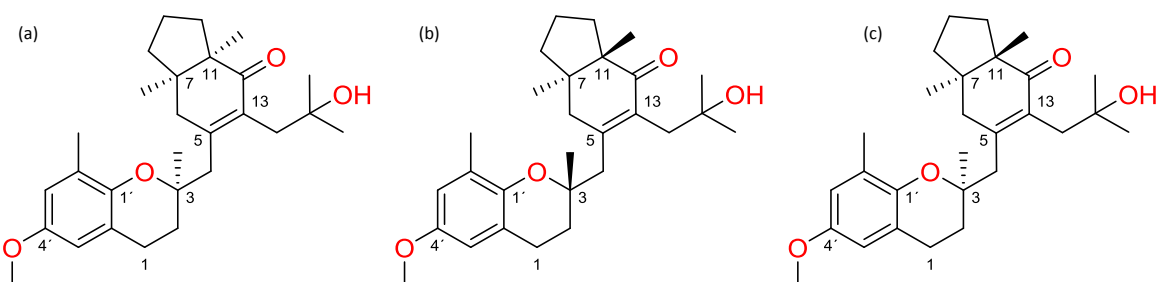
Figure 34. Three different relative configurations were considered for the anisotropic study of the meroditerpene **1**. (3R,7R,11R)-**1**, (a); (3S,7R,11S)-**1** (b) and (3R,7R,11S)-**1** (c).

The conformers of each plausible diasteroisomer (Figure *34*) were created by rotating the flexible bounds (C3-C5 and C13-C14) to alternated positions and to be, subsequently minimized by deeper computational methods. MeO group was established with a value dihedral angle Me-O-C4´-C3´ (θ) of 90°, with freely movement until a minimum energy structure was achieved. Conformers found for each diastereoisomer are displayed from Figure 43 to Figure 45. All conformers were geometrically optimized following Pescitelli's protocol for ECD calculation and Bremond's recommendation.[88,89]

Thus, a three-step optimization was used:

a) Semi-empirical level (PM6),[90]
b) DTF calculations using the Heyd-Scuseria-Ernzerhof functional (HSE06)[91] with the Dunning's correlation consistent basis sets (double zeta) (cc-pvdz).[79]
c) DFT Hybrid Functional from the Truhlar's group (SOGGA11X)[92] in combination of one of the basis sets of Ahlrichs and coworkers (def2tzvp)[93] using as density fitting Def2TZV and Ultra-Fine integration grid. Frequency calculation was carrying on using the last level of theory in order to check a real minimum.
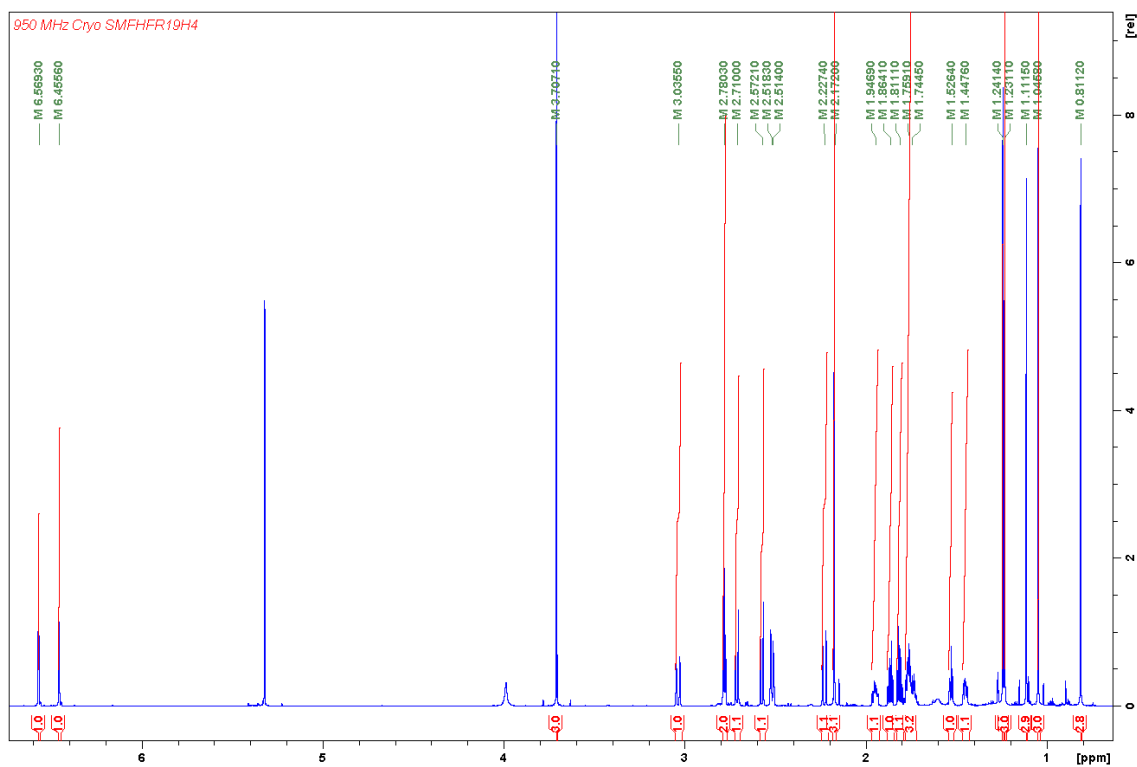
Figure 35. ^{1}H NMR spectrum of compound 1 (CD$_2$Cl$_2$), measured in a 950 MHz Bruker spectrometer.
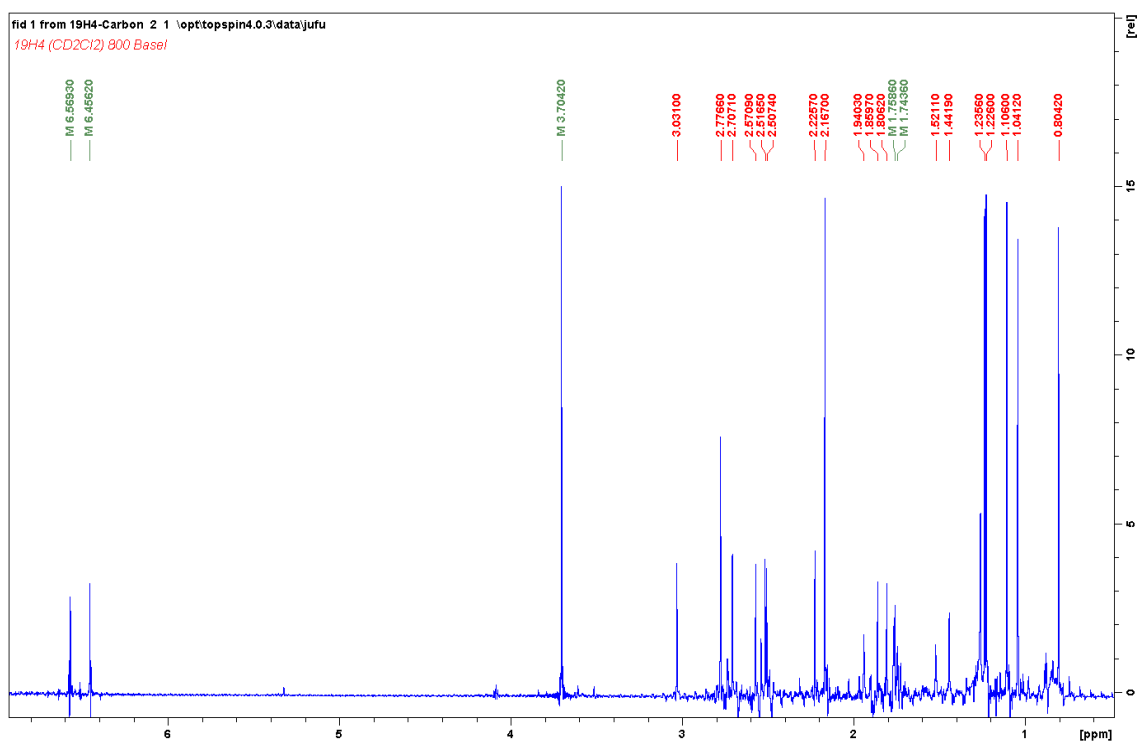
Figure 36. Pure shift ^{1}H NMR spectrum of compound **1** (CD$_2$Cl$_2$), measured in a 800 MHz Bruker spectrometer
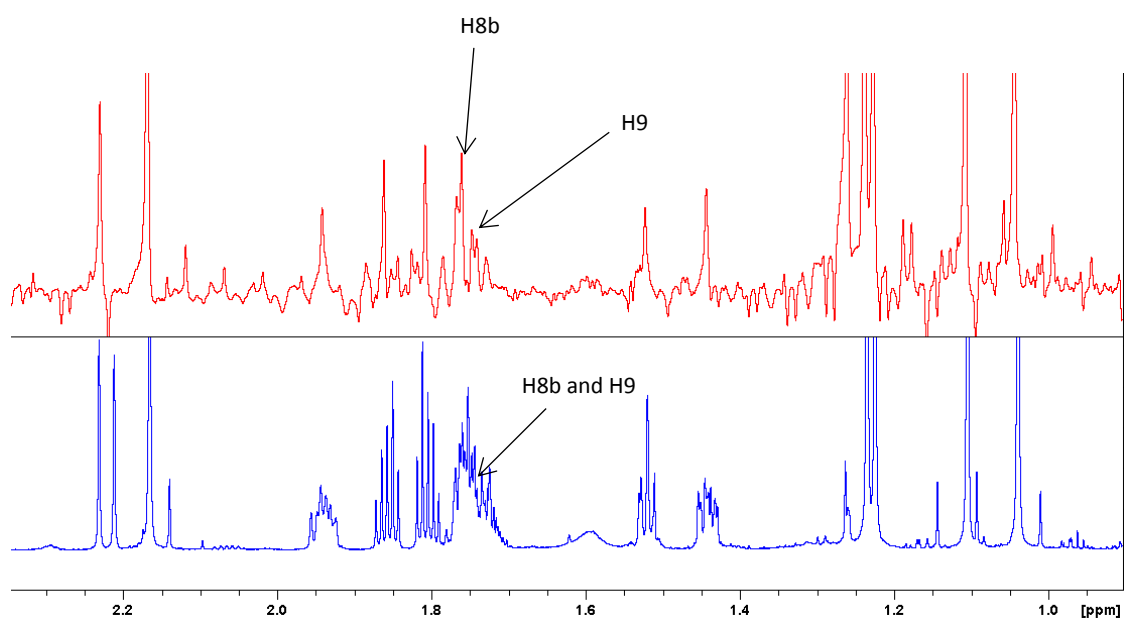
Figure 37. Detail of the ^{1}H NMR spectrum of **1** (CD$_2$Cl$_2$) measured at 800 MHz. (a) Pure-Shift (b) Multiplet which correspond to protons H8b and H9 collapsed in two singlets.
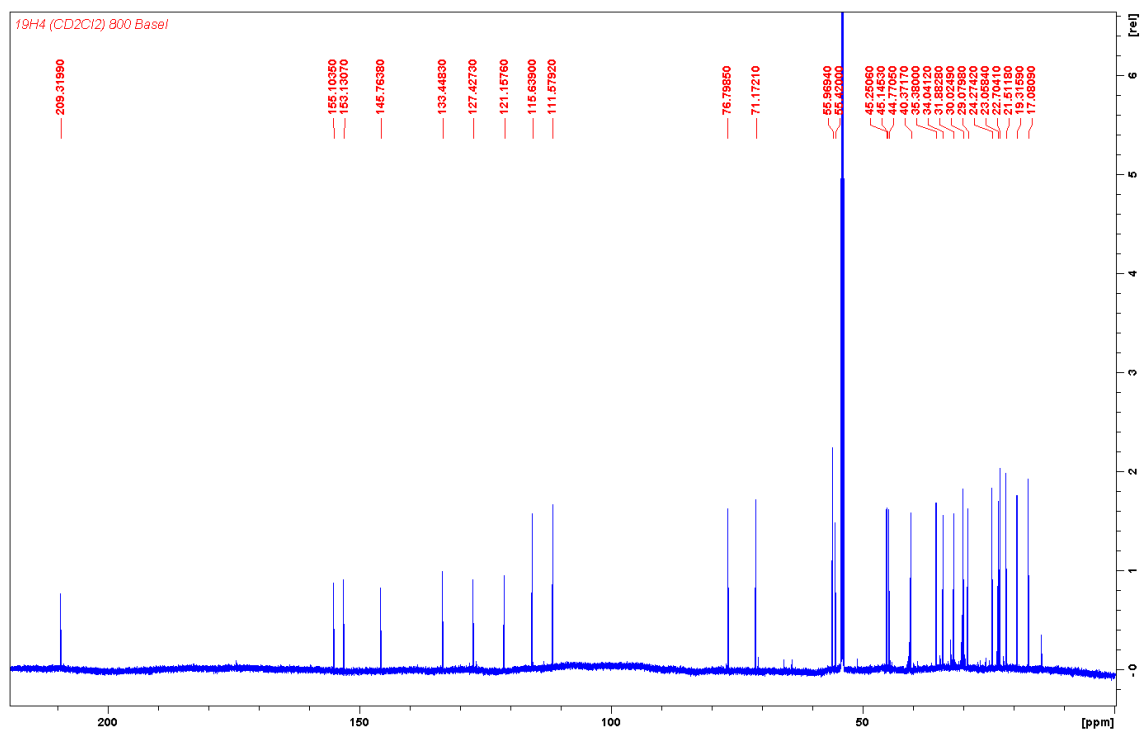
Figure 38. ^{13}C NMR spectrum of compound **1** (CD$_2$Cl$_2$), measured on an 800 MHz Bruker spectrometer.
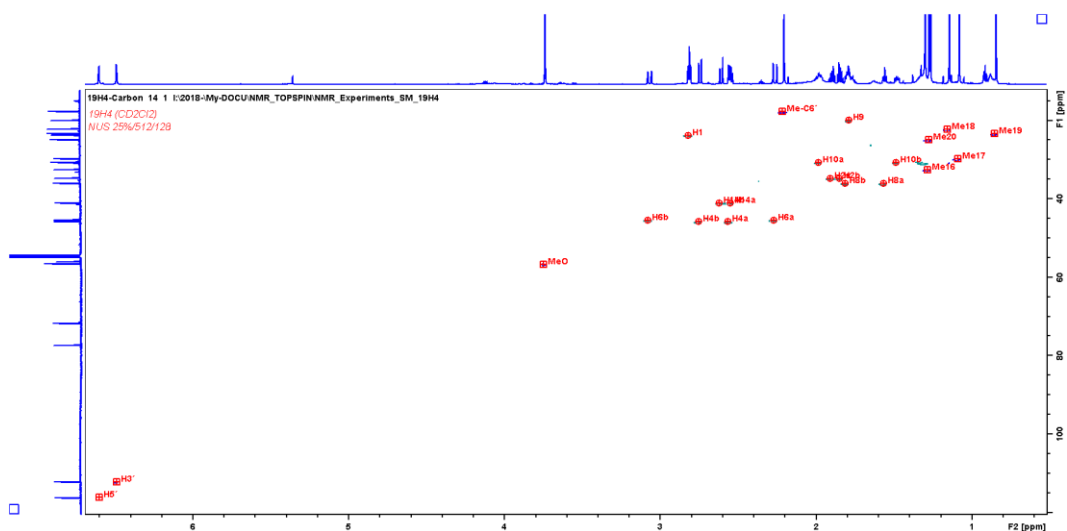
Figure 39. Pure Shift-HSQC spectrum of compound **1** (CD_2Cl_2), measured on an 800 MHz Bruker spectrometer. NUS (25%/512/128)
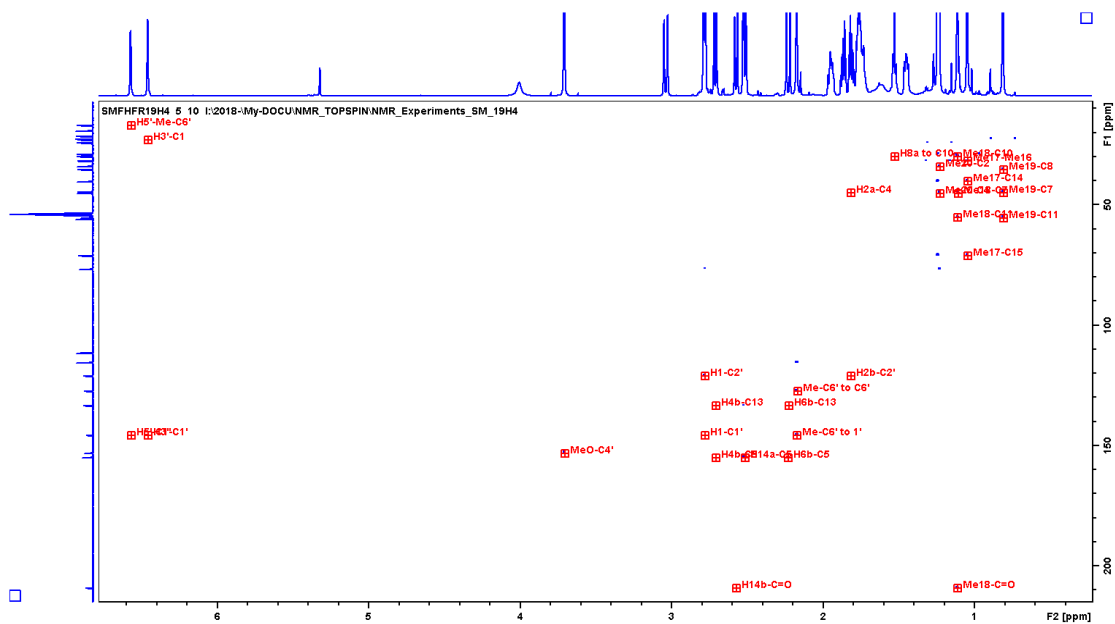
Figure 40. HMBC spectrum of compound **1** (CD_2Cl_2), measured on an 800 MHz Bruker spectrometer
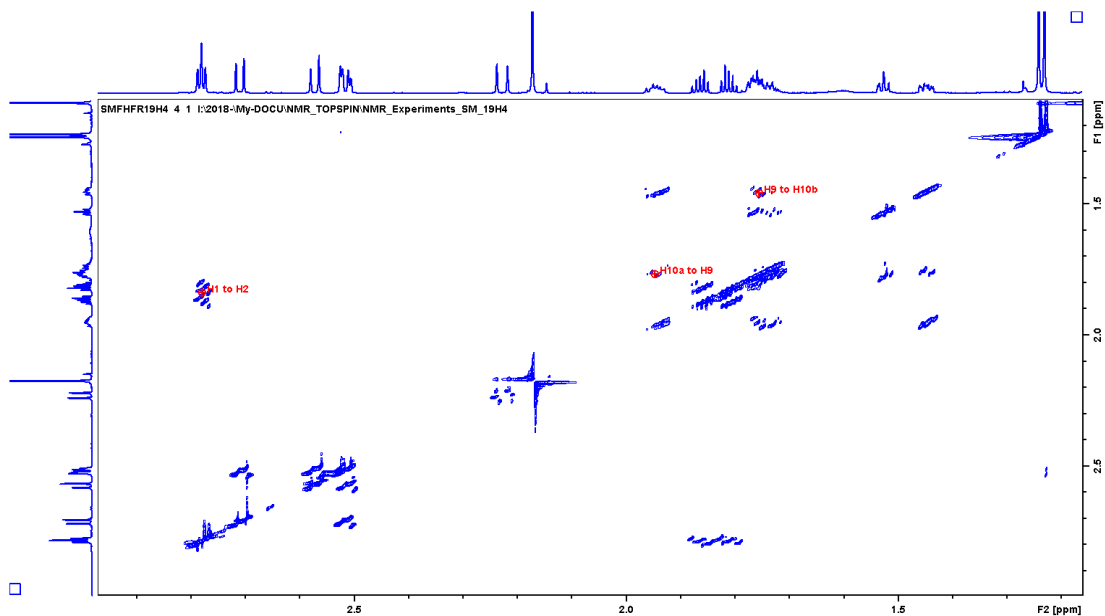
Figure 41. ^{1}H-^{1}H-COSY spectrum of compound **1** (CD$_2$Cl$_2$), measured on an 800 MHz Bruker spectrometer.
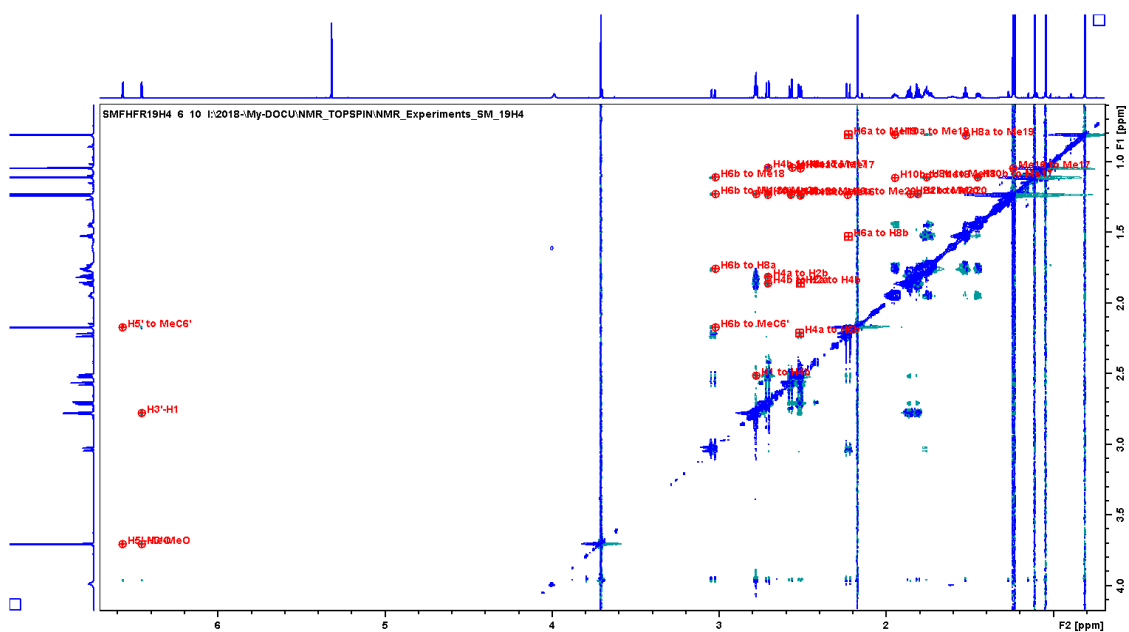
Figure 42. NOESY spectrum of compound **1** (CD$_2$Cl$_2$), measured on an 800 MHz in a Bruker spectrometer.
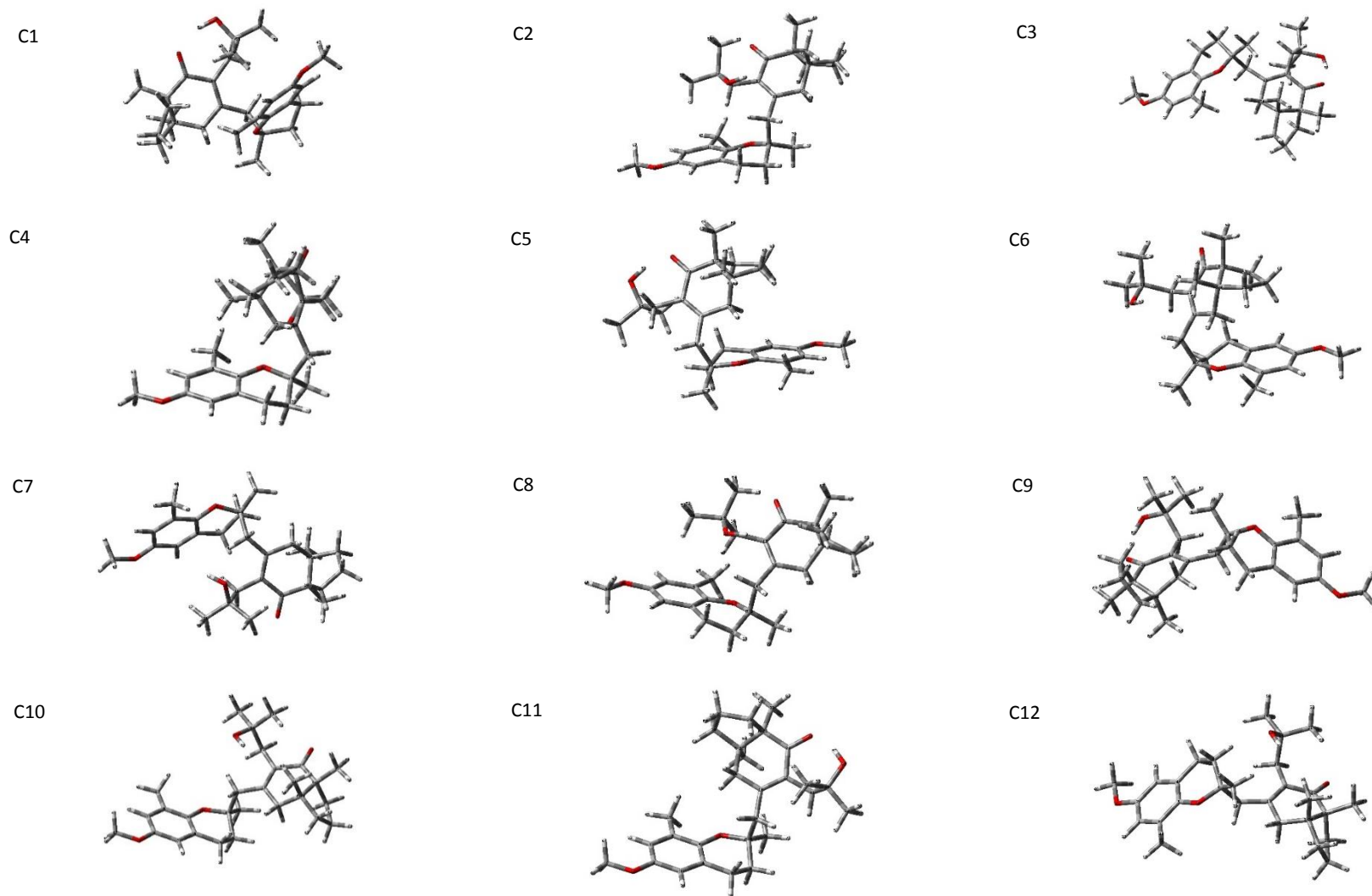
Figure 43. Geometry optimized DFT conformers for (3R,7R,11R)-**1**. Conformers that fulfilled the NOESY constrains are: C1, C2, C3, C7, C8, C9, C10, C11 and C12.
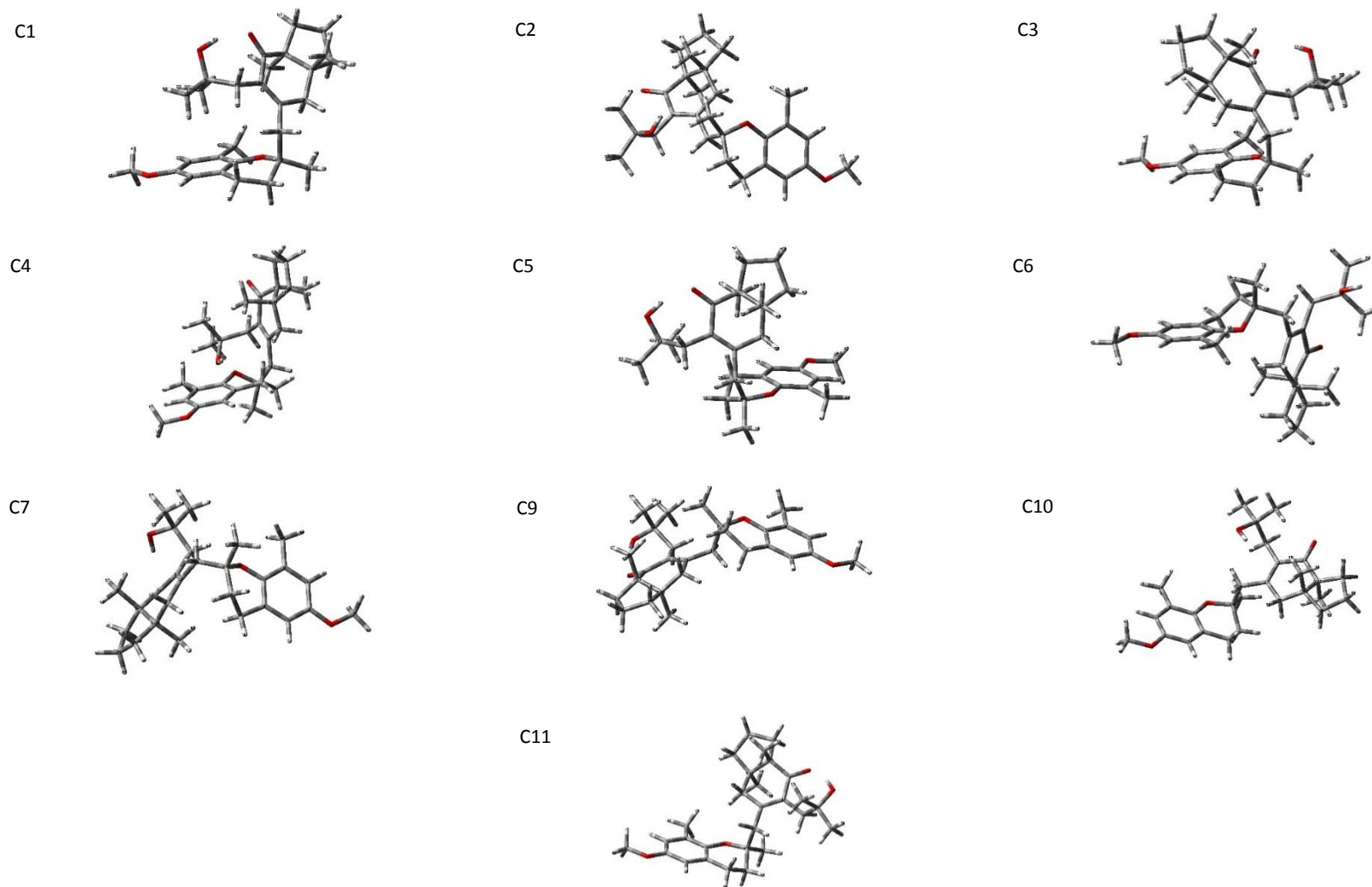
Figure 44. Geometry optimized DFT conformers for (3R,7R,11S)-**1**. Conformers that fulfilled the NOESY constrains are: C1, C2, C3, C9, C10 and C11
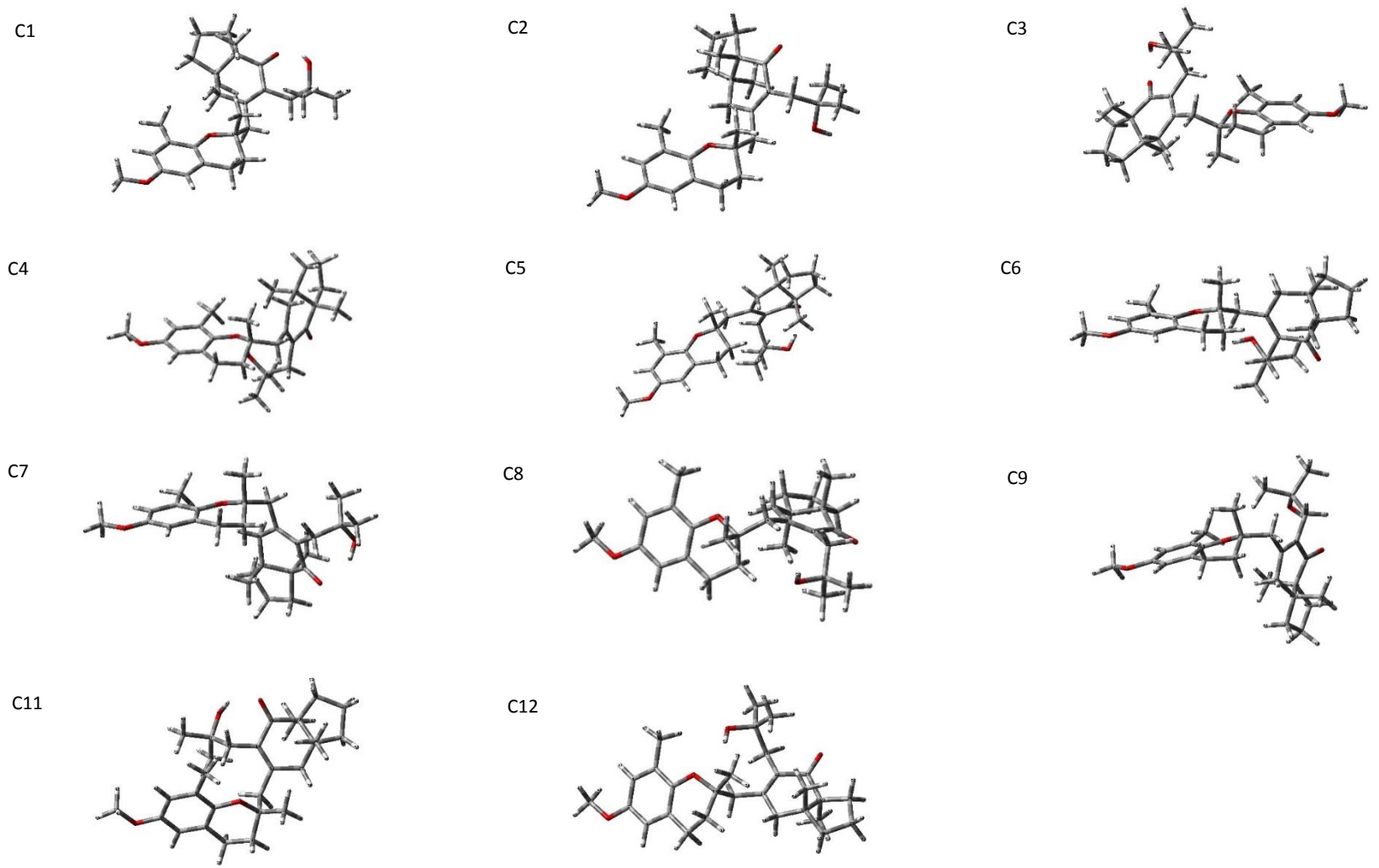
Figure 45. Geometry optimized DFT conformers for (3S,7R,11S)-**1**. Conformers that fulfilled the NOESY constrains are: C1, C2, C3, C4, C5, C6, C9, C11 and C12

1.3.3.3.2 Measurements of the NMR anisotropy parameters: Establishing the relative configuration of **1** by ^{13}C RCSA and RDCs analysis

1.3.3.3.2.1 Carbon RCSA analysis of meroditerpene 1

A first attempt to establish the relative configuration of meroditerpene **1** by ^{13}C RCSA involved the use of a 4 mg (sample in protonated PMMA swallowed in CD$_2$Cl$_2$ using the New Era´s compression device (5 mm OD). Several signals were either obscured or buried under the gel signal, reducing the discrimination capabilities of ^{13}C RCSA's. Therefore, we decided to establish the relative configuration of meroditerpene **1** with the assistance of our recently introduced PMMA-d_8 (70/0.25).

PMMA-$_d$8 and PMMA swallowed in CD$_2$Cl$_2$ has the same degree of alignment, ^{2}H Δv_Q approximately 4.0 Hz. Although, PMMA-d_8 70/0.25 has not been yet tested with CDCl$_3$, we expected a similar mechanical and chemical behavior than the protonated PMMA. Although PMMA-d_8 70/0.25 gel exhibited a low degree of alignment resulting in a small values of anisotropic parameters.

NOESY analysis over **1** indicated that more than one conformation is present. Therefore, to establish the relative configuration by conventional NMR methods was not possible as it was discussed before (Pag. 50). Therefore we want to add our compound to the few collection of flexible natural products which have been solved with RDCs[41] and RCSAs.[56]

Conformers emerged from the conformational searches which were in agreement with NOESY correlations, were used in the RDC fitting using of a multiconformer single tensor (MCST) approach and the population fitted by a combined Levenberg–Marquardt algorithm (see Figure 43 to Figure *45*). The significant assignment of a molecular-fixed-axis system was chosen in such a way that it fulfilled Eckart Condition.

RCSA's data obtained with a ^{2}H Δv_Q of 4.1 Hz at maximum alignment, were analyzed. Q fitting and *c* factors were optimized to its minimum in the software MSpin. In that way we could determine twenty-seven ^{13}C RCSAs for meroditerpene **1** in PMMA-d_8/CD$_2$Cl$_2$ gel using an in-house 3 mm compression device. This result was not achieved by using 4.0 mg of sample in a 5 mm New Era´s compression device with protonated PMMA/CD$_2$Cl$_2$. Values of ^{13}C RCSA's ranged from -7.13 to 2.62 Hz (see Table 6).

Figure 46 shows some significant variations of carbon chemical shifts in the oriented media in **1**. Certain amount of isotropic analyte was always observed because the gel in the compression device did not completely fill the entire sample space, even under maximum compression (Figure 46 panel a). As before, the isotropic signals are easily distinguishable from the corresponding anisotropic signals as their intensities decrease upon compression. As it can be seen in panel b) and d) in Figure 46, ^{13}C RCSA's can takw either positive or negative values.

^{13}C RCSAs were able to discriminate between both plausible diastereomers (3S,7R,11S)-**1** and (3R,7R,11S)-**1** establishing the connection among the stereocenter at C3 and the stereocluster C7-C11 located at four bounds distance.

We decided to study the (3R,7R,11R)-**1** as a plausible option, because, as it was mentioned before, similar meroditerpenes were reported having a *cis* orientation in both methyl groups present at the bicyclo[4.3.0]nonane moiety.[86] Good agreement was achieved between experimental and back calculated ^{13}C RCSAs for (*3S,7R,11S*) configuration ($Q(Q_{CSA})$ = 0.119 (0.163)) as compared with both (*3R,7R,11S*) ($Q(Q_{CSA})$ = 0. 214 (0.333)) and the (3R,7R,11R) configuration ($Q(Q_{CSA})$ = 0.213 (0.336)). (Figure 47, panel a).

Including the chemical shfit anisotropy (CSA) contribution in the computation of the ^{13}C RCSA quality factor (Q_{CSA}) makes the discrimination capabilities of the technique more evident.

Table 6. Carbon residual chemical shift anisotropies (Hz) data for meroditerpene 1 measured in a Bruker spectrometer running at 200 MHz

#C	[13]C RCSA$_{exp}$ (Hz)	Gel shift (Hz)	Error ^{13}C RCSA$_{exp}$ (Hz)	[13]C RCSA$_{calc}$ (Hz)
Me20-	1.27	20.43	0.21	1.175
Me17-	2.27	20.23	0.18	2.888
C2	0.83	5.13	0.24	1.193
C6	0.64	5.86	0.20	0.563
MeO-	1.21	7.45	0.66	1.537
C15	2.62	14.96	0.12	1.573
C2'	-4.01	9.4	0.13	-3.623
C6'	-4.39	2.86	0.18	-4.411
C1'	-5.09	8.66	0.15	-4.941
C5	-3.89	-0.2	0.16	-3.427
C5'	-1.87	11.66	0.22	-1.749
C3'	-2.21	13.09	0.16	-2.178
C3	1.93	13.85	0.16	2.101
C13	-0.58	12.98	0.03	-0.988
C11	1.17	8.52	0.16	1.033
C10	2.25	11.66	0.14	2.115
C8	2.25	12.94	0.27	2.309
C4	0.97	3.16	0.21	0.923
Me-C6'	1.69	11.66	0.58	1.975
Me16-	1.45	9.82	0.13	1.104
Me19-	0.93	11.66	0.17	0.497
Me18-	1.25	13.11	0.20	1.173
C4'	-4.71	12.96	0.25	-4.734
C12=O	-7.13	-17.64	0.14	-7.488

C9	2.62	11.66	0.32	2.483
C1	1.79	11.66	0.27	1.912

C14 was used as references in ^{13}C RCSA calculation.
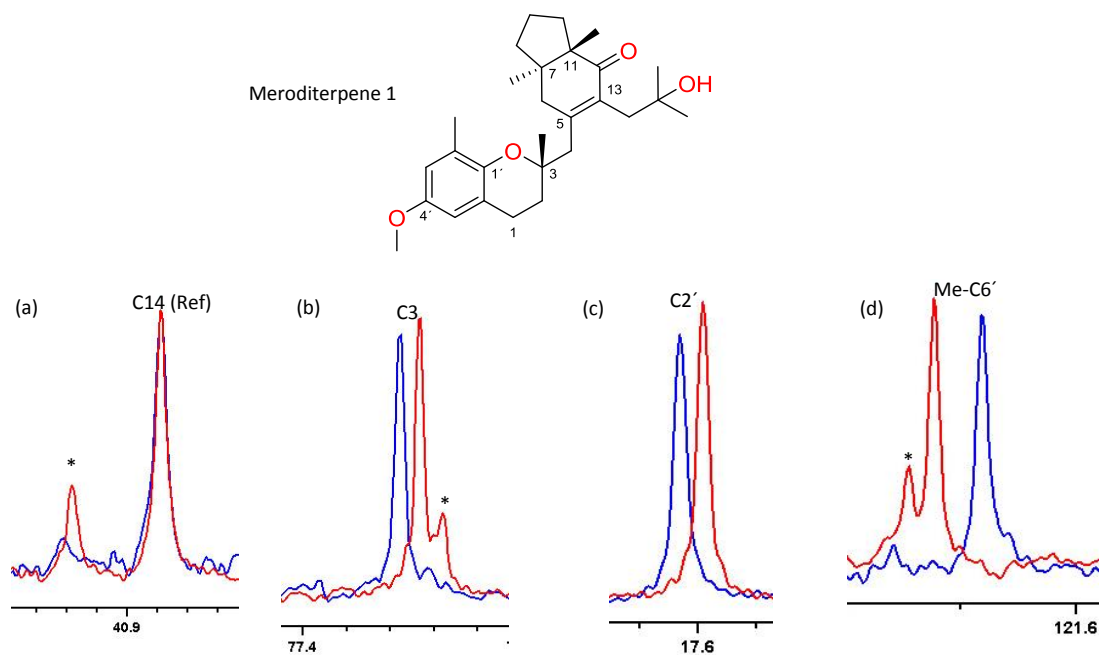
Figure 46. ^{13}C RCSA's obtained with compression devices (3 mm). Panels a)-d) show resonances from the ^{13}C-{^{1}H} 200 MHz NMR spectra for meroditerpene **1** under minimum (red) and maximum (blue) compression. The C14 resonance shown in panel a), was used as the reference resonance. Note the presence of both isotropic (marked with an asterisk) and anisotropic signals for some carbons. Spectra recorded with minimum alignment were recorded under complete relaxation of the PMMA-d_8 gel. Maximum compression ($\Delta vQ = 4.2$ Hz) increased the molar fraction analyte in the gel, therefore isotropic correction was applied.
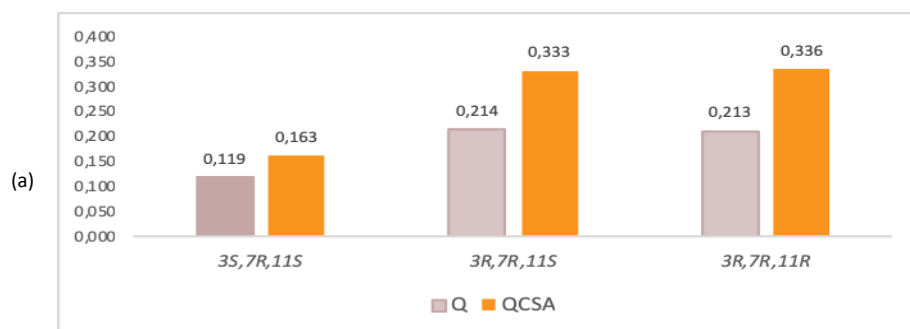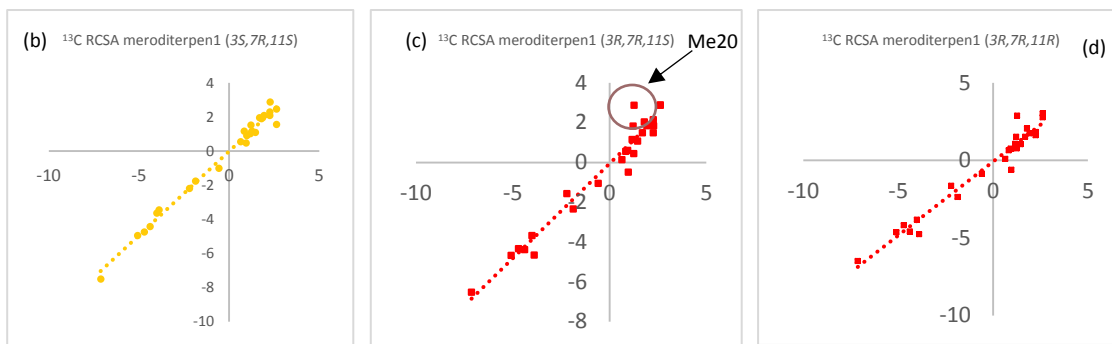
Figure 47. The Q(Q_CSA) factors for the configurations (3S,7R,11S)-**1**; (3R,7R,11S)-**1,** and (3R,7R,11R)-**1** are 0.119(0.163), 0.214(0.333) and 0.213(0.336), respectively. The unscaled Q factors are reported (violet columns). As expected QCSA made the discrimination more evident (orange columns) (a). Anisotropic data fitting (^{13}C RCSA) of meroditerpene **1** measured at 800 MHz for in PMMA-d_8/CD$_2$Cl$_2$ gel. Fitting for carbon residual chemical shift anisotropies of diastereoisomers (3S,7R,11S)-**1** (b), (3R,7R,11S)-**1** (c) and (3R,7R,11R)-**1**. (d) Free parameter c found for each diastereoisomer was 0.091, 0.121 and 0.122 respectably. Correlation coefficient for the fitting of (3S,7R,11S)-**1** is 0.9858. Back calculated ^{13}C RCSA for Me20 in the configuration (3R,7R,11S) was 2.886 Hz. Meanwhile, 1.175 Hz was found for the configuration (3S,7R,11S). Me20 in the fitting corresponding to (3R,7R,11S) appeared as an outlier (green circle), supporting the robustness of the ^{13}C RCSA to distinguish between either R or S configuration.

Discrimination was not only supported by $(Q(Q_{CSA})$, but also for the linearity fitting (Figure 47, panels b-d). It is important to notice, how Me20 emerged as an outlier when *R* configuration was considered at carbon 3 (Figure 47, panel c).

^{13}C RCSA capabilities to distinguish among the three possible configurations of a flexible molecule was checked with retrorsine.[17] Alignment conditions involved the use of PMMA, swollen in CDCl$_3$. Obtained RCSA's, depends, among other parameters, depends on the side of ^{2}H ΔvQ (4.1 Hz) at maximum alignment. The main source of error in chemical shift determination is due the uncertainty in peak position. Therefore, acquiring a ^{13}C spectrum with a good signal-to-noise ratio is mandatory.[39,94]

As ^{13}C RCSA's were rather small, deviation in ^{13}C δ were expected to be significant, thus a Montecarlo Bootstrapping analysis was performed over the data. Chemical shift error (error ^{13}C RCSA$_{exp}$) was independently calculated for each nucleus (Table 6), as the quotient of peak line width between signal to noise ratio. RCSA'ss Standard deviation was calculated using wrror ^{13}C RCSA$_{exp}$ (σ $_{Error\ 13CRCSAexp}$ = 0.13 Hz). Gaussian bell curves[95] derived from Bootstrapping analysis clearly indicates that ^{13}C RCSAs data collected unambiguously assigned (*3S,7R,11S*)-**1** as the correct configuration (Figure 48).

(a)

Frequency
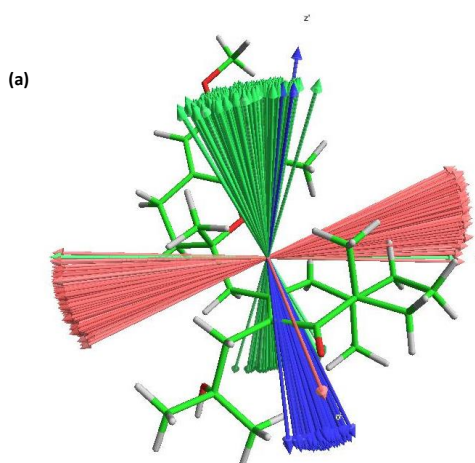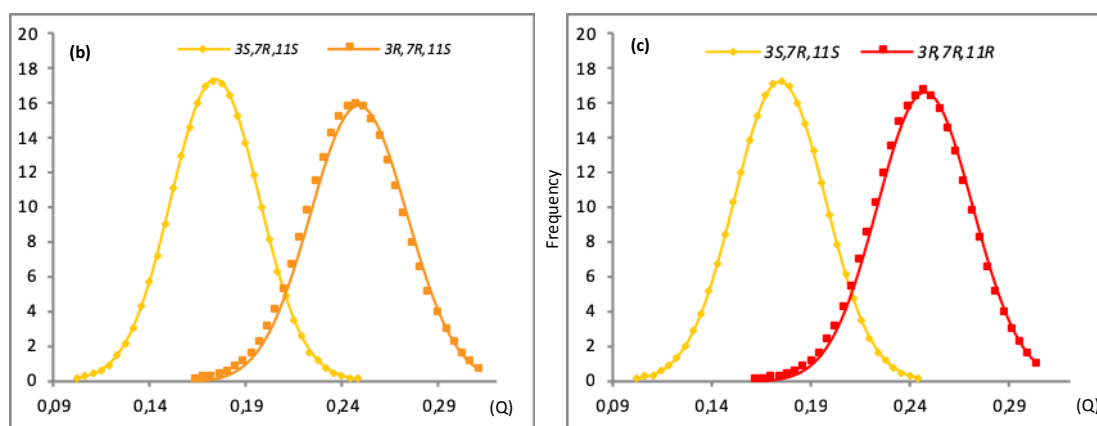
Figure 48. Alignment vectors emerged after Bootstrapping analysis for (3S,7R,11S) configuration. a) Gaussian bell curves for (3S,7R,11S)-**1**; (3R,7R,11S)-**1** and (3R,7R,11R)-**1** are indicated in blue, orange and red respectively. Inspection of bell curves derived from Bootstrapping, as retrorsine ^{13}C RCSA analysis, made discrimination between diastereoisomers evident (b and c). Conservative error of two times σ was used in a 256 sample point Gaussian distribution.

1.3.3.3.2.2 RDC analysis of meroditerpene **1**

It is well-known that proton-proton dipolar signal gets broader under anisotropic conditions, becoming a mayor experimental problem during RDC's measurement. This problem is commonly overcome using the F1 ^{1}H-coupled version of the HSQC experiment.[21,96] Nevertheless, we decide to explore the PMMA-d_8 (70/0.25) capabilities to provide accured RDC values, as sharp lines during RDC analysis when CLIP/CLAP HSQC experiment was used. Resolution was further enhanced by the use of a low viscosity solvent, CD_2Cl_2, and deuterated polymer as demonstrated in Figure 49.
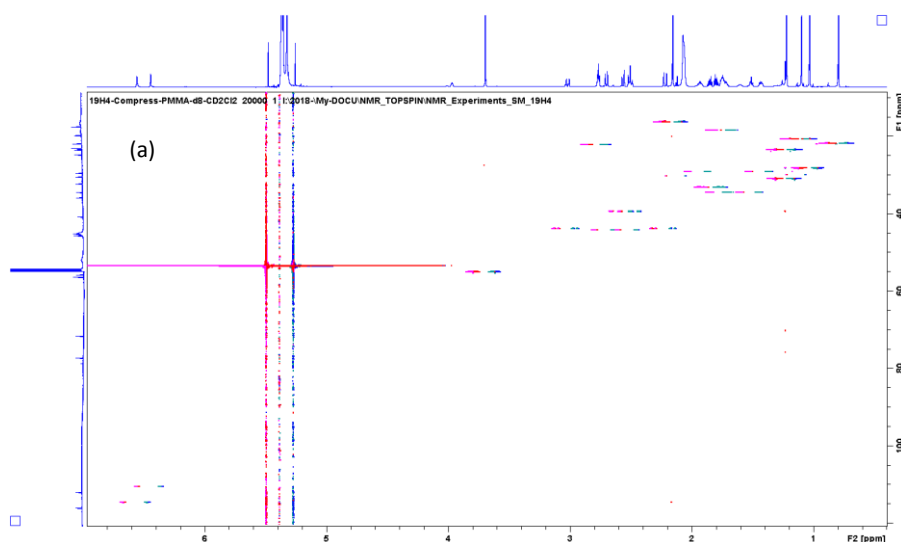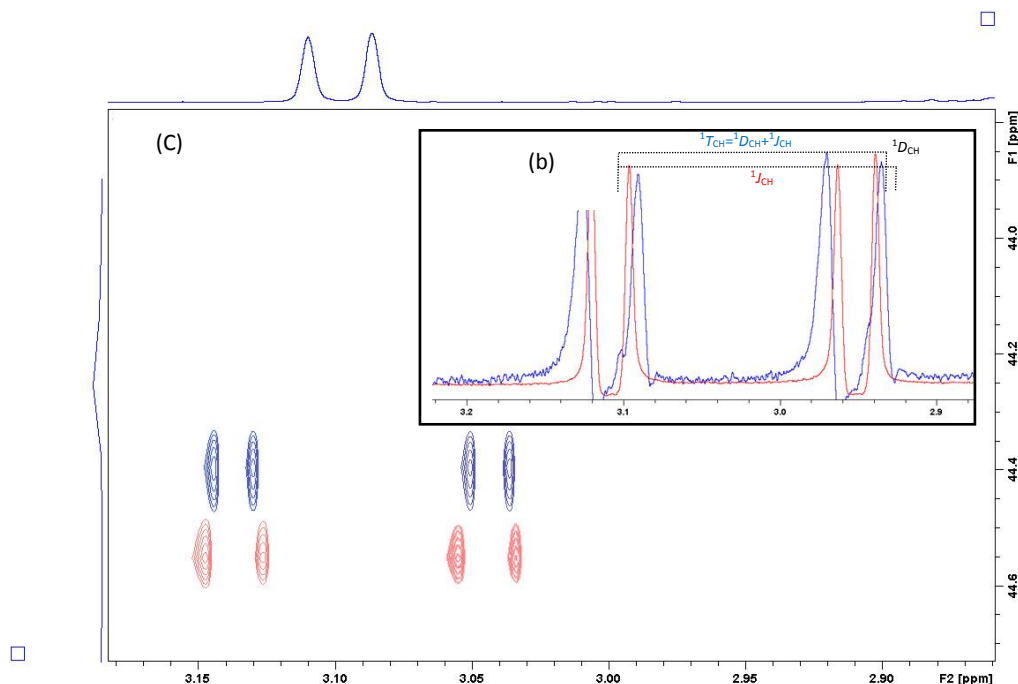
Figure 49. CLIP/CLAP HSQC at maximum compression during RDC's measurement in meroditerpene **1.** a) Extraction of CH coupling ($^1T_{CH}$ and $^1J_{CH}$) from the experimental data collected with the CLIP/CLAP HSQC experiment. b) Expanded region of C6-H6b cross-peak with the isotropic spectrum shown in red and the anisotropic in blue. Note that the deuterated PMMA yielded very sharp lines in anisotropic conditions (c). Peak width 35.1 Hz and Signal-to-Noise ratio showed a value of 244.2, therefore $^1D_{CH} \pm \Delta$ is -1.281 ± 0.144

Before the collection of anisotropic data with a protonated gel in small molecules, we advise check both solvent compatibility and background signal coming from the polymer. Solvent chosen for the analysis was CD_2Cl_2 as meroditerpene **1** decomposes in $CDCl_3$.[85] PMMA-d_8 performed very well at milligram scale (1.6 mg) showing almost no interferences from background signal (Figure 49, panel b). Nevertheless, two RDC could not be accurately extracted because the signal gets broader after polymer compression. In our own experience handling PMMA-d_8, RDC determination can be performed at amounts as low as 1.7 mmol/L.

Even with a low degree of alignment of **1**, resulting in small $^1D_{CH}$ values (maximum and minimum value of 3.04 and -6.72 Hz respectably), 17 RDC's were measured with great accuracy due to the narrow spectral lines (Table 7). Consequently, we have overcome the proton-proton dipolar broadening signal under compression conditions, using PMMA-d_8 gel. A very important consequence is deduced by this approximation: we were able to measure $^1D_{CH}$ by using a F1 ^{1}H-coupled version of a HSQC!

One-bond proton-carbon RDCs ($^1D_{CH}$) are reported as the difference between the signals splitting observed under anisotropic and isotropic condition ($^1T_{CH} = {}^1J_{CH} + {}^1D_{CH}$).[97] (Table 7). NOESY correlation gather from meroditerpene **1** indicated that presents a conformational equilibrium in the aliphatic chain connecting both chromane and bicyclo[4.3.0]nonane moieties.

RDC fitting data of the three possible diastereomers, alignment tensor determination, and calculation of Cornilescu's quality factor (Q) were carried out in MSpin software. Error bars showed in fitting curve and Q factor-bar plot was expresses a 3 times standard deviation, which is expected to contain around 96 % of the data.[95] Standard deviation, was computed by using Montecarlo Bootstrapping module in MSpin software.

Table 7. Meroditerpene **1**, scalar coupling constant $^1J_{CH}$, total splitting $^1T_{CH} = {}^1J_{CH} + {}^1D_{CH}$ and experimental (exp) and calculated (calc) $^1D_{CH}$ values with their corresponding experimental error.

# C	δ^{13}C (ppm)	δ^1H (ppm)	$^1T_{CH}$ (Hz)	$^1J_{CH}$ (Hz)	Exp D_{CH} (Hz)	Calc D_{CH} (Hz)	Error (Hz)
C1	23.1	2.7830	124.64	129.37	-4.72	-4.26	0.03_6
C2	34.1	Ha:1.864	127.12	128.77	-1.64	-2.79	0.08_1
		Hb:1.811	126.32	128.81	-2.48	-2.53	0.20_7
C4	45.2	Ha: 2.518	120.40	127.12	-6.72	-6.41	0.09_2
		Hb: 2.710	124.34	125.72	-1.38	-0.61	0.11_5
C6	44.8	Ha: 2.227	127.40	129.0	-1.62	-1.37	0.08_0
		Hb: 3.035	124.60	125.9	-1.28	-0.75	0.14_4
C8	35.4	Ha: 1.527	126.04	131.81	-5.76	-5.47	0.23_4
		Hb:1.760	*	129.09	*	1.21	-
C9	19.3	1.7445	125.88	131.05	-5.16	-5.52	0.19_0
C10	30.1	Ha: 1.951	131.61	129.81	1.80	1.93	0.35_0
		Hb: 1.448	130.17	132.57	-2.40	-3.74	0.29_6
C14	40.4	Ha: 2.514	125.58	127.04	-1.46	-0.42	0.05_8
		Hb: 2.572	*	125.48	*	8.19	-
Me16-	29.1	1.241	125.48	125.20	0.28	-0.53	0.00_1
Me17-	31.9	1.046	124.56	125.12	-0.56	-2.03	0.01_0
Me18-	21.5	1.1115	130.65	127.60	3.04	1.88	0.01_3
Me19-	22.7	0.8112	127.16	125.44	1.72	1.74	0.01_2
Me20-	24.3	1.2311	128.65	126.32	2.32	1.94	0.01_0
Me-C6´	17.1	2.1720	127.12	127.20	-0.08	0.08	0.00_3
MeO-	56.0	3.707	142.86	143.30	-0.44	-0.77	0.00_3
C3'	111.6	6.462	157.22	156.14	1.08	0.24	0.01_3
C5'	115.7	6.575	158.47	156.38	2.08	1.54	0.01_2

Error (Hz) is the experimental error associated with each D_{CH}[39].

By using $^1D_{CH}$ RDC, configuration (3R,7R,11S) and (3R,7R,11R) were certainty eliminated. The efficacy of the RDC's NMR technique was demonstrated for establishing the relationship between two distant stereoclusters of meroditerpene **1** separated by 4 rotatable covalent bonds. Configuration (*3S,7R,11S)* showed a Q of 0.243 meanwhile (*3R,7R,11S)* and (*3R,7R,11R)* presented a Q 0.768 and 0.822, respectively. Discrimination was supported not only for degree of linearity between experimental and back calculated $^1D_{CH}$ RDC, but also for Bootstrapping Analysis (Figure 50 panel b) carried out on a sample side of 256 (see Table 8, and all alignment tensor found are shown in Figure 50 panel a).

Table 8. Results of the Bootstrapping analysis over $^1D_{CH}$ RDC collected from meroditerpene **1**

Configuración	Average Q	Mínimum Q	Máximum Q	Q Standard deviation
3S,7R,11S	0.243	0.217	0.267	0.009
3R,7R,11S	0.768	0.748	0.787	0.007
3R,7R,11R	0.822	0.803	0.849	0.008
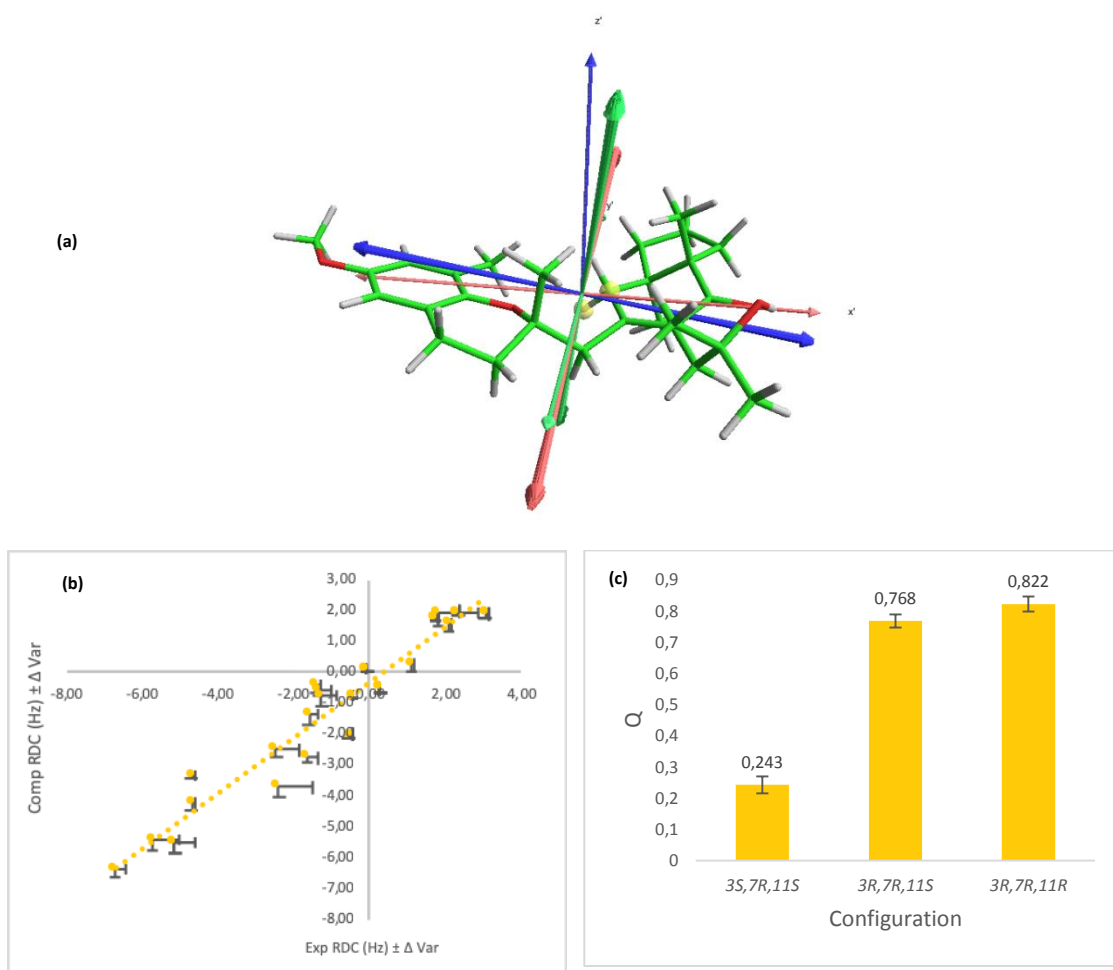
Figure 50. Alignment vectors emerged after Bootstrapping analysis for (3S,7R,11S)-**1** (a). RDC fitting curve of (3S,7R,11S)-**1** (b) and Q factor found for each configuration (from left to right (3S,7R,11S); (3R,7R,11S) and (3R,7R,11R)) (c). Experimental error in both panel b) and c) is equivalent to 3 times standard deviation of RDC, calculated with the bootstrapping module of MSpin by using a Gaussian distribution is a size of 256.

1.3.3.3.2.3 Structural refinement by ^{13}C RCSA

Dipolar couplings have proven to provide long range restraints to solve the structure of proteins[98] and natural products,[99] helping to establish not only the relative configuration but also molecular spatial orientation.

We want to unambiguously establish the relative configuration of the meroditerpene **1** already established by independent ^{13}C RCSA and $^1D_{CH}$ RDC measurements as (3S,7R,11S), by using a structure refinement of meroditerpene **1** within carbon residual chemical shift anisotropy (^{13}C RCSA). We expect that all orientation restraints provided by this refinement on the internuclear vectors and the principal axes of chemical shift anisotropy (CSA) tensors it´s enough. RCSA have been used before in peptides and in proteins.[2,100] however its application on small molecules is scare.

Conformers used in this research were created by staged rotation on routable bonds (see Figure 34) following by DFT geometry optimization. Dihedral angle Me-O-C4´-C3´ ($\theta_{Me-C3'}$) was set as 90° and let it to freely evolve during the optimization process. Value of θ_{Me-C3} was around

180° in all the conformers, for all the different diastereoisomers (see from Figure 43 to Figure 45). Nevertheless, NOESY analysis clearly indicated that the MeO group showed correlation with H5´and H3´, meaning that the group is rather rotating than rigid. Moreover, a slice taken from NOESY experiment make us think that the MeO- rather point out to H3´than to H5´ (Figure 51, panel b).

^{13}C RCSA fitting data was performed again as described before but taken those conformers which contribute mostly to the ^{13}C RCSA fitting. θ_{Me-C3} was changed from 180° to 0° and then DFT geometry optimization and GIAO CST calculation was done as before. Back calculated data is displayed in Table 9. As a consequence of the MeO- rotation Q(Q_{CSA}) factor drops from 0.119(0.163) to 0.105(0.148) and linearity fitting also improves (Figure 51, panel c).

Table 9. Carbon residual chemical shift anisotropies (Hz) data for meroditerpene 1 measured in a Bruker spectrometer running at 200 MHz after structural refinement.

#C	[13]C RCSAexp (Hz)	Gel shift (Hz)	Error ^{13}C RCSAexp (Hz)	[13]C RCSAcalc (Hz)
Me20-	1.27	20.43	0.21	1.16
Me17-	2.27	20.23	0.18	2.67
C2	0.83	5.13	0.24	1.16
C6	0.64	5.86	0.20	0.58
MeO-	1.21	7.45	0.66	1.51
C15	2.62	14.96	0.12	1.87
C2'	-4.01	9.4	0.13	-3.91
C6'	-4.39	2.86	0.18	-4.15
C1'	-5.09	8.66	0.15	-5.02
C5	-3.89	-0.2	0.16	-3.34
C5'	-1.87	11.66	0.22	-1.84
C3'	-2.21	13.09	0.16	-2.18
C3	1.93	13.85	0.16	2.24
C13	-0.58	12.98	0.03	-0.99
C11	1.17	8.52	0.16	1.24
C10	2.25	11.66	0.14	1.92
C8	2.25	12.94	0.27	2.35
C4	0.97	3.16	0.21	0.97
Me-C6'	1.69	11.66	0.58	1.88
Me16-	1.45	9.82	0.13	1.15
Me19-	0.93	11.66	0.17	0.51
Me18-	1.25	13.11	0.20	1.06
C4'	-4.71	12.96	0.25	-4.65
C12=O	-7.13	-17.64	0.14	-7.52
C9	2.62	11.66	0.32	2.54
C1	1.79	11.66	0.27	2.07
C7	-	-	-	0.860

C14 was used as references in ^{13}C RCSA calculation. (-) Not readable, overlapped with polymer background signal

The main goal of this experience was to validate the ^{13}C RCSA as an exceptional option on the refinement of structure of natural products, even at low degree of alignment, like in this case. At the present moment, we understand that ^{13}C RCSA technique is called to capitalize its unique ability to build the alignment vector from carbon chemical shifts, and systems lacking in hydrogens will be greatly benefited.[101]
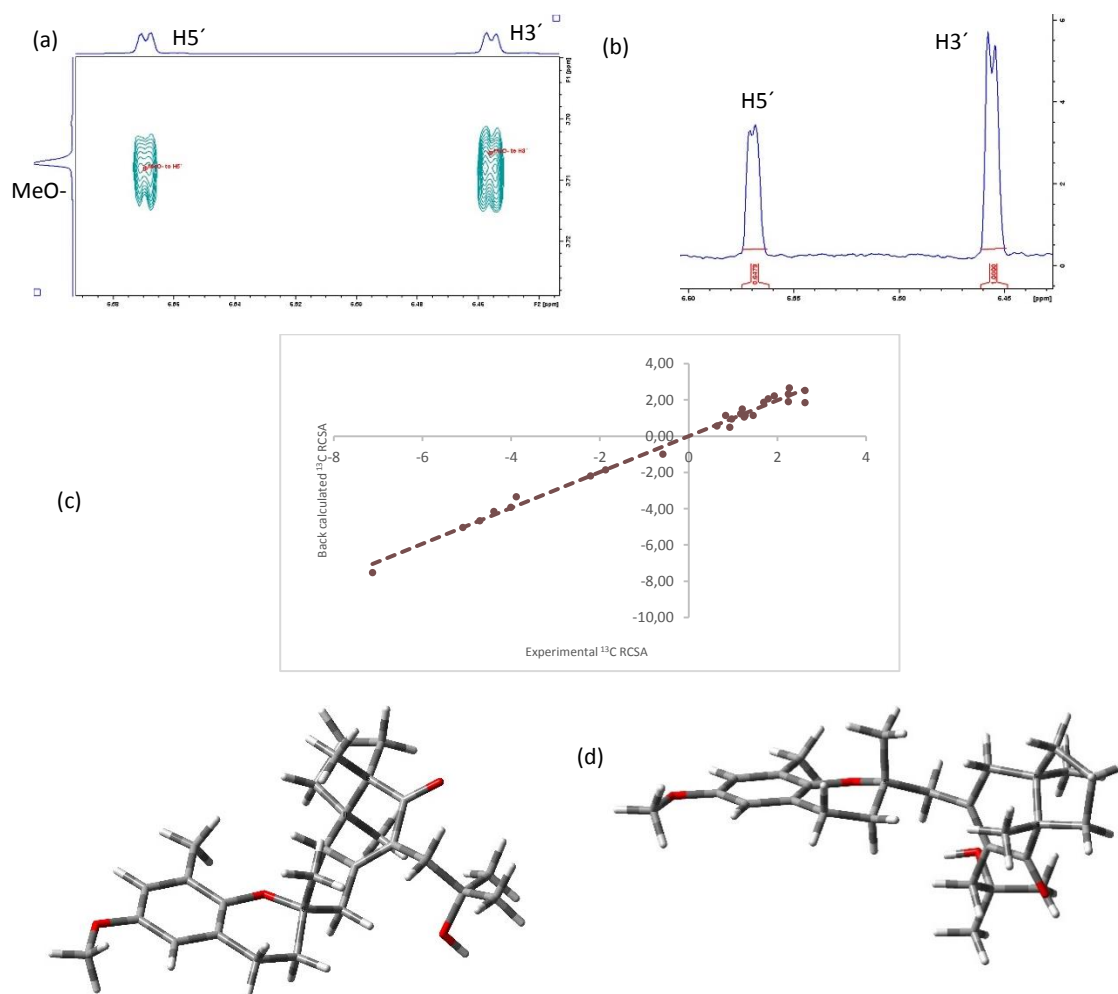
Figure 51. ^{1}H-^{1}H NOESY spectra measured on an 800 MHz Bruker spectrometer, showed a clear correlation between the MeO group and both aromatic protons H3´and H5´ (a). Moreover, a slice taken from the 2D NOESY, showed that θ_{Me-C3} value around 0° is structural more favorable (b) Fitting of (3S,7R,11S)-**1** after rotation around θ_{Me-C3} was taken in account increasing its linearity; correlation coefficient went from 0.9858 to 0.9889, and the *c* free parameter showed a value of 0.088. Major populated conformers for (3S,7R,11S)-**1** acording ^{13}C RCSA data, after structural refinement, are displayed in panel (d).

1.3.3.3.2.4 Low concentration analysis

Some natural products are available in amounts below 200 µg, making its assignment a laborious task.[54,102,103] Anisotropic parameters like $^1D_{CH}$, $^3D_{HH}$ RDC or ^{13}C RCSA are quite difficult to register and interpret. To overcome these challenges, we propose ^1H RCSA as a valid tool to determine the relative configuration of natural products available at microgram levels. We demonstrated the ability to solve a sample of 10 µg strychnine as proof of concept in the New Era´s stretching device (5 mm ID). (Page. 27)

Encouraged by the resulted found with the New Era´s stretching device and liquid crystal media, we decide to study the ^1H RCSA's from our 3 mm compression device prototype with a PMMA-d_8 (75/0.25; CD_2Cl_2) using a concentrated α-santonin sample (*vide supra*). Throughout the data analysis we understood that isotropic shift correction, described by Nath et al.,[22] was also required in ^1H RCSA analysis along with the use of a Pure-Shift ^1H NMR Psyche for accurate ^1H RCSA data extraction.

Having established the relative configuration of meroditerpene **1** (1.6 mg) by independent measurements of ^{13}C RCSA and $^1D_{CH}$ RDC as (*3S,7R,11S*)-**1** (*vide supra*); we decided to explore the capabilities of the data analysis approach described for α-santonin.

PMMA-d_8 compression compatible gel used here belongs to the last generations of deuterated PMMA gel produced by our research group, where background signal rises only for the cross linker, a radical initiator and non-deuterated monomer. At microgram scale, the background signal becomes an important issue, and some signal are either to broad or very weak to be used (see Figure 52).
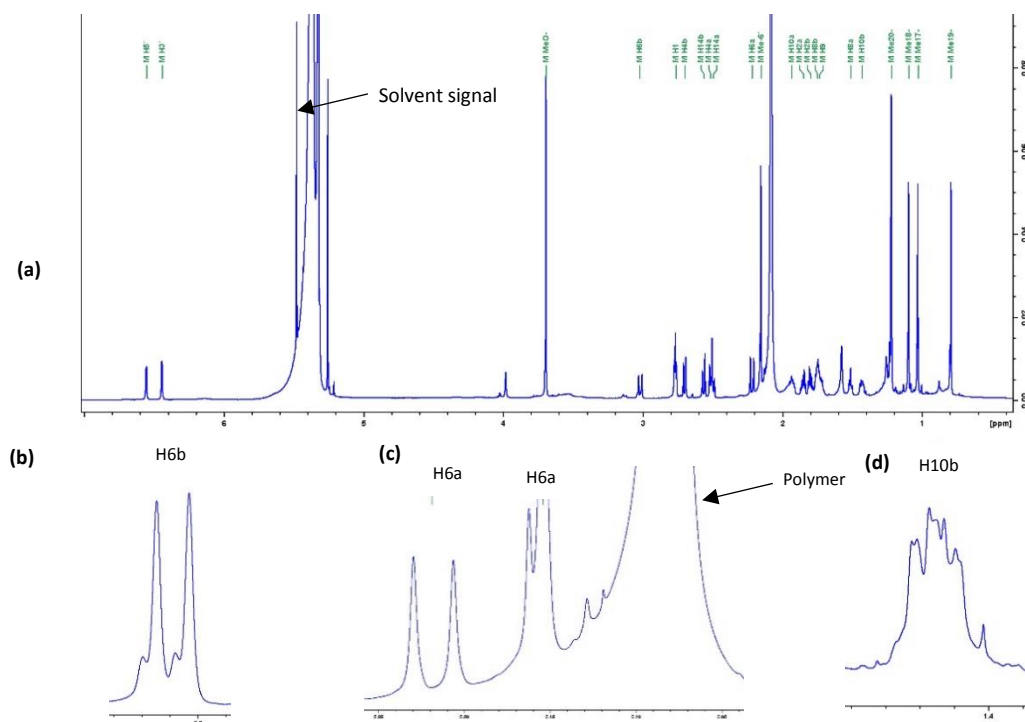
Figure 52. Isotropic ^1H NMR spectrum of meroditerpene **1** (230 µg) measured in an 800 MHz Bruker spectrometer. Number of scans 448. Sample was swollen in PMMA-d_8 (CD_2Cl_2) (a). Extraction of isotropic peak is not straightforward (b). Polymer background signal becomes an important issue, causing some disturbance in compound signal at microgram level within 1.4 to 2.2 ppm section where Me-C6´signal resonates (c). Moreover, complexity of some multiples makes RCSAs extraction too intricate, leaving the doubt of whether or not the isotropic signal is present (d). Therefore, we recommend the use of Pure shift ^1H NMR despite the detriment of sensitivity.

Similar to PMMA-d_8 stretching compatible gel, above described, at low concentration (230 µg) background signal becomes almost visible and overlapping with the analyte signals is likely within a limited region (1.1-2.1 and 3.4-3.7 ppm). Pure Shift ^{1}H NMR 1D-Psyche allowed the extraction of 20 independent ^{1}H RCSAs by both collapsing the complex multiplet patterns to singlets and minimizing the influences of the traces of protonated material in the deuterated polymer. (Figure 53). Nevertheless, some RCSAs were not extracted either due signal broadening or lack of intensity. Figure 53 shows some significant proton chemical shifts of meroditerpene **1**. As in the case of α-santonin, during the use of the compression device certain amount of isotropic analyte was always present in the compression device as the gel does not fill the entire sample space (Figure 53 b). As before, the isotropic signals are easily distinguishable from the corresponding anisotropic signals, as their intensities decrease upon compression. Some signals do not show visible isotropic peaks at relaxed gel position as H3′ (Figure 53, panel a).

[1]H RCSA fitting was carried out by following a similar procedure as described before. [1]H RCSAs could be distinguished between the three proposed diastereomers ((*3S,7R,11S)*-**1**; (*3R,7R,11S)*-**1** *and (3R,7R,11R)*-**1**) establishing the connection among the stereocenter at C3 and the C7-C11 stereocluster in meroditerpene **1**.

RCSA's obtained with [2]H Δv_Q of 4.5 Hz at maximum alignment were analyzed by Data fitting, and *c* factor optimized calculated to its minimum in the software MSpin. It was possible to determine twenty ^{1}H RCSAs for meroditerpene **1** in PMMA-d_8/CD_2Cl_2 gel using an in-house 3 mm compression device from a 2.9 mmol. L^{-1} sample. Being RCSA from H14a, H10a, H8b, H8a and Me16 either obscured polymer signal or too weak to be measured. RCSAs were in a range of -1.36 and 1.12 Hz (Table 10).
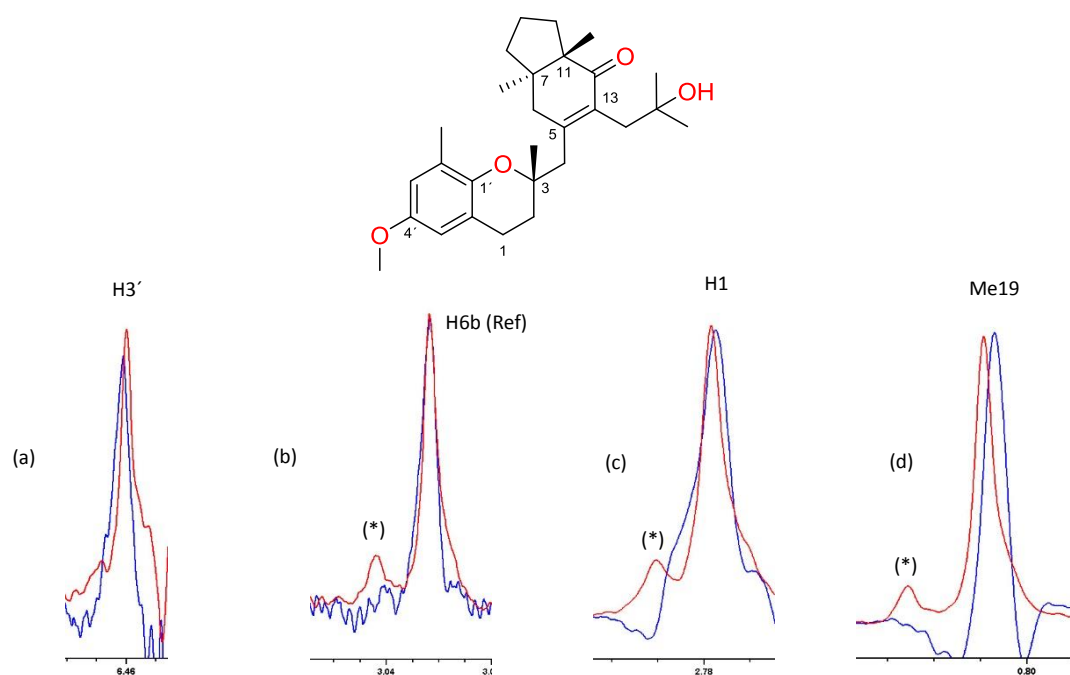
Figure 53. [1]H RCSAs obtained with compression devices (3 mm) from a 230 µg sample. Panels a-d show resonances from the 1D pure shift 800 MHz NMR spectra from meroditerpene **1** observed under minimum (red) and maximum (blue) compression. The H6b resonance shown in panel b, was used as the reference resonance. Note the presence of both isotropic (marked with an asterisk) and anisotropic signals for some protons (panel c & d), while other shows only anisotropic signal. Proton RCSA can take either negative (a) or positive (d) values. Spectra recorded with minimum alignment were recorded under complete relaxation of the PMMA-d_8 gel (70/0.25). Maximum compression (ΔvQ = 4.5 Hz) increased the molar fraction analyte in the gel, therefore isotropic correction is applied.

Table 10. Proton residual chemical shift anisotropies (Hz) data for meroditerpene 1 measured in a Bruker spectrometer running at 800 MHz. Sample was swallow in PMMA-d_8 (70/0.25)/CD_2Cl_2

#H	[1]H RCSAexp (Hz)	Gel shift (Hz)	[1]H RCSAcalc (Hz)
H5´	0.16	-8.17	-0.03$_3$
H3´	-0.24	-8.17	-0.12$_5$
MeO	0.48	-3.84	0.49$_9$
H1	0.00	-3.36	0.23$_4$
H4b	-1.36	-8.17	-1.11$_1$
H4a	-0.32	-8.17	-0.16$_3$
H14a	*		0.58$_9$
H6a	-0.72	-3.60	-0.69$_9$
Me-C6´	0.56	-1.84	0.59$_4$
H10a	*		0.48$_8$
H2a	0.32	-8.17	0.15$_6$
H2b	-0.32	-8.17	-0.20$_9$
H8b	*		0.53$_5$
H8a	*		2.56$_4$
H10b	-0.24	-8.17	-0.38$_2$
Me16-	*		1.48$_3$
Me20	0.40	-8.17	0.28$_2$
Me18	0.88	-4.08	0.73$_2$
Me17	0.72	-3.60	0.81$_9$
Me19	1.12	-1.60	1.20$_3$

[1]H RCSA was computed using H6b as reference. (*) Not readable, and back calculated after the fitting

A good agreement between experimental and back calculated ^{1}H RCSAs for (*3S,7R,11S*)-**1** configuration was achieved ($Q(Q_{CSA})$ = 0.1.93 (0.189)) as compared with both (*3R,7R,11S*)-**1** ($Q(Q_{CSA})$ = 0. 262 (0.265)) and the *(3R,7R,11R)*-**1** ($Q(Q_{CSA})$ = 0. 341 (0.359)). (Figure *54*). Including the chemical shit anisotropy (CSA) contribution in the computation of the Q_{CSA} increases the discrimination capabilities.
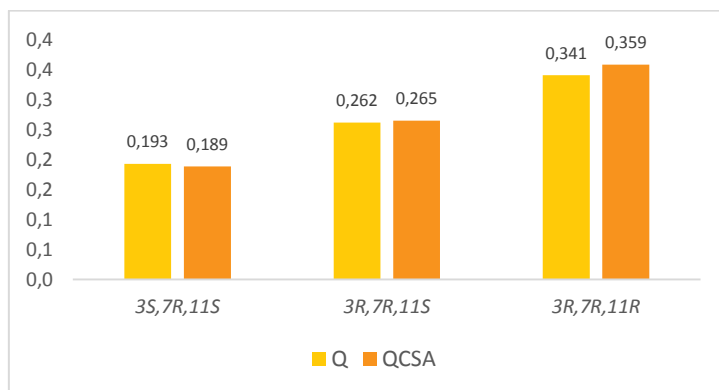
Figure 54. Proton residual chemical shift anisotropy Q(QCSA) bar plot for meroditerpene 1

We would like to close the study of meroditerpene **1**, pointing out the importance of considering the quality of fitting. A visual inspection of the fitting curve always will be necessary to be checked, both its linearity and the presence of outliers or any other kind of anomaly (Figure 55)
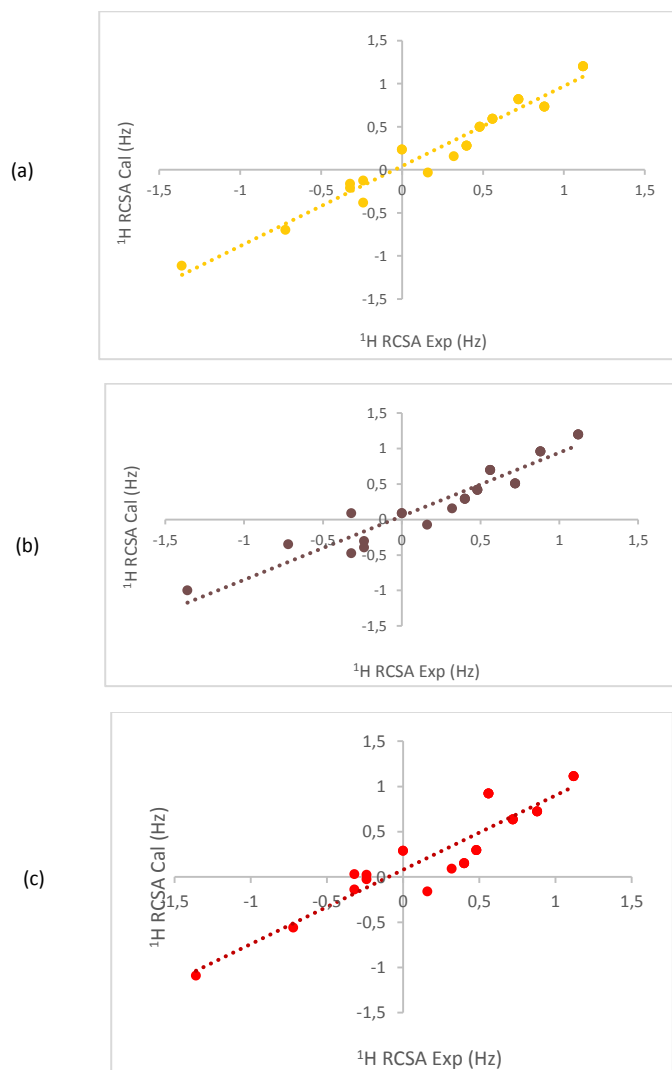
Figure 55. Fitting curve is an important component during the anisotropic study of a small molecule. One not only should take in account the final value of $Q(Q_{CSA})$ but also a reasonable linear behavior most be shown by the experimental and back calculated data. Fitting curve for relative meroditerpene **1** configurations 3S,7R,11S; 3R,7R,11S and 3R,7R,11R are showed in panel a, b and c respectably.

1.3.3.3.2.5 Potential applicability of PMMA-d_8

Two-bond proton-proton residual coupling are also a valuable anisotropic parameter in structural determination. They can be used for structural refinement of macromolecules[104] and small molecules.[105] As in ^{1}H-^{13}C RDC, the angle-dependent dipolar interactions of ^{1}H-^{1}H RDC averages to zero, owing to the uniform distribution of all orientations. Measurement of two-bond proton-proton coupling constants ($^2J_{HH}$) in prochiral CH$_2$ groups in protonated alignment media is not easy due to the usual presence of complex multiplet J patterns, line broadening effects and strong coupling artifacts.[106] Although, the study on small molecules by ^{1}H-^{1}H RDC, 3 bounds or even beyond, analysis is outside the scope of this Thesis Dissertation, nevertheless it is worth mentioned due the fact that line bordering is almost zero in the majority of signals at maximum compression, making the extraction of germinal and long range ^{1}H-^{1}H RDC straightforward from a 1D proton spectrum (see Figure 56).
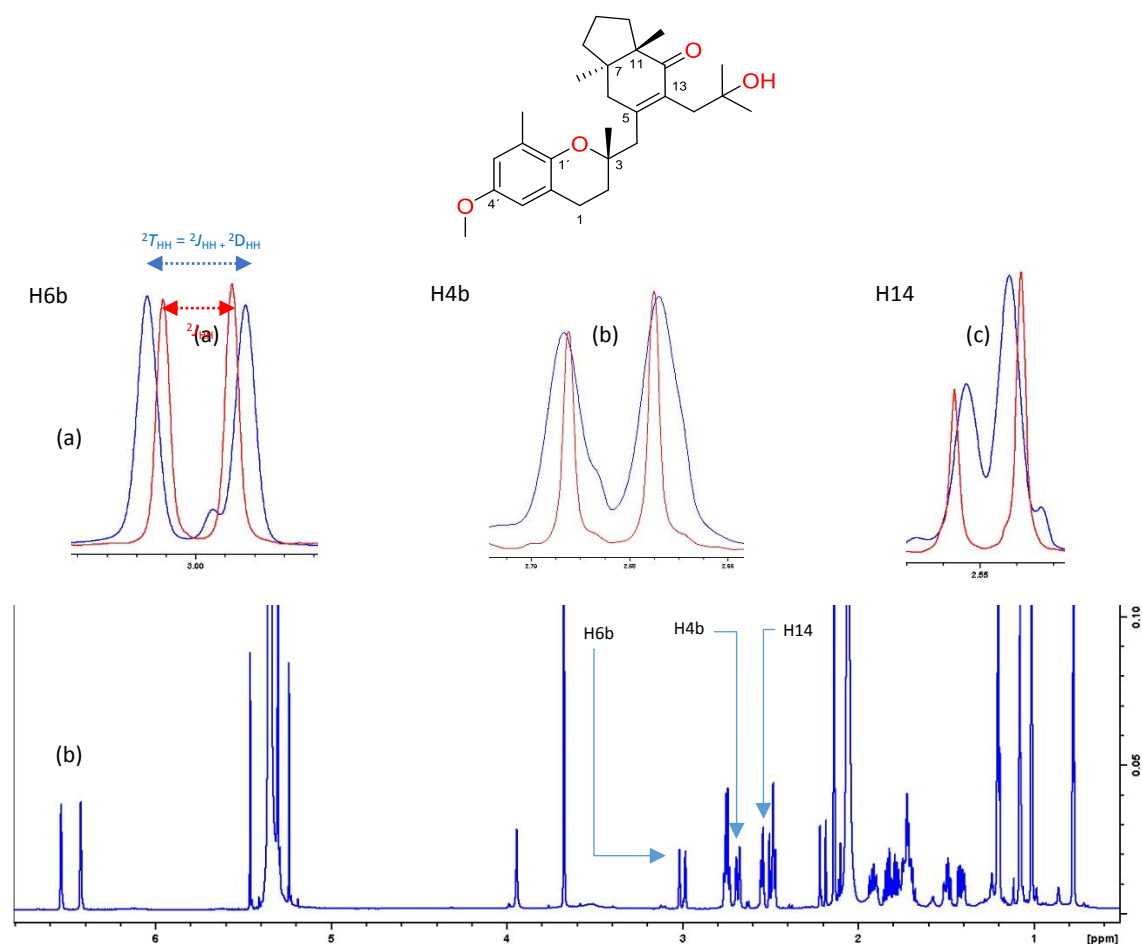
Figure 56. 1D proton spectrum obtained at maximum compression in the semi micro compression device (1.6 mg). Panels a-c show proton resonances from the 1D 800 MHz NMR spectra from meroditerpene **1** observed under minimum (red) and maximum (blue) compression. Spectrum recorded with maximum compression (ΔvQ = 4.2 Hz) shows almost none distortion allowing straight forward ^{1}H-^{1}H RDC extraction. 160 scans.

1.3.3.3.2.6 Experimental section

Methods and materials

Electric Circular Dichroism (ECD) and ultra Violet (UV) spectra were recorded on a JASCO J-815 CD spectrometer (JASCO). [1]H and ^{13}C spectra were recorded on Bruker spectrometers at 950 and 200 MHz, respectively; ^{13}C multiplicities were determined by DEPT spectra and ^{1}H RCSA were recorded on Bruker spectrometers at 800 MHz. All other chemicals were of analytical-reagent or HPLC grade. TLC were performed on silica gel (Merck, Kieselgel 60 F_{254}) plates; the spots were visualized by exposure to UV light (254 nm). Column chromatography was carried on silica gel (Merck, Kieselgel 60). ECD spectra of meroditerpene 1 (Compound 1) was recorded in the region from 225 to 470 nm at a concentration of 2.88×10^{-4} M in CH_2Cl_2 in a 1 mm cell; a total of 5 accumulations at scanning speed 20 nm/min and a temperature of 25 °C. Isolation and purification was done at Centro de Investigacións Científicas Avanzadas (CICA) –Spain. Mass spectra ESIMS was recorded on a LC-Q-q-TOF Applied Biosystems QSTAR Elite and LC-HRMS spectra were done in a LTQ-Orbitrap Discovery coupled to a U-HPLC Accela Thermo Fisher Sci in Servizos de Apoio á Investigación - Universidade da Coruña – Spain. ECD, DFT calculation and both isotropic and anisotropic NMR experiments were carry on at Max Planck Institute for Biophysical Chemistry Facilities, Gottingen-Germany at Griesinger´s Group.

Data processing

Experimental and calculated ECD and UV data were handled with SpecDis V 1.7.[107] NMR data were processed and analyzed in Bruker TopSpin Software V 3.1. Graphics were carried out on Microsoft Excel 365. Geometrical optimization and TDSCF calculation were carried out with the Gaussian 09 suite of programs. Molecular structures were made in ChemDraw V 12.0 and Avogadro V 1.0. Orbitrap files were processing using Xcalibur™ Software - Thermo Fisher Scientific, and its chemical molecular generator module was employed to provide elemental formula. Details regarding anisotropic data processing are elaborated below

Detection of meroditerpenes (Compound 1) by LC-FTMS (Fourier transform spectrometer)

LC-HRMS detection of compound 1 was achieved using a LTQ-Orbitrap XL MS coupled to an LC Accela pump from Thermo Scientific, equipped with an electrospray ionization (ESI) source setup operated in positive ionization mode (*full scan*); separated through a column Terra® (3x100 mm, 5 μm) (Waters) with the following conditions: 13 min gradient from 30 to 95% of MeOH in H_2O (1 % TFA) and 7 min at 95% MeOH; flow rate 350 μL min^{-1}. Mass tolerance is reported in terms of the difference between the theoretical and the measure value of the masses (Δ *m/z* ppm).[108]

Sample preparation

Extraction. The sea weed *Sargassum muticum* (SM) was collected in a rocky shore of the southern coast of Galicia, Praia da Mourisca (Alcabre, Spain) during the summer of 2011 and methanol extract was prepared as described in literature.[85]

Fractionation and isolation. The raw methanolic extract (4.9 g) was dissolved in methanol/water (1:10) and subsequently partitioning with: *n*-hexane (FH), dichloromethane (FD), *n*-butanol (WB) and water (WW). Fractions were concentrated under reduced pressure (temp: 32 °C) yielded FH 0.2 g, FD 0.2 g, WB 0.3 g and WW 2.1 g. The FH (1.1 g) was subjected to NMR-guided fractioning through flash silica gel column chromatography (25 x 2 cm; 80 mL/min) using a stepwise gradient of H/Et$_2$O and Et$_2$O/AcOEt to produce 30 fractions, which were grouped by TLC. Fractions 19 (Fr. 19) shown doublet (d) belonging to two *meta*-coupled aromatic protons (protons 3' and 5') in an aromatic ring part of the bicycling system (6.412 – 6.5327 ppm; J = 2.7 Hz) characteristic of the meroditerpens (Figure 57, **a**). Fr. 19 was afterward purified by RP-HPLC to yield a pure compound **1.**
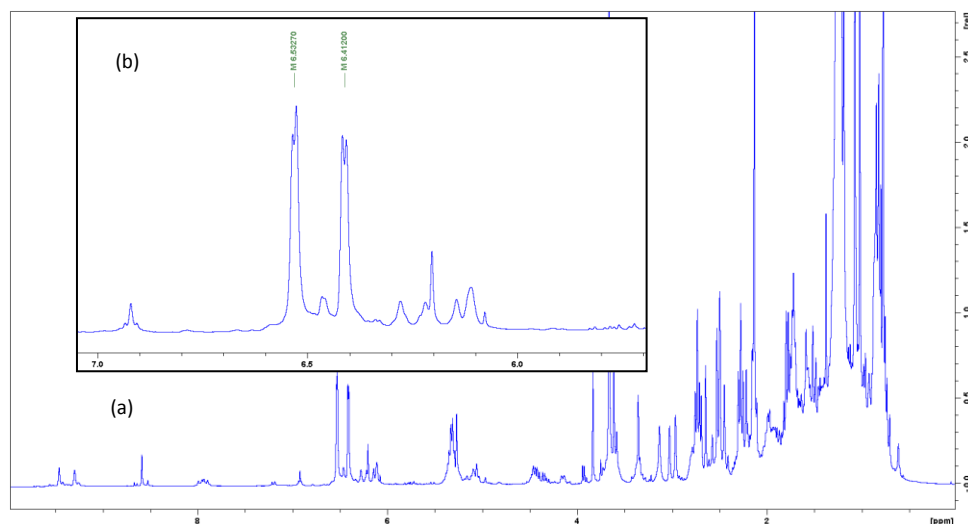
Figure 57. ^{1}H Spectrum (300 MHz, CD$_2$Cl$_2$) of fraction 19 from flash chromatography column (a), characteristic doublet (d) belonging to two meta-coupled aromatic protons from the meroditerpene skeleton (b)

Purification of F.19 (80.3 mg) was further purified by semipreparative HPLC (Atlantis RP-C$_{18}$ column 10 x 100 mm; 4.6 mL/min) equipped with a Wavelength Detector (VWD) at 320 nm, an Agilent pump supplying the following solvent profile: 2.2 min isocratic step (80 v/v ACN/H$_2$O) and 12.3 min gradient step (from 80 to 100 v/v ACN/H$_2$O) to afford compound 1 (27.4 mg; R$_{time}$ = 5.17 min) (Figure 58)
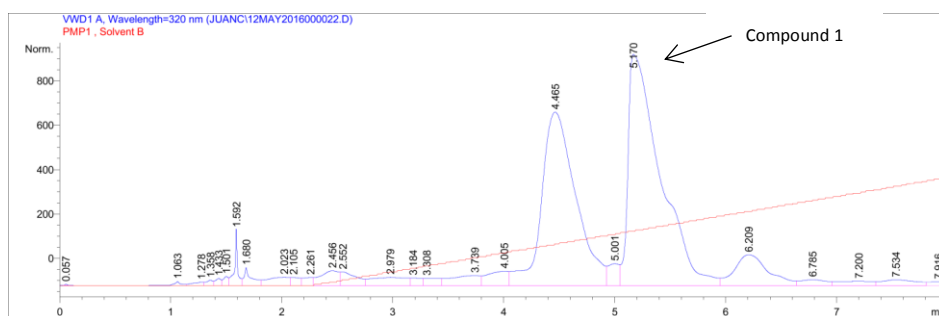
Figure 58. Isolation by HPLC of compound 1 (5.17 min) from Fr. 19. Red line indicated the solvent gradient

Measurements of anisotropic parameters.

Molecular geometries were optimized at the SOGGA11X/DEF2TZVP[92,93] level using the IEFPCM[109] solvent model with CH_2Cl_2 parameters. On these geometries, chemical shielding tensor (CSTs) were calculated usign GIAOs[80] at the MPW1PW91/6-311+g(2g,p)[110] *in vacuo*. The Gaussian UltraFine integration grid was used for all geomtry optimizations, and non imaginary frequency were found. Single Value Decomposition[3] (SVD) fitting of the experimental data was performed on the DFT geometry optimized structures and to the previously calculated CSTs.

To measure RDCs and RCSAs, the compund was disolved in CD_2Cl_2 (sample A 1.6 mg) and (sample B 230 μg) prepared as described for α-santonine in our SMCD prototype (3 mm I.D). (Page 45)

RCSA data were adquiered in fully relaxed PMMA-d_8 (70/0.25) gel, under maximun compression (around 22 % of its length) by usign 1D ^{13}C-NMR (*Zgdc30*) and 1D Pure shift Psyche[25,111] experiments for ^{13}C RCSAS and ^{1}H RCSA respectively. $^1J_{CH}$ were measured in solution (Isotropic conditions) meandwhile $^1T_{CH}$ were measured under the same condition before described by using F2 coupled CLIP/CLAP HSQC[112].

RCSA's analysis was done using the method described by Nath *Et al*.[22] Anisotropic values are expressed in Hz in order to have a significant weight. Gel isotropic shift contribution was automatic compensated[10] and SVD population fitting of the experimental data to the structures and to the calculated chemical shift tensors was performed in MSspin.[9]

Meroditerpene **1** was described by a rather restricted ensemble (*vide supra*), the NMR data was fitted using a single tensor[12] and population fitted using a combined Levenberg–Marquardt algorithm[83]. RDCs were optined from the total splitting ($^1T_{CH}$) observed in the anisotropic spectra and from the $^1J_{CH}$ observed in isotropic solution also using the CLIP/CLAP HSQC experiment experiments using non-uniform sampling (TD2: 1.6K; TD1: 1K; FnTYPE: NUS 26.6%; 136; 24 transients; 2 s recycle delay).[21]

The relation $^1T_{CH} = {}^1J_{CH} + {}^1D_{CH}$ was employed to obtain $^1D_{CH}$. RDCs and RCSAs experimental errors were calculated by Kontaxis *et al.*[94] Error was study by using Monte Carlo's Bootstrapping[113] module in MSpin software, and RCSAs standard deviation error was calculated over experimental values and used during the error analysis.[95] $^1D_{CH}$ RDC's for methyl groups were averaged as described by Sanchez-Pedregal et al.,[114] and methylene group are individually reported. ^{1}H RCSA's of methyl groups and enantiotopic methylene protons were averaged as

described by Nath *et al*. [18] Conformers were oriented to the Eckart frame.[115] Quality of the fits was scored in terms of the Cornilescu quality factor (Q)[84] and Chemical Shift Anisotropic quality factor Q(QCSA) [22]

PMMA-d8 compression compatible (70/0.25) gel

Gel was prepared as decribed by Nath Et al.[22] Nevertheless monomer was sutituided by Methyl methacrylate-*d*8 (70 % v/v) and cross-link density ajusted to 0.25 molar %, in order to make the gel compatible with the 3 mm compression device. The compound thus prepared is named PMMA-*d*8 70/0.25

1.3.4 Structure elucidation of a new natural products with conformational flexibility. Using ^{1}H, ^{13}C RCSA's and RDC along with pure shift HSQC experiments with NUS methodology to find out the relative stereochemistry of tricloromanmindes A and B

1.3.4.1   Introduction

Structural elucidation is an important task for natural product chemists and small molecules researchers involved in the fields of new drug discovery or medicine development. Therefore, the precise assessment of the stereochemical features is critical because all chemical or biological properties are entirely dependent on the chirality of the substance. This difficult task becomes a challenge, and sometimes this is the bottleneck in the full characterization, when a compound contains flexible moieties, such as poly substituted open chains. In this regard the use of anisotropic parameters (RCSA and RDC) provide three dimensional arrangements of relative stereochemistries between different diasteroisomers, that clearly diminishes undesired incorrect structure assignments.

Tricholoma equestre has been identified to be related with numerous cases of severe rhabdomyolysis, a serious syndrome due to a direct or indirect muscle injury that results from the death of muscle fibers and release of their contents into the bloodstream, [116] occurred in France, Lithuania after meals that included the edible wild mushroom. .[117,118] The diagnosis was preceded by typical symptoms fatigue, nausea without vomiting and muscle pain, profuse sweating without fever, and respiratory insufficiency occurred. Most recently, has been found that effects of prolonged consumption in mice causes myo-, cardio- and hepatotoxic effects. [119]

In this section of this thesis dissertation, we will present the structure elucidation of two new compounds, tricholomaminde A and B, associated with the toxicity of T. equestre which were isolated by Professor Liu´s Research Group at Kunming Institute of Botany, Chinese Academy of Sciences (KIB/CAS). Their absolute configurations at stereogenic centers, a toxic and flexible natural products, were elucidated as 2S6S2´S and 2S4R6S2´S, respectively by the combination of *J*-based configuration analysis (JBCA), advanced Marfey's method, density-functional theory calculations (DFT) and electronic circular dichroism (ECD). Moreover, relative configuration of tricholomaminde A and B was confirmed by residual dipolar coupling (RDC) and residual chemical shift anisotropy (^{13}C RCSA and ^{1}H RCSA) respectively; anisotropic measurements were done in our recently introduced universal 3 mm compression device.

1.3.4.2 Isolation and structure elucidation of tricholomaminde A and B

1.3.4.2.1 Isolation of tricholomaminde A and B

The isolation of tricholomaminde A and B, along with the absolute configuration of C-2′ were carry on by Professor Liu´s Research Group at School of Pharmaceutical Sciences, South-Central University for Nationalities, Wuhan, 430074, Hubei, PR China.

Tricholoma equestre (Figure 59), were collected from Arcachon in southwestern France in December 2012 and identified by Prof. Zhu-Liang Yang of Kunming Institute of Botany, Chinese Academy of Sciences. A specimen (No. KIB20121205.11) was deposited at the Kunming Institute of Botany, Chinese Academy of Sciences.

Figure 59. Specimen of *Tricholoma equestre*. Cap of this species measures between 6 to 8 cm, and the stem is round 7 to 10 cm long and its diameter 1.5 cm. Figure taken from Bedry *et al.*[117]

The air-dried fruiting bodies of *T. equestre* (1.5 kg) were extracted three times using 70% MeOH, in a 24 h period each extraction. After filtration and concentration under vacuum, the extract was partitioned in EtOAc and water. The water layer was subjected to a cation exchange resin column chromatography. After washed with deionized water, the total amino acid extract (ACE, 7.4 g) was obtained by eluting with 10–20% ammonia solution. The ACE was separated by using Sephadex LH-20 ® column (eluted with 60% MeOH) to give five fractions. Fraction B (800 mg) was purified by HPLC equipped with a PC-HILIC column, which was eluted with MeCN/H_2O from 85% to 65% in 30 min to afford tricholomamides A (**1**) and B (**2**) (Figure 60).
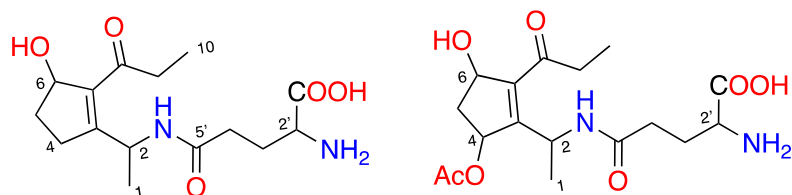
Figure 60. Chemical structures of **tricholomaminde A** (right) and **B** (left) isolated from the wild mushrooms *Tricholoma equestre.*

1.3.4.2.2 Structural elucidation of the stereochemistry at carbon 2' B

The configuration at C-2' in the glutamic acid of tricholomaminde A was determined as *S* by an advanced Marfey's method. [120,121] Tricholomaminde A (0.5 mg) was dissolved in 1 mL HCl (6 N) and heated at 120°C/20 h. Afterwards, the hydrolysate was concentrated to dryness under a stream of N_2 and 50 µL of a 1% solution of 1-fluoro-2-4-dinitrophenyl-5-L-alanine amide (L-FDAA) in acetone and 10 µL of NaHCO$_3$ (1 mol/L) were added, and the mixture was heated at 40 °C for 45 min. The standard amino acid L-Val and D-/L-Leu were treated the same way, and all the reactions were stopped by addition of HCl (5 µL, 2 mol/L). When all these solvents were evaporated, The N[(dinitrophenyl)-5-L-alanine amide] derivatives were redissolved in MeCN/H$_2$O (1:1) followed by HPLC analysis with an Agilent 1100 liquid chromatography system equipped with a Zorbax SB-C18 column (4.6 mm × 150 mm). Solvents: (A) water + 0.05% TFA, (B) MeCN; linear gradient: 0 min 10%, 40min 50%, 1 mL/min). HPLC analysis tricholomaminde A ´s hydrolysate showed the presence of L-glutamic acid. Same method was employed for determine the absolute configuration at C-2´ of tricholomaminde B; which was also established as *S.*

1.3.4.2.3 Absolute Configuration of tricholomaminde A by standard NMR approximation

Workflow used for the determination of absolute configuration of tricholomaminde A and B is described in Figure 61 ECD calculations were carried out by using the protocol established by Pescitelli *et al.*[88]
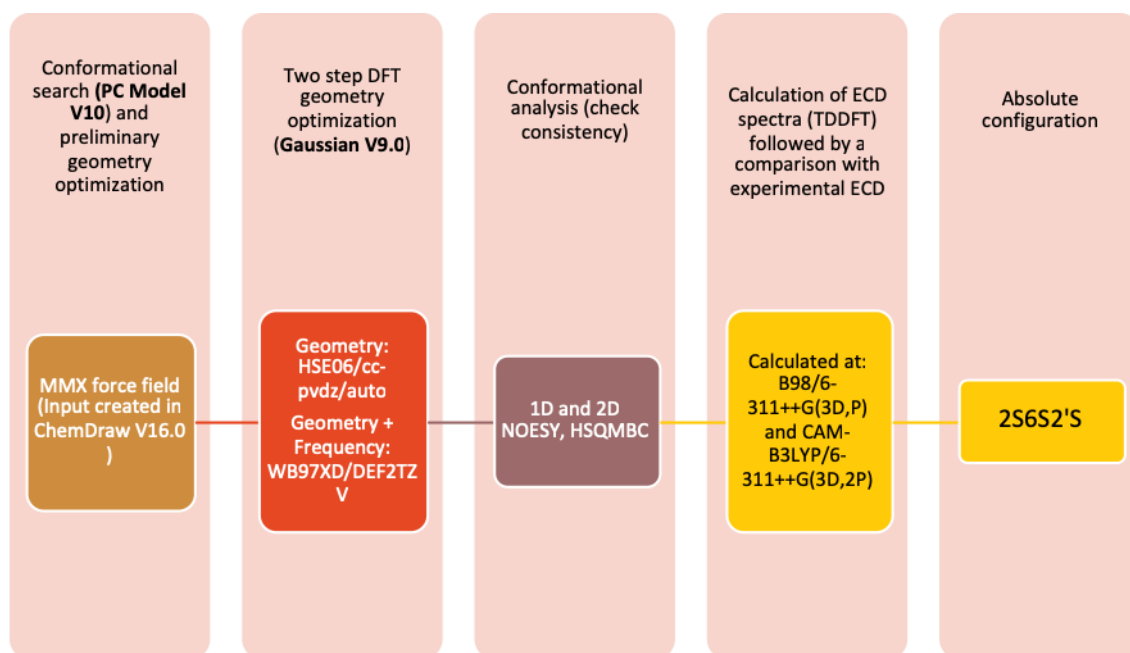
Figure 61. Following the workflow to assign the absolute configuration on flexible molecules by NMR and electronic circular dichroism calculations. Case: tricholomaminde A and B

Carbon and proton chemical shift in CD_3OD of tricholomaminde A are shown in Table 12. As it has been noticed on section 1.3.4.2.2, the absolute configuration of the C2' chiral center was previously assigned as 2'S based on the application of the advanced Marfey's method that was performed by Professor Liu´s Research Group at School of Pharmaceutical Sciences, South-Central University for Nationalities, PR China.

Thus, out of the possible eight theoretically stereoisomers of tricholomaminde A (3 chiral centers), 4 diastereoisomers with R configuration at C2' were excluded from the analysis (see Table 11). The characteristic NOE cross peaks (Figure 67) between H6/H_{pro-S}4 and CH_3-1/H_{pro-R}4 suggested that the relative configuration at C2 and C6 should be either 2S6S or 2R6R. The observed NOE correlations between H2/H9a, H2/H9b, and H2/CH_3-10 indicate that H2 proton is lying in the plane of the olefinic double bond of the cyclopentene ring. The strong NOE between H6/H9a and H6/H9b indicate the close proximity of these protons. Based on these observations, the relative configuration of tricholomaminde A is either 2S6S2'S or 2R6R2'S.
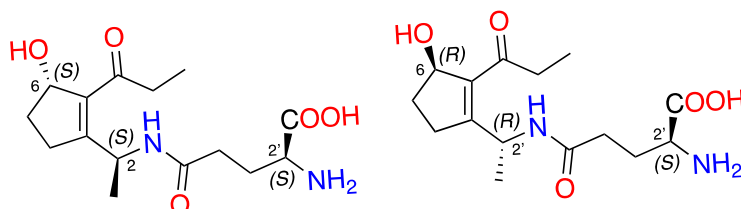
In order to map the entire potential energy surface (PES), 2S6S2'S and 2R6R2'S configurations of tricholomaminde A were subjected to an extensive conformational search using PC Model

version 10.0 from Serena software.[63] As a result 30,000 conformers in a 3.5 kcal/mol window were generated, minimized using MMX force field and further subjected to DFT calculations. The intrinsic flexibility of tricholomaminde A makes it necessary to undertake special considerations during the DFT calculations. A two-step DFT optimization was carried out using the reliable and robust Heyd-Scuseria-Ernzerhof functional (HSE06)[122] and the latest functional from Head-Gordon and coworkers[123] and Ahlrichs'[93] basis sets, respectively.[89] The first and second DFT optimizations were done with the combinations HSE06/CC-PVDZ and WB97XD/DEF2TZV level of theory, respectively. Vibrational frequencies calculated with Gaussian09 showed no imaginary frequencies after the second DFT optimization step for the conformers, suggesting that they are true minima on the PES space.

The DFT optimized conformers of tricholomaminde A that were consistent with the experimental NMR (NOESY/*J*-couplings) data were used for the simulation of ECD spectrum by using Time-Dependent Density Functional Theory (TDDFT).[124] The ECD of the conformers of tricholomaminde A with 2S,6S,2'S and 2R,6R,2'S relative configurations was evaluated with two families of functionals, namely B98 [125] (hybrid functional) and CAM-B3LYP [126] (range-separated hybrid functional, it combines the hybrid qualities of B3LYP and long-range correction) with 6-311++G(3d,p) and 6-311++G(3d,2p) basis sets,[127] respectively.

TDDFT calculated ECD files were processed with SpecDis V. 1.70.1.[107] The conductor-like polarizable continuum model (CPCM) [128] with methanol as solvent was employed for the ECD calculations. Figure 72 b showed a good agreement between the experimental and the TD-DFT calculated (Boltzmann-weighted) ECD of tricholomaminde A. This results strongly supports that the absolute configuration of tricholomaminde A must be 2S,6S,2'S. Furthermore, the ECD of all the individual conformers with 2S,6S,2'S configuration are in good agreement with the experimental ECD of tricholomaminde A. However, the TD-DFT calculated (individual as well as Boltzmann-weighted) ECD of tricholomaminde A with 2R,6R,2'S relative configuration (Figure 73 b) resulted in an enantiomeric ECD compared to the experimental ECD of tricholomaminde A in methanol.

In summary, based on the NMR (NOESY/*J*-couplings) and ECD analysis, the absolute configuration of tricholomaminde A is determined as 2S,6S,2'S.
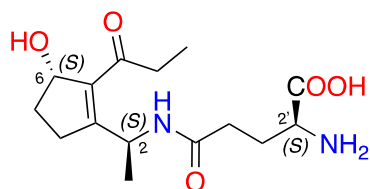
Table 11. Possible relative configurations of tricholomaminde A.

C-2	C-6	C-2'	Remarks
S	S	S	**Absolute configuration:** in excellent agreement with the NOESY/*J*-couplings and ECD
R	R	S	**Excluded,** inconsistent with ECD
R	S	S	**Excluded,** inconsistent with NOESY
S	R	S	**Excluded,** inconsistent with NOESY
R	R	R	**Excluded,** Marfey's method analysis
R	S	R	**Excluded,** Marfey's method analysis
S	R	R	**Excluded,** Marfey's method analysis
S	S	R	**Excluded,** Marfey's method analysis

NOESY: Nuclear Overhauser Effect Spectroscopy, ECD: Electronic Circular Dichroism
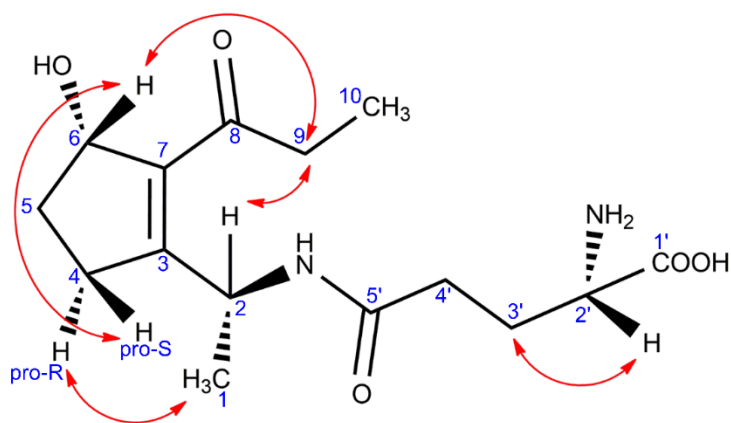
Figure 62. Chemical structure and observed NOE correlations (red arrows) of tricholomaminde A.

Table 12. NMR data of tricholomaminde A in CD$_3$OD (298 K, 700 MHz for ^{1}H and 175 MHz for ^{13}C)

Position	δ$_C$ (ppm)	δ$_H$ (ppm)	J$_{HH}$ (Hz)	J$_{CH}$ (Hz)
NH	-	8.30, d, 1H	NH/2 = 7.0	-
6	79.0	5.17, m, 1H	-	-
2	46.8	5.11, m, 1H	-	C3/H2 = 4.4, C1/H2 = 5.0, C7/H2 = 2.4, C5'/H2 = 2.7
2'	56.2	3.56, t, 1H	2'/3' = 5.8, 5.8	C1'/H2' = 5.4, C3'/H2' = 4.1, C4'/H2' = 5.6
9b	35.9	2.80, dq, 1H	9b/9a = 18.0 9b/10 = 7.2, 7.2, 7.2	C8/H9a = 5.9, C10/H9a = 4.2
9a	35.9	2.66, dq, 1H	9a/9b = 18.0 9a/10 = 7.2, 7.2, 7.2	C8/H9a = 5.3, C10/H9a = 4.2
4pro-R	31.5	2.64, m, 1H	-	-
4'	33.2	2.40, m, 2H	-	-
4pro-S	31.5	2.31, m, 1H	-	-
5a	33.8	2.29, m, 1H	-	-
3'	28.4	2.05, td, 2H	3'/4' = 7.2, 7.2 3'/2' = 5.8	-
5b	33.8	1.66, m, 1H	-	-
1	19.4	1.32, d, 3H	1/2 = 7.2	-
10	8.3	1.07, t, 3H	10/9 = 7.2, 7.2	-
7	140.1	-	-	-
3	161.8	-	-	-
1'	174.3	-	-	-
5'	174.9	-	-	-
8	204.1	-	-	-

Table 13. Boltzmann-weighted populations in both the possible conformations of tricholomaminde A (298.15 K)

	(2R,6R,2'S)-tricholomaminde A		
Conformer	Boltzmann population (%)*	Boltzmann population CPCM (%)**	Boltzmann population IEFPCM (%)**
Conf. 1	12.1	2.9	3.2
Conf. 2	0.0	1.0	1.0
Conf. 3	1.2	24.0	25.5
Conf. 4	1.8	4.0	4.4
Conf. 5	84.8	68.1	65.9
	(2S,6S,2'S)-tricholomaminde A		
Conf. 1	98.6	76.3	78.0
Conf. 2	0.4	6.3	6.1
Conf. 3	0.1	9.0	8.3
Conf. 4	0.0	0.5	0.5
Conf. 5	0.3	1.4	1.4
Conf. 6	0.6	6.5	5.7

*Calculated from Gibbs free energy **Methanol as solvent
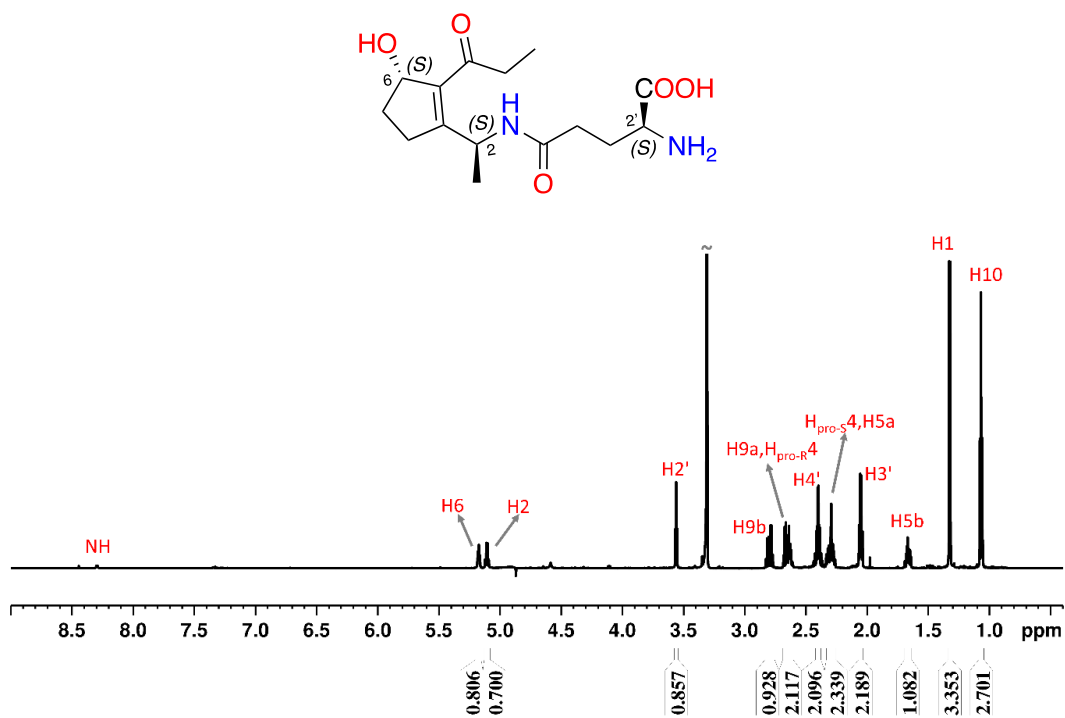
Figure 63. ^{1}H NMR spectrum of tricholomaminde A in CD$_3$OD (298 K, 700 MHz).
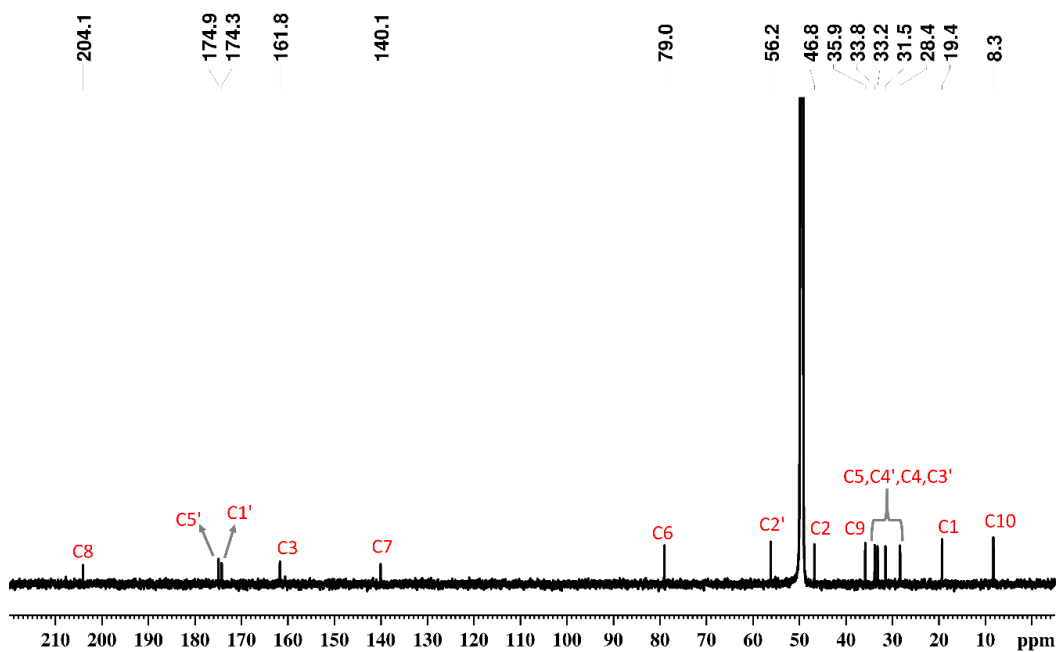
Figure 64. ^{13}C NMR spectrum of tricholomaminde A in CD$_3$OD (298 K, 175 MHz).
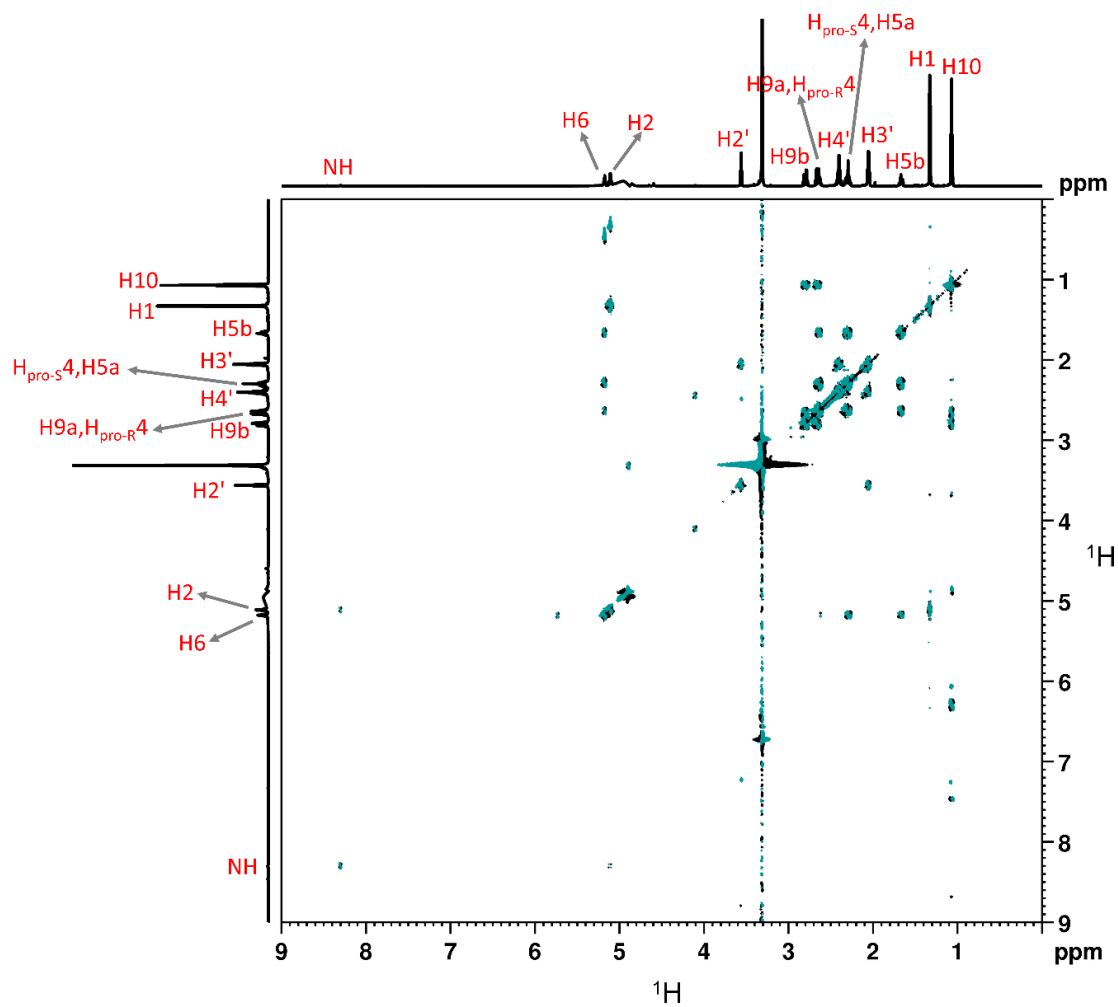
Figure 65. 2D-DQFCOSY (Double-quantum Filtered Correlation Spectroscopy) spectrum of tricholomaminde A in CD₃OD (298 K, 700 MHz). Experimental parameters: TD (F2) = 2048, TD (F1) = 512, NS = 32, DS = 16, D1 = 2.
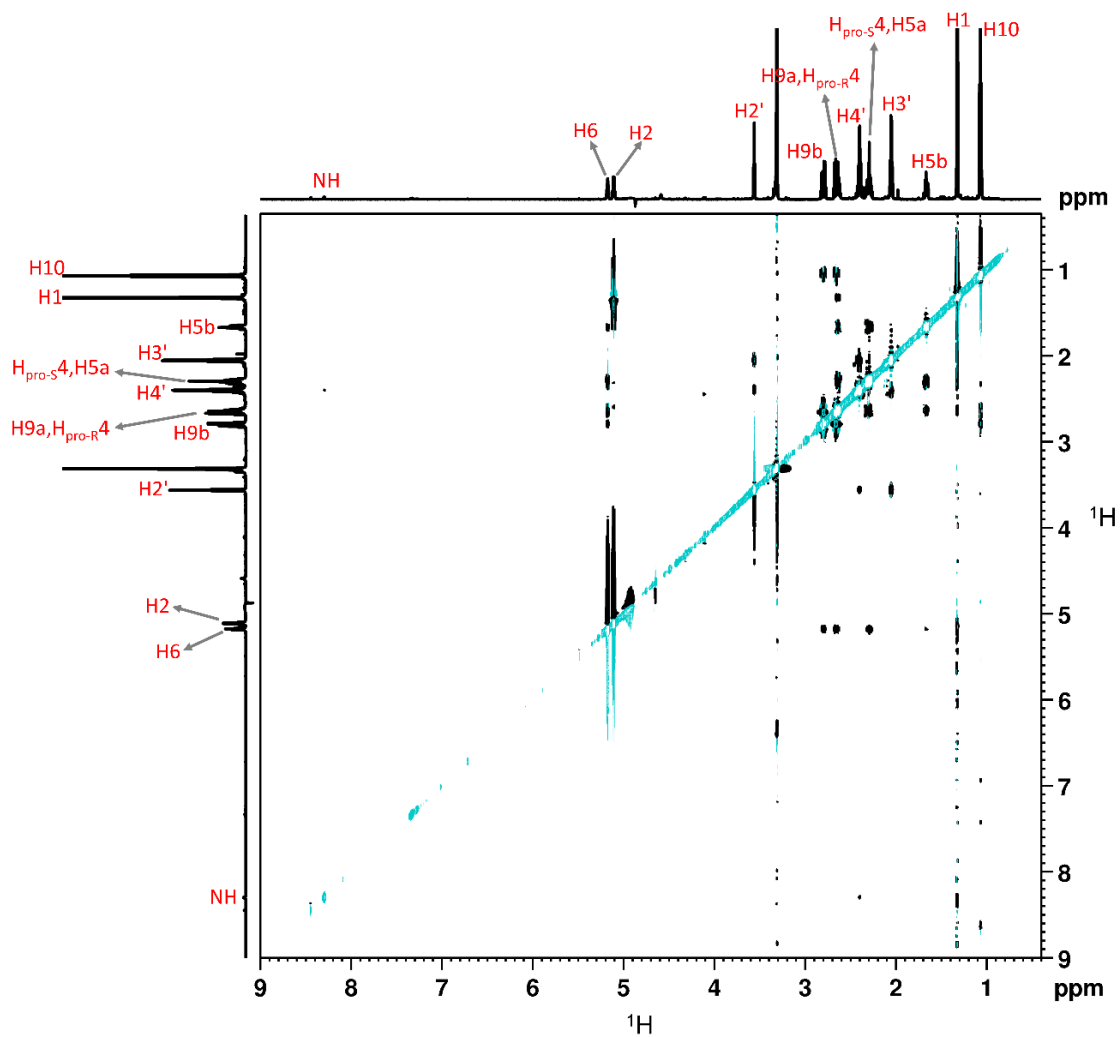
Figure 66. 2D-NOESY (Nuclear Overhauser Effect Spectroscopy) spectrum of tricholomaminde A in CD$_3$OD (298 K, 700 MHz). Experimental parameters: TD (F2) = 8192, TD (F1) = 512, NS = 32, DS = 32, D1 = 2, mixing time (D8) = 500 ms.
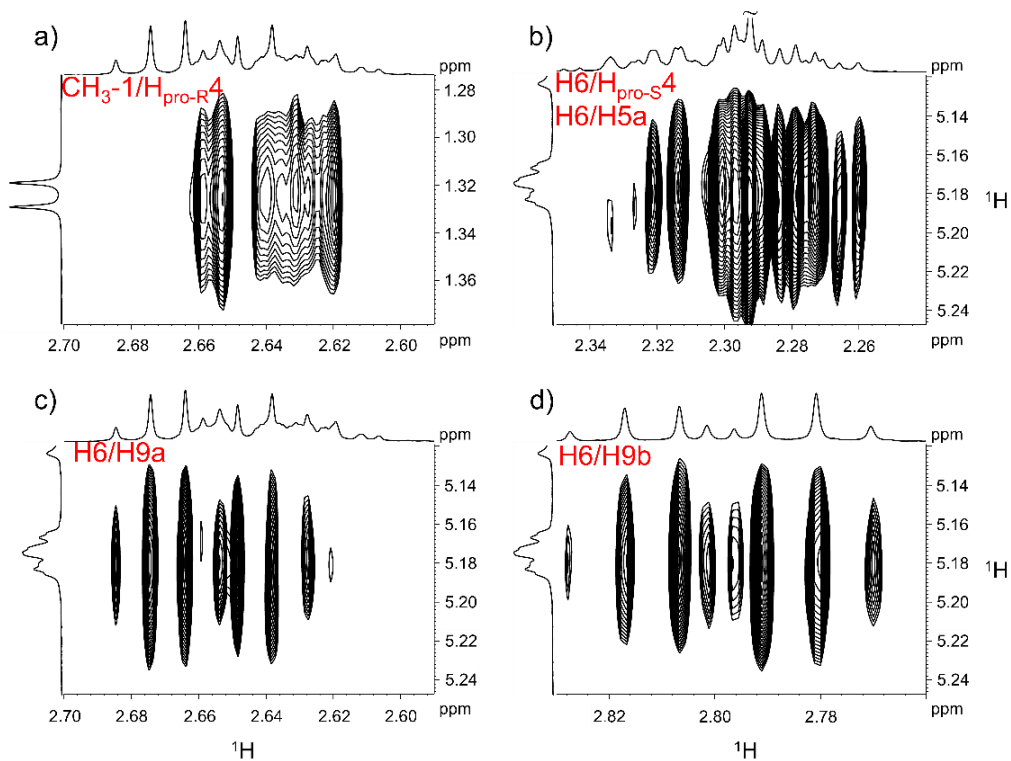
Figure 67. Expanded regions of 2D-NOESY spectrum of tricholomaminde A: the observed characteristic NOE cross peaks between CH_3-1/H_{pro-R}4 (a), H6/H_{pro-S}4 and H6/H5a (b), H6/H9a (c), and H6/H9b (d) protons.
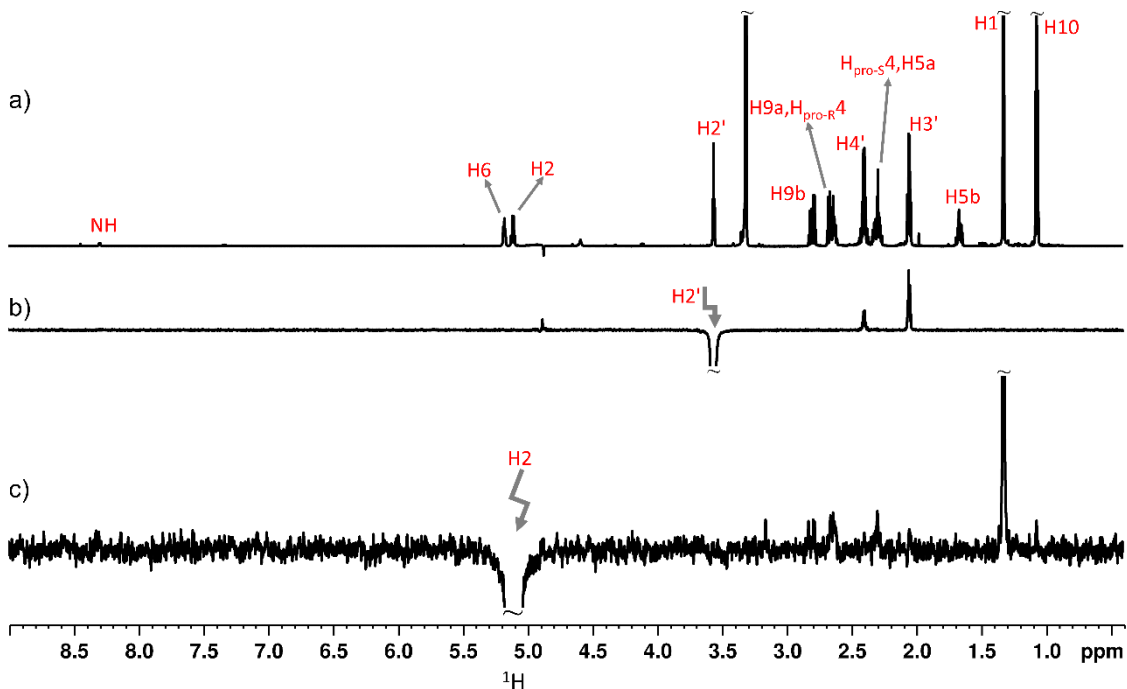
Figure 68. a) ^1H NMR spectrum of tricholomaminde A (CD_3OD, 298 K). b), and c) are selective 1D-NOESY at 3.56 ppm, and 5.11 ppm, respectively. (1D NOESY parameters, acquisition time = 1 sec, mixing time = 500 ms, NS = 1024, DS = 32, D1 = 2).
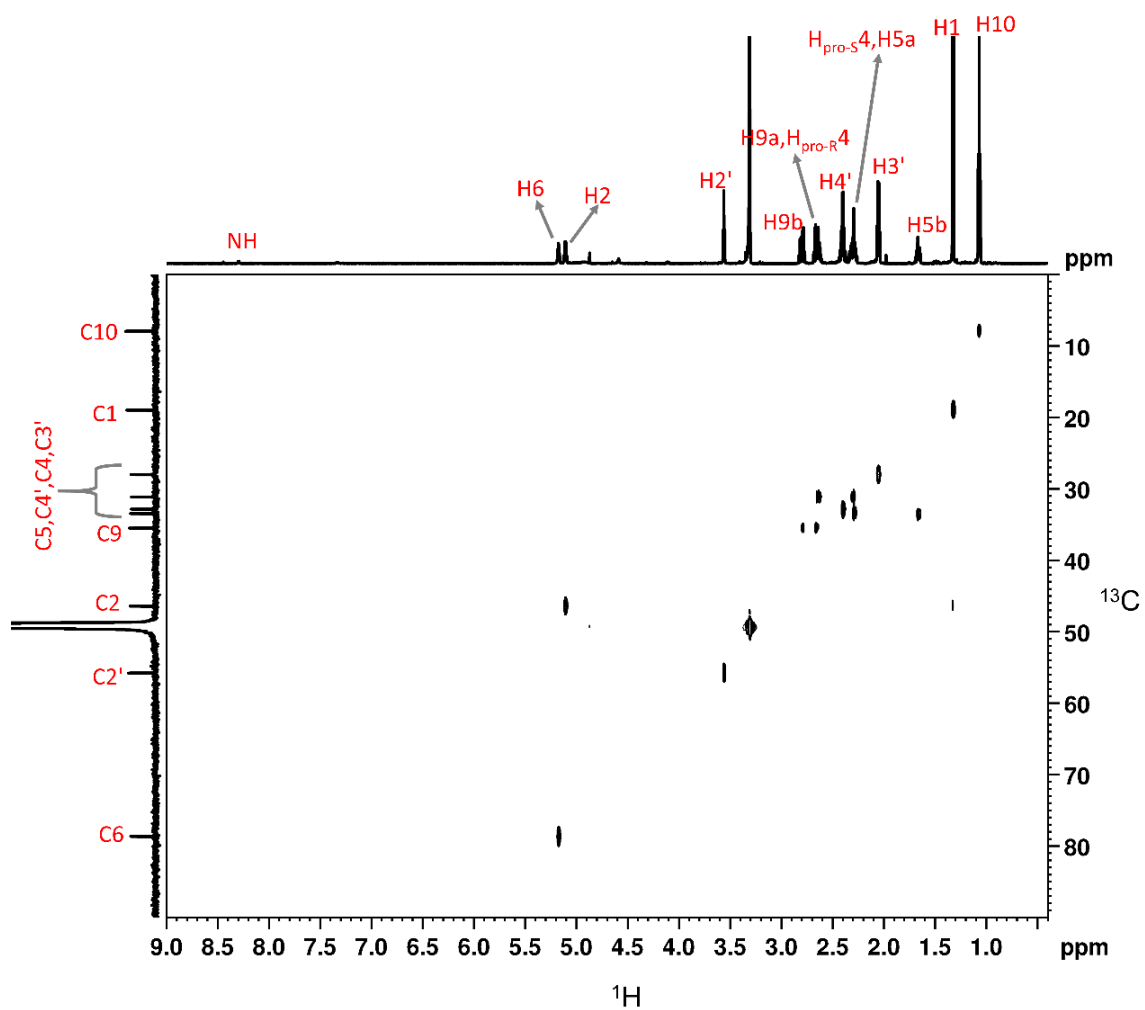
Figure 69. 2D-HSQC (Heteronuclear Single Quantum Correlation) spectrum of tricholomaminde A in CD$_3$OD (298 K, 700 MHz for ^{1}H and 175 MHz for ^{13}C). Experimental parameters: TD (F2) = 2048, TD (F1) = 256, NS = 4, DS = 64, D1 = 2.
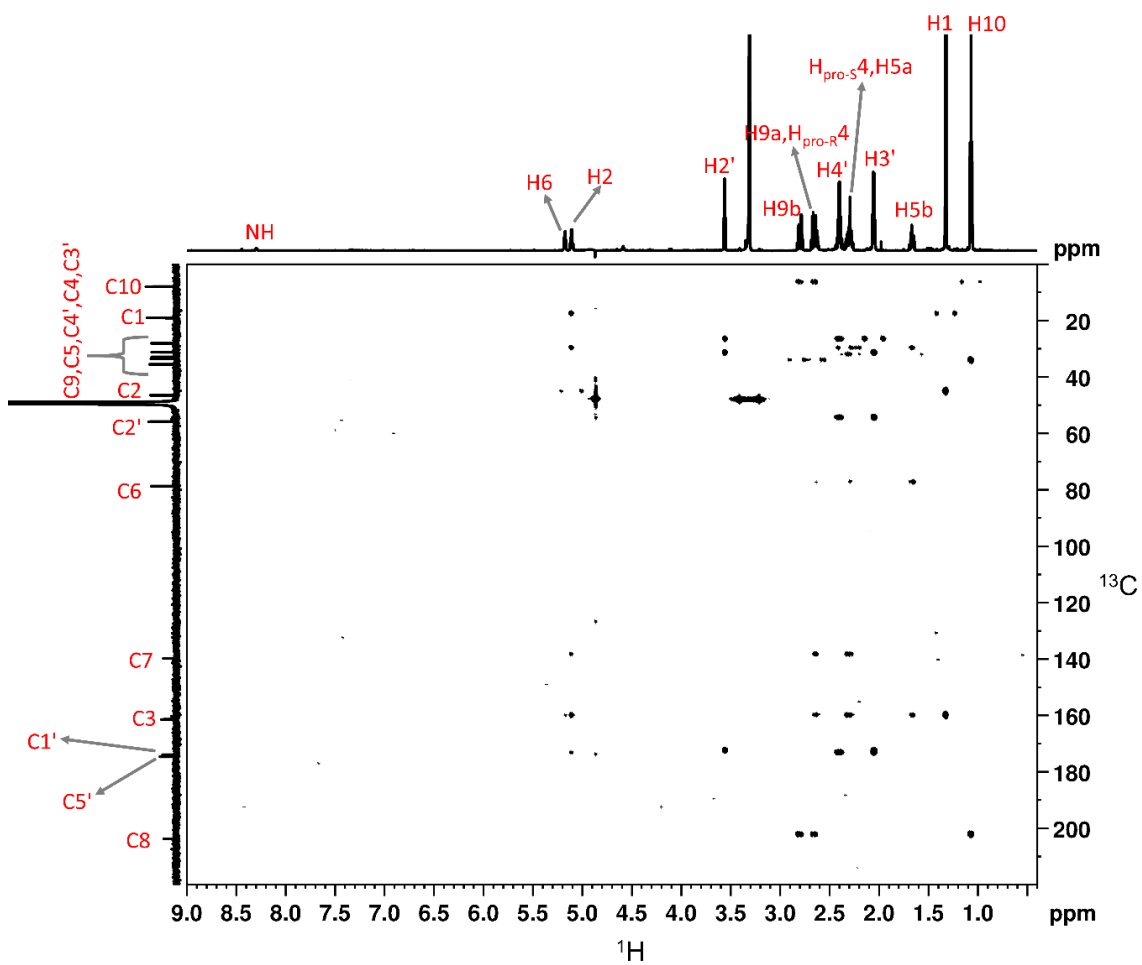
Figure 70. 2D-HMBC (Heteronuclear Multiple Bond Correlation) spectrum of tricholomaminde A in CD₃OD (298 K, 700 MHz for ^{1}H and 175 MHz for ^{13}C). Experimental parameters: TD (F2) = 8192, TD (F1) = 512, NS = 16, DS = 16, D1 = 2, SW (F2) = 9 ppm, SW (F1) = 240 ppm, J$_{CH}$-long range = 8 Hz.
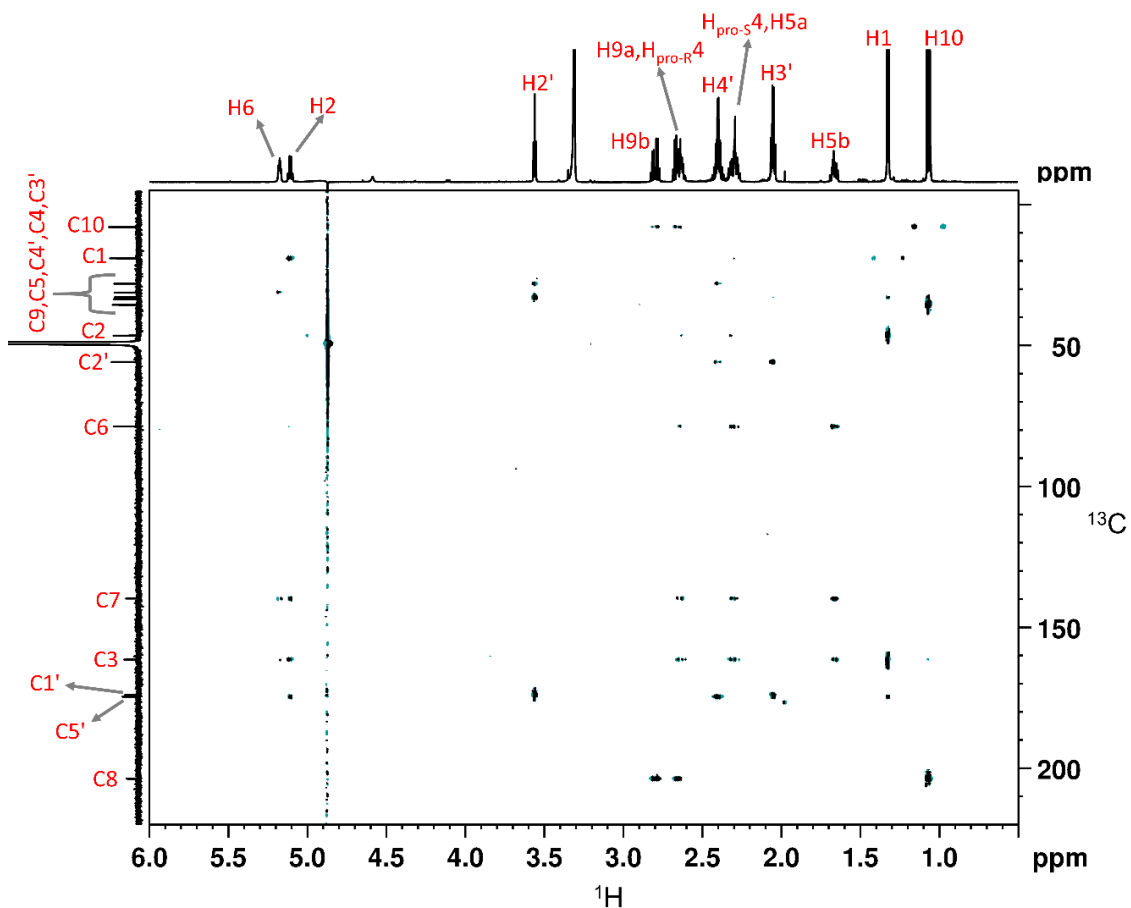
Figure 71. 2D-HSQMBC (Heteronuclear Single Quantum Multiple Bond Correlation) spectrum of tricholomaminde A in CD$_3$OD (298 K, 700 MHz for ^{1}H and 175 MHz for ^{13}C). Experimental parameters: TD (F2) = 6144, TD (F1) = 512, NS = 64, DS = 128, D1 = 2, SW (F2) = 7 ppm, SW (F1) = 258 ppm, J$_{CH}$ = 145 Hz, J$_{CH}$-long range = 2 Hz, 180° shaped pulse length for inversion = 500 μs, 180° shaped pulse length for refocusing = 2000 μs.

Table 14. Comparison between experimental and TD-SCF DFT calculated ECD at CAM-B3LYP/6-311++G(3d,2p) level of theory for individual conformers of (2S,6S,2'S)-tricholomaminde A.
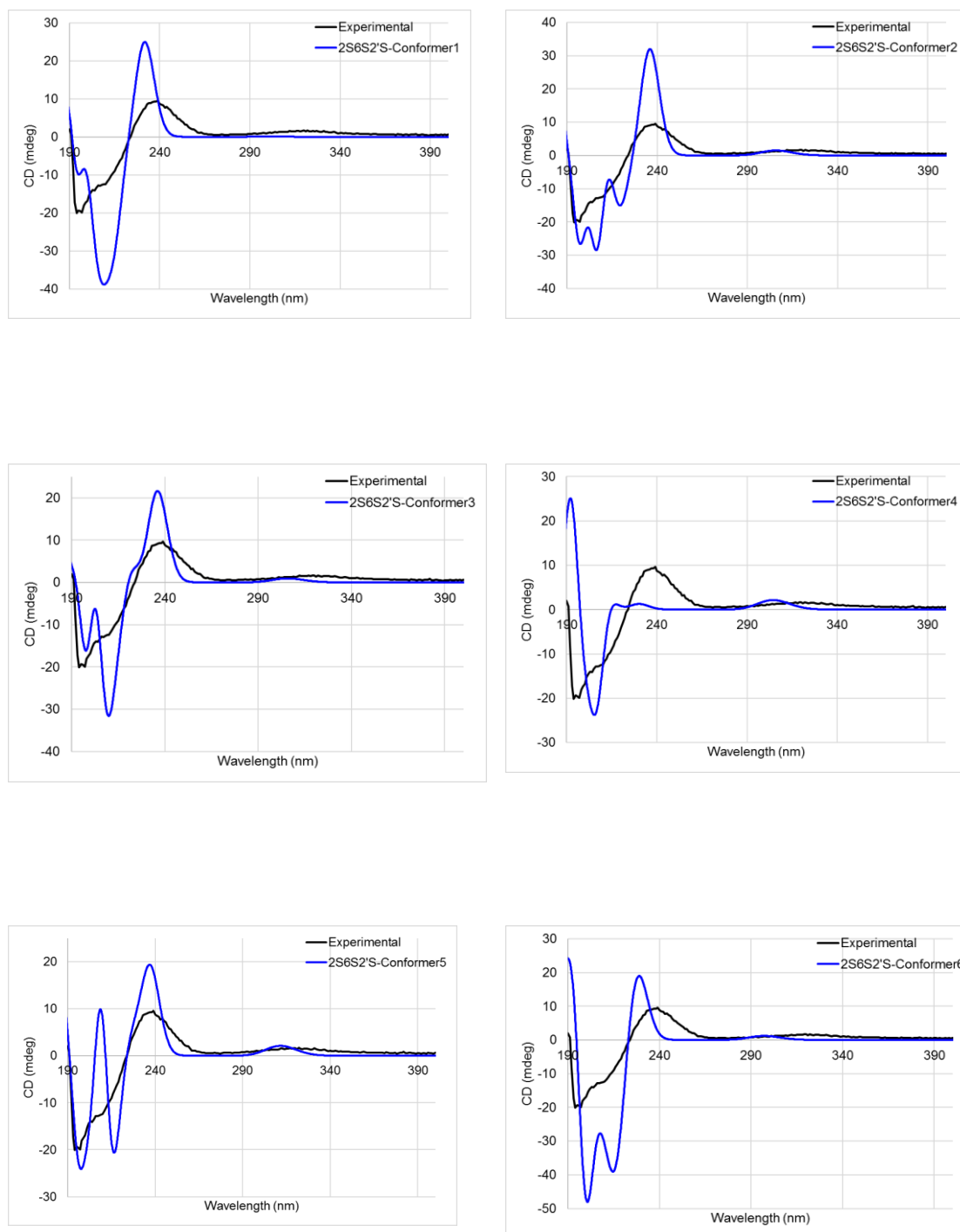
Table 15. Comparison between experimental and TD-SCF DFT calculated ECD at CAM-B3LYP/6-311++G(3d,2p) level of theory for individual conformers of (2R,6R,2'S)-tricholomaminde A.
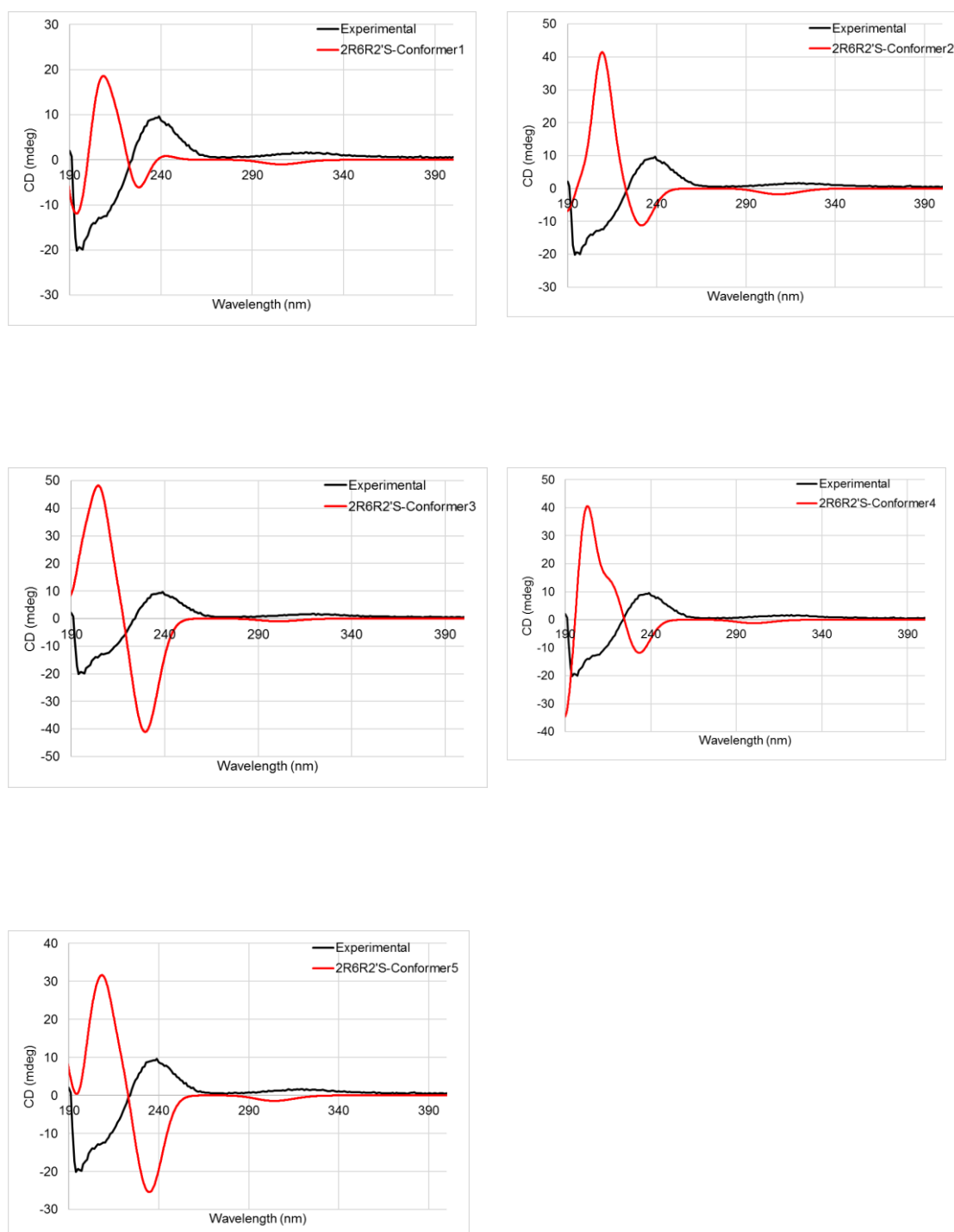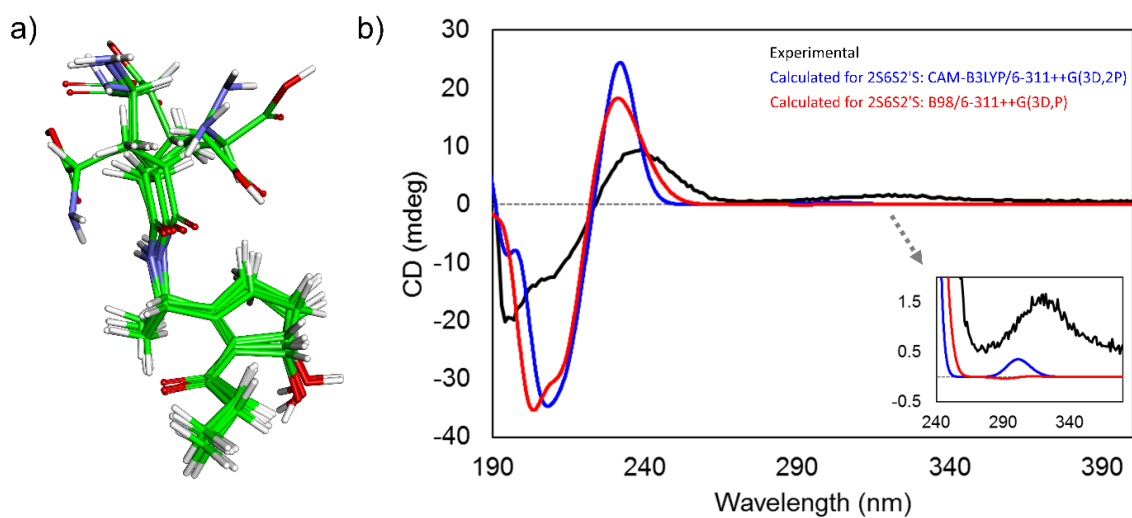
Figure 72. Superimposition of 6 minimum energy conformers of (2S,6S,2'S)-tricholomaminde A that are consistent with the experimental NMR data. b) Comparison between experimental (black solid line) and TD-SCF DFT calculated (Boltzmann-weighted) ECD of tricholomaminde A. Blue and red solid lines are the calculated ECD of tricholomaminde A at CAM-B3LYP/6-311++G(3d,2p) and B98/6-311++G(3d,p) level of theory, respectively. Inset shows good agreement between the calculated and experimental ECD spectra of tricholomaminde A.
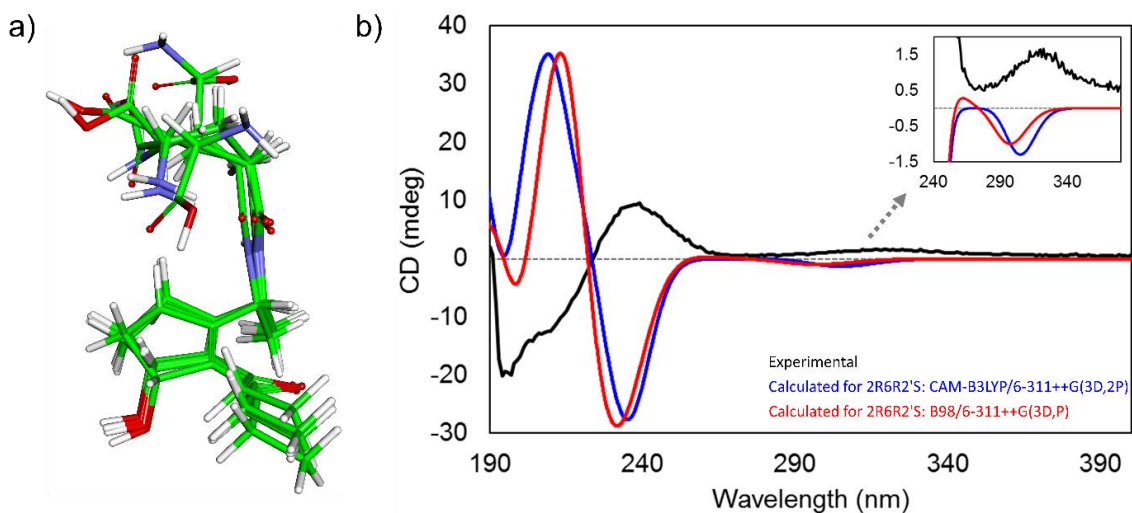
Figure 73. a) Superimposition of 5 minimum energy conformers of (2R,6R,2'S)-tricholomaminde A that are consistent with the experimental NMR data. b) Comparison between experimental (black solid line) and TD-SCF DFT calculated (Boltzmann-weighted) ECD of tricholomaminde A. Blue and red solid lines are the calculated ECD of tricholomaminde A at CAM-B3LYP/6-311++G(3d,2p) and B98/6-311++G(3d,p) level of theory, respectively. Inset shows poor agreement between experimental and calculated ECD of tricholomaminde A.

1.3.4.2.4 Absolute configuration of tricholomaminde B by standard NMR approximation

The structure and relative stereochemistry of tricholomaminde B were assigned by using 1D (^{1}H, ^{13}C, and sel-NOESY) (Table 17) and 2D-(COSY, ROESY, HSQC, HMBC, J-HMBC, and HSQMBC) NMR analysis (see Figure 76 to Figure 84). The absolute configuration of tricholomaminde B was unambiguously determined by using Electronic Circular Dichroism (EDC) analysis. NMR experiments were measured in CD$_3$OD at 298 K. Chemical shifts were referenced to CD$_3$OD (δ_H 3.31 ppm for ^{1}H and δ_C 49.1 ppm for ^{13}C) solvent. A complete set of $^nJ_{CH}$ couplings of tricholomaminde B was extracted by using J-HMBC and HSQMBC experiments. NMR and ECD data were processed using Bruker Topspin V 4.0 and SpecDis Version 1.71,[107] respectively.

With the standard NMR data on hand, we were able to build the planar structure of tricholomaminde B as is depicted in Figure 74. Like its counterpart tricholomaminde A, and based on the chiral HPLC analysis by means of the advanced Marfey's method we obtained the absolute configuration at C2 assigned as S.
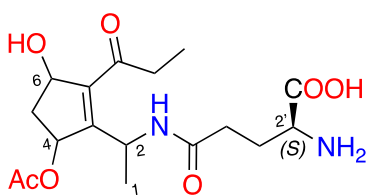
Figure 74 Planar structure of tricholomaminde B

In this second compound, the carbonated skeleton contains 4 chiral centers, indicating 16 theoretically possible stereoisomers of tricholomaminde B, incluing 8 stereoisomers with 2'R configuration, which are removed from the analysis (Table 16). The observed NOE cross peaks between H4/H6, H4/H5β, and H6/H5β suggested that these protons are oriented in the same side of the cyclopentene ring. Hence, the relative configuration at C4 and C6 should be either 4R,6S or 4S,6R. Therefore, 4 out of 8 plausible stereoisomers with either 4R,6R or 4S,6S configurations were removed from the analysis. Besides we observed a characteristic NOE correlation between CH$_3$-1 and CH$_3$-12 protons strongly suggested that the methyl groups are in spatial proximity. Based on these observations, the relative configuration of tricholomaminde B should be either (2S,4R,6S,2'S) or (2R,4S,6R,2'S) (Figure 75).

Figure 75. Two possible chemical structures for (2S*,4R*,6S*,2'S)-tricholomaminde B left and (2R*,4S*,6R*,2'S)-tricholomaminde B (right). Observed characteristic NOE correlations are shown as red arrows

Having deduced the relative configuration of tricholomaminde B, we proceeded with the ECD calculations by using a TD-SCF(DFT) approximation to establish the absolute configuration of the tricholomaminde B.[129] Prior to DFT calculations, two different conformational searches were carried out on (2S,4R,6S,2'S)-tricholomaminde B and (2R,4S,6R,2'S)-tricholomaminde B using MMX force field in the PC Model V10.0.[130] The conformers were fully optimized and vibrational frequencies were calculated at DFT level using the Gaussian09 program, with HSE06/CC-PVDZ/AUTO[79,91] as functional/basis set. The final conformers showing consistency with the experimental NMR data were obtained using NOE derived distances and J-couplings derived dihedrals as post-processing filters (Figure 85).

The ECD (solvent: methanol, model: CPCM)[131,132] spectra of both diasteroisomeric configurations were calculated with the B98 functional and the 6-311++G(3d,p) basis set for energies minimization and the combination CAM-B3LYP/6-311++G(3d,p)[125,126] (number of states 50) for ECD calculations. The theoretical ECD curves showed a λ_{shift} less than ± 30 nm (see Table 18 and Table 19), exhibiting a good agreement between the experimental and the Boltzmann-weighted ECD spectra of (2S,4R,6S,2'S)-tricholomaminde B as is shown in Figure 86. The calculated Boltzmann-weighted ECD spectrum for the diasteroisomeric configuration (2R,4S,6R,2'S)-tricholomaminde B resulted in curve which seemed an enantiomeric ECD spectrum in comparison with the experimental of the natural product (Figure 87).

In summary, we propose the absolute configuration of tricholomaminde B as (2S,4R,6S,2'S), on basis of the NMR (NOESY, J-couplings) and ECD analysis.

Table 16. Discrimination table for the different configuration of tricholomaminde B

S	**R**	**S**	**S**	**Absolute configuration** is in excellent agreement with the NOESY/*J*-couplings and ECD analysis
R	**S**	**R**	**S**	**Excluded,** inconsistent with ECD analysis
R	**R**	**S**	**S**	**Excluded,** inconsistent with NOESY correlations
S	**S**	**R**	**S**	**Excluded,** inconsistent with NOESY correlations
R	**S**	**S**	**S**	**Excluded,** inconsistent with NOESY correlations
S	**S**	**S**	**S**	**Excluded,** inconsistent with NOESY correlations
S	**R**	**R**	**S**	**Excluded,** inconsistent with NOESY correlations
R	**R**	**R**	**S**	**Excluded,** inconsistent with NOESY correlations
R	**R**	**R**	**R**	**Excluded, Marfey's method analysis**
R	**R**	**S**	**R**	**Excluded, Marfey's method analysis**
R	**S**	**R**	**R**	**Excluded, Marfey's method analysis**
S	**R**	**R**	**R**	**Excluded, Marfey's method analysis**
S	**R**	**S**	**R**	**Excluded, Marfey's method analysis**
R	**S**	**S**	**R**	**Excluded, Marfey's method analysis**
S	**S**	**R**	**R**	**Excluded, Marfey's method analysis**
S	**S**	**S**	**R**	**Excluded, Marfey's method analysis**
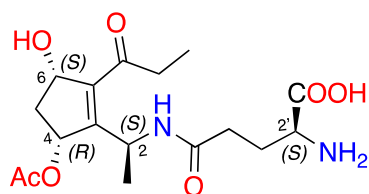
Table 17 NMR spectral data of tricholomaminde B in CD$_3$OD (298 K, 800 MHz for ^{1}H and 200 MHz for ^{13}C)

Position	δ$_C$ (ppm)	δ$_H$ (ppm)	$^3J_{HH}$ (Hz)	$^nJ_{CH}$ (Hz)
NH	-	8.34	-	-
4	76.4	5.47, dd	4/5α = 5.3 4/5β = 7.9	C2/H4 = 1.6, C3/H4 = 5.3, C5/H4 = 1.4, C6/H4 = 1.9, C7/H4 = 4.4, C8/H4 = 1.4, C11/H4 = 3.5
6	73.9	4.99, dd	6/5α = 5.3 6/5β = 7.1	C3/H6 = 6.6, C4/H6 = 7.1, C7/H6 = 4.4
2	46.5	4.80	-	C3/H2 = 3.9, C4/H2 = 7.4, C7/H2 = 2.6, C5'/H2 = 2.5
2'	55.7	3.57, t	2'/3' = 5.8, 5.8	C1'/H2' = 5.5, C3'/H2' = 4.7, C4'/H2' = 5.7
5β	41.2	2.86	-	C3/H5β = 4.5, C4/H5β = 1.2
9a	35.3	2.85, dq	9a/9b = 18.4 9a/10 = 7.2, 7.2, 7.2	C8/H9a = 5.6, C10/H9a = 4.8
9b	35.3	2.69, dq	9b/9a = 18.4 9b/10 = 7.2, 7.2, 7.2	C8/H9b = 6.3, C10/H9b = 4.7
4'a	32.8	2.40	-	-
4'b	32.8	2.36	-	-
12	21.2	2.11	-	C4/H12 = 1.2, C11/H12 = 7.2
3'	27.7	2.05	-	C2'/H3' = 4.7, C4'/H3' = 4.7
5α	41.2	1.50, dt	5α/5β = 13.9 5α/4 = 5.3 5α/6 = 5.3	C3/H5α = 1.2, C4/H5α = 8.1, C6/H5α = 7.4, C7/H5α = 1.2
1	20.4	1.45, d	1/2 = 7.2	C2/H1 = 4.6, C3/H1 = 4.5, C5'/H1 = 1.1
10	7.6	1.08, t	10/9 = 7.2, 7.2	C8/H10 = 5.3, C9/H10 = 4.9
7	143.2	-	-	
3	154.6	-	-	
11	172.3	-	-	
1'	173.8	-	-	
5'	175.0	-	-	
8	203.7	-	-	

Figure 76. ^{1}H NMR spectrum of tricholomaminde B in CD$_3$OD (298 K, 800 MHz)
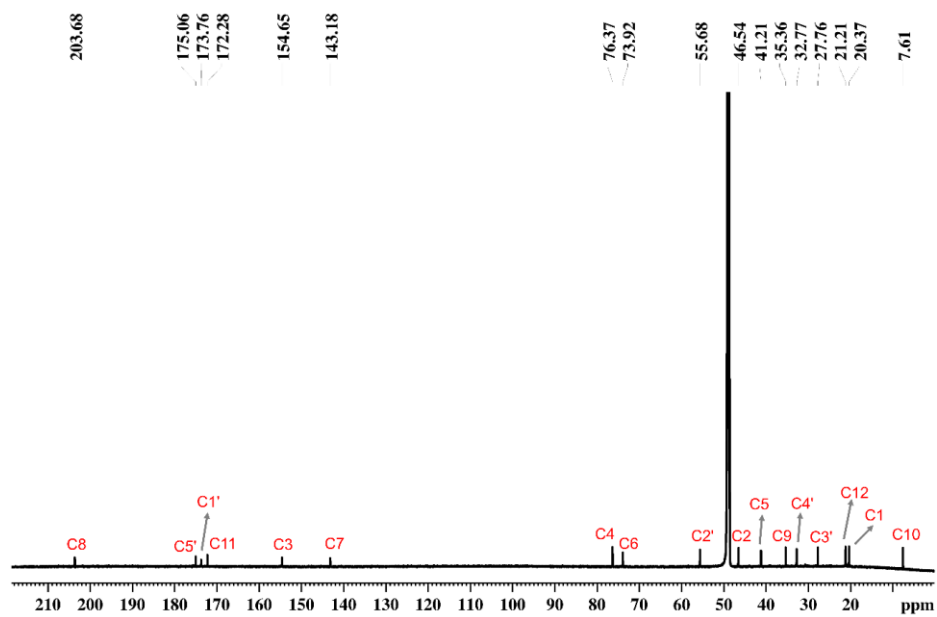
Figure 77. ^{13}C NMR spectrum of tricholomaminde B in CD$_3$OD (298 K, 200 MHz).
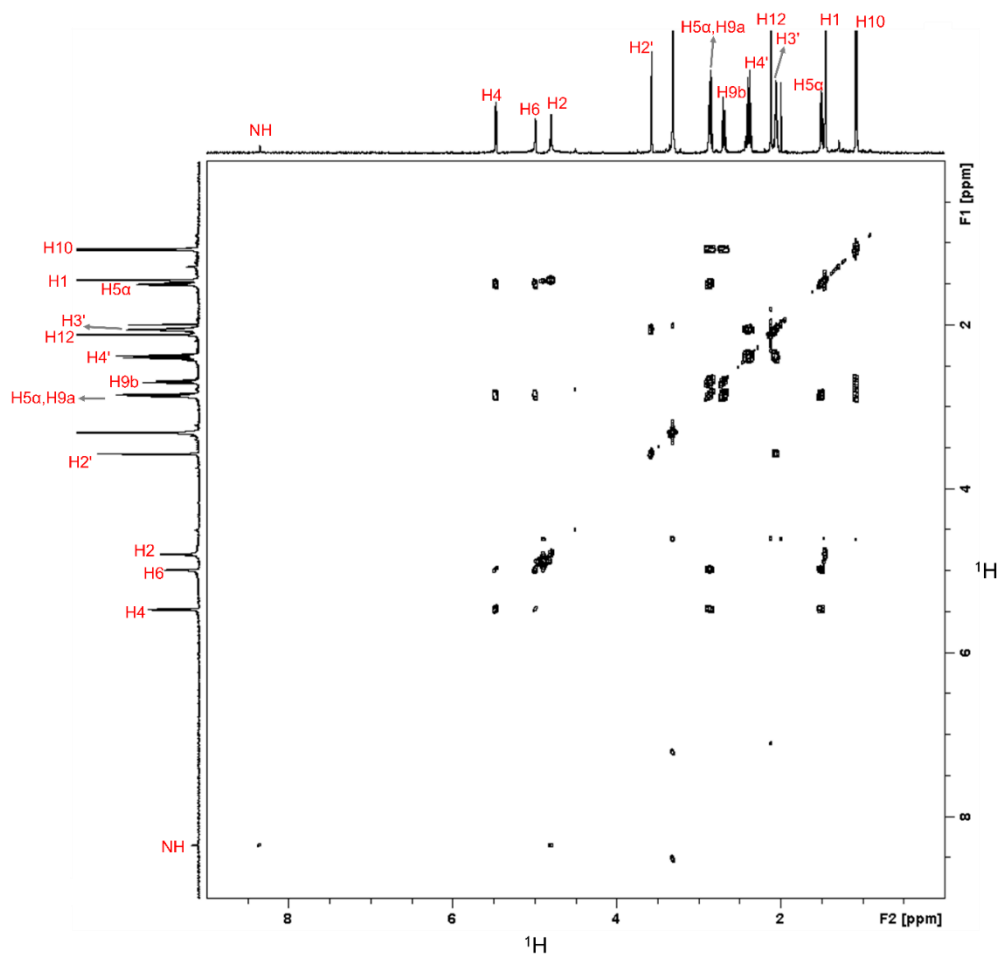
Figure 78. 2D-COSY (Correlation Spectroscopy) spectrum of tricholomaminde B in CD$_3$OD (298 K, 800 MHz). Experimental parameters: TD (F2) = 4096, TD (F1) = 512, NS = 16, DS = 8, D1 = 2, Experimental time = approx..6 hrs.
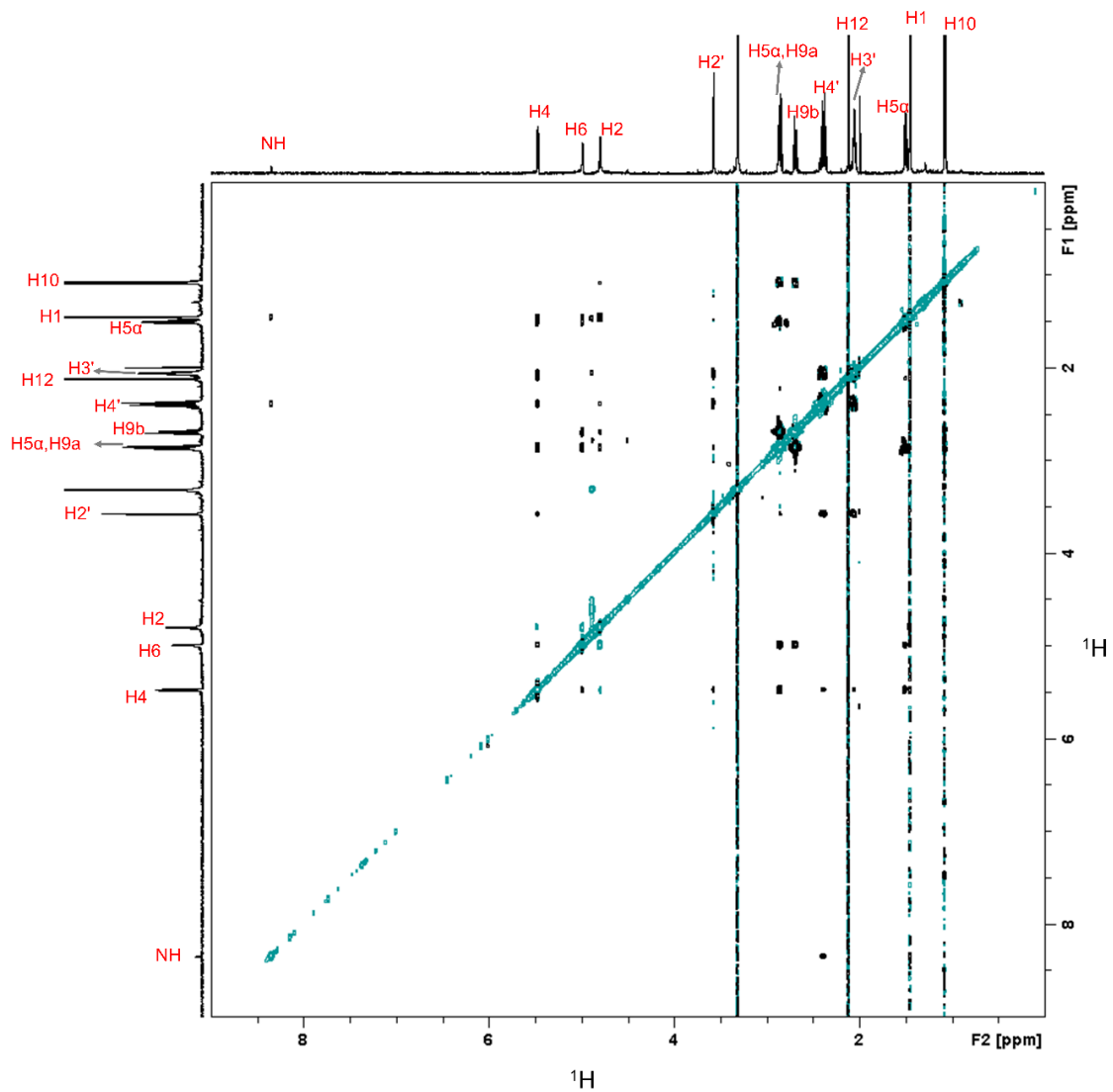
Figure 79. 2D-ROESY (Rotating-frame Overhauser Effect Spectroscopy) spectrum of tricholomaminde B in CD$_3$OD (298 K, 800 MHz). Experimental parameters: TD (F2) = 8192, TD (F1) = 512, NS = 40, DS = 16, D1 = 2, ROESY spin-lock pulse length = 250 ms, Experimental time = ~16 hrs.
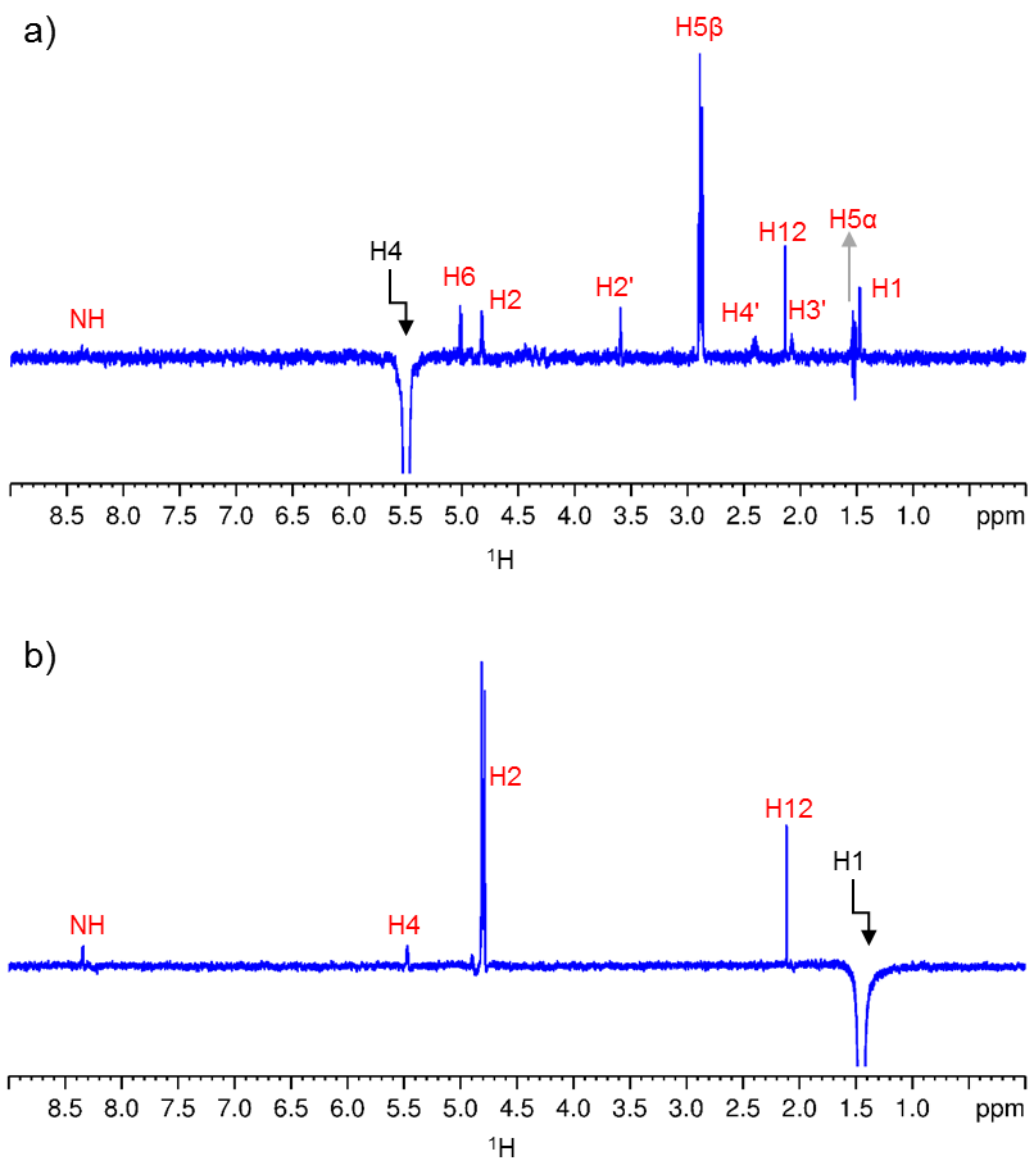
Figure 80. a) and b) are the 1D selective NOESY spectra of tricholomaminde B irradiated at 5.47 and 1.45 ppm, respectively, in CD_3OD (298 K, 800 MHz). Acquisition time = 1 sec, NOESY mixing time = 500 ms, NS = 1000, DS = 16, D1 = 2, Experimental time = ~1 hr.
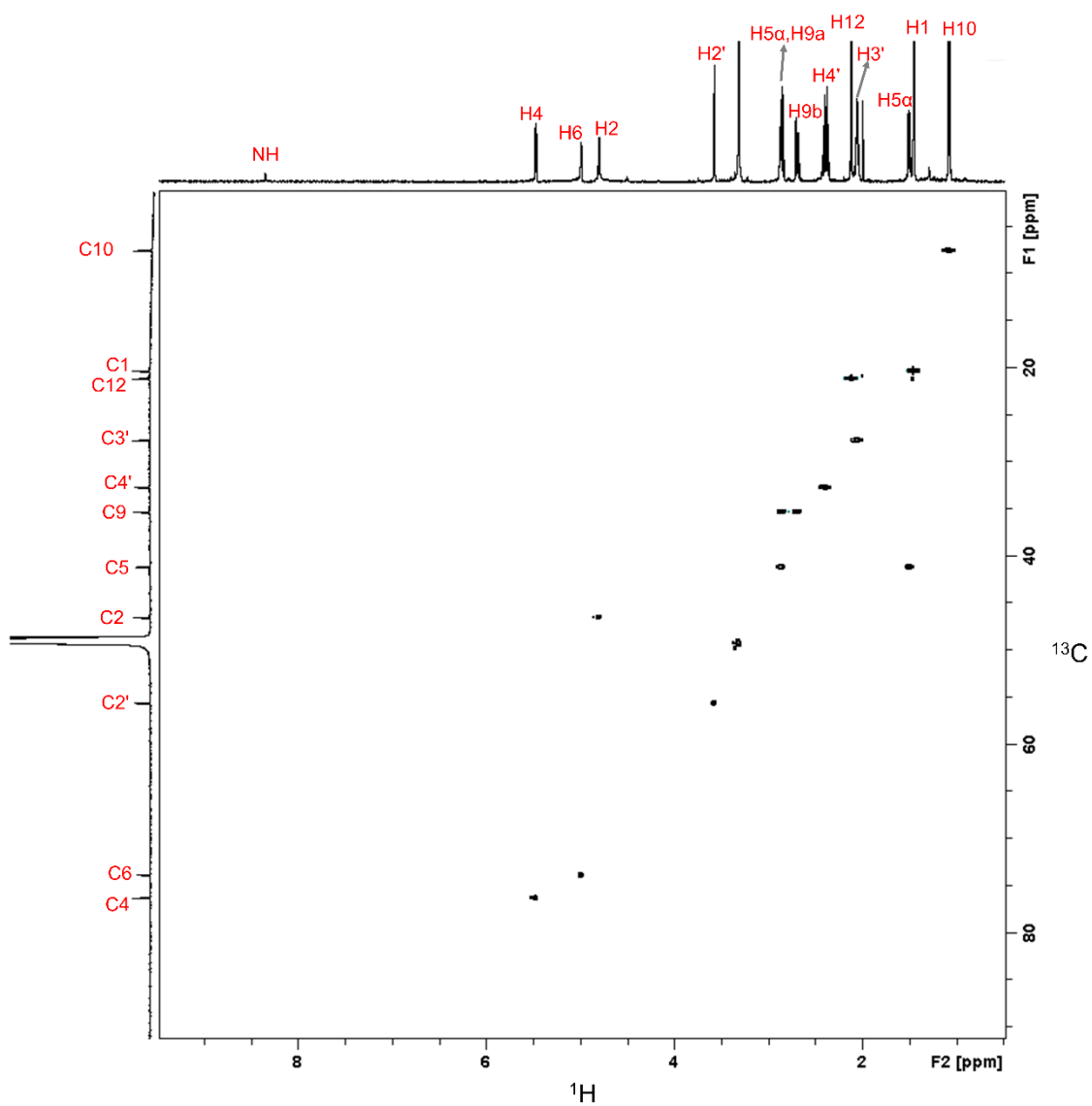
Figure 81. 2D-HSQC (Heteronuclear Single Quantum Correlation) spectrum of tricholomaminde B in CD$_3$OD (298 K, 800 MHz for ^{1}H and 200 MHz for ^{13}C). Experimental parameters: TD (F2) = 2048, TD (F1) = 512, NS = 8, DS = 8, D1 = 2, Experimental time = ~2 hrs.
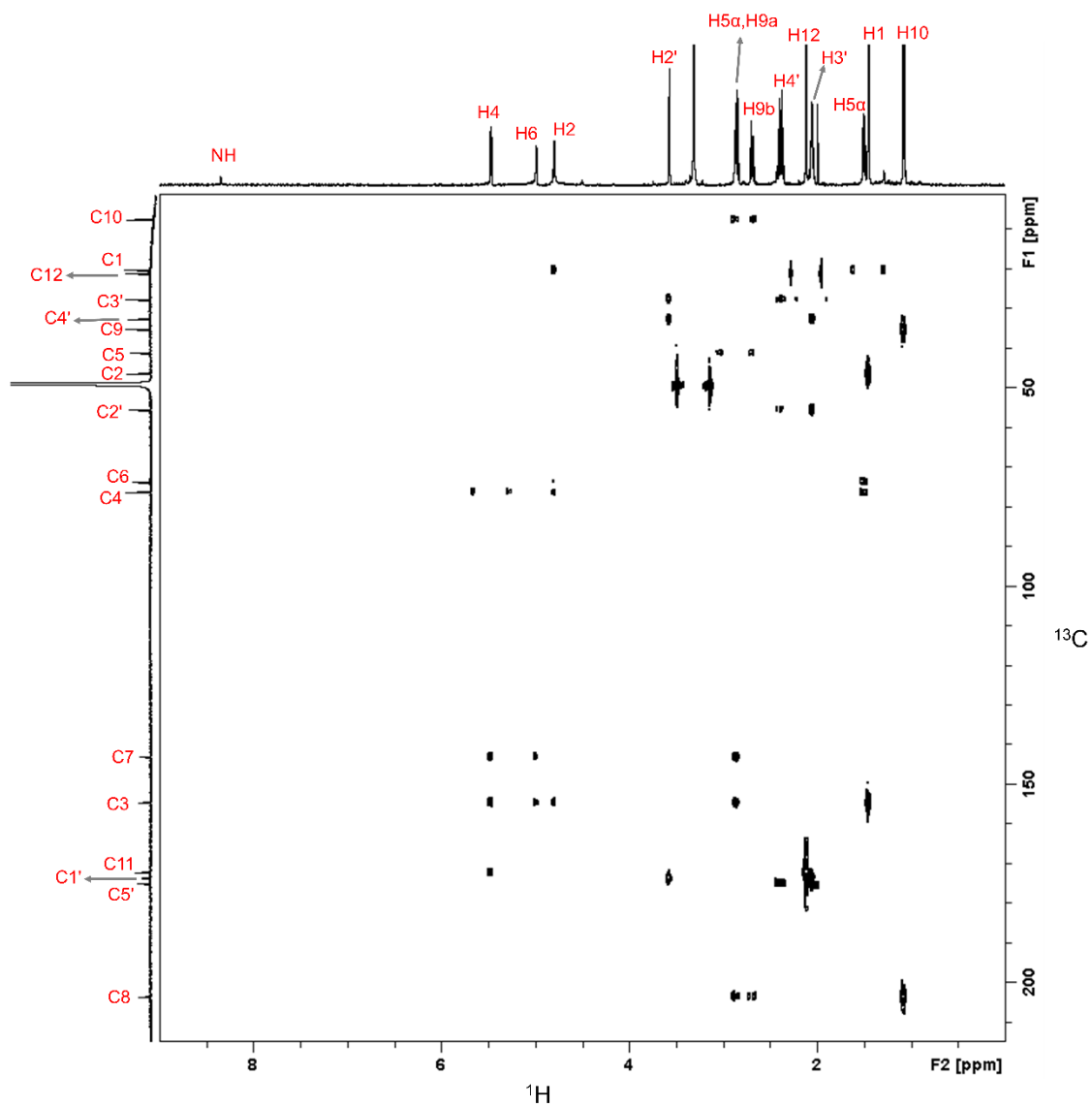
Figure 82. 2D-HMBC (Heteronuclear Multiple Bond Correlation) spectrum of tricholomaminde B in CD₃OD (298 K, 400 MHz for ^{1}H and 100 MHz for ^{13}C). Experimental parameters: TD (F2) = 4096, TD (F1) = 512, NS = 32, DS = 16, D1 = 2, SW (F2) = 10 ppm, SW (F1) = 240 ppm, J_{CH}-long range = 8 Hz, Experimental time = ~12 hrs.
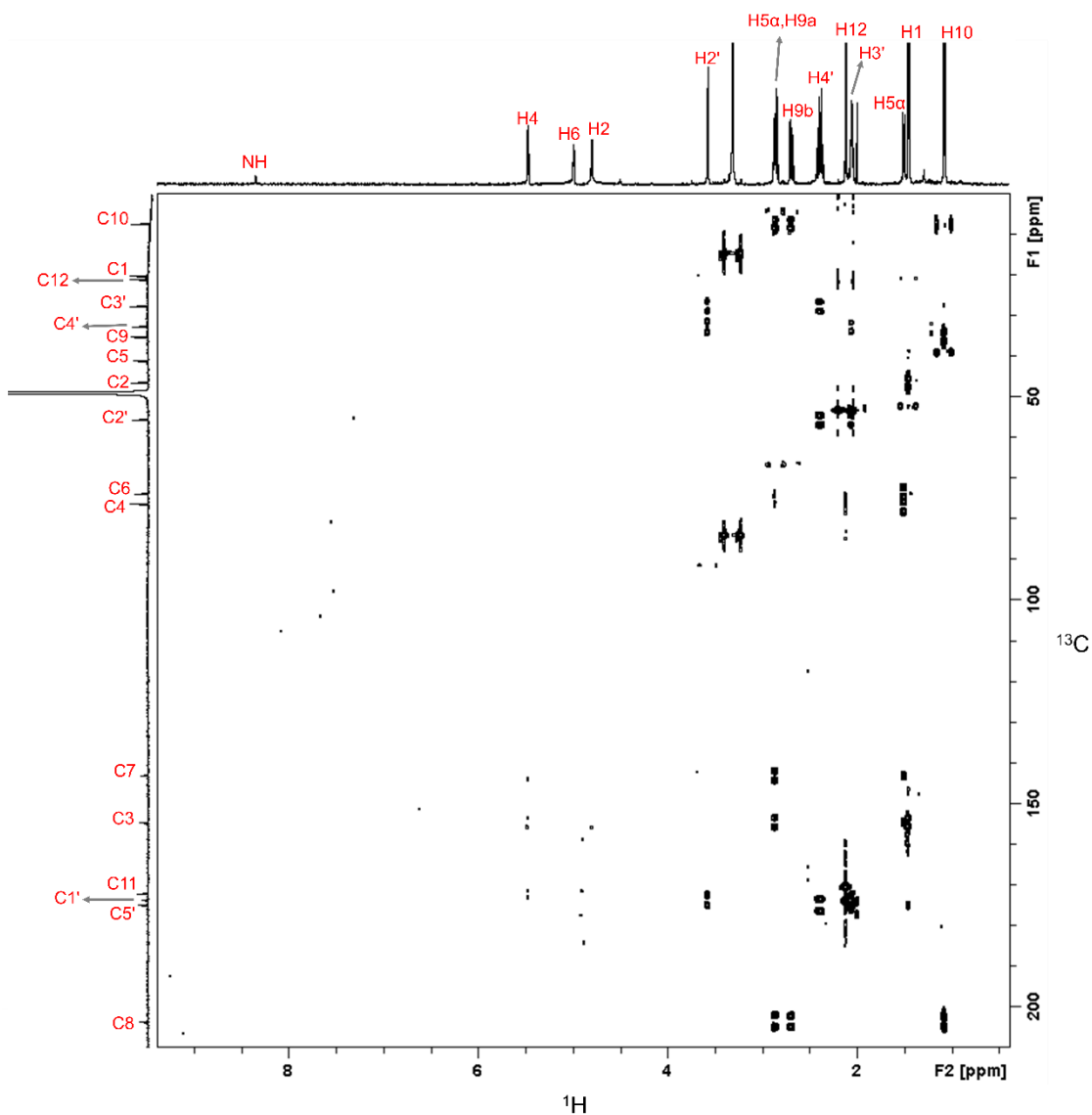
Figure 83. 2D-J-HMBC (JCH-coupled Heteronuclear Multiple Bond Correlation) spectrum of tricholomaminde B in CD$_3$OD (298 K, 800 MHz for ^{1}H and 200 MHz for ^{13}C). Experimental parameters: TD (F2) = 4486, TD (F1) = 512, NS = 48, DS = 64, D1 = 2, SW (F2) = 10 ppm, SW (F1) = 250 ppm, JCH-long range = 1 Hz, ^{1}J$_{CH}$ (min) = 125 Hz, ^{1}J$_{CH}$ (max) = 165 Hz, 180° shaped pulse length for inversion = 500 μs, 180° shaped pulse length for refocusing = 2000 μs, Experimental time = ~20 hrs.
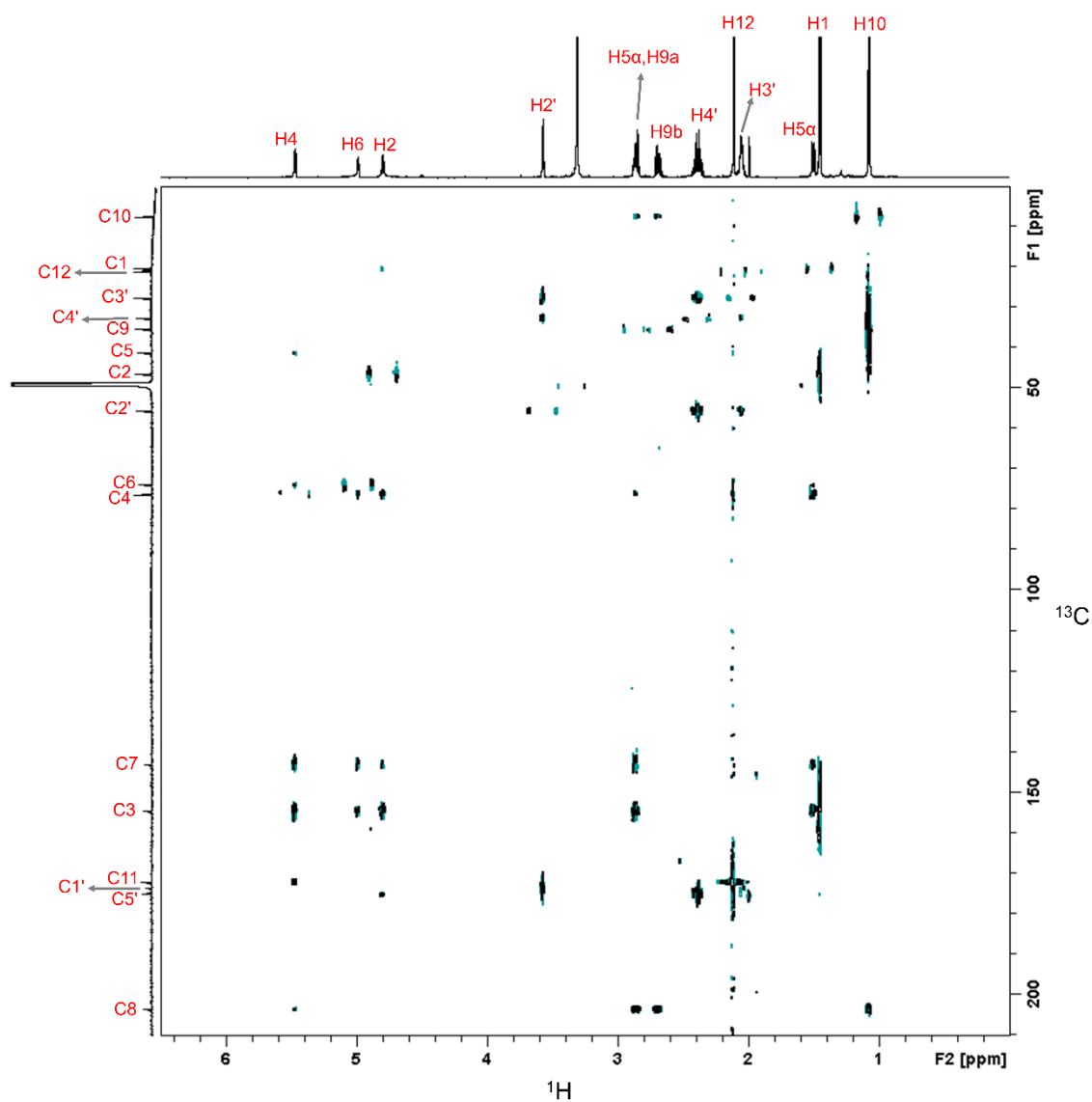
Figure 84. 2D-HSQMBC (Heteronuclear Single Quantum Multiple Bond Correlation) spectrum of tricholomaminde B in CD$_3$OD (298 K, 700 MHz for ^{1}H and 175 MHz for ^{13}C). Experimental parameters: TD (F2) = 6144, TD (F1) = 512, NS = 64, DS = 32, D1 = 2, SW (F2) = 7 ppm, SW (F1) = 212 ppm, J$_{CH}$ = 145 Hz, J$_{CH}$-long range = 6 Hz, 180° shaped pulse length for inversion = 500 μs, 180° shaped pulse length for refocusing = 2000 μs, Experimental time = ~24 hrs.
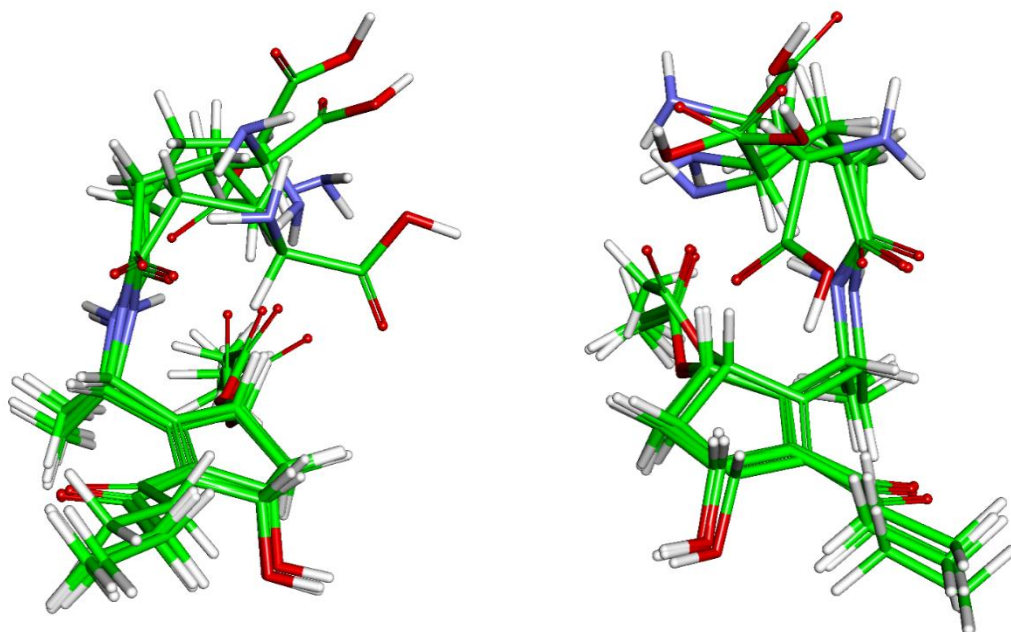
Figure 85. Superimposition of 4 DFT optimized conformers of (2S,4R,6S,2'S)- tricholomaminde B (left) and (2R,4S,6R,2'S)-tricholomaminde B (right) that are consistent with the experimental NMR restraints.

Table 18. Parameters obtained (SpecDis V1.71) for the comparison between experimental and calculated ECD spectra of LFTE-33 (2S,4R,6S,2'S).

(2S,4R,6S,2'S)-tricholomaminde B	CAM-B3LYP/6-311++G(3d,p)	B98/6-311++G(3d,p)
σ (eV)	0.16	0.16
λ_{shift} (nm)	2	-23
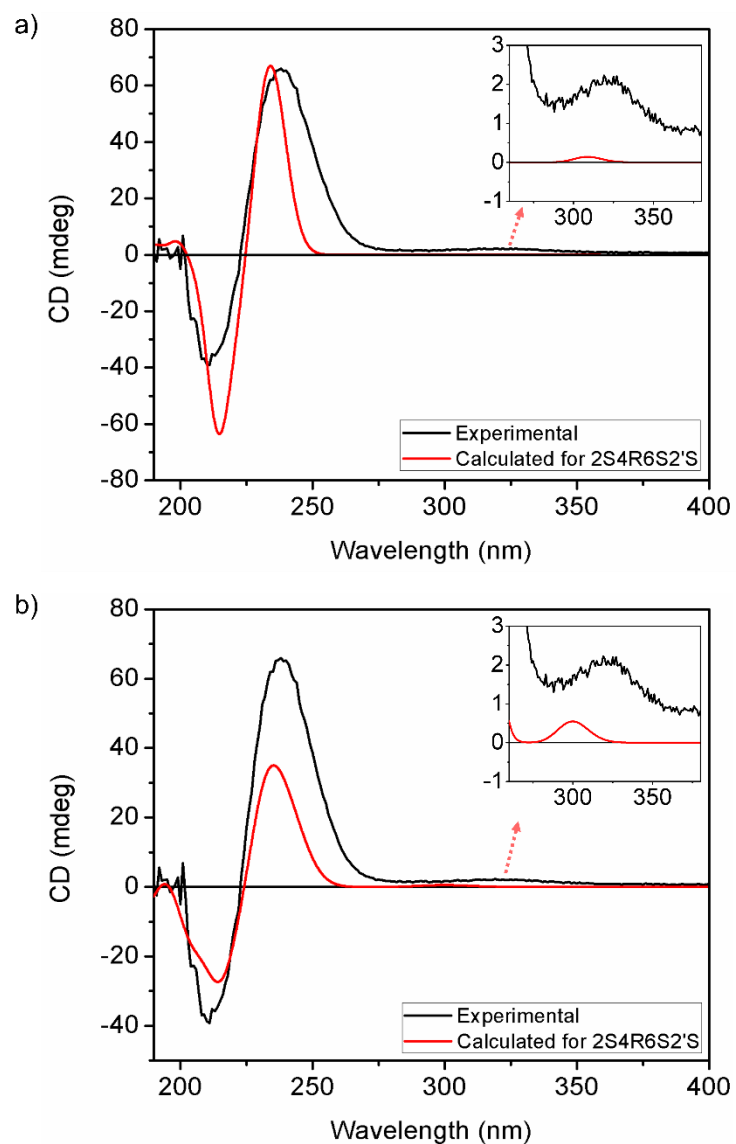
Figure 86. a) and b) are the comparison of Boltzmann-weighted ECD spectra calculated with CAM-B3LYP/6-311++G(3d,p) and B98/6-311++G(3d,p) level of theory, respectively, with the experimental ECD spectrum of tricholomaminde B in methanol. Inset: The comparison of expanded regions of small positive CD band (between 260 and 380 nm) shows good agreement between the experimental and calculated ECD spectra of tricholomaminde B.

Table 19. Parameters obtained (SpecDis V1.71) for the comparison between experimental and calculated ECD spectra of (2R,4S,6R,2'S)-tricholomaminde B.

(2S,4S,6R,2'S)-tricholomaminde B	CAM-B3LYP/6-311++G(3d,p)	B98/6-311++G(3d,p)
σ (eV)	0.16	0.16
λ_{shift} (nm)	3	-23
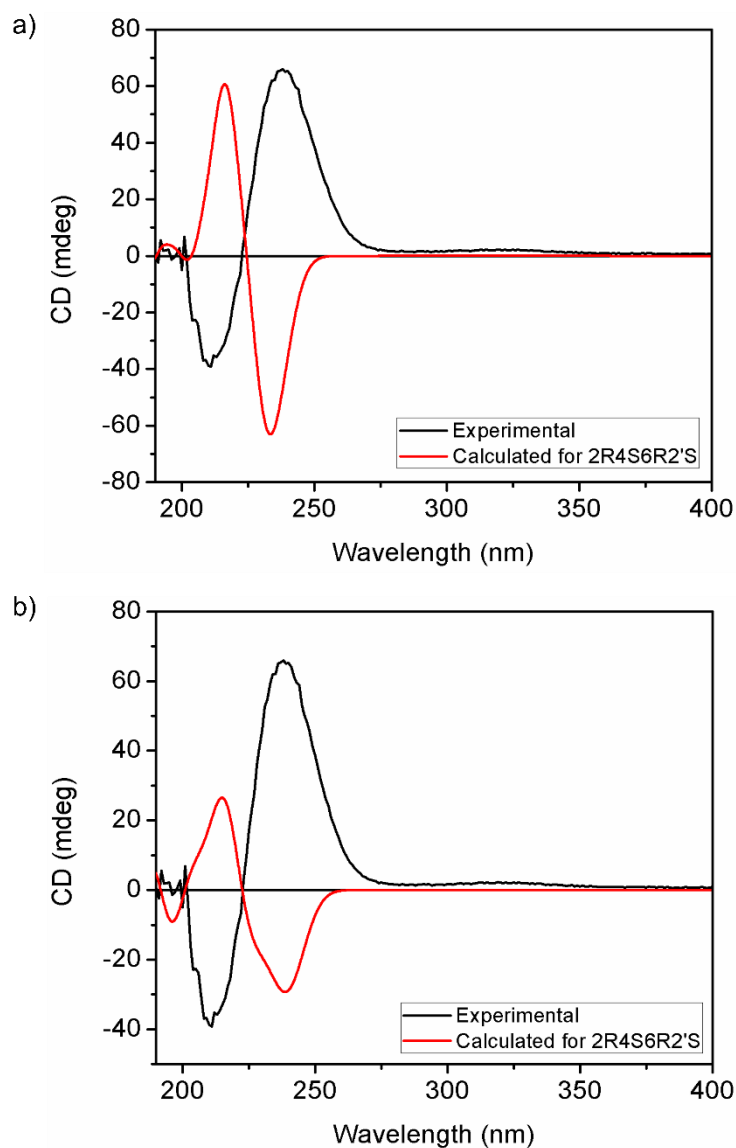
Figure 87. a) and b) are the comparison of Boltzmann-weighted ECD spectra calculated with CAM-B3LYP/6-311++G(3d,p) and B98/6-311++G(3d,p) level of theory, respectively, with the experimental ECD spectrum of tricholomaminde B in methanol.

1.3.4.2.4 Establishing the relative configuration of tricholomamide B by ^{13}C and ^{1}H RCSA's

1.3.4.2.5 Alignment media: preparation of poly-DEGMEMA (di(ethylene glycol) methylethermethacrylate)

Poly-DEGMEMA gel was prepared as previously described in the literature.[60] Hilgenberg's 2 mm NMR tubes (internal diameter 1.6 mm) used in the synthesis were either pre-silanized with a 10% (v/v) solution of 1,1,1,3,3,3-hexamethyldisilazane in toluene for 24 hrs or by using Sigmacote® for 15 minutes. Subsequently, the tubes were emptied and dried in an oven (40 ºC/ 24h). Both polymerization inhibitor, potentially present in the monomer (DEGMEMA) form, and the cross-linker EGDMA (ethylene glycol dimethacrylate) were removed over a basic alumina column. 2,2'-azobis(4-methoxy-2,4-dimethylvaleronitrile) (V-70) was used as initiator for polymerization. Three stock solutions were prepared:

- *Solution A*: 1.4 mL of DEGMEMA monomer and 0.6 mL of MeOH.

- *Solution B*: 200 μL EGMDA and 1240 μL DEGMEMA.

- *Solution C*: 14 mg of V70 in 1 mL of MeOH.

In a falcon tube were mixed: 2 mL of stock *solution A*, 20 μL of *solution B* and 32 μL of *solution C*. After exhaustive mixing of the above constituents the solution was transferred to the silanized NMR tubes, which were subsequently capped and kept in a water bath at 50 °C for 6 hrs. After polymerization, tubes were opened, and then the gel was allowed to dry. The polymer gels were carefully removed from the NMR tubes and washed three times in methanol (24 hrs each) in order to remove any residual monomer. Poly-DEGMEMA gels were dried on a glass surface turning out in a sticky and flexible material. All the gels were handled with extreme care and we observed a change in their proportions during the drying/swelling processes.

For RDC, ^{13}C and ^{1}H RCSAs measurements, 2.4 cm gel sticks were used and swollen in CD_3OD inside a Hilgenberg's 3 mm NMR tube (part number 2001749) for at least 24 hours. The gel used in the present study showed a ^{2}H quadrupolar splitting of 5.9 Hz (Figure 94), at maximum compression. All the chemicals were purchased from Sigma Aldrich and V-70 was obtained from Wako Chemicals.

1.3.4.2.5.3 NMR sample preparation for ^{13}C and ^{1}H RCSAs measurements

800 μg of tricholomamide B were dissolved in 50 μL of CD_3OD and transferred to a Hilgenberg's 3 mm NMR tube. A pre-swelled fully relaxed poly-DEGMEMA gel was gently pushed inside the tube, adding some microliters of solvent until fully cover the gel. Diffusion of the sample inside the gel was achieved by pumping gently several times with a 2 mm O.D glass plunger.[43] Anisotropic conditions were induced by our designed 3 mm compression device prototype (Our SMCD not only reduces the mass of the alignment media, but its background signal, been fully compatible with the commercially available 3 mm NMR tubes.

Tricholomamide B (Figure *60* right) was aligned in poly-DEGMEMA/CD$_3$OD gel (75/0.3) using the variable compression/relaxation method with an in-house 3 mm compression device (USMCD). HSQC pure shift experiments were acquired with the fully relaxed and compressed gel (at a ^{2}H quadrupolar splitting of 5.9 Hz, ^{2}H NMR spectra were recorded on a 800 MHz Bruker Avance III spectrometer operating at 122.89 MHz for ^{2}H, with accumulation of 8 transients. NMR experiments for tricholomamide B were recorded on a 800 MHz Bruker Avance III spectrometer operating at 800.53 MHz and 201.32 MHz for ^{1}H and ^{13}C, respectively. Carbon and Proton Residual chemical shift anisotropies (^{13}C, ^{1}H- RCSAs) were simultaneously measured using real-time pure shift HSQC experiments with non-uniform sampling (TD2: 1.4K; TD1: 512; FnTYPE: NUS 31.2%; 512; 64 transients; 2 s recycle delay).[21,24,27,133] ^1J = 135 Hz and sine squared window function was applied in both F1 and F2 dimensions prior to Fourier transformation.

1.3.4.2.5.4 Computational details:

Carbon and Proton CSA parameters were computed using the Perdew-Wang exchange as modified by Adamo and Barone combined with PW91 correlation (mPW1PW91),[110] paired with the 6-311+G(2d,p) in vacuum. This combination provided accurate prediction of isotropic δ_C and δ_H prediction in small molecules and an acceptable mean absolute error. [134] All DFT calculations were carried out using Gaussian09 suite program.

1.3.4.2.5.5 ^{13}C and ^{1}H RCSAs analysis of tricholomamide B:

^{13}C and ^{1}H RCSAs were obtained by using the methodology described by *Nath et al*., and *Marco et al*.,[18,22,23] which anisotropic data is measured directly from an HSQC experiment. In our case C4 and H4 were chosen as carbon and proton references, respectively and the remaining data was extracted from a real-time pure shift HSQC experiments.

Alignment tensors were calculated through the singular value decomposition module (SVD)[3] provided in MSpin-program.[9] ^{1}H and ^{13}C RCSAs values were expressed in Hz.[4] Tricholomamide B are described by a rather restricted ensemble (Figure 85), the NMR data was fitted using a single tensor [12] and population fitted using a combined Levenberg–Marquardt algorithm. [83] Conformers were oriented to the Eckart frame.[115]

^{1}H RCSAs of methyl groups and enantiotopic methylene protons were averaged as described by Nath et al.[18] The isotropic contribution correction parameter c was optimized until the minimum Q factor was achieved using the procedure recently described by F. *Hallwass et al*.[10,22] ^{13}C and ^{1}H RCSAs were fitted separately and quality of the fits was scored in terms of the Cornilescu quality factor Q and Q_{CSA}. [19] Finally we show the fitting as a combination of ^{1}H and ^{13}C RCSA's using Equation 12. We are rather trusting on Q_{CSA} for the fit of RCSAs data, since it removed the large size variation of the ^{13}C and ^{1}H chemical shift tensors.[22]

$$Q_{\text{1H RCSA+13C RCSA}} = \sqrt{Q_{\text{13C RCSA}}^2 + Q_{\text{1H RCSA}}^2} \qquad \textit{Equation 12}$$

As it was mentioned before, absolute configuration at C2′ of tricholomamide B was assigned as *S* based on the chiral HPLC analysis (*vide supra*). NMR analysis (NOEs and *J*-couplings) indicates that the relative configuration of tricholomamide B should be either (2S,4R,6S,2'S) or (2R,4S,6R,2'S) [36,135,136] An extensive computational study over the diastereomers yielded 5 and 4 conformers for (2S,4R,6S,2'S) and (2R,4S,6R,2'S) configurations, respectively (Figure 85). Tricholomamide B are both flexible and demand the use of a multi conformer single tensor (MCST) approach with fit to populations for the possible configurations and their conformers. The significant assignment of a molecular-fixed-axis system is needed, allowing a proper separation of the internal motion and reorientation in the molecule. This coordinate system was chosen in such a way that it fulfils Eckart Condition, [137] preventing that the nuclear displacements results in the movement of the center of mass and excluding any contribution of the displacements to an overall rotation of the molecule. [41] Configurations 2S,4R,6S,2'S and 2R,4S,6R,2'S show envelope conformations, some with C5 down and others with C5 up; therefore C5 is excluded from Eckart frame (Figure 85) We assumed as has always been done that conformational equilibrium is not significantly affected by the alignment media.

[13]C-RCSAs proved to be promising NMR structural parameters for the assignment of structure and relative configuration of rigid as well as flexible small molecules. Both the relative configuration of strychnine and the flexible alkaloid retrorsine were unambiguously determined by ^{13}C-RCSAs in poly(methyl methacrylate) gel and also in liquid crystal poly-Υ-(benzyl-L-glutamate) [22,56] to induces the need weak alignment.

Ten ^{13}C RCSAs were determined for tricholomamide B in poly-DEGMEMA/CD$_3$OD gel using a in-house 3 mm compression device from a Pure shift HSQC experiment (Figure 90 a), with a range of 21.4 Hz. The remaining signals are either obscured by the large gel background signal or belonging to quaternary carbons (Figure 90 a), with a range of 21.4 Hz. The remaining signals are either obscured by the large gel background signal or belonging to quaternary carbons (Figure 92)

Despite the fact that we have only 10 ^{13}C RCSAs, from protonated carbons, we can complement them below with ^{1}H RCSAs, we conducted a study whether these RCSAs are already able to assign the relative configuration.

[13]C RCSAs were able to discriminate between both the diastereomers and establish the connection among all the stereocenters in tricholomamide B (Figure 90 c).). Good agreement is achieved between experimental and back calculated ^{13}C RCSAs for 2S,4R,6S,2'S configuration ($Q(Q_{CSA})$ = 0.095 (0.123)) as compared to 2R,4S,6R,2'S configuration ($Q(Q_{CSA})$ = 0.186 (0.214)) of tricholomamide B. Proportionality constant *c* for 2S,4R,6S,2'S and 2R,4S,6R,2'S has a value of 0.249 and 0.271 respectably. As is described in the literature [22], including the chemical shit anisotropy (CSA) contribution in the computation of the ^{13}C RCSA quality factor (Q_{CSA}) increases the discrimination capabilities of the technique.

The efficacy of ^{1}H RCSA NMR technique is also demonstrated for establishing the relationship between two distant chiral centers C2 and C2' of tricholomamide B separated by 5 rotatable covalent bonds. In the ^{1}H RCSA, huge polymer background hinders the extraction of proton RCSAs for C9 and C5 carbons (Figure 93), respectively. [1]H RCSA tricholomamide B are shown in Figure 91 c

Data consistency was checked by computation on the intertensor angle [57,138] ($\theta_{1H-RCSA,13C-RCSA}$) resulting in an angle of 3.1°; which is in agreement with the expected indicating that A1H-RCSA and A13C-RCSA are to a very high degree collinear.

Finally, we simultaneously used ^{13}C-RCSAs and 1H-RCSAs and evaluate the quality of the fit with a combined quality factor that combines Cornilescu Q-factor and QCSA for ^{13}C, ^{1}H-RCSAs keeps the assignment of tricholomamide B as 2S,4R,6S,2'S; as expected including the CSA contribution in the quality factor improves the discrimination (Figure 88).
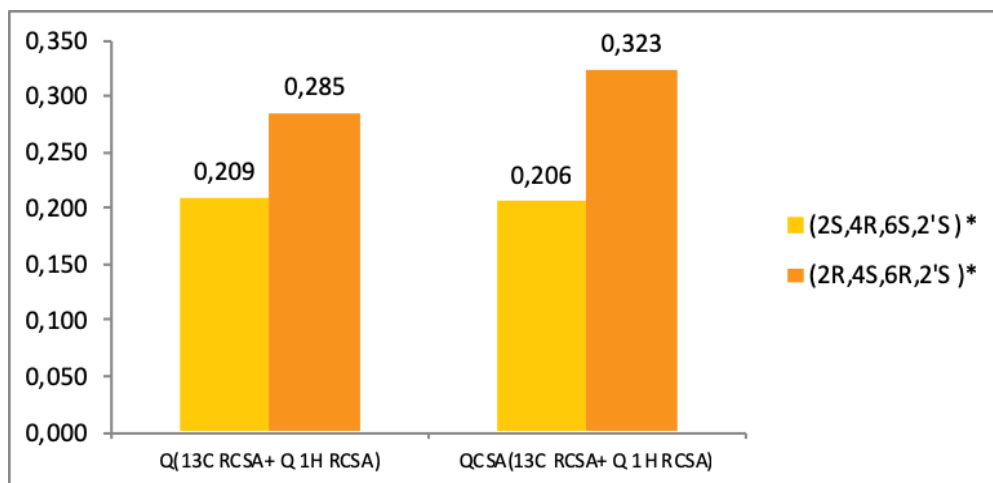
Figure 88. RCSA-based stereochemical analysis of both possible configuration of tricholomamide B, measured in our 3 mm compression device prototype. The quality of the fit is expressed as a combined quality factor ($Q_{13C\ RCSA\ +\ 1H\ RCSA}$) where the correct configuration has the lowest Q value

In summary, the conformation and absolute configuration of a new natural product with a flexible side chain attached to a partially rigid five member ring were unambiguously determined by using a combination of isotropic (NOEs and *J*-couplings)/anisotropic (^{13}C and ^{1}H RCSAs) NMR analysis and DFT calculation of ECD. Therefore, the absolute configuration of tricholomamide B is 2S4R6S2'S.
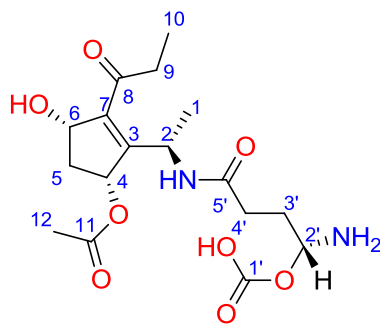
Figure 89. Absolute configuration of tricholomamide B

Carbon	Exp (Hz)	Comp (Hz)
C6	2.25	2.381
C2	-3.72	-4.551
C2'	-13.000	-12.099
Me10-	3.04	2.275
Me1-	0.24	0.473
Me12-	0.3	0.078
C3'	1.91	2.304
C4'	4.06	4.167
C5	8.38	8.822
C4	Ref	Ref

(a)

(b)

(c)

Alignment tensor information:

(d)

A'x=-1.986e-01

A'y=-6.956e-01

A'z= 8.942e-01

(e)
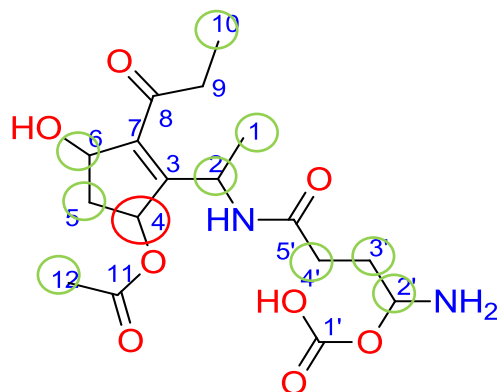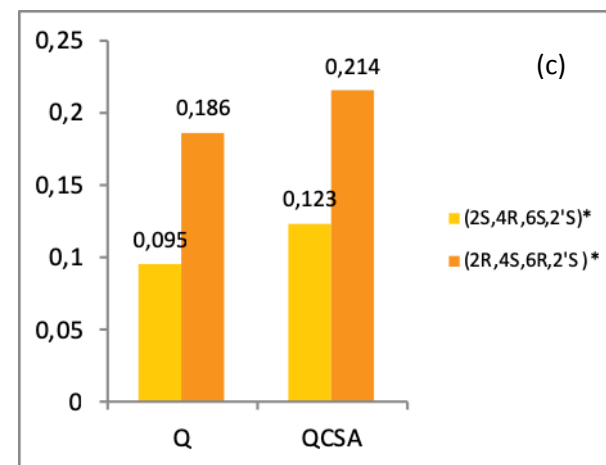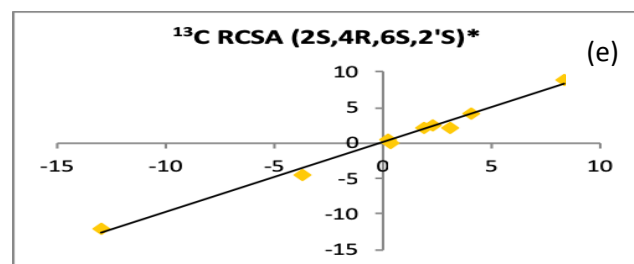
^{13}C RCSA (2S,4R,6S,2'S)*

Configuration	Q	QCSA
(2S,4R,6S,2'S)*	0.095	0.123
(2R,4S,6R,2'S)*	0.186	0.214

(f)

Figure 90. Anisotropic data fitting (^{13}C RCSA) of tricholomamide B measured at 800 MHz for ^{1}H in poly-DEGMEMA/CD$_3$OD gel. Experimental and back calculated carbon residual chemical shift anisotropies (^{13}C-RCSA) (a), extracted carbon RCSA are green marked and reference carbon is red marked (b), quality factor ^{13}C RCSA information for tricholomamide B for both possible configuration 2S,4R,6S,2'S and 2R,4S,6R,2'S (c) Alignment tensor information of (2S,4R,6S,2'S)* (d), fitting from carbon residual chemical shift anisotropies (^{13}C-RCSA) (e) and Q factor and QCSA of both possible configurations

(a)

Proton	Exp. (Hz)	Comp. (Hz)
H6	-6.08	-5.088
H2	-3.6	-2.374
H2'	-3.6	-4.722
Me10-	-1.04	-1.037
Me1-	-4.56	-4.663
Me12-	-3.52	-4.002
H3'	-2.64	-2.459
H4'	-2.88	-2.429
H4	Ref	Ref

Alignment tensor information:

(d)

A'x= 1.248e-01
A'y= 2.475e+00
A'z=-2.600e+00

(e) 2S,4R,6S,2'S (^{1}H RCSA)

(f)

Configuration	Q	QCSA
(2S,4R,6S,2'S)*	0.159	0.165
(2R,4S,6R,2'S)*	0.216	0.242
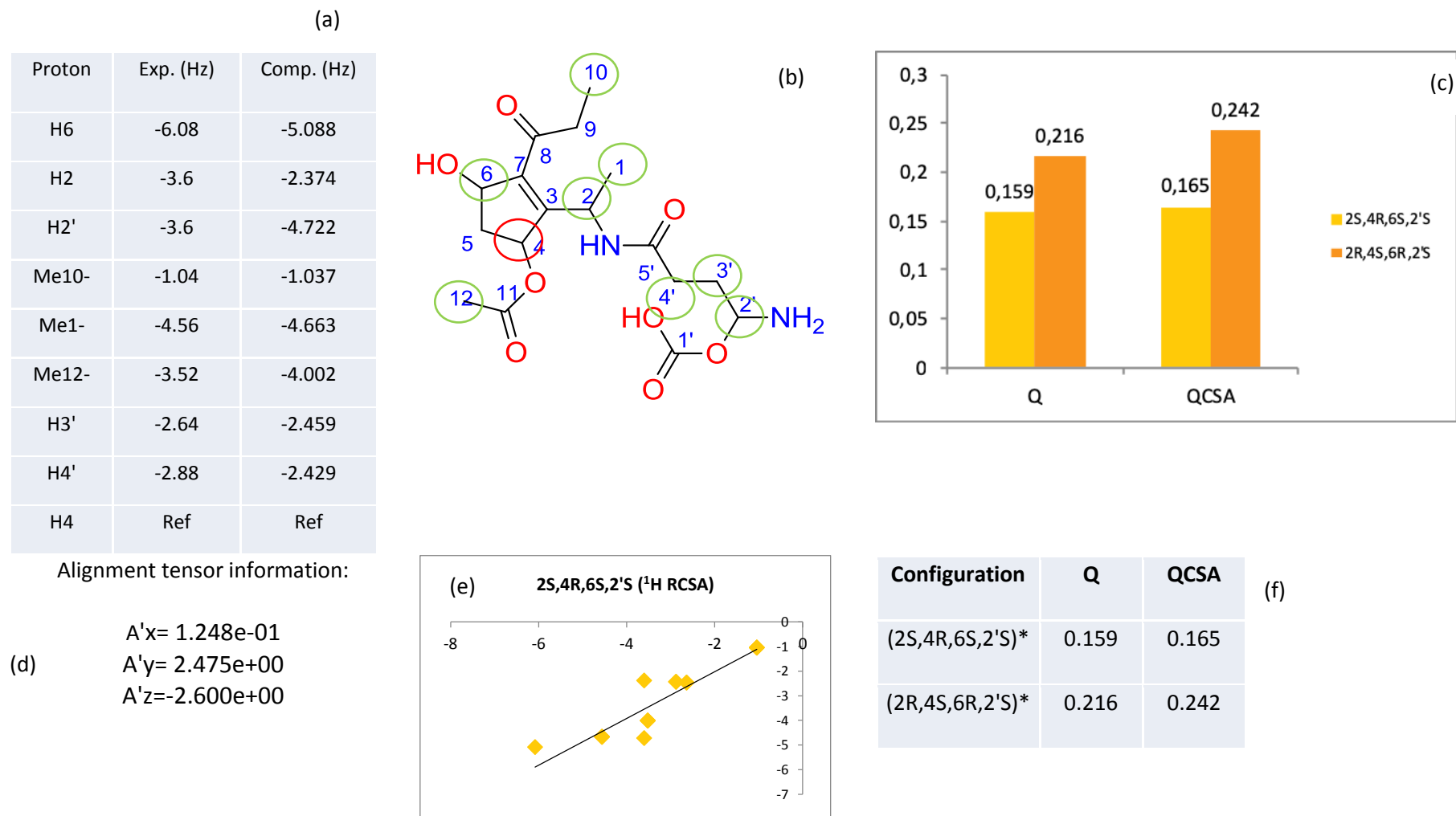
Figure 91. Anisotropic data fitting (^{1}H RCSA) of tricholomamide B measured at 800 MHz for 1H in poly-DEGMEMA/CD$_3$OD gel. Experimental and back calculated proton residual chemical shift anisotropies (^{1}H-RCSA) (a), extracted anthropic data are green marked and reference proton is red marked (b), quality factor ^{1}H RCSA information for tricholomamide B for both possible configuration (2S,4R,6S,2'S)* and (2R,4S,6R,2'S)* (c) Alignment tensor information of (2S,4R,6S,2'S)* (d), fitting for proton residual chemical shift anisotropies (^{1}H-RCSA) (e) and Q factor and QCSA of both possible configurations
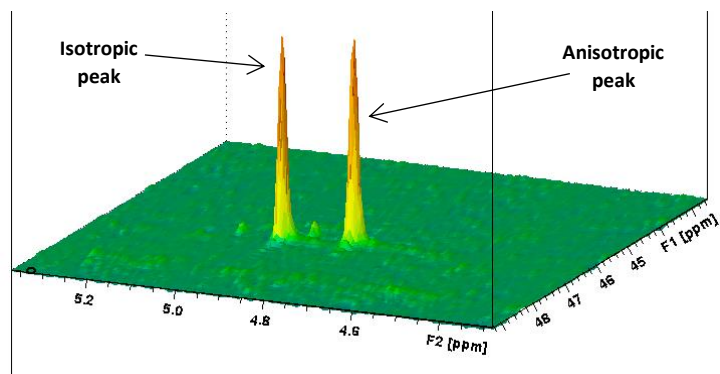
(a) Fully relaxed gel
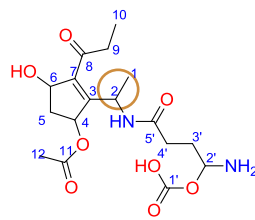
Tricholomamide B
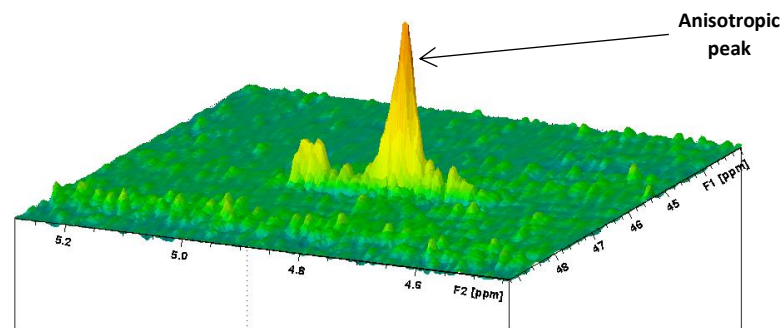
(c) Maximum Compressed gel

(b)

(d)
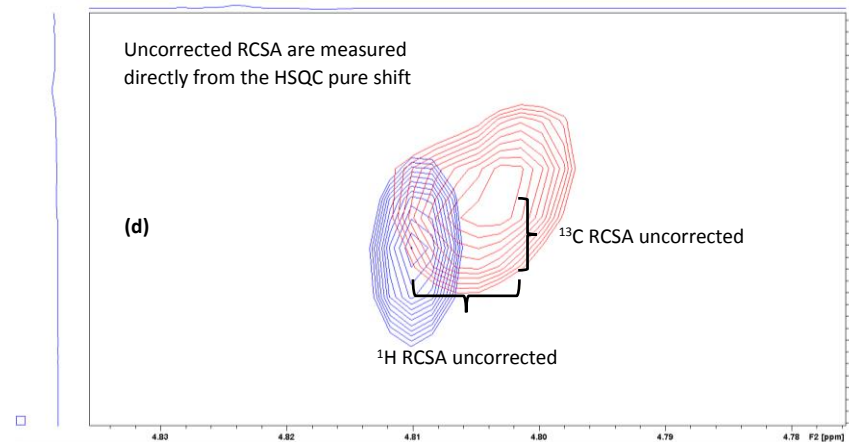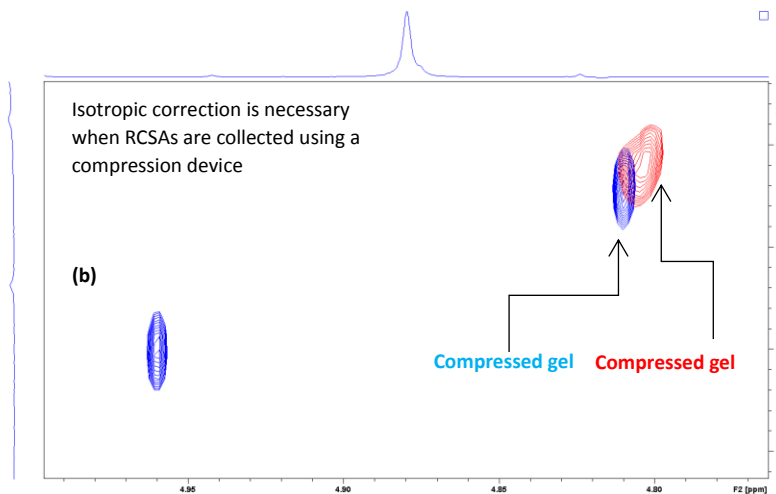
Figure 92. Real-time pure shift HSQC experiment of Tricholomamide B; detail of C2 oblique mode of HSQC pure shift of fully relaxed **(a)** 2D projection HSQC pure shift of fully relaxed **(b)** C2 oblique mode of HSQC pure shift of fully compressed **(c)** 2D projection HSQC pure shift of fully compressed gel, isotropic peak is missing **(d**
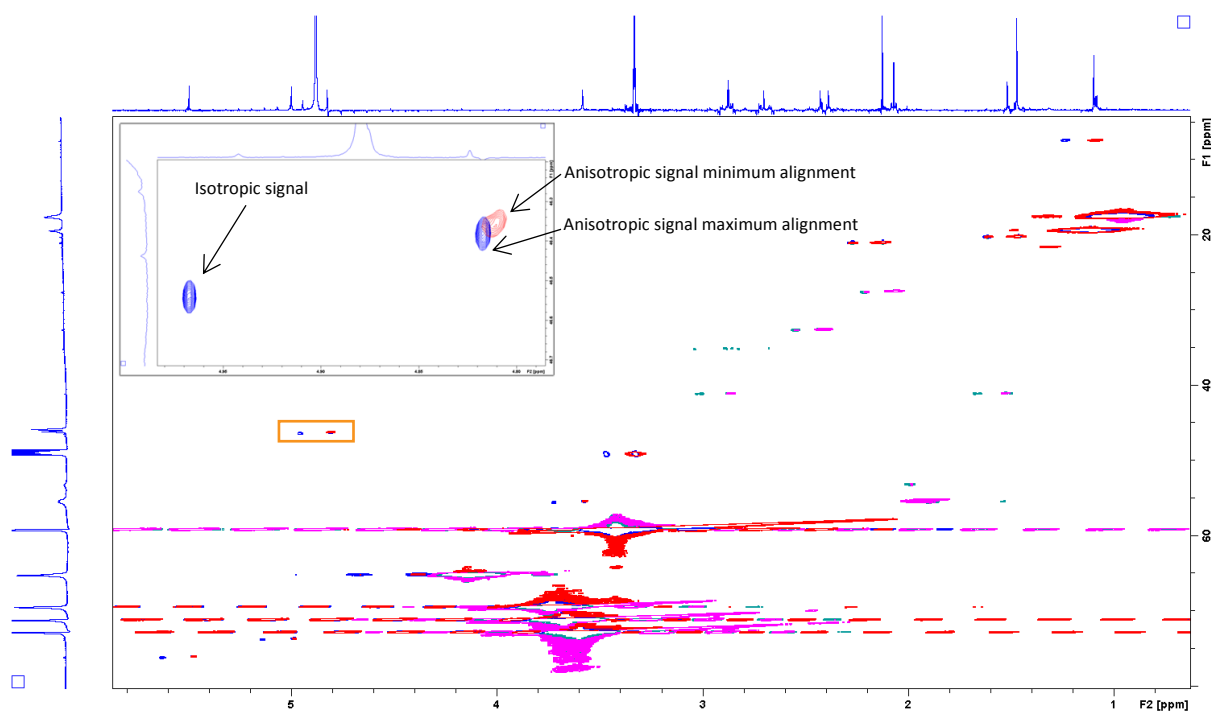
Figure 93. Isotropic (blue) and anisotropic (red) CLIP-HSQC spectra of tricholomamide B (298.1 K, CD$_3$OD, 800 MHz for ^{1}H and 200 MHz for ^{13}C)
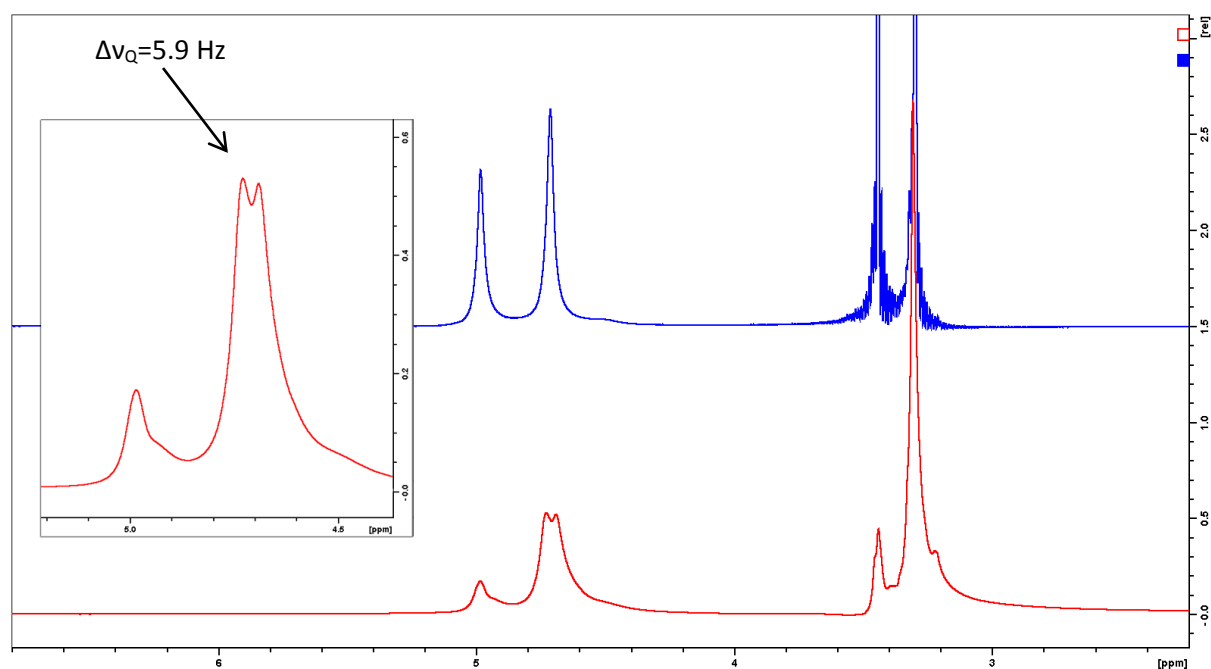
Figure 94. [2]H spectrum of fully relaxed (blue line) and compressed (red line) poly-DEGMEMA gel (70/0.3) used in the present study.

1.3.4.2.6. Establishing the relative configuration of tricholomamide A by Residual Dipolar Coupling (RDCs)

After successfully established the absolute configuration of tricholomaminde A by NOESY and *J*-based analysis, we decided to test the capabilities of RDCs with a 3 mm compression device prototype to connect the 2′ with the stereocluster the group formed by C2 and C6 (Figure 60 right). The general approach to determine the relative configuration of flexible natural product by residual dipolar coupling (RDCs) is depicted in Figure *6*.[41]

1.3.4.2.6.1 Experimental details

The gel used as alignment media was prepared as described before, as well as the sample preparation (the sample mass was 500 µg). Splitting in deuterium channel (ΔvQ), was obtained from a ^{2}H NMR spectrum, showing a quadrupolar splitting value (-OD) of (4.4 Hz) at maximum compression (*Figure 98*). ^{2}H NMR spectra were recorded on a Bruker Avance III 800 spectrometer operating at 122.89 MHz for ^{2}H and 8 transients were accumulated.

NMR experiments for tricholomamide A were recorded also on a Bruker Avance III 800 spectrometer operating at 800.53 MHz and 201.32 MHz for 1H and 13C, respectively. Direct $^1J_{CH}$ coupling and RDCs were measured from F1 *J*-scaled BIRD version of HSQC experiment (*hsqcetgpipjcsp.2*) under both isotropic and anisotropic conditions were acquired with a scaling factor of 8. Experiment time was speed up by using non uniform sampling (TD2: 1262; TD1: 768; FnTYPE: NUS 50%; 192; 112 transients; 2 s recycle delay)[21] (Figure 99). A sine squared window function was applied in both F1 and F2 dimensions prior to Fourier transformation. RDCs experimental error was calculated by Kontaxis *et al.,* [94] (Equation 13) Where; peak line width, peak signal to noise ration and *J* scaling are represented by LW, SN and K respectively.

$$\sigma = \frac{lw}{SN * K}$$

Equation 13

1.3.4.2.6.2 RDCs analysis of tricholomamide A:

Alignment tensors were calculated through the singular value decomposition method (SVD) [3] provided in MSpin-program.[9] $^1D_{CH}$ RDCs value were expressed in Hz. $^1D_{CH}$ RDCs were extracted from a CLIP-HSQC experiment using Topspin 3.1.[133] Residual dipolar couplings were determined as $D = T - J$; where T and J are the C-H couplings measured from CLIP-HSQC recorded in anisotropic (poly-DEGMEMA/CD$_3$OD gel) and isotropic (CD$_3$OD as solvent) conditions, respectively.[139] As the molecule is described by a rather restricted ensemble, the NMR data was fitted using a single tensor [12]. Conformers were oriented to the Eckart frame [137] $^1D_{CH}$ RDCs of methyl groups were averaged as described by Sanchez-Pedregal et al. [114] and Methylene group are reported as the average of the coupling of CHa and CHb. The quality of the fits was scored in terms of the Cornilescu quality factor Q.[19]

The absolute configuration of C2' chiral center was assigned to be S as in Tricholomamide A. NMR analysis (NOEs and *J*-couplings) indicates that the relative configuration of tricholomamide A should be either 2R6R2'S or 2S6S2'S. [36,135,136] An extensive computational study over the diastereomers yielded 5 and 6 conformers for 2R6R2'S and 2S6S2'S configurations, respectively

Tricholomamide A is highly flexible and demands the use of a multi conformer single tensor (MCST) approach with and populations Boltzmann averaged for the possible configurations and their conformers. The significant assignment of a molecular-fixed-axis system is needed; that allows a proper separation of the internal motion and reorientation in the molecule. This coordinate system was chosen in such a way that it fulfils Eckart Condition; preventing that the nuclear displacements results in the movement of the center of mass and excluding any contribution of the displacements to an overall rotation of the molecule [41]. Configurations 2R6R2'S and 2S6S2'S show envelope conformations, some with C5 down and others with C5 up; therefore C5 is excluded from Eckart frame (Figure 72 and Figure 73 a). We assumed as has always been done that conformational equilibrium is not significantly affected by the alignment media.

The efficacy of the RDCs NMR technique is demonstrated for establishing the relationship between two distant chiral centers C2 and C2' of tricholomamide A separated by 5 rotatable covalent bonds. In the RDC analysis, extraction of RDCs for C9, C2′ and C4' carbons was not possible. $^1D_{CH}$ RDCs and $^1J_{CH}$ couplings of tricholomamide A are shown in Table 20. The ^{13}C-^1H RDCs of tricholomamide A buried under the gel signal were back computed after the SVD fitting.

Eight RDCs were extracted and accurately measured on tricholomamide A, with a range of 7.2 Hz (*Table 20*). Correct stereochemistry of tricholomamide A (2S6S2′S) showed the lowest Q factor when RDCs experimental values are fitted to the diasteromeric structures. RDCs show a good fit, with a Q factor of 0.277 for the correct ensemble of structures, the other proposed configuration (2R6R2′S) with a Q factor 0.431. (*Figure 96*, panel a and c). Discrimination was checked by running a Monte Carlo Bootstrapping analysis shown in *Figure 96*, panel b

Good configuration discrimination was achieved using RDCs combined with Poly-Degmema gel for tricholomamide A.

Table 20. Tricholomamide A ^{13}C and ^{1}H chemical shift, scalar coupling constant [1]J_{CH}, total splitting [1]$T_{CH} =$ [1]$J_{CH} +$ [1]D_{CH} and experimental (exp) and calculated (calc) [1]D_{CH} values with their corresponding experimental error.

# C	δ^{13}C (ppm)	δ[1]H (ppm)	[1]T_{CH} (Hz)	[1]J_{CH} (Hz)	Exp D_{CH} (Hz)	Calc D_{CH} (Hz)	Error (Hz)
6	76.8	5.16	143.25	146.51	-3.25	-3.30	0.49
2	44.5	5.10	142.53	145.79	-3.26	-3.36	0.60
2´	53.8	3.54	-	144.14	-	-2.03	-
9	33.5	a: 2.78 b: 2.64	-	125.32	-	-0.91	-
4	29.2	a: 2.63 b: 2.30	131.7	128.08	3.62	3.09	0.27
4´	30.9	a: 2.39 b: 2.35	-	131.21	-	-3.90	-
5	31.6	a: 2.29 b: 1.64	128.02	130.69	-2.68	-2.16	0.62
3´	26.0	2.04	130.41	130.88	-0.47	0.96	0.22
1	17.0	1.31	129.77	128.54	1.22	0.55	0.26
10	6.0	1.06	128.01	127.38	0.63	0.63	0.16

[a] Residual dipolar coupling for Methylene group are reported as the average of the coupling of CHa and CHb. (-) Either not present or not measurable (overlapping with polymer signal). [b] The error associated with the measurement of coupling splitting T was calculated using

1.3.4.2.6.3 Establishing the relative orientation of H5a and H5b by chemical shift tensor calculation

The relative orientation of C5 methylene protons of tricholomamide A was unequivocally assigned using chemical shift tensor calculation at DFT level (Table 21) which, however, is not possible with the conventional NMR structural parameters such as NOEs and *J*-couplings; following a methodologies well described elsewhere.[140] Chemical shift tensor was calculated by using MPW1PW91/6-311G+(2d,p) basis set/functional combination[110] and referenced to tetramethylsilane. Quality of the assignment was estimated based on correlation coefficient (R^2), mean absolute error (MAE) and root mean square error between theoretical and experimental NMR chemical shifts [141]. Distinguishing was entirely done based on ^{1}H chemical shift calculation by taking into account the Boltzmann distribution of conformers (Figure *97*), the combined R^2 (0.864), MAE (0.433) RMSDs (0.658) between experimental and calculated ^{1}H NMR shifts were able to determine the correct assignment of C5's prochiral protons in tricholomamide A (*Figure 95*)

In summary, the structure and absolute configuration of a new natural product with a flexible side chain attached to a partially rigid five member ring were unambiguously determined by using a combination of isotropic (NOEs and *J*-couplings)/anisotropic (^{13}C-^{1}H RDCs) NMR analysis and DFT calculation of ECD. Therefore, the absolute configuration of tricholomamide A was proposed as (2S,6S,2'S) (Figure 98, panel a).

Table 21 Correlation coefficients (R^2)), mean absolute error (MAE) and root mean square error (RMSE) between the estimated proton chemical shift for both possible combinations of C5's prochiral protons in tricholomamide A

Configurations	C5		R^2	MAE	RMSE
	δ ^{1}H (1.66 ppm)	δ ^{1}H (2.99 ppm)			
Hα,Hβ-4S6S2'S	Hα	Hβ	0.833	0.505	0.711
Hβ,Hα-4S6S2'S	Hβ	Hα	0.864	0.433	0.658
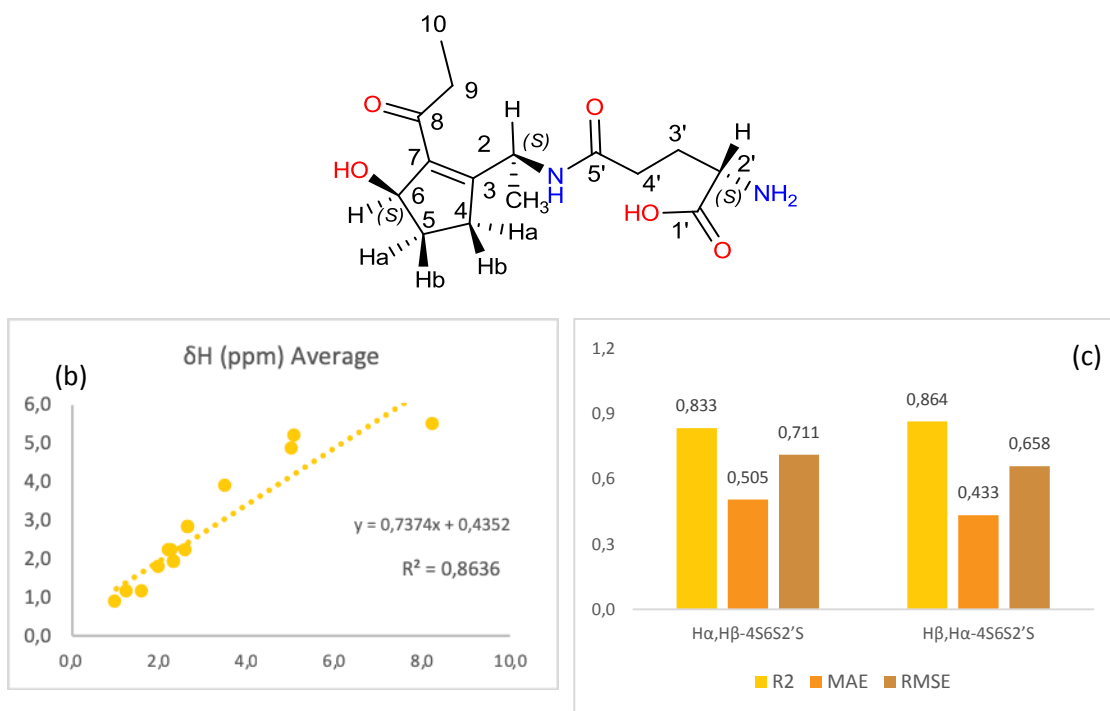
Figure 95. Absolute configuration of tricholomamide A and assignment of the diastereotopics protons of C5 by ^{13}C-^{1}H RDCs chemical shift calculation at DFT level (a) correlation curve for configuration Hβ,Hα-4S6S2´S, showing the highest R^2 (0.8636). Bar plot of the indicators used in the assignment of prochiral protons attached to C5 (c)

(a)

(b)

(c)
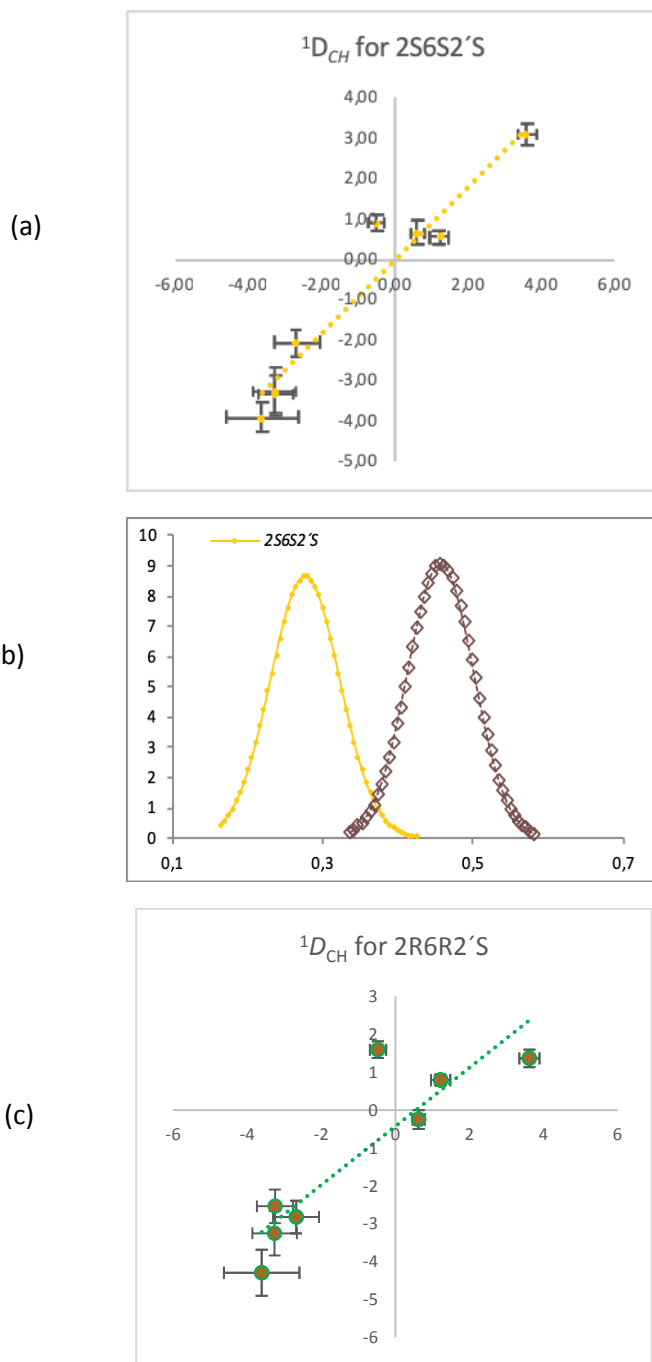
Figure 96. Error analysis over the back calculated $^1D_{CH}$ is calculated by the Monte Carlo Bootstrapping module in MSpin software: size population was 256 and 1TCH error estimated. RDCs fitting for the expected configuration of tricholomamide A (2S6S2´S), including its experimental error (panel a), Bootstrapping analysis for both feasible configurations (panel b) showing that RDCs analysis yields a good level of discrimination between for possible configurations and RDCs fitting for the other expected configuration of tricholomamide A (2R6R2´S), including its experimental error (panel c). it is worth to mention that tricholomamide A -2S6S2´S not only yields the lowest Q (0.277) but also the fitting with the best linearity, 0.92 vs 0.72
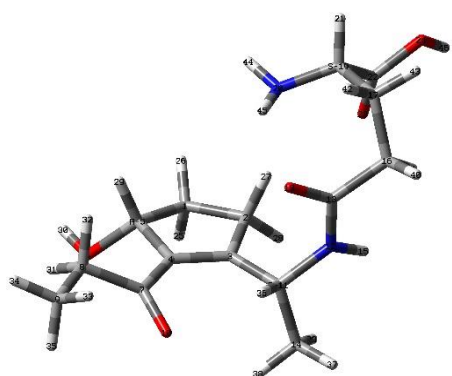
5.05 % (-1071.76272236 Eh)   5.66 % (-1071.76283047 Eh)
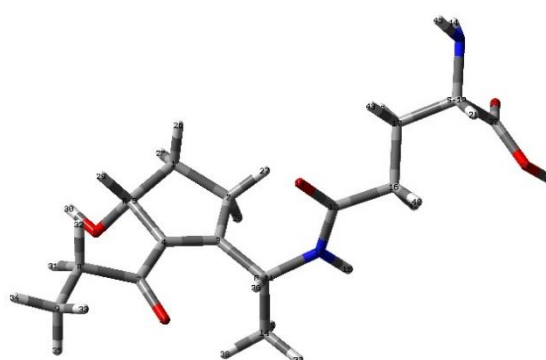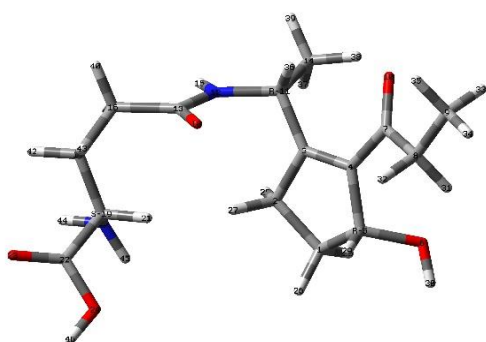
31.20 % (-1071.76444050 Eh)   22.9 % (-1071.76414863 Eh)
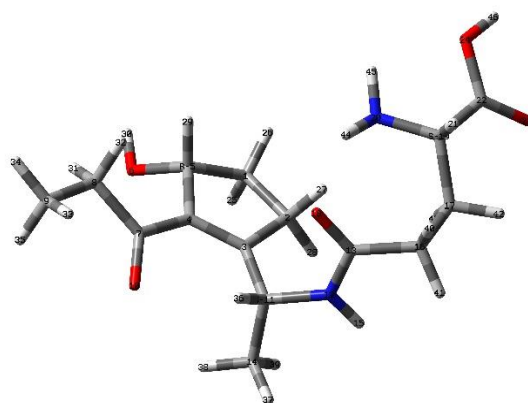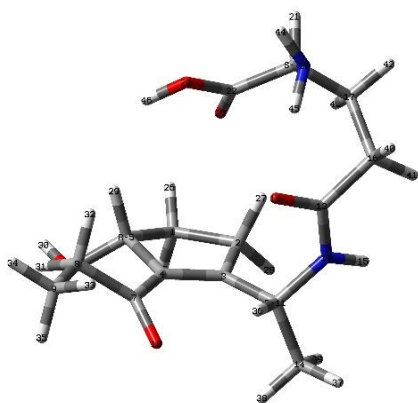
35.19 % (-1071.76455416 Eh)

Figure 97. Energy and Boltzmann averaged population of the conformers of tricholomamide A – (2R6R2'S)*. Energy was carry on in Gaussian V 9.0 at DFT level using the functional/ basis set combination MPW1PW91/6-311+G(2d,p)

Δv_Q=4.4 Hz
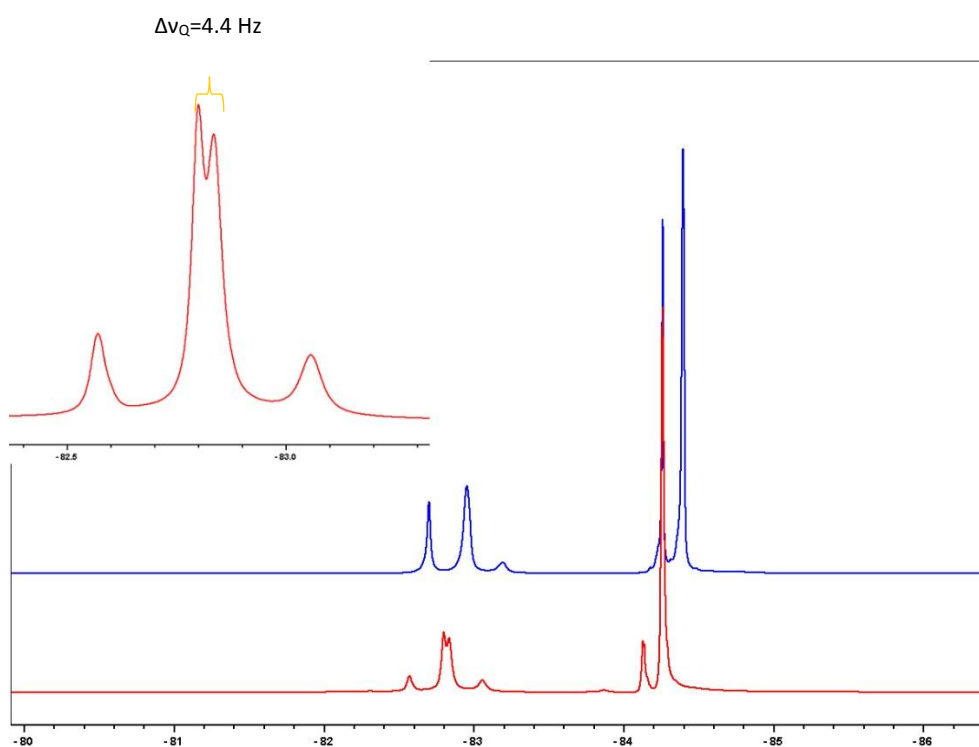
Figure 98. ^{2}H spectrum of fully relaxed (blue line) and compressed (red line) poly-DEGMEMA gel (75/0.3) used in tricholomamide A study, compressed in 3 mm compression device prototype
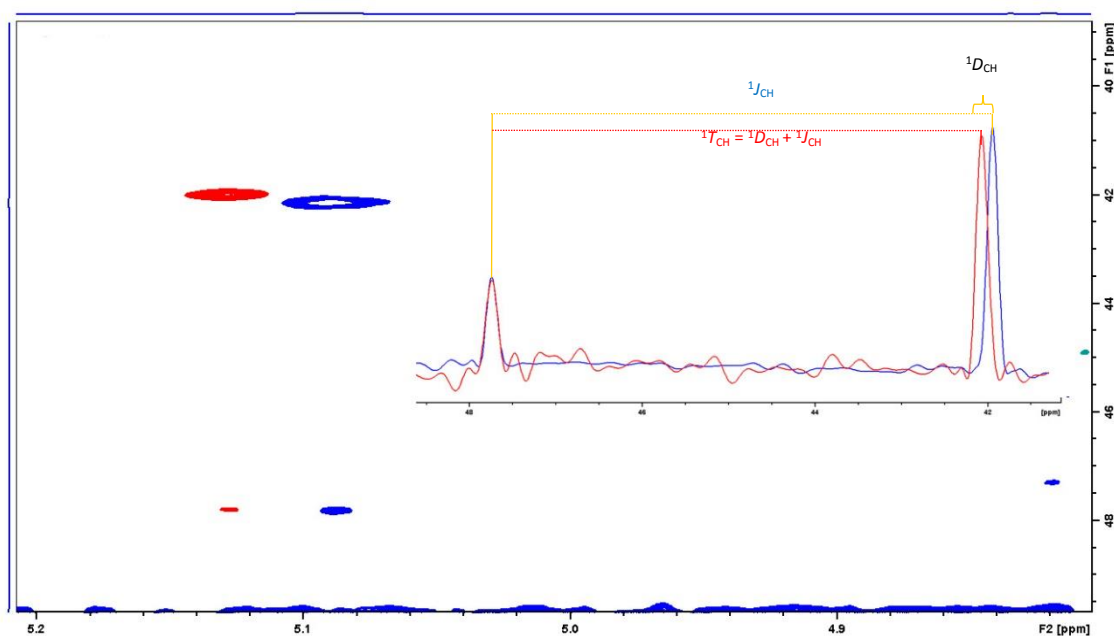
Figure 99. Extraction of CH coupling ($^1T_{HC}$ and $^1J_{CH}$) from experimental data collected with J-scaled IRD HSQC (K = 8). Expanded region of C2-H2 Cross-peak with isotropic spectrum shown in blue and anisotropic spectrum in blue. Low viscosity of methanol combined with the small amount of gel mass (22 mg) provides sharp lines in anisotropic conditions. Experimental error of $^1T_{CH}$ was estimated in 0.60 Hz by the methodology described by Kontaxis et al.,

1.3.5 Development of semi micro stretching for measuring anisotropic parameters (RDCs and RCSAs)

1.3.5.1 Introduction

Development of new alignment media, improvement of existing NMR pulse sequences and applications of non-uniform sampling techniques, and improvement in alignment devices are still active research topics with many drawbacks and challenges to be overcome. We show the robust extraction of residual dipolar coupling (RDC) of two rigid molecules: progesterone and strychnine at micro gram scale (i.e. 800 μg and 700 μg , respectively) using Poly-DEGMEMA and PMMA by using micro-stretching device. The use of the 3 mm Hilgenberg stretching devices demands some refinement in currently existing recipes, which is also discussed in herein. Stretching device introduced herein are the result of a cooperation agreement among our research groups QUIMOLMAT-PRONAMAR (Coruña University-Spain), Max Planck Institute for Biophysical Chemistry (Göttingen-Germany), Gauhati University (Guwahati-India) and the German glass company Hilgenberg (Malsfeld-Germany). Introduction of the stretching device in the semi micro scale opens up the possibilities for measuring another anisotropic parameters such as ^{13}C and ^{1}H RCSA when the restricted amount of simple is available.

1.3.5.2 Measurements at low sample concentration

Background polymer signal is one of the main reasons for missing signal during anisotropic measurements. Moreover, recently discovered natural products are available only in scare amounts [54,142] Four ways can be point out to mitigate the possibilities of buried analyte signal under the alignment media background: using sample amount in milligram scales [143], employing tailored HSQC pulse sequences as clip/clap experiment [112] or clip/clap broadband proton-decoupled [144], silencing the background gel signal by deuteration [66,70] and reducing the alignment media's signal to the minimum by using a 1.7 mm diameter compression device [145]

As a first approach, we tested the influence of the polymer mass in signal sensitivity using a 5 mm New Era´s compression device and our in-house built 3 mm compression device with PMMA gel sticks (70/0.25) swelled in CD_3Cl. The gel mass used was 45 and 22 mg respectively. Figure 100 displays 13C-$\{^1H\}$ spectrum of strychnine (1 mg) in a fully relaxed gel (800 scans in a 800 MHz Bruker spectrometer equipped with a cryo probe). The panels of the figure displays data extraction; for panel C4, isotropic and anisotropic contribution can be extracted from both devices. For panel C2, as was described elsewhere, isotropic an anisotropic contribution collapses into one signal for some carbons. For panel C23, signals look sharper and well defined in the 3 mm semi-micro compression device (SMCD), meanwhile they look broad in the New Era compression device device. It is worth to mention that it hinders the extraction of data and sometimes leads to miss undertaking and finally the most dramatic is panel C15, where the

signal is completely missing in New Era compression device device. In summation, broad and missing signals can easily either reduces the discriminate capability or, even worse, guide to wrong conclusions.
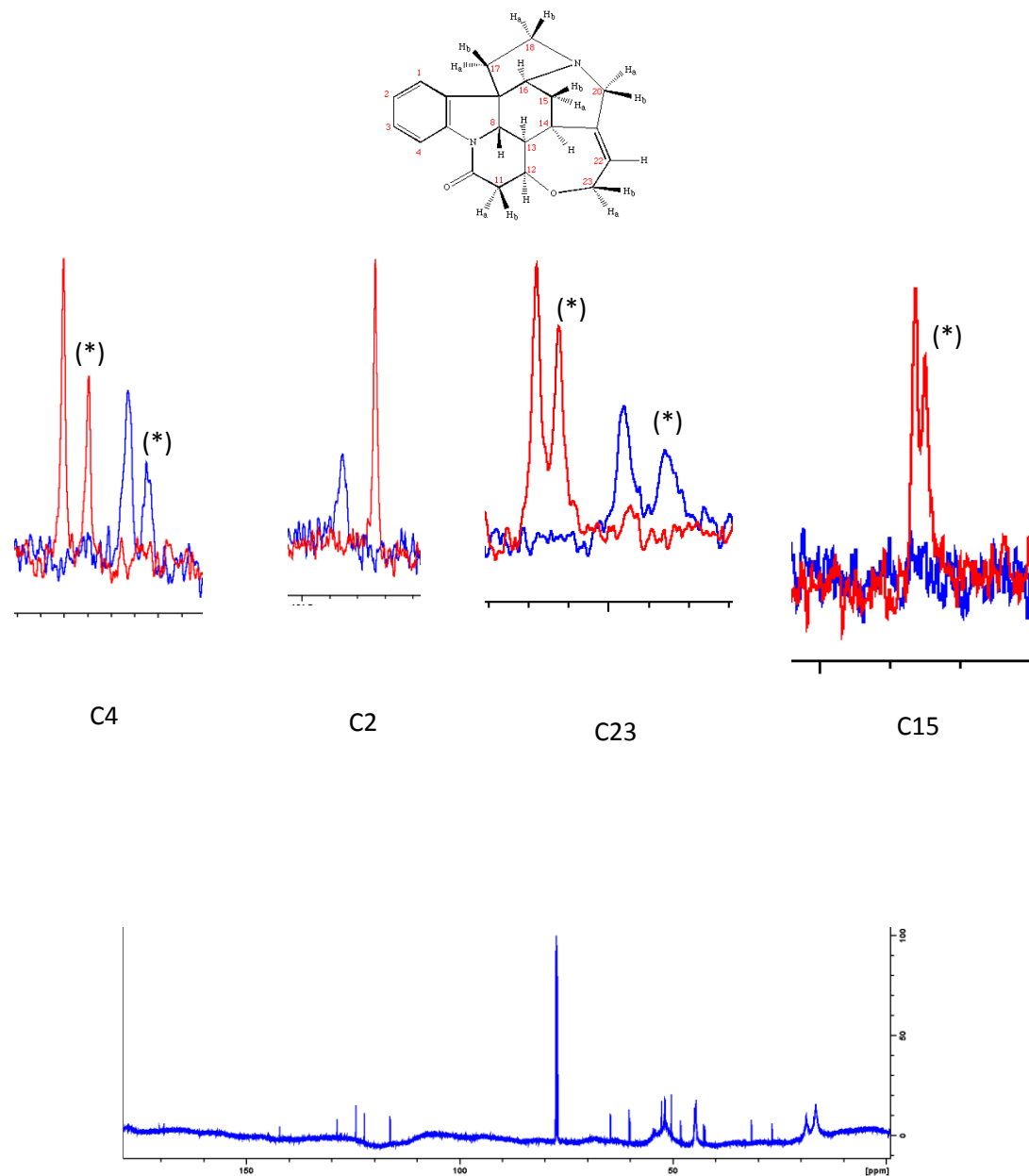
Figure 100. 200 MHz 1D ^{13}C-{^{1}H} spectrum of strychnine (1 mg) dissolved in a relaxed PMMA/CDCl$_3$ gel displayed the individual isotropic (*) and anisotropic contributions. They were measured in 5 mm New Era´s compression device (Blue line) and measured in a 3 mm in house compression device (red line)

1.3.5.3 Hilgenberg 3 mm Stretching device description:

The main goal of developing semi-micro stretching device (SMSD) is to measure RDCs and RCSAs at micro gram scale in combination with the deuterated PMMA gels introduced by our research group this year only, when other devices suffer from few disadvantages. Device was

designed at the Max Planck Institute for Biophysical Chemistry (Göttingen) and was manufactured by the German glass company Hilgenberg. The device, as the one described by Liu et al. [16], consists of an two side open NMR tube, with an outsider diameter of 3 mm. The tube provides two sections with different inner diameters for introducing different alignment conditions necessary for RCSA measurement. The gel stick is initially swollen in a 5 mL Eppendorf, and was delivered into the larger diameter section (2.2 mm). At this point, gel may not get stretched or slightly stretched and provided minimum alignement condition and spectra were collected. Afterwards, the swollen gel is moved through the device and pushed into the narrower section of the tube and thus maximum alignment condition is obtained .The device is now available only with 3 different narrowed section diameters and are compatible with both 5 mm and 3 mm cryoprobes. This device is provided by the company either with Teflon ® or Rubber stoppers, which are compatible with CH_3Cl, MeOH and DMSO. So far our research group have developed formulation for PMMA, PMMA-D_8 and Poly-DEGMEMA gels for these devices for CH_3Cl and MeOH soluble samples. By using SMSD and PMMA-D_8, , it was possible to accurately measure [1]H-RCSAs and subsequently determine relative configuration of Briarane 3, a new Diterpene isolated from *Briareum asbestinum*. Nevertheless, up to now $^1D_{CH}$ has not been reported at micro gram levels using SMSD. Herein, we test again the capabilities of the new device and report the discrimination among all the possible diastereoisomers of two well known small molecules, viz., progesterone (800 µg) and strychnine (550 µg) by using RDCs

Gel stick is delivered inside the larger diameter section (2.2 mm) by using a reduced and modified version of the New Era´s device, and, the main difference is that the chamber and the plunger are made of Teflon and neither metallic parts nor o-ring are used. During the delivery of gel, there is a funnel that guides the gel and slightly extrudes from the chamber to the 2.2 mm tube section. Generally gel is tight enough to be held by the device and does not give any deuterium splitting. Sometimes, few drops of deuterated solvent are added from the other end of the tube to help the delivery and stretching process.
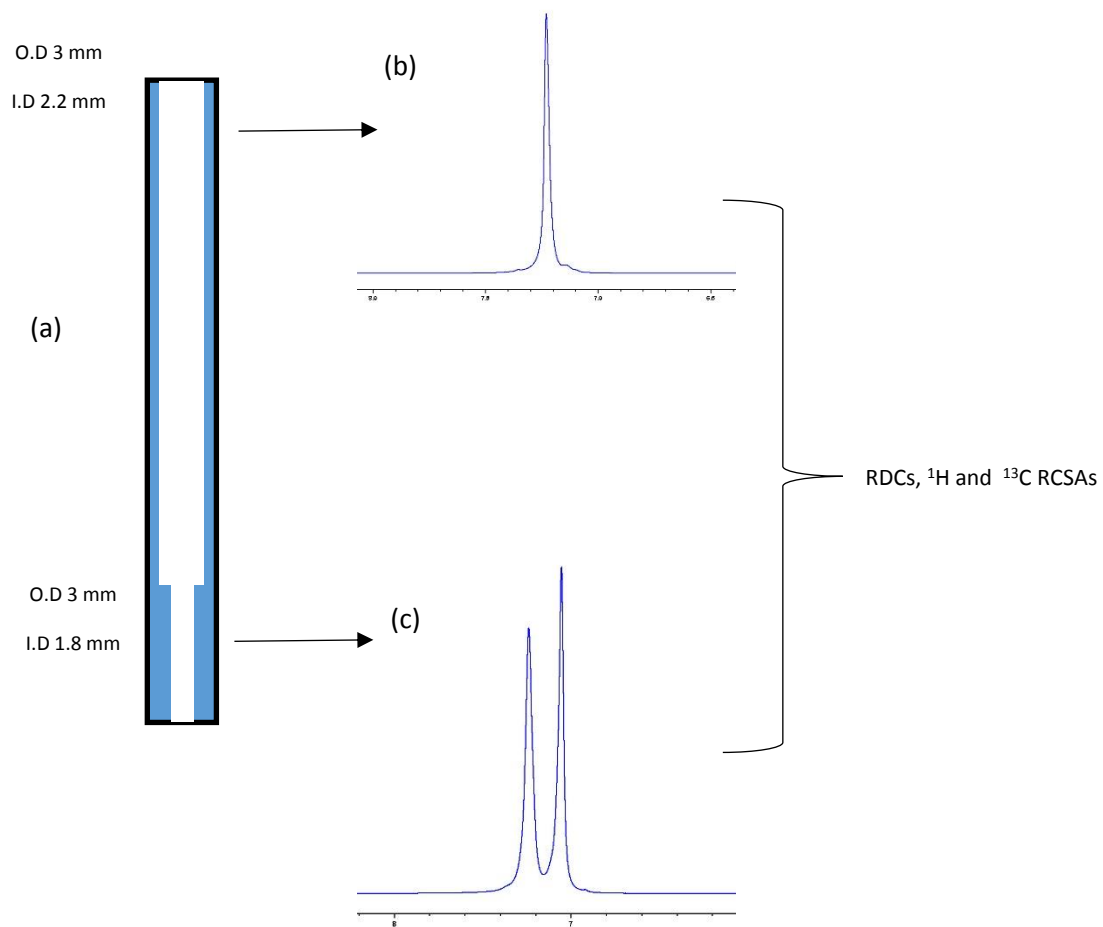
Figure 101. Workflow chart to obtain anisotropic parameters (RCSA and RDC) using the SMSD. Representation of the used SMSD used in this study (a). ^{2}H spectra of PMMA (70/0.05)/CDCl$_3$ under minimum (b) and maximum(c) alignment conditions.
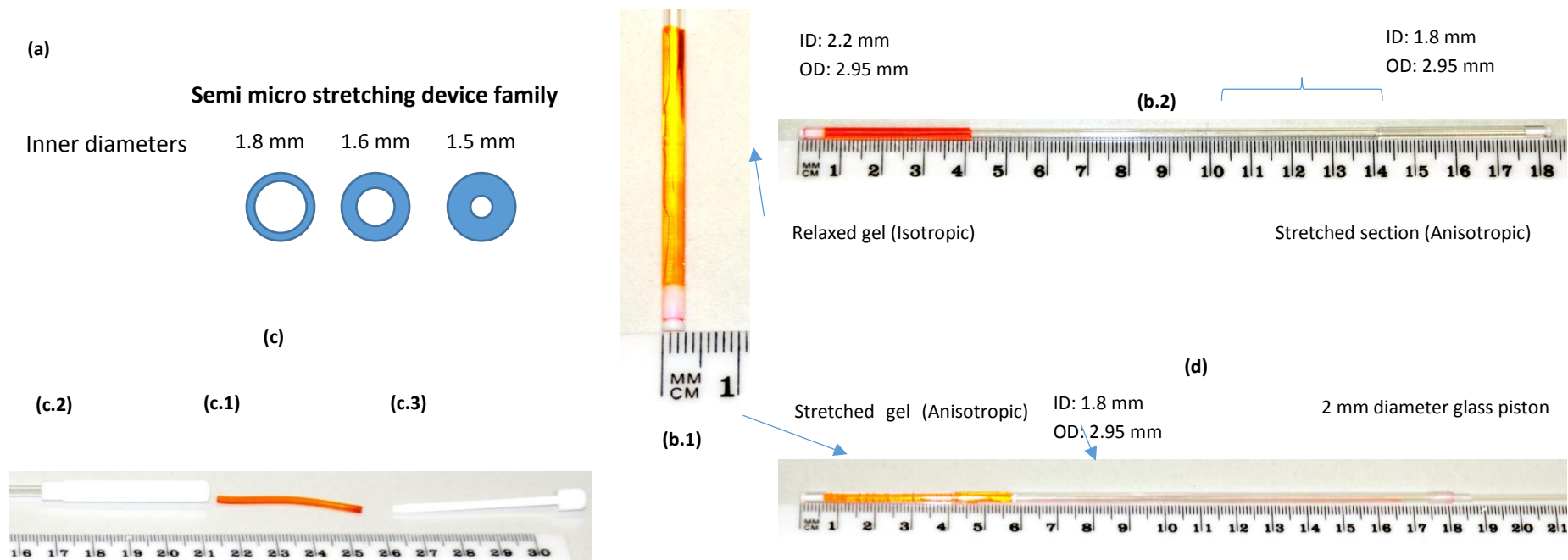
Figure 102. Hilgenberg´s Semi micro stretching device. Family of device has three different inner diameters from 1.5 until 1.8 mm (a), devices are basically an smaller version of those manufactured by New Era; a highly resistant boro silicate 3 mm (b.1) glass NMR tubes provided with to open sides and two inner diameters (b.2) Sample solution is swallowed in the gel stick (c.1), in a procedure that takes 24 h, and send inside the SMSD using a dedicated delivery device comprising a chamber (c.2) a piston (c.3) When the sample is insede the tube the analysis is carry on as described before in literature, the aligment medium is stretched by pushing if from the wide region of the device (2..2 mm) into the narrow section (1.8 mm) with a solid glass 2 mm piston. Piston is keeped in its final position by wrping with Teflon® tape (d). Gel used here is a PMMA-H8 70/0.04 swalloed in CDCl3 with a natural pigment

1.3.5.4 Measuring of RDC in 3 mm Hilgenberg´s Semi Micro Stretching Device: The Case of Progesterone

Poly-DEGMEMA gel was prepared using previously described procedures. [60] For their synthesis, Hilgenberg's 1.7 mm NMR tubes (Internal diameter 1.6 mm) were pre-silanized using Sigmacote® before carrying out the polymerization reactions. Subsequently, the tubes were emptied and dried in an oven (40 ºC/ 24h). Polymerization inhibitor potentially present in the monomer (DEGMEMA) and the cross-linker EGDMA (ethylene glycol dimethacrylate) were removed by both over a basic alumina column. For polymerization, the initiator employed was 2,2'-azobis(4-methoxy-2,4-dimethylvaleronitrile) (V-70). Three stock solutions were prepared; *Solution A*: 1.4 mL of DEGMEMA monomer and 0.6 mL of MeOH. *Solution B*: 200 µL EGMDA and 1240 µL DEGMEMA. *Solution C*: 14 mg of V70 in 1 mL of MeOH. In a falcon tube were mixed: 2 mL of stock *solution A*, 20 uL of solution B and 32 µL of *solution C*. After thorough mixing of the above constituents the solution was transferred to the silanized NMR tubes, which were subsequently capped and kept in a water bath at 50 °C for 6 hrs. After polymerization, tubes were opened, and the gel was allowed to dry. The polymer gels were carefully removed from the NMR tubes and washed three times in methanol (24 hrs each) in order to remove any residual monomer. Poly-DEGMEMA gels were dried on a glass surface and they are sticky and flexible, and therefore have to be handled with utmost care. Gels change their proportions significantly during the drying/swelling processes. For one bond CH RDC ($^1D_{CH}$) measurements, 2.4 cm gel sticks were used and swollen in CD_3OD inside a 5 mL Eppendorf for at least 24 hours. The gel used in the present study shows a ^2H quadrupolar splitting of 3.51 Hz, at stretching in a Hilgenberg 2.2/1.6 mm. Different amount of alignment are found changing either cross liker concentration or the inner diameter in the narrower section of the device (See SI). All the chemicals were purchased from Sigma Aldrich and V-70 was obtained from Wako Chemicals.

Progesterone, is an endogenous steroid and a hormone involved in ovulation, mammary gland development, establishment and maintenance of pregnancy in vertebrates and humans [146], was used to test the alignment capabilities of Hilgenberg´s 3 mm stretching device (2.2/1.6 mm) to afford high quality anisotropic data. Different monomer/cross linker concertation were to prepare the Poly-DEGMEMA stretchable Gel, yet the 70/0.2 is most suitable one of the 2.2/1.6 mm stretching device. This molecule has six stereocenters with the well-established configuration 8*S*,9*S*,10*R*,13*S*,14*S*,17*S* (Figure 103) leading 32 possible diastereomer. For clarity, the configuration of the stereocenters will be shown including the numbers and following the same order for every diastereomer.[147]
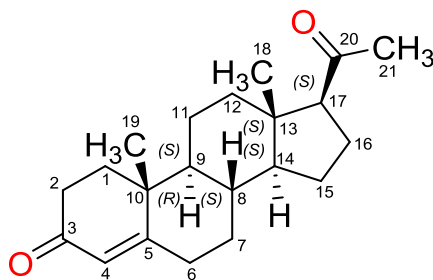
Figure 103. Chemical structure of progesterone

Progesterone (800 µg) was dissolved in CD$_3$OD (200 µl) and placed in a 5 mL Eppendorf with a Poly-DEGMEMA stick for 28 h and delivered inside the SMSD, using the device shown in Figure 102 c.1 to c.3. The solvent deuterium signals show a ΔH$_Q$ value of 3.5 Hz for the stretchable gel in the 3 mm stretching device 2.2/1.6 mm. Isotropic and anisotropic data was collected as usual, by moving the gel from the wide tube section (2.2 mm) to the narrow one (1.6 mm) by the assistance of a 2.0 mm glass plunger provided by Hilgenberg. J-scaled BRID HSQC spectra (hsqcetgpipjcsp.2) with a scaling factor of 8 were acquired under both isotropic and anisotropic conditions. [21]

1.3.5.4.1 Results and Discussion

Poly-DEGMEMA stretchable gel described here is inexpensive and easy to prepare handle. There is no requirement of either laboratory arrangement nor inner gas current for their preparation unlike Poly(acrylonitrile) (PAN) [148] or PMMA gels [43] Polymer background, can obscured some sample signals, mainly at low sample concentrations, this can be overcome by reducing the weight of gel as in the stretching device introduced hereby. Supporting information shows those section that could be obscured by the polymer signal. Gel mechanical properties are compatible with different stretching devices, yet is useless after one use. Sample can be recovered with a methanol extraction, as in other gels [149]

Before the collection of anisotropic data in small molecules, one should check not only solvent compatibility but also the signal coming from the polymer. DEGMEMA monomer deuteration is rather expensive; around 9000 €/gram of monomer according to Polymer Source (https://www.polymersource.com/). Therefore we recommend overlapping of J-scaled BRID HSQC spectra of the sample and the gel before measuring anisotropic data collection, in order to evaluate any possible signal missing. Signals between 3.1; 58.0 and 4.5; 72.0 ppm (^{1}H δ;^{13}C δ) are expected to be buried under polymer signal. Moreover, while low degree of alignment results in small $^1D_{CH}$ values (maximum and minimum value of 4.54 and -1.27 Hz respectably), and allows the extractions of 15 RDCs with great accuracy due to the narrow spectral lines. Here is, we have overcome the proton-proton dipolar broadening signal under stretching conditions using the F1 ^{1}H-coupled version of HSQC experiment for RDCs measurements Figure *104*
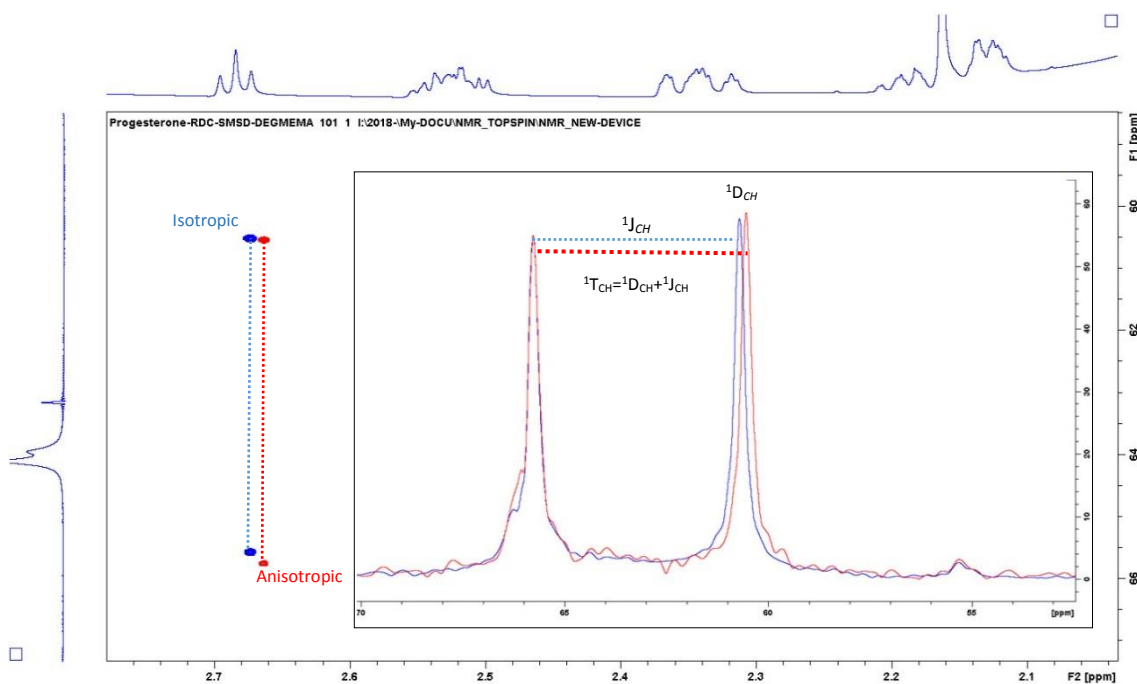
Figure 104. Extraction of CH coupling ($^1T_{CH}$ and $^1D_{CH}$) from the experimental (800 µg of progesterone) data collected with Hilgenberg´s 3 mm stretching device measured in a 800 MHz Bruker Spectrometer. Expanded region of C17-H17 isotropic spectrum is shown in blue and anisotropic is spectrum is shown in red

One-bond proton-carbon RDCs ($^1D_{CH}$) are reported as the difference between the signals splitting observed under anisotropic and isotropic condition ($^1T_{CH} = {}^1J_{CH} + {}^1D_{CH}$) [97] (Table 22). Progesterone is a rather rigid molecule, due the low level of flexibility present in its structure; therefore non-conformational equilibrium is expected, except the possible rotation associated with Me21. RDC fitting data, of all 32 possible diastereomers, alignment tensor determination, and calculation of Cornilescu's quality factor (Q) were carried out in MSpin software [9,19]

Table 22. Progesterone ^{13}C and ^{1}H NMR chemical shift, scalar coupling constants $^{1}J_{CH}$, total splitting $^{1}T_{CH}=^{1}J_{CH}+^{1}D_{CH}$, and experimental (Exp) and calculated (Calc) ^{1}DCH values

#C	δ_C (ppm)	δ_H (ppm)	$^{1}T_{CH}$ (Hz)	$^{1}J_{CH}$ (Hz)	Exp D_{CH} (Hz)	Exp Calc (Hz))
1	36.97	a: 2.0886 b: 1.7135	130.06	128.34	1.72	1.48
2	34.03	a: 2.3249 b: 2.5056	129.73	127.72	2.01	1.81
3	202.46	-	-	-	-	-
4	124.34	5.7174	159.98	159.28	-0.70	-0.66
5	175.12	-	-	-	-	-
6	33.36	a: 1.9080 b: 1.0891	129.84	127.62	2.23	1.81
7	34.85	a: 2.2872 b: 2.4790	130.46	128.36	2.10	2.17
8	36.92	1.6455	128.84	124.30	4.54	4.24
9	55.31	1.0321	127.79	124.02	3.77	4.24
10	39.88	-	-	-	-	-
11	23.94	a: 2.1417 b: 1.6942	NR	NR	NR	2.35
12	40.12	a: 2.0939 b: 1.5018	128.59	126.81	1.78	1.73
13	45.22	-	-	-	-	-
14	57.36	1.2385	128.89	124.74	4.15	4.24
15	25.47	a: 1.7473 b: 1.2947	133.76	131.50	2.27	2.42
16	22.29	a: 1.5070 b: 1.6786	128.61	126.31	2.27	1.90
17	64.68	2.6481	131.43	127.17	4.26	4.20
18	13.81	0.6780	123.99	125.18	-1.18	-1.33
19	17.82	1.2385	125.62	126.89	-1.27	-1.19
20	212.33	-	-	-	-	-
21	31.72	2.1225	126.88	126.92	-0.04	-0.11

Residual dipolar coupling for CH2 groups are reported as the average of couplings of CHa and CHb (-) quaternary carbons (NR) not readable, buried on gel signal

The 32 possible structures were created in Gauss view V 5.0, geometries werr optimized at DFT level (6-31+g(d,p)) and saddle point confirmation was done with a frequency calculation at the same level of theory. A single structure was considered for each diastereoisomer due to the inherent molecule rigidity. Q factor of the correct structure is expressed in terms of the average of 2 structures with the same skeleton coordinates but with the expected rotation, of Me21. The single tensor approximation with fit populations was used during structure refinement. Chemical shift tensor (CSA) calculation was done in Gaussian Suite V 9.0 as well at B3LYP/6-311G++(2d,p) level. Quality of the fitting is quantified in the form of Cornilescu quality (Q) factor. By using $^{1}D_{CH}$ RDC, all the 31 wrong configuration were certainty eliminated. Structure of progesterone, here in used, matches with X-ray structure reported, a refinement over the structural bases on the rotation of Me21, resulting in a Q factor of 0.088 for the *8S9S10R13S14S17S,* next two best configuration are 8S9S10R13R14S17R and 8S9R10S13S14S17S (Q=0.118). Discrimination is supported by a Bootstrapping analysis. Results provide a good agreement between proposed structure of progesterone and RDCs measures, *vide infra.* Goals of this short study were shown the compatibility of Poly-DEGMEMA gel (70/0.2) with a stretching device and the utilities of the semi micro stretching device (2.2/1.6 mm) , introduced herein as first time as a valid tool for extracting anisotropic parameters at microgram scale. In summation, 3 mm Hilgenberg stretching devices up the possibility to afford anisotropic

measurements (RDCs,[1]H & [13]C RCSA) at micro gram scale which reduces in the polymer background signal. It is noteworthy that sample concentration inside the gel does not changes during the experiment and therefore no isotropic shift correction is required
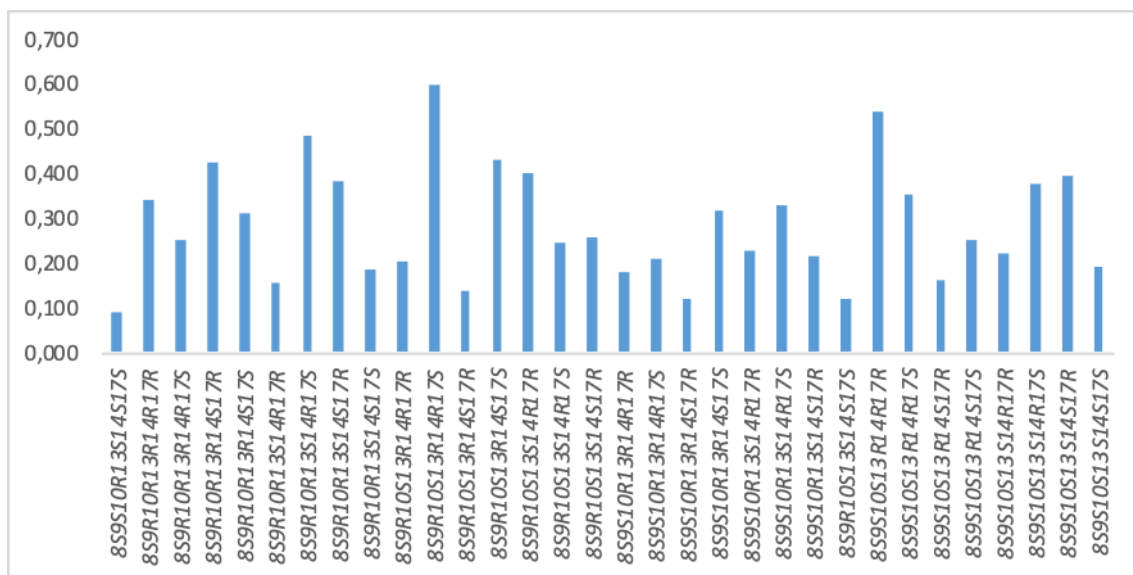
Figure 105. The Q factors bar plot of progesterone and its possible diastereomers, for the two closest configurations 8S9S10R13S14S17S and 8S9S10R13R14S17R are 0.088 and 0.118, respectively.

1.3.5.4.2 Bootstrapping analysis:

Q-factor difference between the correct configuration of progesterone (*8S,9S,10R,13S,14S,17S*) and two of the feasible diastereoisomers (*8S,9S,10R,13R,14S,17R* and *8S,9R,10S,13S,14S,17S*) is only 0.03. Impact of experimental error in the RDC fitting was evaluated using a Monte Carlo bootstrapping[113] procedure, with the module present in MSpin. This computer intensive resampling method have been widely applicable and allows the treatment of more realistic models when the amount of sample point is scare. Basic idea behind of the method is that, in absence of any other information about the distribution, the observed sample contains all the available information regarding the underlying distribution, and therefore resampling the data is the best guide to what can be expected from resampling from the distribution. For bootstrapping, 2000 simulated data sets were generated by sampling a Gaussian distribution centered on each experimental RDCs with a given standard deviation of 0.08 Hz, around of the 6% of the minimum RDC value measured, SVD fitting was performed for each set and back predicted RDC values and Q's were then averaged over the 2000 different computations and the corresponding standard deviations were computed. The comparison of the Gaussian curves for progesterone and the suspicious Q factors are depicted in *Figure 106*. The average Q factor of progesterone is 0.092±0.007 and 0.121±0.006 for (*8S,9S,10R,13R,14S,17R)* and 0.121±0.006 for (*8S,9R,10S,13S,14S,17S)*, respectively. An inspection of the curves allows to see a clear and unequivocal discrimination between the possible configurations.
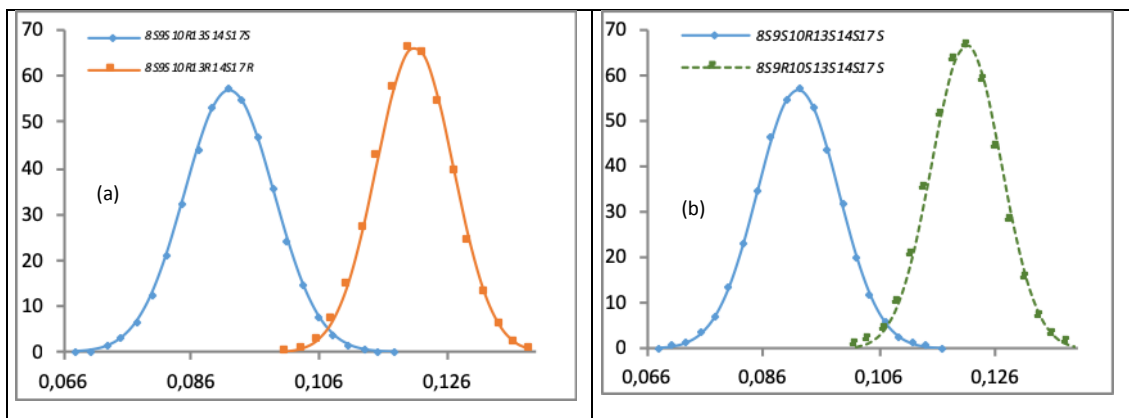
Figure 106. Gaussian curves of Monte Carlo bootstrapping of progesterone 8S9S10R13S14S17S (blue curve) and two suspicious diastereoisomers 8S9S10R13R14S17R (panel a, orange) and 8S9R10S13S14S17S (panel b, green)

1.3.5.4.3 Progesterone structure refinement:

RDCs induced by anisotropic media are not only a powerful tool for determination of the configurations of small molecules but also refinement in its conformation [105]. It has even led to the development of software by which using RDCs and other experimental NMR restraints provide a solution to practical problems as Computer-Assisted 3D Structure Elucidation (CASE-3D) [150] and molecular dynamics with orientational constraints technique (MDOC) [151]

Progesterone has a rather rigid ring system. Several staged conformers were created by changing the dihedral angel (H17,C17,C20=O,CH$_3$(21)) and lead it move freely during geometry optimization at DFT level, afterward Cornilescu's Q factor was calculated independently for each of them. An analysis on the NOESY (*noesyph*) of progesterone shows strong correlations from Me21 to H7, Me18, and weak correlations to both H12a and H12b, nevertheless only H16b shows a NOESY correlation meanwhile H16a correlation is absent (Figure 107). Based on this evidence Figure 108 shows a proposed structure refinement for progesterone by using RDCs.
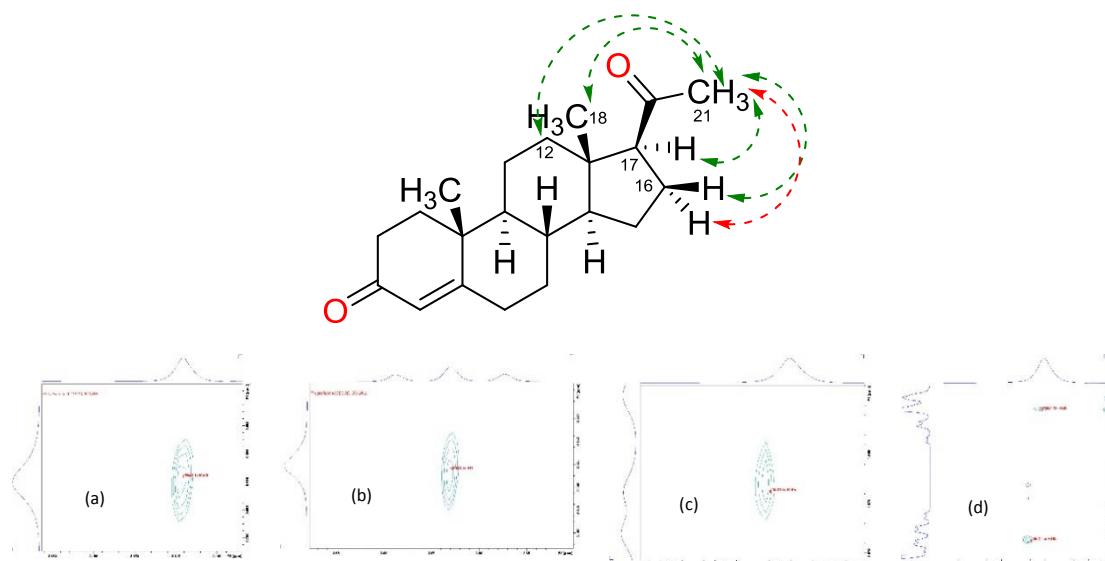
Figure 107. NOESY correlations observed in progesterone from Me21 are green marked, those missing are indicated in red. From left to right; Me21 to Me18 (a), Me21 to H17 (b), Me21 to H16b (c) and Me21 to H12a and H12b (d)
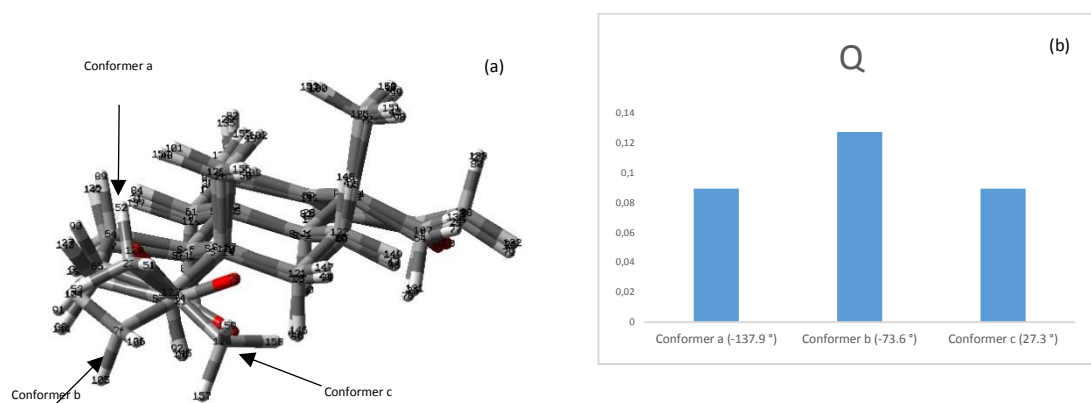
Figure 108. Progesterone structure can be refined based on residual dipolar couplings measured by using Hilgenberg 3 mm stretching device. Three different conformers of progesterone were find after allowing free rotation of Me21 (panel a) conformer a and b Q (0.089) (panel b). The existence of conformers a and c is supported by NOESY correlation, meanwhile conformer b is ruled out not only by its high Q but also by the absence of the expected H16a NOESY correlation

Application of ^{1}H RCSA at micrograms scale
assisted with deuterated gels: The case of briarane-3

Next, as a more challenging example, we used ^{1}H RCSA data for the configuration analysis of Briarane 3, a briarane diterpenoid isolated and purified from *Briareum asbestinum* collected in Yucatan Peninsula in Mexico. Although the planar structure is known for more than two decades using isotropic NMR data, its relative and absolute configuration for the 9 consecutive stereogenic centers has not been determined yet.

Use of NOE distance restraints fixed the relative configuration at C2, C3, C4, C5 and C16 as S, R, R, S and R, respectively and leaves the relative configurations at C1, C9, C10 and C14 undetermined. This provides a total of sixteen configuration and half of them are enantiomers. However, there is strong NOE correlation between the methyl group at C10 and C14 indicating that these bulky two methyl groups are syn position. The absence of NOE correlation between H1 and methyl group at C10 indicates that these proton are anti position. The NOE data also supports that H1 and methyl group at C14 are also at anti position. These data leaves the relative configurations configuration of C1 and C10 either RR or SS, which is the further corroborated by the presence of medium sized HMBC correlations between carbon of the methyl at C10 and H1; carbon of the methyl at C14 and H1. This has reduced the number to unknown relative configurations to only four (Figure 109). To determine these configurations, we measured 1H RCSA of Briarane 3 swollen in PMMA-d8 gel using micro stretching device with 2.2 and 1.8 mm inner diameters. The sample amount was only 35 μg and experimental RCSAs range from 1.8 to 3.2 Hz at a ^{1}H frequency of 800 MHz. The fitting of the 1H RCSA data to three possible configurations furnished a lower Q factor of 0.087 for 1S,2R,3R,4R,5S,9R,10S,14R,16R indicating it as the correct relative configurations since other configurations have Q factor of 0.137 or even higher (Figure 109). Since structural elucidation at micro gram scale is always a concern for natural products chemist, Figure 110 displays a 2D HMBC experiment of a 35 ug sample of Briarane 3 recorded at 800 MHz NMR spectrometer. In order to prove that capabilities of our groups allows such kind of analysis
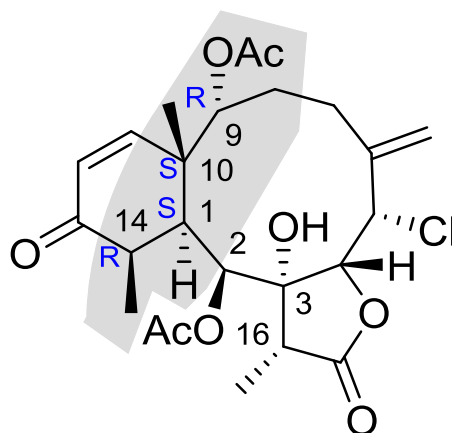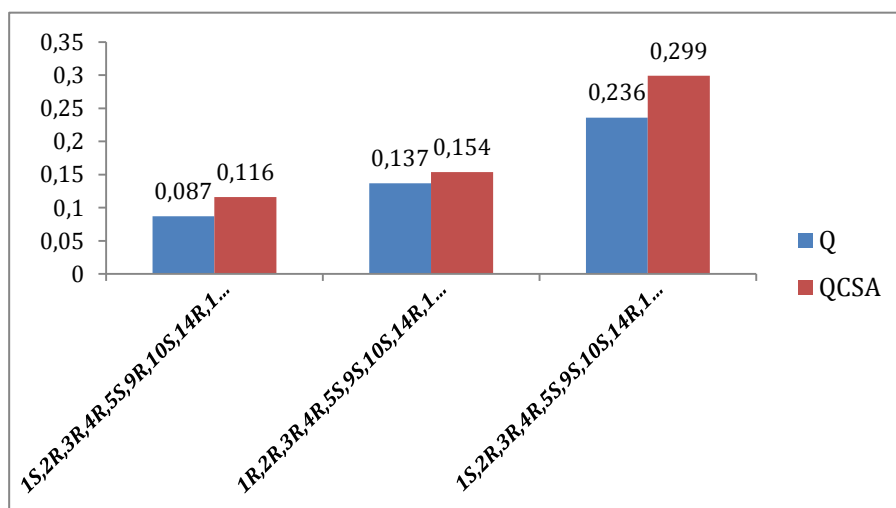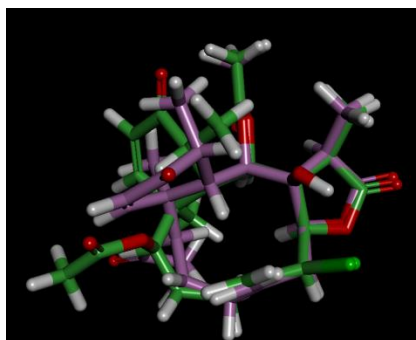
Figure 109. Underwater photo of *Briareum asbestinum* from the Briarane 3 was isolated (a). Structure of Briarane 3; the configuration of carbons in the shaded area remains undetermined by the isotropic NMR restraints. (b) Bar plot for the RCSA Q factors and the superposition of different conformers for the correct configuration is shown on the top of the bar plot (c)

Figure 110. HMBC spectrum of 35 ug sample of Briarane 3 recorded at 800 MHz NMR spectrometer in CDCl$_3$ solvent. Sample was analyzed in a 1.7 mm OD capillary tube

Chapter 2

Bioactive Marine Natural products: Isolation and detection assisted by Liquid Chromatography-High Resolution Mass Spectroscopy

2.1. Introduction

The potential of natural products as sources for new drugs is still largely unmapped. Only a small percentage of organisms has been rigorously investigated in the search of interesting compounds and only few of them were submitted to pharmacological screening. Moreover, when a particularly activity has not been tested in the organism, this have to be considered as 'uninvestigated' in relation to any other pharmacological activity. Microorganisms, plants or animals contain a huge amount of secondary metabolites. Therefore, any chemical investigation of one of them will reveal only a very narrow spectrum of its constituents.

Searching for novel secondary metabolites in natural sources is a laborious task that frequently involves interdisciplinary work from different fields such as botany, pharmacognosy, pharmacology, chemistry, toxicology, etc. Secondary metabolites are often minor constituents of complex mixtures and their identification is a challenging key step in natural products research. Several approaches are used: (a) bio-guided fractionation procedure of bioactive extracts which has the problem of isolating known bioactive compounds. In these cases, dereplication processes are needed,[152,153] (b) search for unique chemical constituents by NMR and LC/MS followed by their isolation and a broad evaluation in diverse biological assays, and (c) targeted approaches that are focused on the identification and quantification of known compounds based on LC-MS and MS/MS data.[154,155]

Workflow for detection of biomolecules from natural sources by LC-HRMS

Bioactivity-guided and targeted natural product study by LC/MS implies several steps shown in Figure 111.

Solvent extraction.[156] Basically, it progresses through as follows: the solvent penetrates into the solid matrix; the solute dissolves in the solvents; the solute is diffused out of the solid matrix; the extracted solutes are collected.

Bio-assay. Metabolite detection in the extract and fractions is achieved by a testing procedure for estimating the presence of a bioactive substance. For example, chrome azurol S (CAS) assay is used to evaluate the siderophore production in microorganism extracts.[157] However, the assays in some cases are not applicable to complex matrixes as they are not sufficiently sensitive and can suffer from matrix interferences.

Fractionating. The fractionation depends on the physical or chemical difference of the individual natural products. Column chromatography (CC), gel filtration (GF) and solid phase extraction (SPE)[158] are the most useful ones.

Metabolite presence confirmation by LC/HRMS. The Figure 111 displayed the workflow chart from a raw extract to a bioactive natural products detection that was applied to different natural extracts and a variety of bioactive natural products in this chapter. LC/HRMS technique was the main strategy for detection and quantification of the selected bioactive natural products.
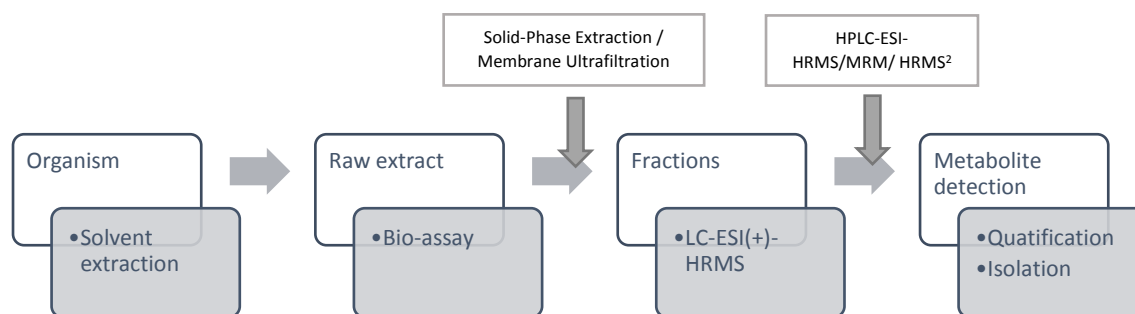
Figure 111. Procedure for detection or quantification of the active principles from natural sources by LC-HRMS techniques as strategic analytical screening tools during the natural product searching process.

In the following paragraphs, some special considerations and equipment are described

Sample purification

A previous sample preparation procedure is needed to carry out metabolite detection by LC/MS due to the complex matrix interferes with detection. Most of the sample preparation techniques include gel filtration, solid-phase extraction and ultrafiltration membrane. Gel filtration chromatography (GF), commonly referred to as size exclusion chromatography, is a method for the separation of molecules on the basis of their size and shape.[159,160] Separation is achieved using a porous matrix to which the molecules, for steric reasons, have different degrees of access (Figure 112 panel a). Therefore, compounds are eluted from the GF column in decreasing order of size. Sephadex ® LH-20, G-10 and G-25 are widely used in natural product isolation.[161] Solid-phase extraction (SPE) uses solid particles, chromatographic packing material, usually contained in a cartridge type device, capable of retaining the target analytes, washing away undesired components, and washing off /eluting the desired analytes with another solvents into a collection tube.[162] SPE sample fractionating consist in four steps (depicted on Figure 112 panel b): conditioning, loading sample, washing and eluting. The advantages of SPE can be summarized as: simplification of complex sample matrix along with compound purification, reduce ion suppression or enhancement in MS applications, capability to fractionate sample matrix to analyze compounds by class trace concentration (enrichment) of very low level compounds. The application of this technique in the siderophore detection in this study allowed us to speed up the process.[158,163,164]
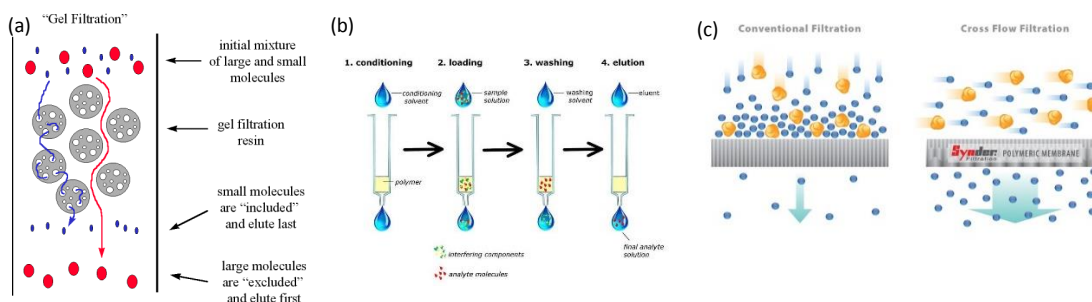
Figure 112. (a) Separation by Gel filtration (GF); (b) The four-step solid-phase extraction (SPE) procedure and (c) difference between conventional vs. tangential Flow Unlike conventional filtration where solids and solutes immediately accumulate on the membrane surface, tangential flow creates a sweeping (or shearing) force along the surface of the membrane to provide for longer filter life and less frequent cleaning cycles under normal operating conditions.[v]

Tangential ultrafiltration flow (UF), also referred as "cross flow filtration," is a size-based technique in which the sample is constantly recirculated across a permeable membrane, progressively concentrating components that do not pass the membrane pores. The main difference between filtration and cross flow filtration is shown in Figure 112 panel c. Most studies use polysulfone membranes with a nominal size cutoff from 5 to 20 nm and a molecular weight of 100–100,000 Da.[165] Different types of ultrafiltration membranes can be used to separate heavy metals, macromolecules, and suspended solids.[166]

HPLC equipment set up

Among the current available options for analyte separation using HPLC, the most common is reversed phase chromatography (RP). Reversed-phase high-performance liquid chromatography (RP-HPLC) involves the separation of molecules on the basis of hydrophobicity.[167] The stationary phase is composed of porous silica particles linked to alkyl chains (C4, C5, C8, C18), where C18 offers better performance.[168] The separation depends on the hydrophobic binding of the solute molecule from the mobile phase to the immobilized hydrophobic ligands attached to the stationary phase, i.e., the sorbent. The solute mixture is initially applied to the sorbent in the presence of aqueous buffers, and the solutes are eluted by the addition of organic solvent to the mobile phase. A typical mixture consists of two solvents, being MeCN/H_2O and MeCN/H_2O the most commonly used. Elution can proceed either by isocratic conditions, where the concentration of organic solvent is constant, or by gradient elution, where the amount of organic solvent is increased over a period of time. The solutes are,

---

[v] Figures were taken from http://www.mikeblaber.org reference[297] and http://synderfiltration.com respectably

therefore, eluted in order of increasing molecular hydrophobicity. Reversed-phase HPLC can be improved by the addition of mobile phase modifiers and buffers to control ionization of the sample molecules.

Mass analyzers

Mass analyzers play a crucial role in the metabolite detection. It is the component of the mass spectrometer where the ionized masses are separated on the basis of their charge to mass ratios (m/z) and outputs them to the detector where they are detected and later converted to a digital output. Different types of mass analyzers have been combined with HPLC for the analysis of natural products:[169] quadrupole (Q), ion trap (IT), time-of-flight (TOF), Fourier transformer (FT) and Orbitrap.[170,171] Each mass analyzer has its own special characteristics, specific applications and its own advantages and limitations. I will briefly describe the quadrupole (Q), Triple quadrupole and MS/MS techniques because they were used in the current study.

(a) Triple quadrupole and MS/MS

Triple quadrupole analyzers (QqQMS/MS) was selected for tetrodotoxin detection due to its high sensitivity and specificity.[172] QqQMS/MS is configured so that the ions of interest pass through a sequence of three quadrupole mass filters,[173,174] as is depicted in Figure 113, panel a. The first quadrupole (Q1) selects ions of interest that were generated in the ion source, based on its mass-to-charge ratio (m/z); these ions are called precursor (parent) ions. The second quadrupole (Q2) is typically used as a collision chamber to generate fragment or daughter ions for the precursor ions with the help of an inert gas. The advantage of argon over the nitrogen as the collision gas is because argon is heavier and promotes more robust fragmentation. The fragment ions with high ion intensity and specificity are, once again, selectively transmitted through a mass analyzer. The third quadrupole (Q3) is used to select and conduct specified fragment ions to the electron multiplier. The use of Q2 for ion fragmentation is optional and allows the user to collect simple MS data or MS/MS data depending upon specific needs. Triple quadrupole instruments are quite flexible and allow the user to monitor and collect: (1) simple MS ion data, (2) full-scan fragmentation data, (3) specific ion fragmentation data (Selected reaction monitoring (SRM) or Multiple reaction monitoring (MRM)), (4) neutral loss data, or (5) precursor ion data.[175] The major advantages of triple quadrupole analyzers are the relatively low cost and small size, robustness, wide dynamic area and ease of use and maintenance
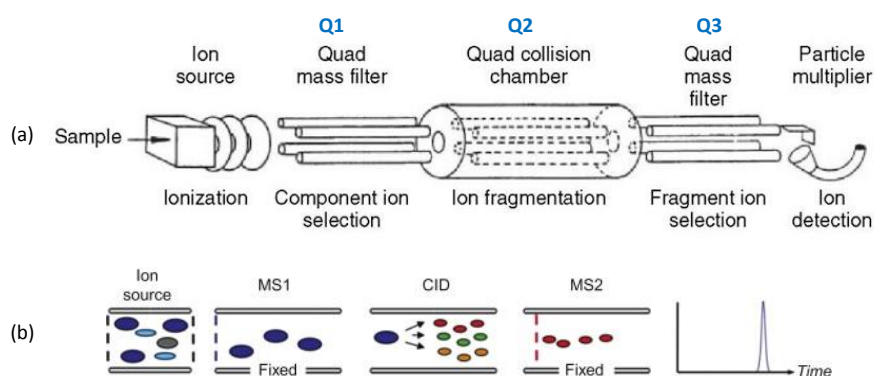
Figure 113. Conceptual diagram of the triple quadrupole mass spectrometer showing each component [173] and schematic diagram of the SRM operation. Metabolites introduced into the QqQMS/MS are first selected by their parent *m/z*, then fragmented, and finally the selected fragments (transitions) are recorded by their *m/z* and plotted to record abundance.[176]

Application of selected reaction monitoring (SRM)[176] to multiple product ions from one or more precursor ions is kwon as Multiple reaction monitoring (MRM) being the most common method for quantitation of analytes by LC/MS/MS. In MRM, ions are selected to make it through the first quadrupole and into the collision cell (Figure 113, panel b). These ions are referred to as the precursor, or parent, ions and they are fragmented inside the collision cell. Certain fragment ions referred to as product, or daughter, ions are selected to make it through the second quadrupole. The transition from precursor/parent ion to product/daughter ions is referred to as an ion transition.

(b) Hybrid-MS system Liquid chromatography Mass Spectroscopy coupled to analyzers Orbitrap

The second mass analyzer used in the present research work was the Thermo Orbitrap®. Since its commercial introduction, this hybrid-MS system Liquid chromatography Mass Spectroscopy coupled to the high-resolution mass spectrometry analyzers Orbitrap[177] (LC/HRMS) has emerge as a fast, efficient and sensitive tool for exploring new natural products.[178,179] This technique allowed researches not only the detection and quantification of known natural products but also the discovery of new promising structures from plants,[180] animals[181] and microorganisms.[182]

The Orbitrap analyzer, developed by Makarov,[183,184] operates by radially trapping ions about a central spindle electrode. An outer barrel-like electrode is coaxial with the inner spindle like electrode and mass/charge values are measured from the frequency of harmonic ion oscillations, along the axis of the electric field, undergone by the orbitally trapped ions. This axial frequency is independent of the energy and spatial spread of the ions. Ion frequencies are measured non-destructively by acquisition of time-domain image current transients, with subsequent fast Fourier transforms (FFTs) being used to obtain the mass spectra. Mathematical

behind Orbitrap is beyond the scope of this study, yet it is well described in literature.[183] Features of the Orbitrap include high mass resolution (up to 150 000), large space charge capacity, high mass accuracy (2–5 ppm) and a mass/charge range of at least 6000.[171] Figure 114 shows the experimental arrangement used by the equipment employed in the current study
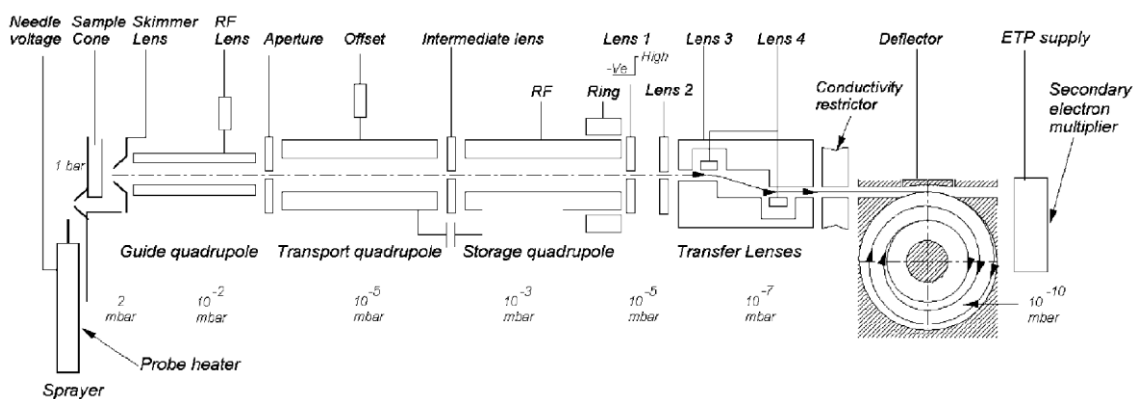
Figure 114. Orbitrap mass spectrometer´s experimental arrangement. Ions are produced by the electrospray ion source (extreme left). Ions then proceed through the source, collision quadrupole, and selection quadrupole and then pass into the storage quadrupole. The storage quadrupole serves as an ion accumulator and buncher, allowing a pulsed mass analyzer such as the Orbitrap to be coupled to a continuous source like an electrospray ionization source. After accumulation and bunching in the storage quadrupole, the exit lens ('Lens 1') is pulsed low, the ion bunches traverse the ion transfer lens system and are injected into the Orbitrap mass analyzer (extreme right). [171]

LC/HRMS has a high mass resolving power and flexibility and allows the user to monitor and collect: (1) Full scan mode, (2) Selected ion monitoring (SIM) and (3) Selected reaction monitoring (SRM); among others. All the fore mention were used in the correct study.

Full scan monitoring provides a qualitative picture of the composition of the sample. It involves scanning the mass range beginning at the smallest mass of fragment ions to the highest mass expected for the fragments.[185] When it is not clear the *m/z* of the biomolecule of interest, it is useful to run a full scan of the sample before limiting the search for identification and quantification of species of interest in the sample. Parameters affecting the accuracy are analyte concentration and complexity of the matrix, therefore a pre concentration or purification of the matrix is needed. Unlike the FS, the mass spectrometer operation in Selected ion monitoring (SIM) is set in such a way that the abundances of ions of one or more specific *m/z* values are recorded rather than the entire mass spectrum.[186] It is employed to minimize matrix interferences and to improve detection limits in those cases where the concentration of the analyte in the sample is very low.

The last detection mode used with LC/HRMS was Selected Reaction Monitoring (SRM). This scan mode has a high potential for detection/quantification of biomolecules that occurs at

very low concentration in complex mixtures. In a SRM experiment, data acquired from a predefined precursor ion and one of its fragments corresponding to a particular *m/z* are selected by the two static mass filters in the instrument and monitored over time for precise quantification. A series of transitions (precursor/fragment ion pairs) in combination with the retention time of the targeted molecule can constitute a definitive assay.[187,188] The selectivity resulting from the two filtering stages combined with the high-duty cycle results in quantitative analyses with extreme high sensitivity.

2.2 Objectives

The main objective in this chapter is the detection and, in some cases, the isolation and quantification of specific bioactive natural products from marine sources using LC/HRMS that was crucial in the development of different research projects. The different approaches of LC/HRMS techniques employed in each case demonstrate their possibilities and limitations in the field of natural products

More specifically, the aims were

- Detection/isolation of siderophore production in several pathogenic marine bacteria: siderophores type vanchrobactin in three species belonging to *Vibrio* genus, detection of piscibactin in a *Vibrio alginolyticus* mutant, the siderophore produced by *Edwardsiella tarda* and *Photobacterium damselae* subsp. *damselae*.
- Detection/ quantification of AHLs in three marine emerging pathogenic *Vibrio* spp.
- Detection of tetrodotoxin (TTX) in *Diodon hystrix* collected in El Salvador.

2.4 Estudio de los sideróforos de bacterias patógenas de peces de acuicultura

2.4.1 Introducción

Los sideróforos, compuestos orgánicos de bajo peso molecular, son producidos por muchos microorganismos, como bacterias y hongos, con el fin de vencer la limitación en la disponibilidad de hierro existente en la mayoría de hábitats en el que viven.[189,190] Dado que el hierro es un elemento fundamental, el desarrollo de un sistema de biosíntesis de sideróforos influye directamente en su supervivencia.[191] Es por ello que en el caso de las bacterias patógenas se ha demostrado que los sideróforos constituyen un importante factor de virulencia.[192] Poseen un gran número de potenciales aplicaciones tanto en clínica como en agricultura.[193]

En esta sección de la presente Tesis Doctoral se abordará la identificación de los sideróforos producidos por distintas bacterias patógenas en acuicultura.

2.4.2 Detección de vancrobactina en diversas especies del género *Vibrio*

2.4.2.1 Antecedentes

Nuestro grupo de investigación de la UDC, en colaboración con el grupo de microbiología de la USC liderado por el Dr. Manuel L. Lemos, logró aislar y caracterizar vanchrobactina como el sideróforo correspondiente al segundo sistema de captación de hierro (III) empelado por la bacteria patógena de peces *Vibrio anguillarum*, responsable de la vibriosis.[194] Además, se logró determinar que FvtA es la proteína de membrana externa receptora de vancrobactina y postulándose que es el sideróforo ancestral de esta especie.[195,196] Estudios más recientes realizados por Butler y col. encontraron que tanto vancrobactina como su dímero y trímero forman parte del sistema de captación de hierro (III) en una cepa de *V. campbellii.*[197]

2.4.2.2 Objetivo

Con el fin de determinar si la biosíntesis de sideróforos de tipo vancrobactina se encuentra extendida en otras especies de *Vibrio*, en esta parte de la presente Tesis Doctoral se planteó estudiar su presencia en cuatro especies: *V. ordalii, V. metschnikovii, V. harveyi* y *V. pelagius,*

2.4.2.3 Materiales y métodos

El procedimiento general para la detección de los sideróforos del tipo vancrobactina en las bacterias objeto de estudio se muestra en la siguiente figura.
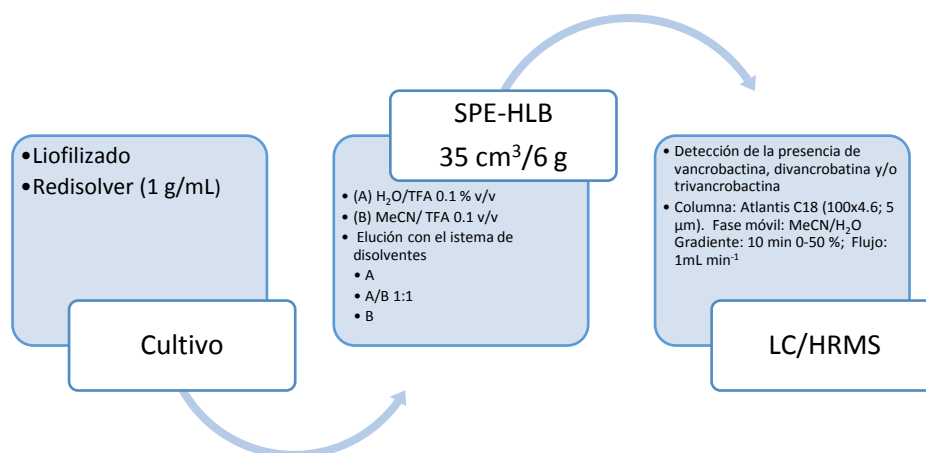
Figure 115 La preparación de la muestra implica eliminación de interferencias en la matriz a analizar (liofilizado) y concentración del analito mediante SPE[164,198] usando cartuchos de HLB Oasis®. La detección se llevó a cabo utilizando Cromatografía Líquida de Alta Eficacia (HPLC) acoplada a espectrometría de masas de alta resolución con ionización por electro espray (HRESIMS) que resultó muy eficiente en la detección de sideróforos.[199,200] El procesado de datos se hizo usando el Software Xcalibur™.
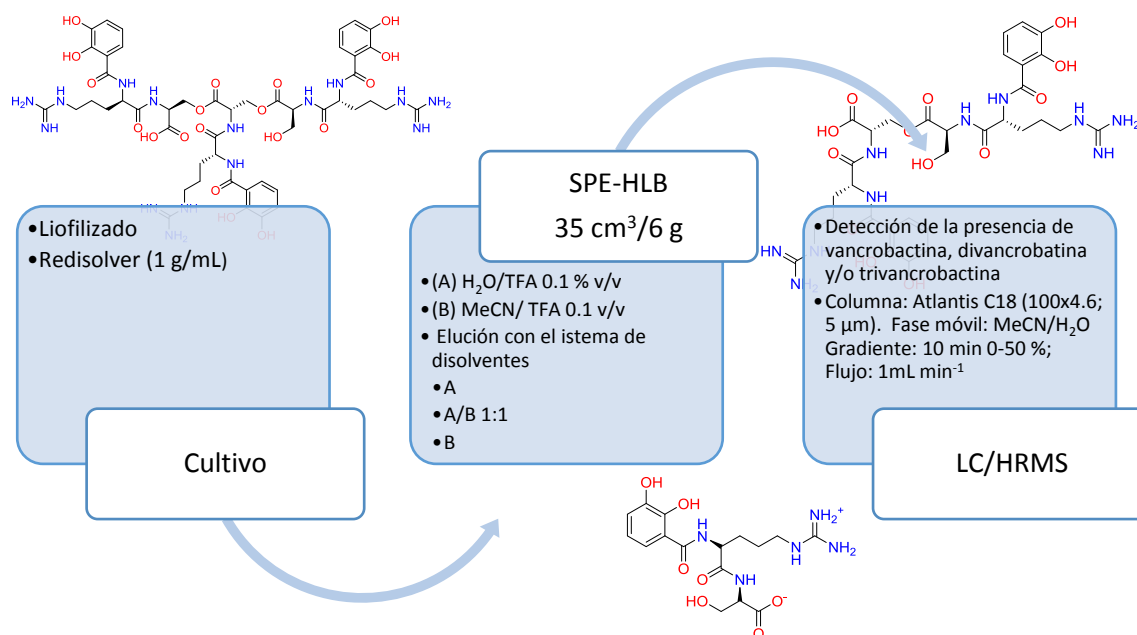
Figure 116. Esquema de trabajo utilizado en la detección de sideróforos del tipo vancrobactina mediante SPE-LC/MS en cuatro especies del género *Vibrio*.

Estudio de *V. ordalii*

Un litro de un cultivo libre de células de *V. ordalii*, cultivado en condiciones deficientes de hierro, fue liofilizado para dar 4.642 g de material. Un gramo de dicho material se sometió a una extracción en fase sólida (SPE) en un cartucho de HLB Oasis®, empleando como fase móvil agua (disolvente A) y acetonitrilo (disolvente B), cada uno conteniendo 0.1% TFA (v/v). En primer lugar, el cartucho se acondicionó y equilibró con 60 mL de disolvente B y 60 mL de disolvente A, y a continuación se introduce la muestra disuelta en agua (1 g/mL). A continuación, se hizo pasar 60 mL del disolvente A, 30 mL de una mezcla 1:1 de disolventes A/B y finalmente 30 mL del disolvente B, obteniéndose tres fracciones: V48L1, V48L2 y V48L3 (Figure 117), que una vez concentradas a sequedad pesaron 193.3, 20.4 y 5.0 mg, respectivamente.[198] Los sideróforos vancrobactina y divancrobactina se detectaron en la fracción V48L2 mediante LC/HRESIMS con un tiempo de retención de 4.68 (Figure 119) y 5.49 min (Figure 120), respectivamente, a partir de sus iones [M+H]$^+$ a *m/z* 398.1676 (calculado para $C_{16}H_{24}N_5O_7$, *m/z* 398.1670) y 777.3162 (calculado para $C_{32}H_{45}N_{10}O_{13}$, *m/z* 777.3162), respectivamente. En ambos casos Δ*m/z* estuvo por debajo del máximo límite permitido.[171]
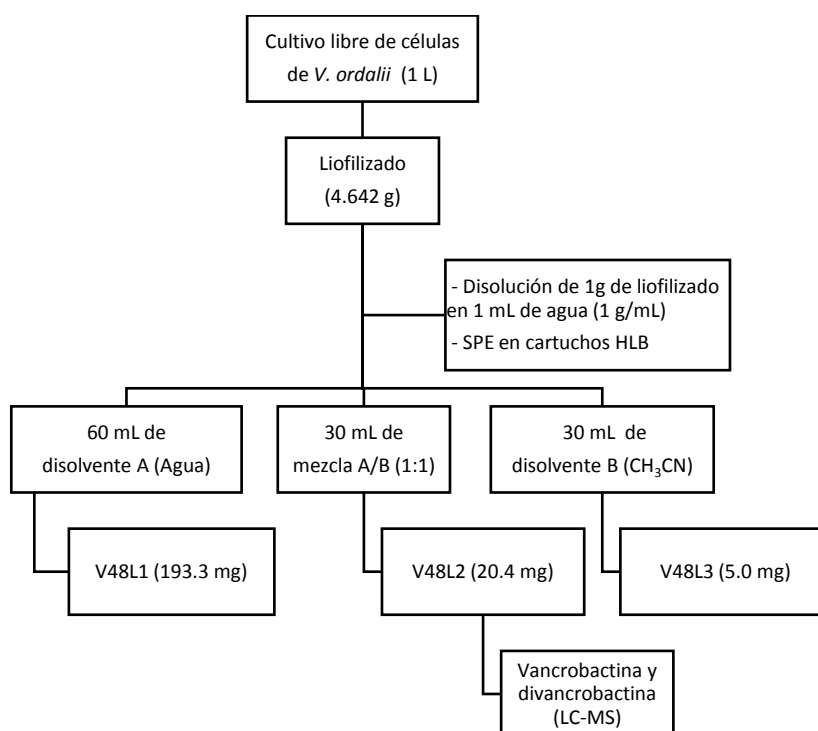
Figure 117. Diagrama de flujo empleado en la detección de vancrobactina y divancrobactina en los sobrenadantes del cultivo libre de células de Vibrio ordalii.

Estudios de V. metschnikovii, V. harveyi y V. pelagius

Repitiendo el mismo proceso se logró detectar la presencia de sideróforos tipo vancrobactina en las especies *V. metschnikovii, V. harveyi* y *V. pelagius*. En la Tabla 23 se muestra las fracciones en las que fueron detectadas en cada especie. Los cromatogramas y los espectros de masas de alta resolución se muestran en el material suplementario.

Tabla 23. Sideróforos del tipo vancrobactina detectados en las especies *V. metschnikovii, V. harveyi* y *V. pelagius*.

Bacterias	Fracciones	Masa de la fracción (mg)	Sideróforo detectado	
			Vancrobactina (*)	Divancrobactina (**)
V. metschnikovii	V62L1	608.0	-	-
	V62L2	35.0	**+**	**+**
	V62L3	8.4	-	-
V. harveyi	V15L1	728.5	-	-
	V15L2	19.3	-	-
	V15L3	3.3	**+**	**+**
V. pelagius	V99L1	633.1	-	-
	V99L2	21.2	**+**	**+**
	V99L3	1.5	**+**	**+**

(*) Detectado como $[M+H]^+$ (**) Detectado como $[M+H]^+$ y $[M+2H]^+$

2.4.2.4 Resultados y conclusión

El análisis químico de los sobrenadantes de los cultivos libres de células de cuatro especies de *Vibrio*, empleando una metodología de SPE desarrollada en nuestro grupo de investigación basada en el empleo de cartuchos HLB y la técnica LC/HRMS, permitió detectar la presencia de sideróforos tipo vancrobactina en todos ellos. Las propiedades de retención y separación de los cartuchos poliméricos HLB se fundamentan en su dual carácter hidrofílico-lipofílico de estas resinas. La naturaleza y la altamente área específica superficial de esta resina polimérica permite extraer y separar de forma rápida y eficiente metabolitos hidrofílicos a partir de extractos crudos usando cantidades mínimas de disolvente.[198] El estudio de sideróforos del tipo vancrobactina en cuatro especies de *Vibrio* se llevó a cabo por medio de su detección a partir de 1 g de sobrenadante liofilizado del cultivo libre de células de las bacterias objeto de estudio (Figure 115). Para ello, cada uno de ellos se sometieron a un fraccionamiento mediante extracción en fase sólida (SPE) usando cartuchos HLB Oasis® y posterior análisis por LC/HRMS. De esta forma se logró detectar, la presencia de vancrobactina y su dímero, divancrobactina, (Figure 118) en cepas de *V. ordalii, V. metschnikovii, V. harveyi* y *V. pelagius.* De los resultados obtenidos (Tabla 23) se deduce que la producción de sideróforos de tipo vancrobactina no está restringida a *V. anguillarum*, se encuentran dispersos en muchas especies de este género y que deben de tener una larga historia evolutiva asociada al género *Vibrio*. Se propone que este tipo de sideróforos puede ser considerado un marcador del género de *Vibrio* para la familia *Vibrionaceae*, al igual que la sideróforo catecólico enterobactina, presente en prácticamente todas las enterobacterias.[201]
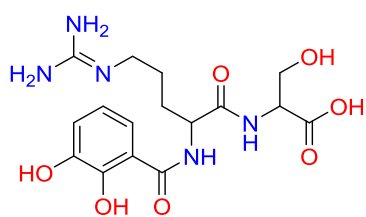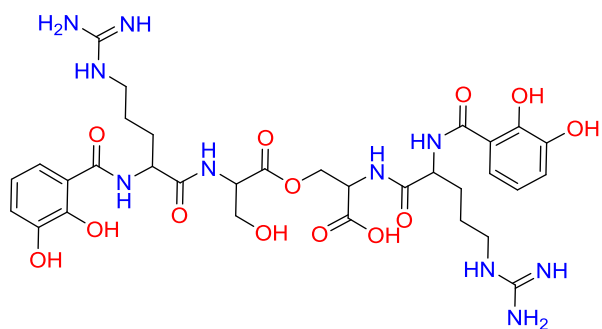
Vancrobactina (a)   Divancrobactina (b)

Figure 118. Sideróforos tipo vancrobactina identificados en *V. metschnikovii*, *V. ordalii*, *V. harveyi* y *V. pelagius*.
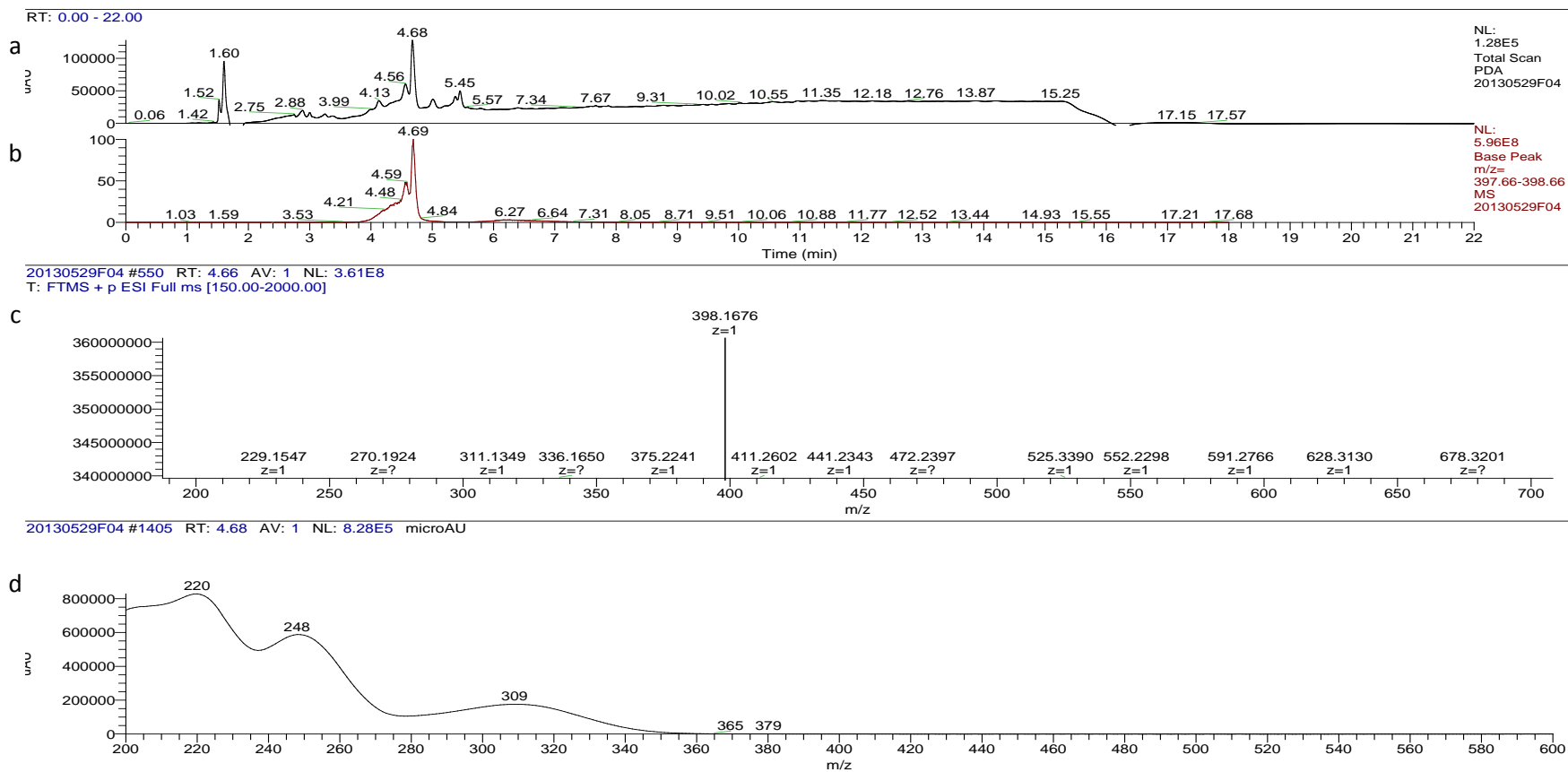
Figure 119. (a) Cromatogramas LC-DAD-MS de la fracción de V48L2 (H₂O/CH₃CN 1:1) obtenida mediante extracción en fase sólida (cartucho OASIS ®HLB) de un cultivo libre de células cultivado en condiciones de deficiencia de hierro de *V. ordalii*; (b) Cromatograma resultante de la monitorización selectiva de los iones de relación *m/z* 397.66-398.66; (c) HRMS del compuesto eluído con un t*ᵣ* de 4.68 min e identificado como vancrobactina; (d) Espectro de UV del compuesto eluído con un t*ᵣ* de 4.68 min y que coincide con el de vancrobactina.
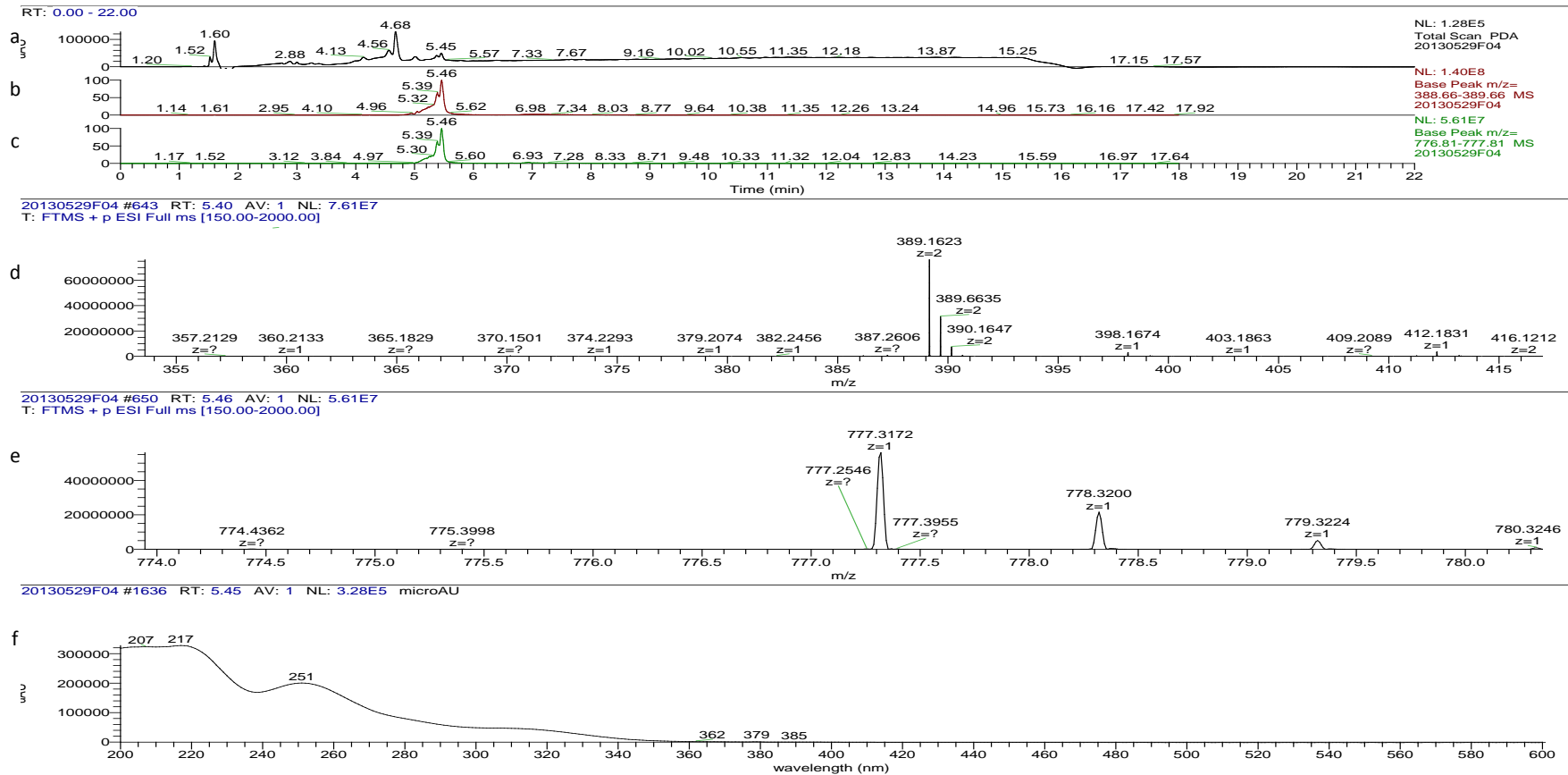
Figure 120. (a) Cromatogramas LC-DAD-MS de la fracción de V48L3 (eluida con CH₃CN) obtenida mediante extracción en fase sólida (cartucho OASIS ®HLB) de un cultivo libre de células cultivado en condiciones de deficiencia de hierro de *V. ordalii*; (b) Cromatograma resultante de la monitorización selectiva de los iones de relación *m/z* 388.66-389.66; (c) Cromatograma resultante de la monitorización selectiva de los iones de relación *m/z* 776.81-777.81; (d) HRMS del compuesto eluído con un t$_R$ de 5.46 min e identificado como el ion [M+H]$^{+2}$ de divancrobactina; (e) HRMS del compuesto eluído con un t$_R$ de 5.46 min e identificado como divancrobactina ; (f) Espectro de UV del compuesto eluído con un t$_R$ de 5.46 min min.

2.4.3 Detection of the siderophore piscibactin from *Photobacterium damselae* subsp. *piscicida* in *Vibrio alginolyticus* by transference of its plasmid-borne pathogenicity island

2.4.3.1 Background

Photobacterium damselae subsp. *piscicida* (formerly *Pasteurella piscicida*) is a Gram-negative rod-shaped marine bacterium that was first isolated in natural populations of white perch (*Morone americanus*) and striped bass (*M. saxatilis*) in 1963 during a massive epizootic in the Chesapeake Bay.[202,203] It is the pathogenic bacteria responsible of a septicemia called photobacteriosis, one of the most important fish diseases in marine aquaculture due to its substantial mortality on infected organisms, its global distribution and its resistance to a variety of antibiotics. It is associated with substantial economic losses worldwide like Japan (*Seriola quinqueradiata*),[204] Taiwan (*Rachycentron canadum*),[205] among others. Our research group was able to identify and isolate the galium (III) complex of the siderophore responsible of the iron uptake of *P. damselae* subsp. *piscicida* that was named as piscibactin. Its structure was supported by DFT calculation (Figure 121).[194] Although the total synthesis of piscibactin has not been achieved yet, a stereoselective synthesis of prepiscibactin, a possible intermediate in the biosynthesis of piscibactin, was recently published by our group.[206]
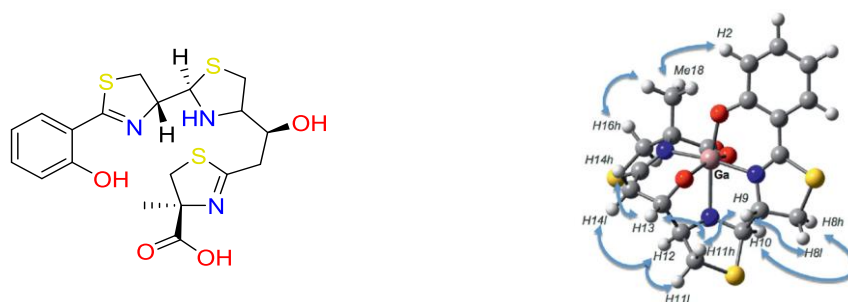
Figure 121 Structures of the siderophore piscibactin and its Ga(III) complex.

A gene cluster that resembles the yersiniabactin high-pathogenicity island (HPI) encodes piscibactin biosynthesis. This HPI-like cluster is part of a hitherto-uncharacterized 68-kb plasmid named pHDP70 that would encode a complete siderophore system. To test this hypothesis, a project was initiated to study whether the conjugative transfer of the pHDP70 plasmid is sufficient for piscibactin synthesis and utilization capabilities from *P. damselae* subsp. *piscicida* to a mollusk pathogenic *Vibrio alginolyticus* strain. Firstly, the siderophore vibrioferrin synthesis was abolished by inactivation of the biosynthetic gene *psvA* in *Vibrio alginolyticus* strain AR13 to give a mutant strain that cannot growth under iron deficient conditions. Then, the conjugative transfer of the pHDP70 plasmid to that *Vibrio alginolyticus* mutant strain restored its capacity to produces siderophore and, consequently, to grow under low-iron conditions. In order to confirm

these findings, it was necessary to see if the *Vibrio alginolyticus* pPHDP70 transconjugant strain deficient in siderophore vibrioferrin synthesis is able to biosynthesize piscibactin.

2.4.3.2 Objective

The main goal in this case is the detection of piscibactin in a *Vibrio alginolyticus* pPHDP70 transconjugant mutant strain deficient in siderophore vibrioferrin synthesis in order to prove that the biosynthesis capabilities of piscibactin are transferrable at low frequencies from *P. damselae* subsp. *piscicida* to a mollusk pathogenic *Vibrio alginolyticus* (Figure 122).
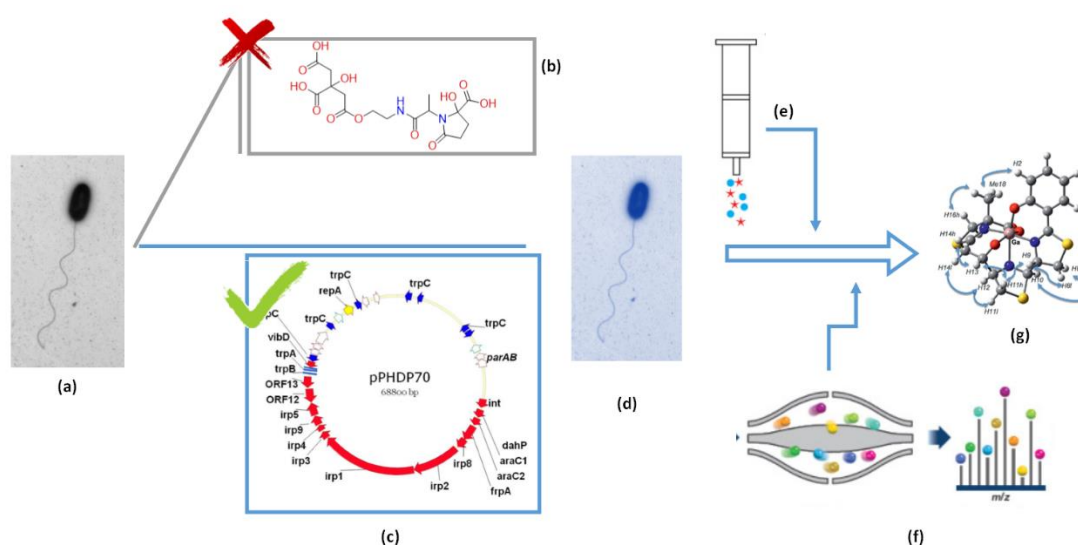
Figure 122 Infographic representation of procedure used on identification of siderophore piscibactin in *Vibrio alginolyticus*; in a mollusk pathogenic *Vibrio alginolyticus* strain (a) the siderophore vibrioferrin synthesis was abolished (b), afterwards the conjugative transfer of the pHDP70 plasmid was done, creating a mutant strain (c). The mutant strain restored its capacity to produces siderophore (d). Siderophore piscibactin presents is established by solid phase extraction (e) followed by piscibactin Ga(III) complex detection by LC/HRMS (f) [vi]

2.4.3.3 Material and methods

A 1.36 L batch of the centrifuged cell-free culture broth of a *Vibrio alginolyticus* pPHDP70 transconjugant *mutant* (AR43)(a mutant strain that was deleted its capability of the production of its own siderophore, vibrioferrin[207]) was concentrated under vacuum to 410 mL (Figure 123). A portion of 75 mL was transferred to a round-bottom flask, and 4.0 mg of GaBr$_3$ was added slowly over 5 min and gently stirred for another 10 min. After incubation at 4°C for 24 h, the solution was passed through an Oasis hydrophilic lipophilic balanced (HLB) cartridge (Waters) (35 cm^3, 6 g), which was previously conditioned and equilibrated with 60 mL of acetonitrile

(solvent B) and 60 mL of water (solvent A). Then, it was eluted with 30 mL of the following mixtures of solvent A and solvent B: 1:0, 7:3, 1:1, 7:3, and 0:1. The fraction eluted with a 1:1 mixture of A/B, named VAPGL3 (3.0 mg), was subjected to high performance liquid chromatography (HPLC)-high-resolution electrospray ionization mass (HRESIMS) analysis using a Atlantis dC18 column (100 by 4.6 mm, 5 μm) with a 35.0-min gradient from 10 to 100% CH_3CN-H_2O, then 5 min at 100% CH_3CN, and finally a 10.0-min gradient from 100 to 10% H_2O-CH_3CN, at a flow rate of 1 ml min^{-1}.[194] Thus, a compound with retention time (t_R) of 8.82 min was detected that showed by HRESIMS the $[M+H]^+$ ion at m/z of 519.9943/521.9927 and the distinctive gallium isotopic ratio (3:2) in concordance with those of piscibactin-Ga(III) complex (Figure 124).
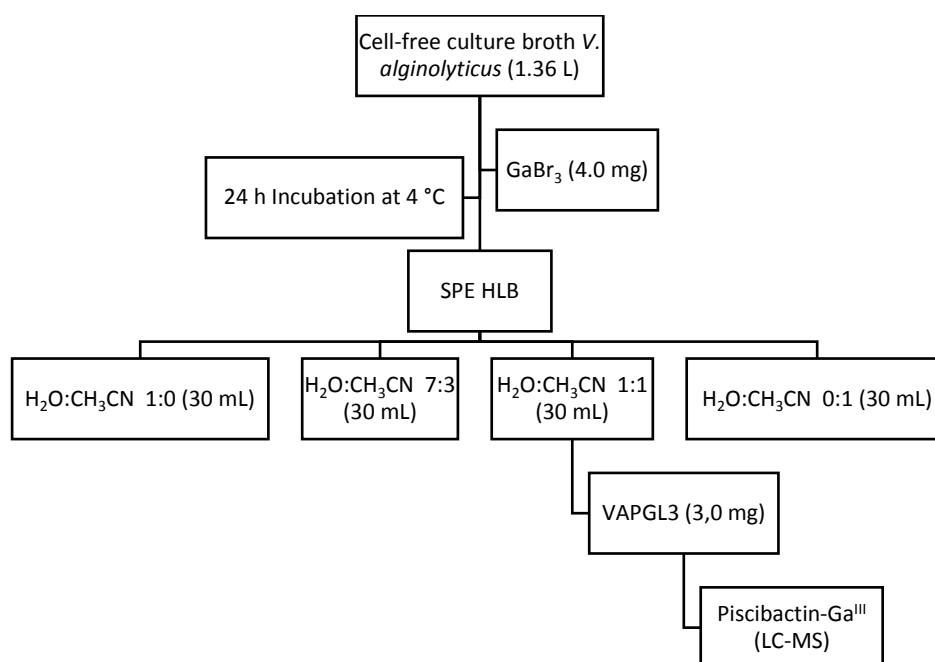
Figure 123. Flowchart for the detection of piscibactin as its Gallium (II) complex in the cell free broth of a *V. alginolyticus* mutant strain.

2.4.3.4 Results and conclusions

In order to test if *V. alginolyticus* pPHDP70 transconjugants is able to produce piscibactin, we used the methodology based on HLB cartridges and liquid chromatography-mass spectrometry (LC-MS) that we developed for isolation of piscibactin.[194] In this way, cell-free culture supernatants of strain *V. alginolyticus* AR43 were incubated with an excess of GaBr$_3$, fractionated through HLB cartridges, and submitted to LC-HRMS analysis. This analysis allowed to detect the presence of piscibactin. Following its conjugative transfer, the detection of piscibactin demonstrated that pPHDP70 restored the capacity of a vibrioferrin mutant of *V. alginolyticus* to grow under low-iron conditions. This result provides strong evidence that pPHDP70 encodes the necessary biosynthetic, transport, and regulatory functions to enable synthesis and utilization of piscibactin following its conjugative transfer to a different species.

Collectively, these findings highlight the importance of pPHDP70 and the horizontal transmission of this plasmid-borne piscibactin synthesis gene cluster in the marine environment that may facilitate the emergence of new pathogens.
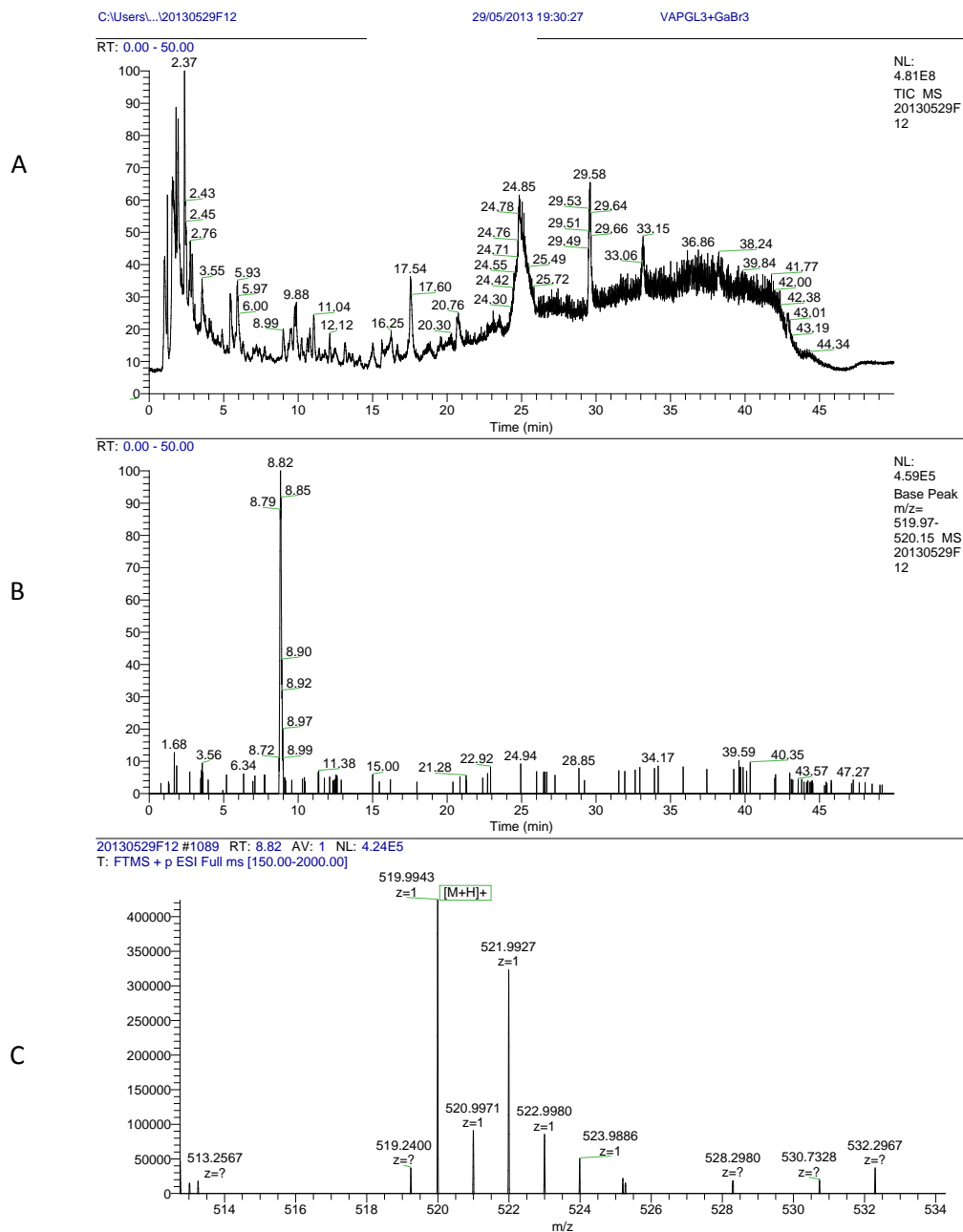
Figure 124. LC-MS experiments for the detection of the piscibactin-Ga(III) complex. (A) Total ion chromatogram (TIC) of the fraction eluted with H_2O-CH_3CN (1:1) from the Oasis HLB cartridge (VAPGL3) containing piscibactin-Ga(III) complex; (B) extracted mass chromatogram (m/z 519.97 to 520.15) showing the peak with retention time of 8.82 min; (C) (+)-HRESIMS of the peak at a t_R of 8.82 min identified as piscibactin-Ga(III) complex: m/z 519.9943/521.9927 ([M+H]$^+$); calc. for $C_{19}H_{21}N_3O_4S_3Ga$, 519.9950/521.9941. Chromatographic conditions: Atlantis dC18 column (100 by 4.6 mm, 5 μm) (Waters); 35-min gradient from 10 to 100% of CH_3CN in H_2O, then 5 min at 100% CH_3CN, and finally 10 min from 100 to 10% CH_3CN in H_2O; flow rate, 1 ml min^{-1}.

2.4.4 Detection of vibrioferrin as the siderophore produced by *Edwardsiella tarda*

2.4.4.1 Background

Edwardsiella tarda is a Gram-negative pathogenic bacterium that affects a wide range of hosts including both freshwater and marine fish.[208,209] It is related to the development of a disease called edwardsiellosis, a virulent infection that caused acute enteric septicemia, associated with significant economic damage in the aquaculture industry worldwide. [210] Although edwardsiellosis has been studied for many years, however, the major virulence factors of *E. tarda* are still poorly understood.

2.4.4.2 Objective

The main objective in this case was to identify the siderophore responsible of the iron uptake of *E. tarda* as one of the virulent factors of this bacterium. Insights gained on *E. tarda* pathogenesis may prove useful in the development of new methods for the treatment of infections as well as preventive measures against future outbreaks.[211]

2.4.4.3 Materials and methods

A total of 414 g of Amberlite® XAD-4 resin was added to the cell-free culture supernatants (2 L) of *E. tarda*, previously acidified with HCl to pH 2.5 and then stirred for 18 h. Afterwards, the mixture was poured into a chromatographic column and then washed with 5.5 L of water (fraction PDX1), 0.4 L of H_2O:MeOH (1:1) (fraction PDX2) and finally 1.2 L de MeOH (fraction PDX3) (see Figure 125). These three fractions were lyophilized to obtain 54.8 g of fraction PDX1, 30.6 mg of fraction PDX2 and 351.3 mg of fraction PDX3. Siderophore activity was evaluated by the colorimetric assay using the Chrome-Azurol S (CAS) dye.[212] The active CAS fraction PDX1 was submitted to HPLC-HRMS analysis using a Atlantis dC18 (100 x 4.6 mm, 5 μm) column (Waters) with a mobile phase consisting of a 35 min gradient from 10 to 100% CH_3CN in H_2O (v/v), then 5 min at 100% CH_3CN and finally 10 min from 100% to 10% CH_3CN/H_2O (v/v), at a flow rate of 1 mL min^{-1}.[213] All measurements were performed on an ESI ion trap mass spectrometer LTQ-Orbitrap Discovery attached to an Accela HPLC system (Thermo Fisher Sci). Accurate mass measurements were taken using the FT-MS Orbitrap module at a resolution >30 000 FWHM (full width at half maximum) for obtaining elemental composition of the [M+H]$^+$ and [M+Na]$^+$ ions within ± 1–3 ppm accuracy.

The extracted mass chromatogram of that siderophore active fraction (*m/z* 434.12-436.12) (Figure 127, panel b) showed the presence of a compound with retention time of 1.83 min that displayed a high-resolution mass spectrum (Figure 127, panel c) that showed the

[M+H]$^+$ and [M+Na]$^+$ ions at *m/z* 435.1249 (calculated for C$_{16}$H$_{23}$N$_2$O$_{12}$, *m/z* 435.1251) and 457.1066 (calculated for C$_{16}$H$_{22}$N$_2$NaO$_{12}$, *m/z* 457.1070), respectively that were in concordance to those of vibrioferrin. The extracted mass chromatogram (*m/z* 388.60-411.80) (Figure 127, panel d) showed the presence of a compound with retention time of 2.80 min that displayed a high-resolution mass spectrum (Figure 127, panel e) with [M+H]$^+$ and [M+Na]$^+$ ions at *m/z* 389.1194 (calculated for C$_{15}$H$_{21}$N$_2$O$_{10}$, *m/z* 389.1191) and 411.1013 (calculated for C$_{15}$H$_{20}$N$_2$NaO$_{10}$, *m/z* 411.1010), respectively, corresponding to the photoproduct of vibrioferrin (Figure *126*, right).[214] In this way, the siderophore vibrioferrin (Figure 126) was detected by *E. tarda*.
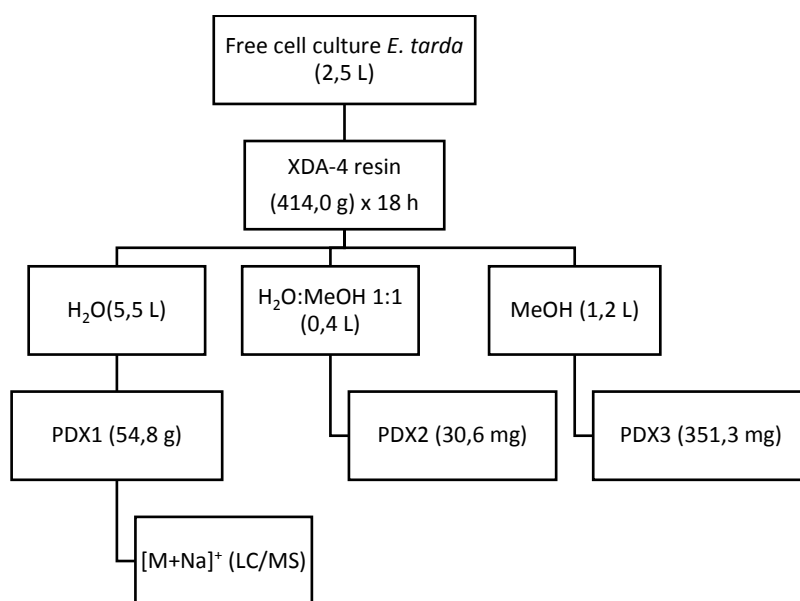
Figure 125. Flowchart of vibrioferrin detection in *E. tarda* by using an Amberlite® resin (XAD-4) and LC/HRMS analysis.

2.4.4.4 Results and conclusions

Vibrioferrin (C$_{19}$H$_{29}$N$_2$O$_1$), a member of the carboxylate class of siderophores bearing two α-hydroxy acid groups, was first reported from the enteropathogenic estuarine bacterium *Vibrio parahaemolyticus.*[215,216] The later detection in the dinoflagellate *Gymnodinium catenatum*[213] suggested that its production is not restricted to genus *Vibrio*.
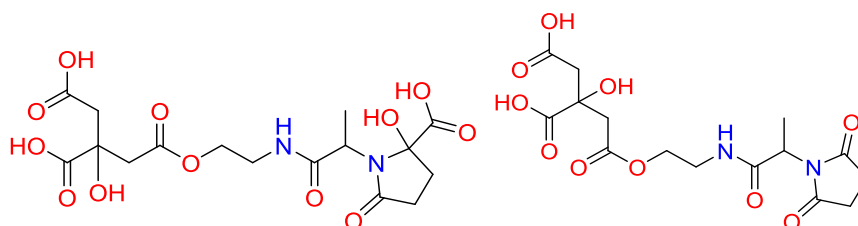
Figure 126. Structure of the siderophore vibrioferrin (left) and its photo degradation product (right).

The structure of vibrioferrin was confirmed by total synthesis.[217] It shows a strong sequestering ability not only with iron (III) but also with boron (VFB). Production of vibrioferrin is highly dependent on the iron concentration of the medium, with increased production occurring under low-iron conditions.

As part of a more extensive project in order to find correlations between the presence of virulence genes, related with three aspects typically involved in bacterial pathogenesis (chondroitinase activity, quorum sensing and siderophore-mediated ferric uptake systems), in the genome of *E. tarda* strains isolated from turbot in Europe and their phenotypic traits, a study of the siderophore produced by *E. tarda* was initiate.

The application of a methodology based on the use of XAD 4 Amberlite resins and followed by further RP-HPLC (RP-18 H_2O/MeCN) to a cell free culture of *E. tarda*, allowed to identify vibrioferrin as the siderophore responsible of the iron uptake system of this bacterium. These results unambiguously confirmed that the siderophore produced by *E. tarda* ACC35.1 is vibrioferrin. Furthermore, we demonstrated for the first time that *E. tarda* produces the siderophore vibrioferrin
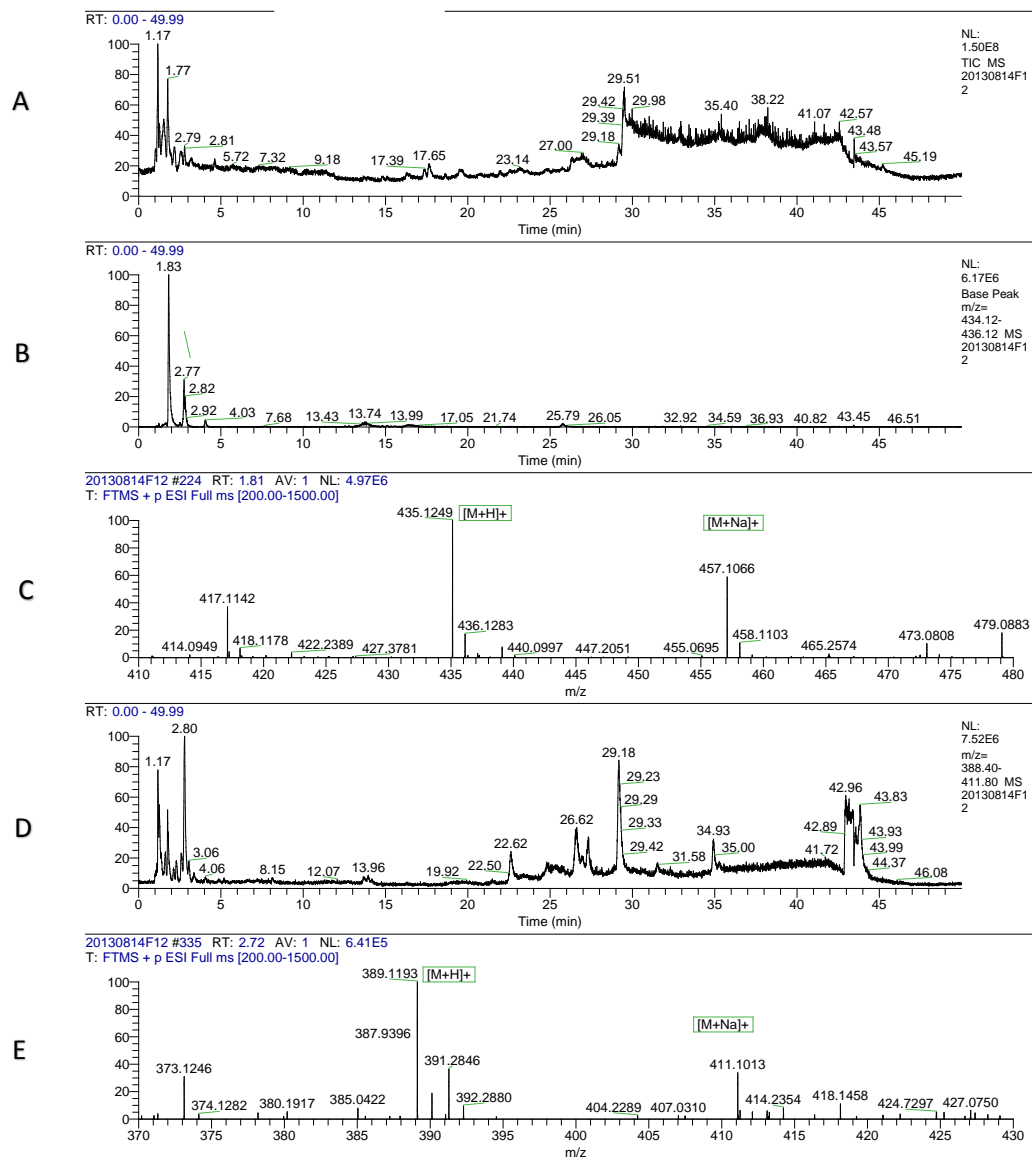
Figure 127 (a) LC-MS chromatogram of the fraction PDX1 obtained by XAD-4 resin extraction of iron-deficient cell-free culture of *E. tarda*. (b) Extracted mass chromatogram (*m/z* 434.12-436.12) showing the peak at t$_R$ = 1.83 min. (c) High-resolution mass spectrum of the peak at 1.83 min identified as vibrioferrin. (d) Extracted mass chromatogram (*m/z* 388.60-411.80) showing the peak at t$_R$ = 2.80 min. (e) High-resolution mass spectrum of the peak at 2.80 min identified as the major photoproduct of vibrioferrin.

2.4.5 Identification of the siderophore produced by some strains of the Marine Pathogen *Photobacterium damselae* subsp *damselae*

2.4.5.1 Background

Photobacterium damselae subsp *damselae* (Pdd) is a Gram-negative bacterium (Vibrionaceae) that has a wide pathogenic potential against many marine animals and also against humans.[218] Our research group could demonstrate that some strains of this bacterium acquire iron through the siderophore vibrioferrin.[219,220] However, there are other virulent strains that do not produce vibrioferrin but they still give a strong positive reaction in the CAS test for siderophore production.[221] In an *in silico* search on the genome sequences of this type of strains it was no possible to find any gene clusters which could be related to a known siderophore system.

2.4.5.2 Objective

The main goal in this section was to identify the siderophore secreted by a *Photobacterium damselae* subsp *damselae* (Pdd) strain RM71 which lacks of vibrioferrin production.

2.4.5.3 Materials and methods

A 6 L batch of centrifuged cell-free culture broth of *Pdd* strain RM71 was divided into five portions which were loaded onto a XAD-4 resin (Radius Column: 2.8 cm, resin mass: 120 g) (Figure 128). After washing with distilled water (1.3 L) with a flow rate of 0.8 mL/min, the resin was eluted with a methanol/water (1:1) mixture followed by methanol. The siderophore and CAS activities remained in the fraction eluted with water which was then lyophilized to give 86.2 g of a solid. This solid was washed with MeOH (4 times × 290 mL) to yield, after removal of the solvent, 54.53 g of a non-methanol-soluble white solid that was CAS positive and siderophore active.[222] The material was dissolved in H_2O and chromatographed on a Sephadex LH-20 column which was eluted with a 9:1 mixture of H_2O in MeOH at a flow rate of 1.8 mL/min.[156] The collected fractions were submitted to CAS assay and the positive fractions were concentrated under vacuum to afford a CAS-positive fraction (37.6 g). Part of that fraction (21.0 g) was divided in three batches and chromatographed on a Sephadex R G-25 Fine[223] column which was eluted with 760 mL of H_2O using a flow rate of 4.5 mL/min. The eluted fractions were submitted to CAS assay and a chloride test for the presence of salts. Fractions displaying an intense color change with the CAS reagent (CAS positive) and with a relatively low amount of salts were pooled and lyophilized. The lyophilized material (400 mg) was dissolved in H_2O and chromatographed on a Sephadex R G-10 column using H_2O (87 mL) as eluent at a flow rate of 1.6 mL/min. Again, the

eluted fractions were submitted to the same test as before to afford 53.5 mg of a salt-free and CAS–positive fraction. Final purification of this fraction was achieved by HPLC using a Discovery R HS F5 (100 × 4.6 mm, 5 μm) column[224] with a mobile phase consisting of an isocratic mixture of 0.3% of CH_3CN in H_2O (each containing 0.1% HCO_2H) for 1.4 min and then, a gradient from 0.3 to 6.0% of CH_3CN in H_2O (each containing 0.1% HCO_2H) over 15.8 min at a flow rate of 1.2 mL/min. The CAS-positive fractions, eluted with a retention time of 2.98 min, were pooled and concentrated in vacuum to provide 2.1 mg of a compound which was identified as citrate by its ^{1}H NMR (500 MHz in D_2O) δ (ppm): 3.00 (2H, d, J = 15.7 Hz, H-2), 2.84 (2H, d, J = 15.7Hz, H-4) and (−)-ESIMS data: m/z 191 [M −H]$^-$.
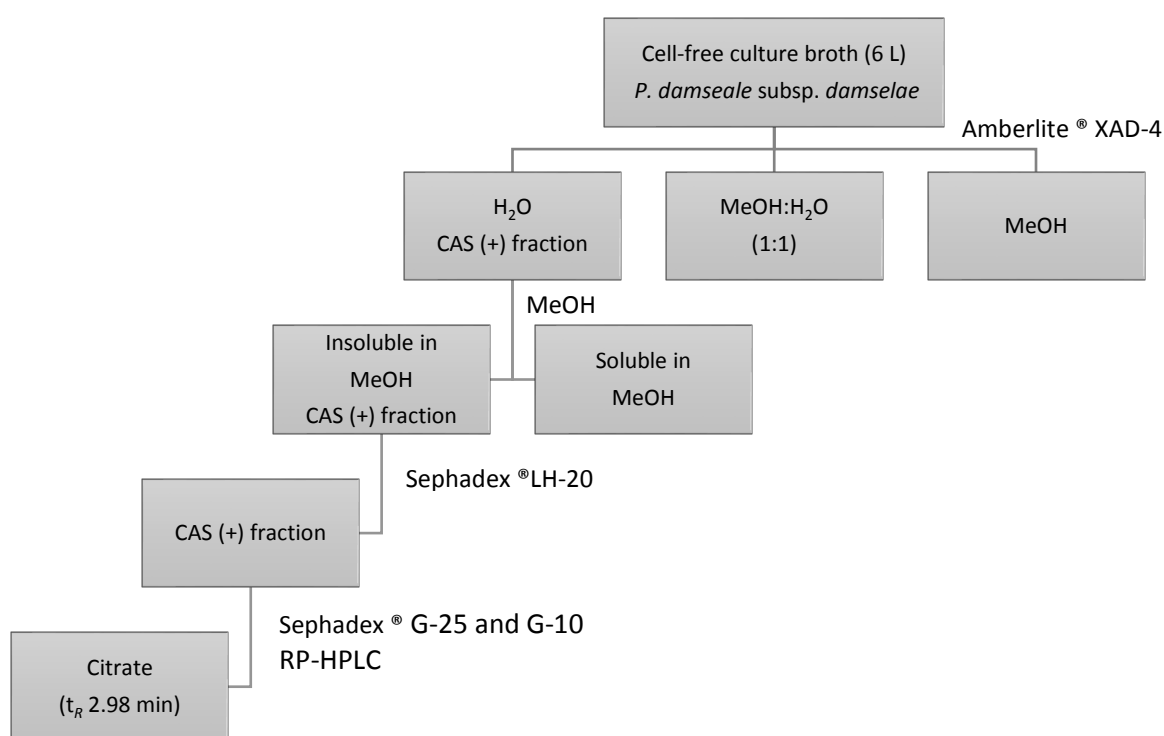
Figure 128. Flowchart of the isolation of citrate from the iron-restricted culture supernatants of *Pdd* strain RM71.

2.4.5.4 Results

To identify compounds with siderophore activity secreted by a *Pdd* strain RM71, the cells were grown under iron restricted conditions (CM9 with 35 μM 2,2'-dipyridyl) and the supernatant was subjected to a bioguided fractionation based on the CAS reactivity and siderophore activity. The cell-free supernatants were submitted to successive column chromatographies (Amberlite XAD4 resin and size exclusion on Sephadex LH-20, G-25, and G-

10) to give a CAS reactive and siderophore active fraction (Figure 128). Finally, HPLC purification of that fraction afforded a pure compound which spectral data (NMR, MS) were coincident to those of citrate (Figure 129). Hence, the CAS-reactive molecule produced by *Pdd* strain RM71 was unequivocally identified as citrate, and no other molecules with siderophore activity could be identified in the supernatants.
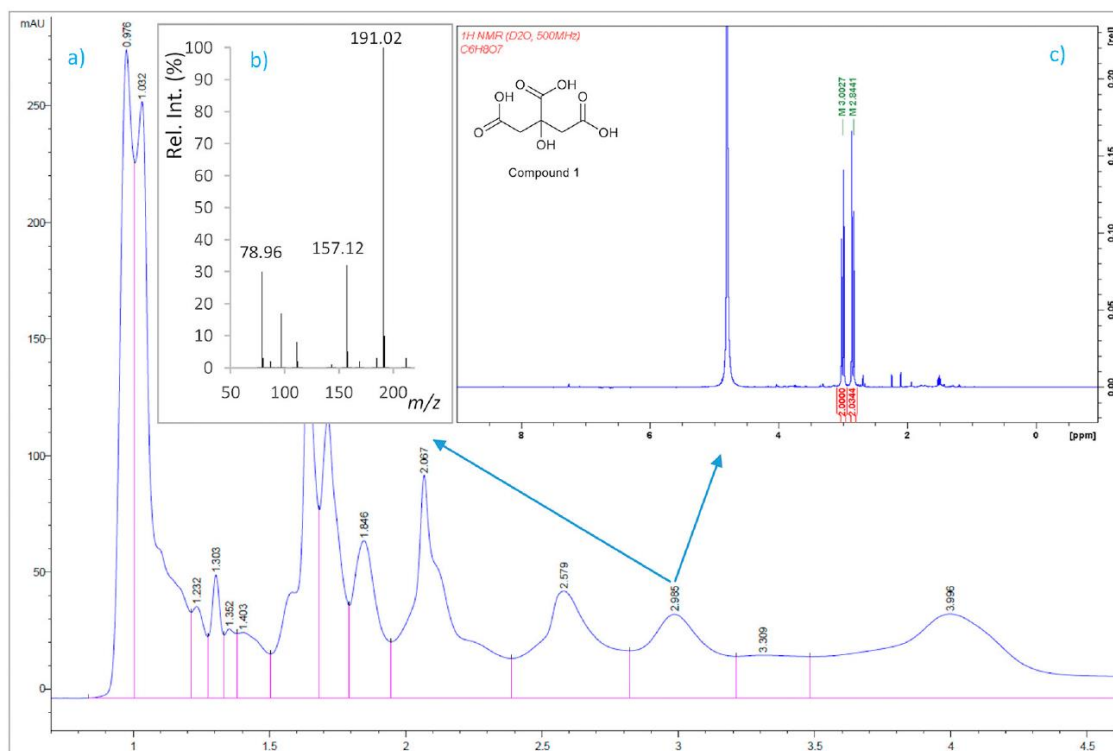
Figure 129. Isolation by HPLC and chemical analysis of citrate from the iron-restricted culture supernatants of the marine pathogen *Photobacterium damselae* subsp *damselae* (Pdd) strain RM71: (a) HPLC chromatogram of the CAS active and salt-free fraction eluted from the Sephadex® G-10 column. (b) (–)ESI mass spectrum and (c) ^{1}H NMR spectrum in D$_2$O (500 MHz) of the isolated compound identified as citrate.

Although, at neutral pH, citrate has lower affinity for iron than conventional siderophores, it is considered a high-affinity iron carrier, and it produces a CAS-positive reaction at concentrations above 0.1 mM. [225] Endogenous citrate secretion was described previously in other pathogenic bacteria and it is associated to intracellular iron homeostasis. However, while most bacteria can use externally supplied ferric citrate to fulfill their nutritional requirement for iron, there are two examples of bacteria which secrete citrate in order to get iron: *Pseudomonas syringae* [226] and *Bradyrhizobium japonicum*.[227] One plausible explanation for the use of citrate as iron carrier is that since citrate is a precursor for vibrioferrin,[228] mutation of a vibrioferrin biosynthetic gene would result in the accumulation of precursors, and in this case citrate would be exported out of the cell to avoid toxicity. The cell would then use external citrate as an alternative iron carrier. The advantages of using citrate or vibrioferrin for iron uptake are unclear. From the results described here we could deduce that vibrioferrin use would be a better

strategy since all strains that produce this siderophore do not accumulate citrate. However, the vibrioferrin affinity constant for iron is not particularly high, with respect to citrate. [214,229]

2.4.5.5 Conclusions

As conclusion, this work shows that although some strains of the marine pathogen *Pdd* produce vibrioferrin as siderophore, most pathogenic strains release endogenous citrate to the extracellular environment in response to iron deprivation, and that this trait have a positive effect in the cell fitness when it grows under extreme iron-restricted conditions. Although the production of another citrate-based or other compounds with siderophore activity cannot be completely discarded, our results suggest that endogenous citrate, besides being part of other siderophores, can be itself used for iron uptake by *Pdd*.

Citrate is produced by most microorganisms via the TCA cycle [230] and, although it is not a powerful chelator, it binds Fe(III) forming a ferric-dicitrate complex.[229] In this form, citrate can be used by many bacteria, including *Pdd*, as a source of iron.[231–234] Furthermore, citrate is a common moiety of many polycarboxilic siderophores.[235]

2.5 Detection and quantification of *N*-acylhomoserine lactones (AHLs) in three marine emerging pathogenic *Vibrio* spp.

2.5.1 Background

Bacterial infectious diseases produced by *Vibrio* are the main cause of economic losses in aquaculture. During recent years it has been shown that the expression of virulence genes in some *Vibrio* species is controlled by a population-density dependent gene-expression mechanism known as quorum sensing (QS), which is mediated by the diffusion of signal molecules such as *N*-acylhomoserine lactones (AHLs). QS Disruption, especially the enzymatic degradation of signaling molecules, known as quorum quenching (QQ), is one of the novel therapeutic strategies for the treatment of bacterial infections.

2.5.2 Objective

The main goal in this case was the detection and quantification of AHLs in three aquaculture-related pathogenic *Vibrio* strains, *V. mediterranei* VibC-Oc-097, *V. owensii* VibC-Oc-106 and *V. coralliilyticus* VibC-Oc-193 in order to correlate the QS signal molecules to the expression of virulence factors in these bacteria. The selection of these bacteria was based on their virulence and high production of AHLs.

2.5.3 Material and methods

A liter of whole culture of each strain was grown in MB medium to stationary phase (OD600 2.8) and extracted twice with an equal volume of dichloromethane, evaporated and resuspended in CH_3CN (Figure 131).[236] For the analysis, each extract was purified by solid phase extraction[198] and analyzed by high-performance liquid chromatography coupled with Fourier-transform and high resolution mass spectrometry (HPLC/FT-HRMS)[237] using full scan (FS) and selected ion monitoring (SIM) modes in a Thermo Scientific Accela LC system coupled to a LTQ Orbitrap. The software Xcalibur 3.0 was used for data processing in both cases. For the HPLC/FT-HRMS FS mode analysis, the extract was passed through a 0.22 µm PTFE syringe filter before injection and 10 µl of each filtered solution was analyzed (mass range from *m/z* 50 to 500). Analyses were carried out using an Atlantis dC18 column (100 mm × 4.6 mm, 5 µm); and a gradient mixture of CH_3CN (solvent A) and H_2O (solvent B) containing 0.1% (v/v) formic acid at flow rate of 350 µL/min (Table 24). In the case of the analysis by HPLC/FT-HRMS *SIM* mode, each extract was passed through an Oasis HLB cartridge, which had previously been conditioned and equilibrated with 500 µL of CH_3CN and 500 µL of H_2O. Then, two fractions were eluted with 500 µL of CH_3CN and H_2O mixtures (1:1 and 1:0), and 10 µL of the fraction eluted with a mixture of CH_3CN/H_2O (1:0) was analyzed. In this case the analysis was conducted in a Scharlau KromaPhase C18 column (150 mm × 4.6 mm, 5 µm) using again a gradient mixture of CH_3CN (solvent A) and H_2O (solvent B), containing 0.1% (v/v) formic acid at flow rate of 80 µL/min (*Table 24*). Precision and accuracy were calculated from the relative standard deviation of the replicates (<15%) and

by direct comparison of mean measured levels of spiked analytes with expected concentrations for unextracted standards, respectively. The external standard method was used for quantification.[238] LC-MS/MS peak areas were calculated and used to build calibration curves of peak area ratio against analyte concentration using unweighted linear regression analysis (Figure 130, see also Supplementary Material)
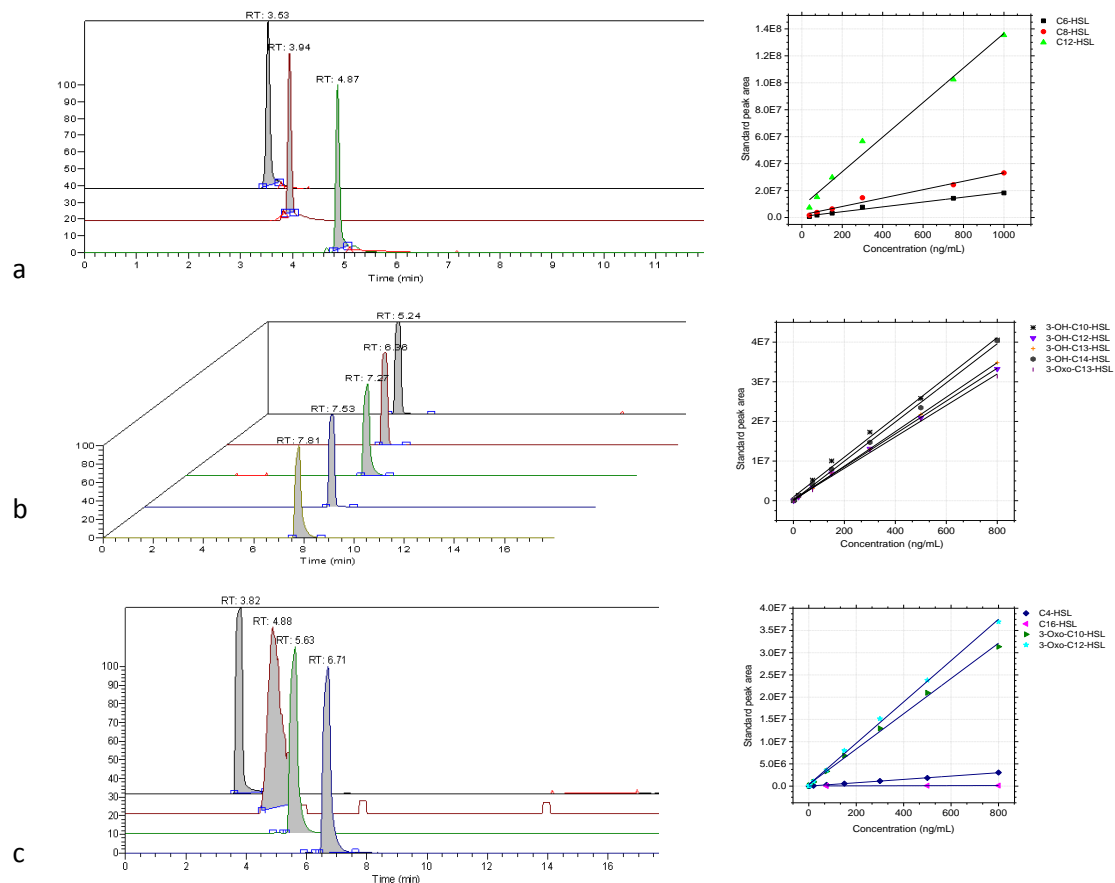
Figure 130 Selected ion chromatograms of the standards used for the quantification of AHLs by HPLC/FT-HRMS SIM Mode. 800 ng/mL (a) and 1,000 ng/mL (b and c). External calibration curves by adding C4-HSL, C16-HSL, 3-O-C10-HSL, 3-O-C12-HSL, 3-O-C13-HSL 3-OH-C10-HSL, 3-OH-C12-HSL, 3-OH-C13-HSL and 3-OH-C14-HSL

The lower limit of quantification was defined as the concentration at which a signal/noise ratio of 10:1 was achieved.
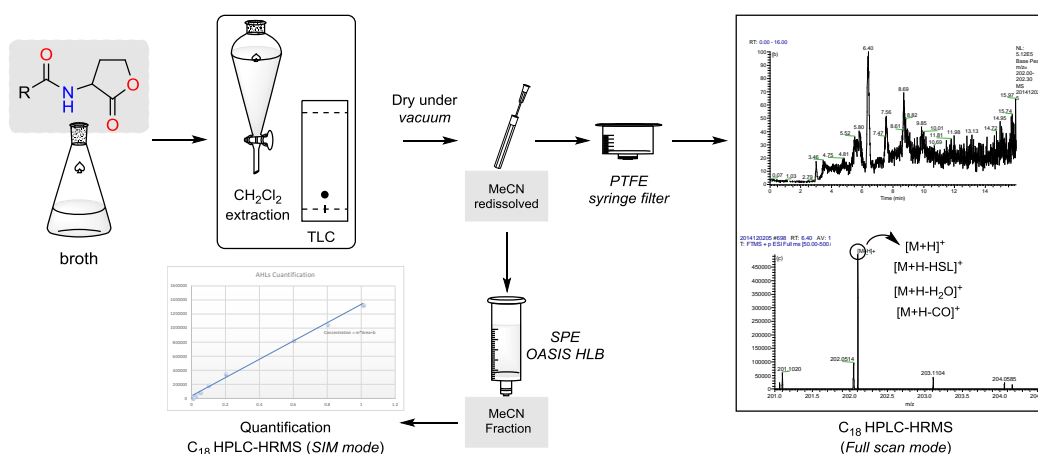
Figure 131. HPLC/FT-HRMS (*full scan* and *SIM modes*) analyses workflow for identification and quantification of AHLs from *Vibrio mediterranei* VibC-Oc-097, *Vibrio coralliilyticus* VibC-Oc-193, *Vibrio maritimus* VibC-Oc-082 and *Vibrio owensii* VibC-Oc-106.

Table 24. Chromatographic profiles used in the HPLC/FT-HRMS FS and SIM mode analyses.

Mode	Step	Time (min)	% CH₃CN (0.1% formic acid)
FS [a]	1	0	30
	2	5	80
	3	7	95
	4	12	95
	5	13	30
	6	16	30
	7	18	90
SIM [b]	1	0	0
	2	1	0
	3	1.5	50
	4	5.5	90
	5	8	99
	6	13	99
	7	13.2	0
	8	18	0

[a] Flow rate of 80 µL/min
[b] Flow rate of 350 µL/min

Identification of AHLs by HPLC/FT-HRMS analysis

Signal molecules produced by *V. mediterranei* VibC-Oc-097, *V. owensii* VibC-Oc-106 and *V. coralliilyticus* VibC-Oc-193 were identified and quantified from a large quantity of an early stationary phase culture of each strain.

The identification of AHLs in each strain was initially carried out by HPLC/FT-HRMS SIM mode analysis using a mixture of twelve AHL standards (**Table 25**). Detection of further autoinducer molecules was performed by HPLC/FT-HRMS FS mode analysis, which showed the [M+H]⁺ ion peaks of additional AHLs (C9-HSL, C13-HSL, 3-OH-C5-HSL, 3-OH-C6-HSL and 3-OH-C7-HSL) (**Table 26**). However, the existence of these AHLs could not be confirmed due to the lack of the appropriate standards. Nevertheless, their presence was corroborated by the occurrence in their (+)-high-resolution electrospray ionization mass spectrometry analysis [(+)-HRESIMS] of the characteristic [102 + H]⁺ ion peak corresponding to the homoserine lactone fragment and

the [M+H-18]⁺ and [M+H-101]⁺ ion peaks which correspond to the loss of H_2O and the HSL moiety [239] (**Table 26** and Figure 132. See also Supplementary Material)
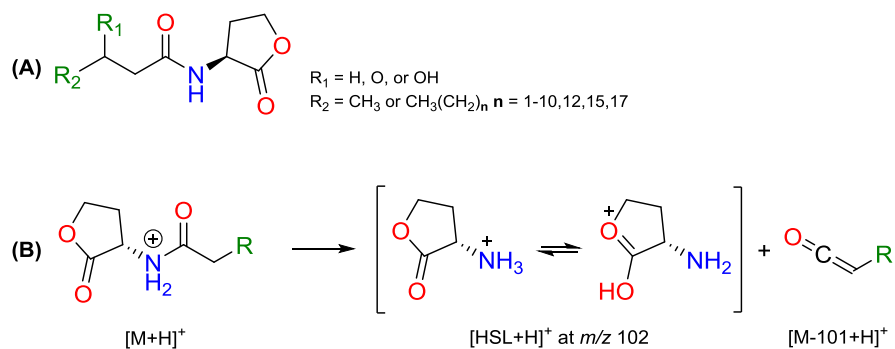
Figure 132. Chemical structures of AHLs. (A) General AHL structure. (B) Mass spectrometry fragmentation pathway of AHLs

For example, the presence of 3-OH-C6-HSL and C13-HSL in *V. owensii* VibC-Oc-106 was corroborated by HPLC/FT-HRMS FS mode analysis through the detection of the corresponding [M-18+H]⁺ ion peak at *m/z* 198.1123 (calc. for $C_{10}H_{16}NO_3$, 198.1125) for the first HSL and the detection of the [HSL+H]⁺ ion peak at *m/z* 102.0549 (calc. for $C_4H_8NO_2$, 102.0550), for the second HSL (Table 26, Figure 133 and Figure. 134). In a similar way, presence of 3-OH-C5-HSL in *V. mediterranei* VibC-Oc-097 was confirmed by HPLC/FT-HRMS FS mode analysis through the detection of the corresponding [M-18+H]⁺ ion peak at *m/z* 184.0968 (calc. for $C_9H_{14}NO_3^+$, 184.0968) (Table 26 and Figure 135).
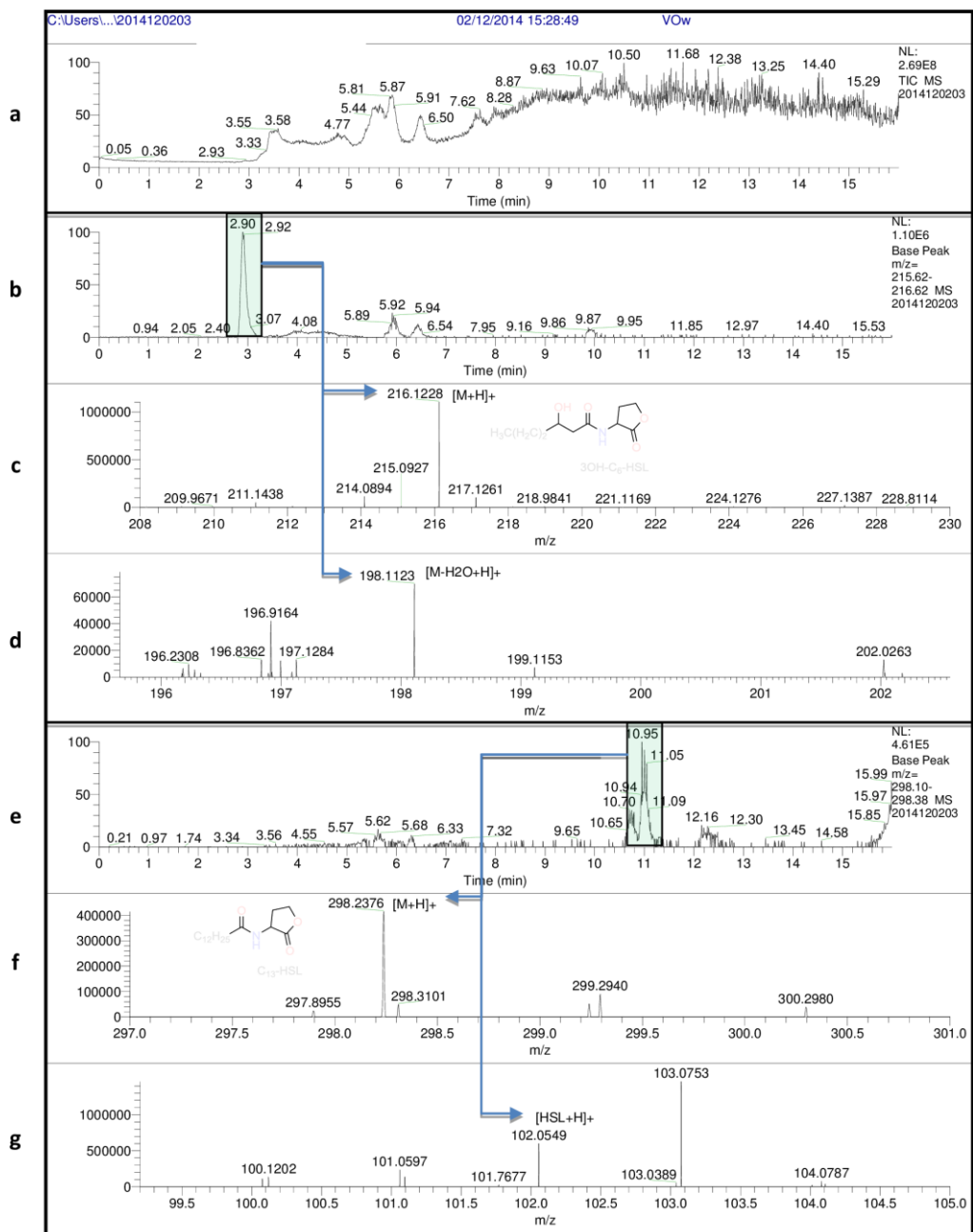
Figure 133. HPLC/FT-HRESIMS (FS mode) experiments for the detection of *N*-acylhomoserine lactones from *Vibrio owensii* VibC-Oc-106. (a) Total ion chromatogram. (b) Extracted mass chromatogram (*m/z* 215.62±216.62) showing the peak at t_R = 2.90 min. (c) Expanded regions of the (+)-HRESIMS of the peak at t_R = 2.90 min identified as 3-OH-C6-HSL showing the ion peaks [M+H]$^+$ at *m/z* 216.1228 (calc. for $C_{10}H_{18}NO_4$ 216.1230). (d) [M-H$_2$O+H]$^+$ at *m/z* 198.1123 (calc. for $C_{10}H_{16}NO_3$ 198.1125). (e) Extracted mass chromatogram (*m/z* 298.10-298.38) showing the peak at t_R = 11.00 min. (f) Expanded regions of the (+)-HRESIMS of the peak at t_R = 11.00 min identified as C13-HSL showing the ion peaks [M+H]$^+$ at *m/z* 298.2376 (calc. for $C_{17}H_{32}NO_3$ 298.2377). (g) [HSL+H]$^+$ at *m/z* 102.0549 (calc. for $C_4H_8NO_2$ 102.0550).
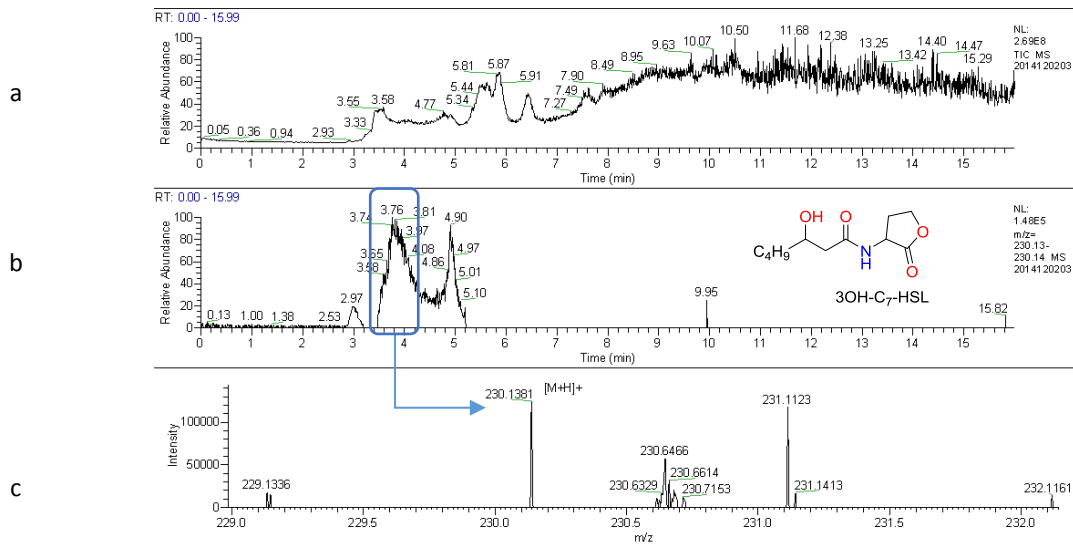
Figure. 134 HPLC/FT-HRESIMS experiments for the detection of N-acylhomoserine lactones from *Vibrio owensii* VibC-Oc-106. Total ion chromatogram (a). Extracted mass chromatogram (m/z 230.13-230.14) showing the peak at t_R = 3.82 min (b). Expanded regions of the (+)-HRESIMS of the peak at t_R = 3.82 min identified as 3-OH-C7-HSL showing the [M+H]$^+$ ion peak at *m/z* 230.1381 (calc. for $C_{11}H_{20}NO_4$ 230.1387) (c)
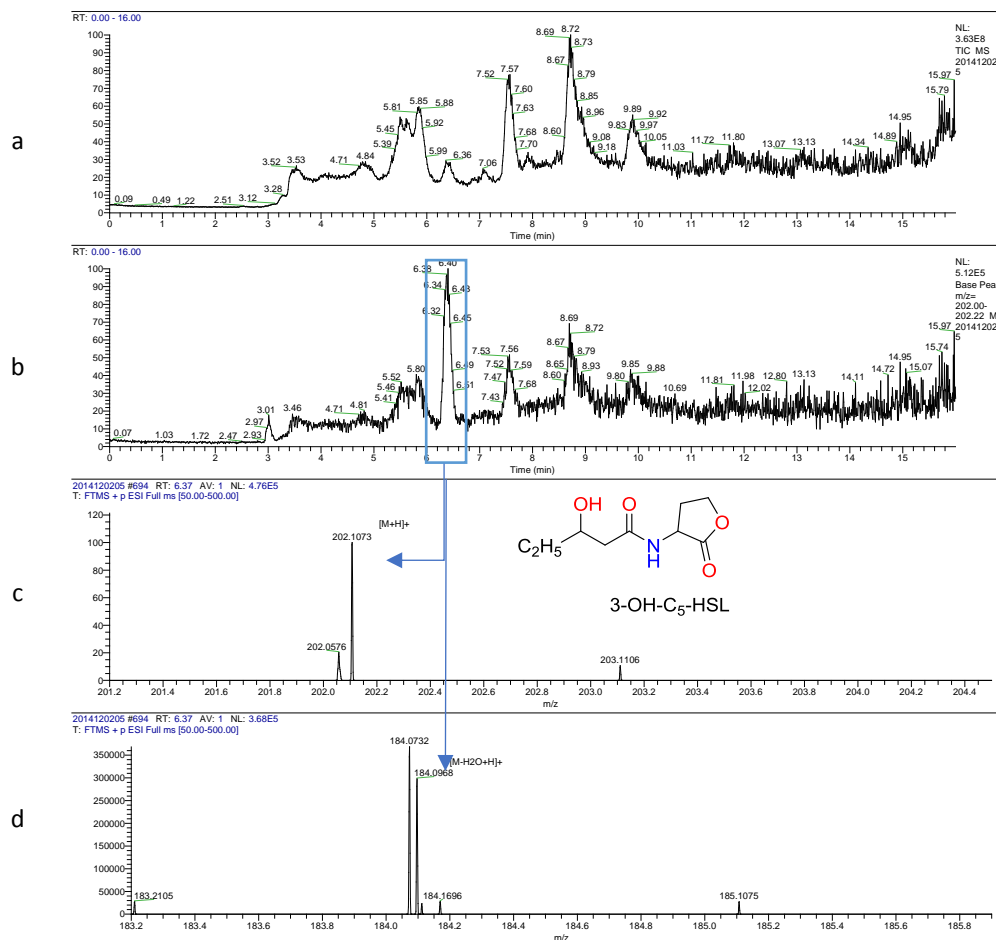
Figure 135. HPLC/FT-HRESIMS experiments for the detection of N-acylhomoserine lactones from *Vibrio mediterranei* VibC-Oc-097. Total ion chromatogram (a). Extracted mass chromatogram (*m/z* 202.00-202.22) showing the peak at t_R = 6.37 min (b). Expanded region of the (+)-HRESIMS of the peak at t_R = 6.37 min identified as 3-OH-C5-HSL showing the ion peaks [M+H]$^+$ at *m/z* 202.1073 (calc. for $C_9H_{16}NO_4$ 202.1074) (c). Expanded region of the (+)-HRESIMS of the peak at t_R = 6.37 min identified as 3-OH-C5-HSL showing the [M-H$_2$O+H]$^+$ ion peak at *m/z* 184.0968 (calc. for $C_9H_{14}NO_3$ 184.0968) (d).
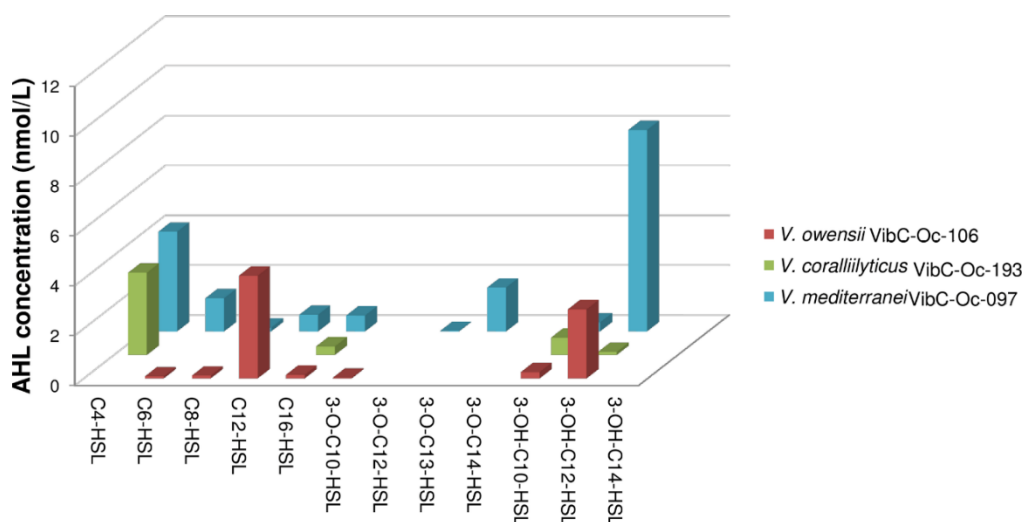
Figure 136. Concentration of the major AHLs quantified in *Vibrio mediterranei* VibC-Oc-097, *V. owensii* VibC-Oc-106 and *V. coralliilyticus* VibC-Oc-193 using HPLC/FT-HRESIMS (SIM mode).

The results show a different AHL-profile for each bacterium strain (Table 25 and Table 26). If the percentage in which the molecules are present in the strains tested is considered, 3-OH-C12-HSL is the most predominant in *V. mediterranei* VibC-Oc-097, C4-HSL is the most abundant in *V. coralliilyticus* VibC-Oc-193 and C12-HSL is the most commonly produced by *V. owensii* VibC-Oc-106. Furthermore, the highest concentration of all the identified AHLs corresponds to 3-OH-C12-HSL in *V. mediterranei* VibC-Oc-097 (Table 25 and Figure 135).

Table 25 AHLs identified by HPLC/FT-HRMS SIM mode analysis in *Vibrio mediterranei* VibC-Oc-097, *V. owensii* VibC-Oc-106 and *V. coralliilyticus* VibC-Oc-193.

AHL identified	Ion quantification (*m/z*)	Retention time [b] (min)	Concentration of AHLs (nmol L^{-1}) [a]		
			V. mediterranei VibC-Oc-097	*V. owensii* VibC-Oc-106	*V. coralliilyticus* VibC-Oc-193
C4-HSL	172.0965	3.82	4.00	*nq*	**3.3**
C6-HSL	200.1281	3.53	1.33	0.08	*Nq*
C8-HSL	228.1594	3.94	0.15	0.11	*Nq*
C12-HSL	284.222	4.87	0.67	**4.12**	*Nq*
C16-HSL	304.2846	4.88	0.64	0.14	0.34
3-O-C10-HSL	270.17	5.63	*Nq*	0.03	Nq
3-O-C12-HSL	298.2013	6.71	0.02	*nq*	*nq*
3-O-C13-HSL	312.2169	7.27	1.76	*nq*	*nq*
3-O-C14-HSL	326.2326	7.81	*Nq*	*nq*	*nq*
3-OH-C10-HSL	272.1856	5.24	0.36	0.25	0.69
3-OH-C12-HSL	300.2169	6.36	**8.08**	2.77	0.12
3-OH-C14-HSL	328.2482	7.53	Nq	nq	nq

[a] Calculations were made from the adjusted peak areas from each strain. Data relate to those AHLs which were positively identified against a standard and those that produce a significant quantification ion signal (R>30,000; mass tolerance < 1 ppm).
[b] Retention time of the standards used in the quantification process. *nq* not quantifiable (limit of detection of AHLs < 0.10 ng mL^{-1})

Table 26. AHLs detected by HPLC/FT-HRMS FS mode analysis in *Vibrio mediterranei* VibC-Oc-097 and *Vibrio owensii* VibC-Oc-106

Microorganism	AHL detected	Retention time (min)	Principal product ions (m/z)	Identity of principal product ions
V. mediterranei VibC-Oc-097	3-OH-C5-HSL	6.37	202.1072 184.0968	[M+H]+, [M-H2O+H]+ a
V. owensii VibC-Oc-106	3-OH-C6-HSL	2.90	216.1228, 198.1123	[M+H]+, [M-H2O+H]+
	3-OH-C7-HSL	3.82	230.1381	[M+H]+
	C13-HSL	11.00	298.2376 102.0549	[M+H]+, [HSL+H]+ b

a [M-H$_2$O+H]+ is the result of a loss of water
b [HSL+H]+ corresponds to the HSL moiety

2.5.4 Results and conclusions

In the case of pathogens which depend on QS to regulate virulence, such as some species of *Vibrio*, the degradation of the AHL signal molecules through QQ could become a good alternative for fighting pathogenicity as pathogen numbers are reduced rather than directly being killed.[240] For instance, *V. coralliilyticus* is a highly spread marine pathogen that has been associated with disease in a variety of marine species from geographically distinct global regions. Moreover, its increasing resistance against antibiotics has been reported in Caribbean region and southwest coast of India.[241] For example, *V. coralliilyticus* is extending its host range to bivalve species such as the hard clam (*Mercenaria mercenaria*), the flat oyster (*Ostrea edulis*), the bay scallop (*Argopecten irradians*), the green-lipped mussel (*Perna canaliculus*) and the naval shipworm (*Teredo navalis*), constituting a serious threat for the bivalve industry, being one of the most important emerging pathogens responsible for larval mortality detected in bivalve hatcheries in France, New Zealand, India and the United States.[242–244] Other species, such as *V. owensii* and *V. mediterranei* have also been associated to other organisms apart from coral: crustaceans such as the ornate spiny lobster (*Panulirus ornatus*)[245] and mollusks such as the blue mussel (*Mytilus edulis*) or the Manila clam (*Venerupis philippinarum*).[246,247]

In this study, we have carried out an in-depth characterization of the AHL signal molecules of three *Vibrio* strains selected by the analysis of their AHL profiles and the virulence capacity of the species to which they are related: *V. mediterranei* VibC-Oc-097, *V. owensii* VibC-Oc-106 and *V. coralliilyticus* VibC-Oc-193. A previous TLC analysis displayed the existence of a high AHL diversity amongst the three selected species.[248,249] Since the TLC technique only provides limited information concerning the nature of signal compounds present in the extracts, HPLC/FT-HRMS analyses was crucial for determining the structures of these potential signal molecules.[219,237] In this analysis, the whole culture of each strain instead of the cell-free supernatant was used to prepare the extract. For this reason, we were able to enhance the extraction of long-chain AHLs, because otherwise their low permeability through the cell membrane limits their extraction and detection.[250] With respect to the organic solvent needed for the AHL extraction, dichloromethane was employed, although no differences were detected when ethyl acetate was used.[251] FT-HRMS analysis showed a high diversity for the production of AHLs molecules by the tested strains, the long-acyl chains AHLs being more predominant in three of the *Vibrio* species analyzed.

This is the first report where the signal molecules have been characterized in these emerging marine pathogens. Furthermore, this study allowed to correlate to presence of AHLs with the expression of virulence factors in the emerging pathogenic species *V. owensii*, *V. mediterranei* and *V. coralliilyticus*. For example, it was found in this project that the AHL defective strains of each selected *Vibrio* produced a significant reduction of the virulence in vivo in brine shrimp (*Artemia salina*). This research contributes to the development of future therapies based on AHL disruption, one of the most promising alternatives for fighting infectious diseases in aquaculture.

2.6 Detection of tetrodotoxin (TTX) in *Diodon hyxtris* collected in El Salvador

2.6.1 Background

Tetradotoxin (TTX) is a non protein toxic with a molecular weight of 319 widespread in either terrestrial vertebrates [252] or invertebrates [253], bacteria [254] and fishes including porcupine fish *Diodon hystrix*.[255,256] The lethality of this potent neurotoxin is due to block action potentials by binding to voltage gated sodium channels (VGSCs) resulting in respiratory paralysis that causes death. [258] The minimum lethal dose (MLD) in human is estimated to be approximately 10000 mouse unit (MU), approximately 2 mg.[259] It has been proposed that TTX production in fish is produced by bacteria present in the sea environment. [260,261]

The puffer fish *Diodon hystrix* (Linnaeus, 1758) (Diodontidae) stands out as one of the most powerful shell-crushing predators of mollusks on the world's tropical coast.[262]. *D. hystrix* is characterized by having spines on the caudal peduncle, dark spots on the fins and a wide head, as well as minor differences in the number of fin rays.[263] This fish is widespread in tropical and subtropical waters of the Atlantic, Indian and Pacific Oceans:[263] Circumtropical eastern Pacific: from San Diego in California (USA) to Chile, including Galapagos Island; Western Atlantic: Bermuda, Massachusetts (USA), and northern Gulf of Mexico to Brazil. [264] Although *D. hystrix* is distributed in El Salvador throughout its entire coast from estuary of the Rio Paz (13°44'39" N y 90°07'58" W) to Meanguera Island (87º 46'), this fish is rarely consumed by locals and there was not any reported poisoning by ingestion yet. On the other hand, it has been reported that one or more species of puffer fish, including *D. hystrix*, are the most potent ingredients of "zombie potions" which contain tetrodotoxin. However, it has been proved that TTX is not the causing agent of zombification process in the Haitian practice of Voodoo.[265,266]

Some intoxication cases with *D. hystrix*, showing the symptoms of TTX poisoning, have been observed either after consuming in Hawaii (USA) [267] and Papua New Guinea [268] or after minor stabs from the spines of a porcupine fish to an aquarium curator in the Netherlands.[269] However, TTX presence was not confirmed by analytical methods.[270,271] Most recent studies using LC MS/MS quantified TTX presence in some specimens of *D. hystrix* (Malaysia).[272]

Tetrodotoxin (TTX) is found in organisms from warm waters, especially in Asia and Pacific Oceans. Tropical Pacific Ocean adjacent to El Salvador is characterized by a high content of suspended material, coastal currents and surface temperatures between 26 to 31 °C. These conditions favor the occurrence of several tropical species, such as *Diodon hyxtris* (Diodontidae).

2.6.2 Objectives

The main goal in this case is to detect the presence of TTX from *Diodon hyxtris* collected in El Salvador by developing a robust and highly sensitive detection method using LC-MS/MS methodology based on a three-stage approach plus a post-acquisition processing (Figure 137):

(a) Sample screening by multiple reaction monitoring (MRM) analysis to quickly identify the possible toxin presence using a API 3200 (Applied Biosystems) equipped with a triple quadrupole MS/MS

(b) LC-ESI(+)-HRMS-full scan analysis using an ion trap-Orbitrap instrument (LTQ Orbitrap XL, Thermo Scientific) to collect high resolution mass data.

(c) and Selected Reaction Monitoring (LC-ESI(+)-HRMS2).
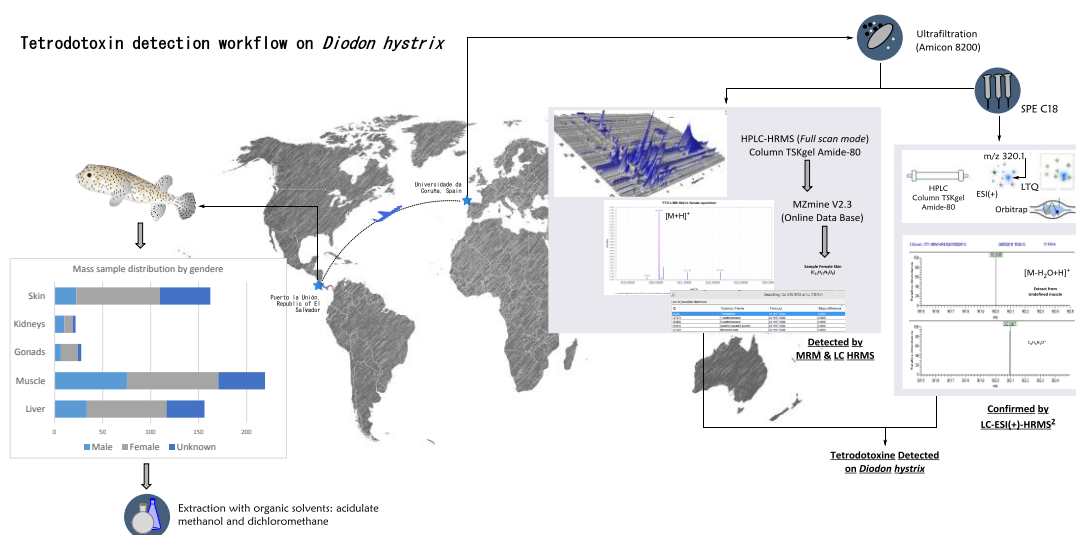
Figure 137. Infographic representation of procedure used on identification of tetrodotoxin on *Diodon hystrix.*

2.6.3 Materials and methods

Specimens

Specimens of three female, one male and two undefined gender each of *Diodon hystrix* (**Table 27**) were collected on October 1st, 2014 at Punta Chiquirín in La Union, El Salvador (13°17'31.01'' N, 87°47'03.60'' O) (**Figure 138**). Samples of *D. hystrix* were separated by gender, dissected to obtain organs of liver, muscle, ovary/testis, kidney and skin and they were immediately kept on ice, transported to the laboratory and kept frozen below -20°C.

Table 27. Characteristics of the *Diodon hystrix* specimens collected.

Gender	Mass (g)	Average Length (mm)	Extract	Liver (g)	Gonads (g) (**)	Kidney (g)	Skin (g)	Muscle (g)
Female	913.9 (*)	199.3	Organs	82.9	17.7	8.5	87.2	95.4
			Raw extracts	10	7.6	3.4	10.0	10.0
			Ultra-filtration (***)	65.4	156.3	400.8	45.3	227.6
Male	1177.3	406.0	Organs	33.5	6.5	10.1	22.5	75.3
			Raw extracts	10.0	4.0	4.8	10.0	10.0
			Ultra-filtration	160.4	29.9	52.2	39.9	914
Undefined	461.9	184.0	Organs	39.8	3.5	3.2	52.6	48.6
			Raw extracts	10.0	4.0	4.8	10.0	10.0
			Ultra-filtration	75.3	9.7	17.2	143.2	125.2

Extract: Organs, total mass of different organs on the fishes collected on Puerto de la Unión (Salvador). Raw extracts: mass of acidulated methanol extracts from different organs. Ultra-filtration: mass of extract founds after ultra-filtration procedure. (*) Specimens mass come from 3 females, 1 male and 2 undefined gender, respectively (**) Gonads are referred as: Male, testicles. Females, ovaries. Undefined gender, gonads. (***) Mass express in mg.
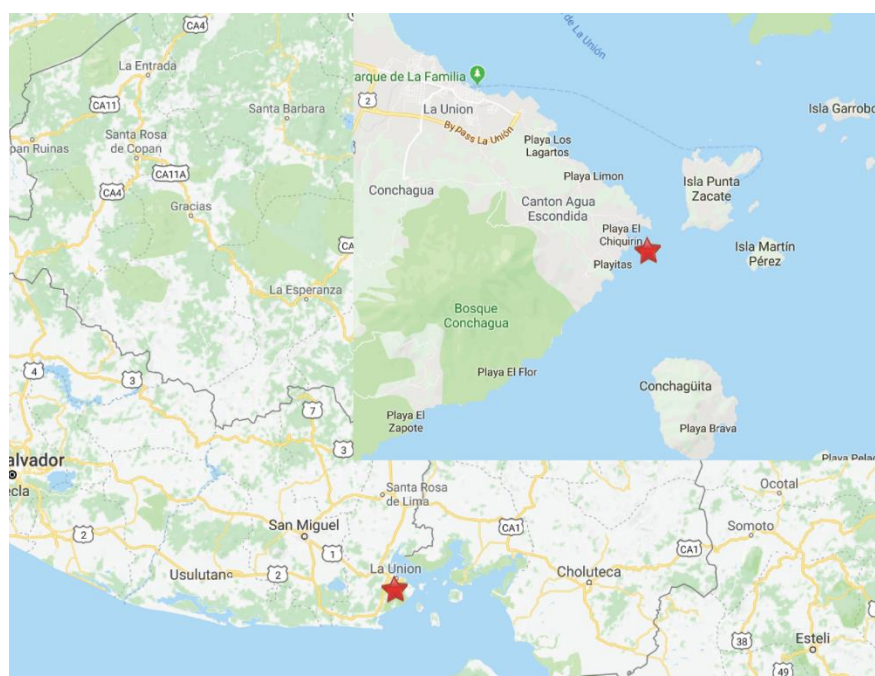
Figure 138. Punta Chiquirín, La Unión, Republic of El Salvador

Sample preparation

Sample preparations were carried out by using a methodology previously described[273] as follow: Tissues were homogenized, two times, using an ultrasonic bath at 55 Hz (5 min) in 40 mL of a solution MeOH/H$_2$O 1:4 (1 % CH$_3$COOH). The resulting extract was centrifuged at 10000 rpm/30 min to give a supernatant. The methanol of the supernatant was removed under reduced pressure in a rotary evaporator to afford an aqueous extract that was washed two times with 25 mL of chloroform. The resulting aqueous layer was ultra-filtered (Amilcon ® system) using two membranes filters of 100.000 Da and 10.000 Da, submitted to Bio Gel P-2 column chromatography and finally lyophilized before being analyzed following the guidelines given in SANTE/11945/201 5 (**Figure 139**).
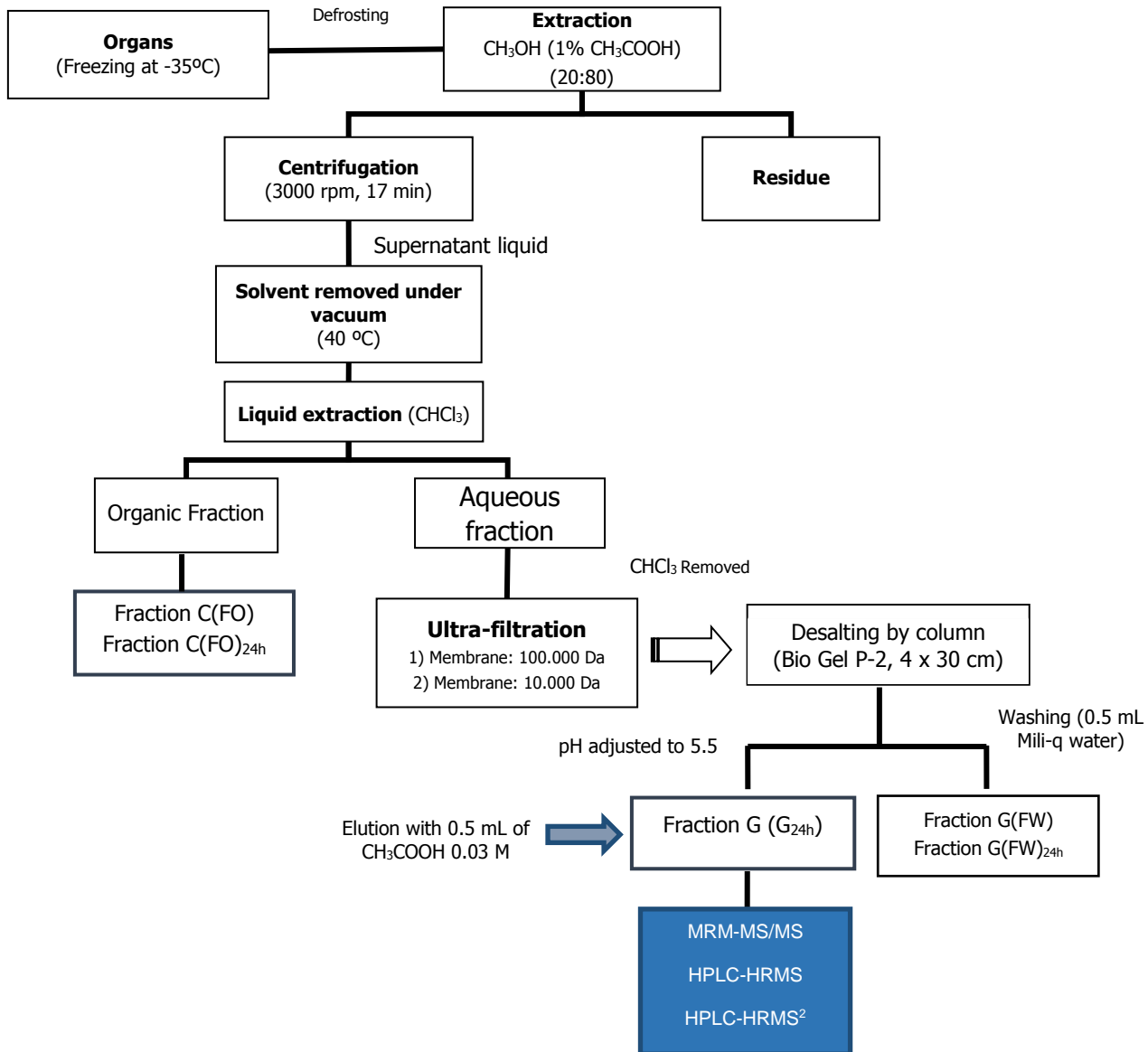
Figure 139. Chart flow process employed in the TTX detection from *Diodon hystrix.*

Methodologies used in tetrodotoxin detection

MRM-MS/MS

Multiple reaction monitoring (MRM) is a targeted mass spectrometry (MS) technique that allows the detection and quantification of specific molecules in a complex mixture.[274] MS/MS measurements were carried out using a LC-MS/MS API 3200 System (Applied Biosystems) equipped with a triple quadrupole MS/MS, allowing to enhance sensitivity and selectivity. Quadrupole filtrates the ions of interest in a process called Collision Induced Dissociation (CID); ions generated by ESI are measured in the mass analyzer to obtain the *m/z* value of each. A selected ion (the precursor) is isolated and fragmented by collision with a neutral target gas. As a consequence of the inelastic collision, a portion of the translational energy is converted into internal energy of the ion, leading to the following decomposition. The resulting ions (daughter ions) are again analyzed to give the corresponding fragmentation spectrum for the selected ion. The retention time, *m/z* and fragment ion transitions are taking in account for a positive identification.[275,276]

The analysis conditions were the following: Mobil phase: $CH_3CO_2NH_4$ 16 mM/MeCN (3:7), pH 5.5, 40.0 min isocratic elution on a TSKgel Amide-80 for Hydrophilic Interaction Liquid Chromatography (HILIC) column (150 x 2.0 mm i.d.; 5µm, Tosho, Tokyo Japan), flow 0.2 mL/min column oven temperature: 25°C. Sample volume injection: 5 µL. Two ion transitions: 320→302 and 320→162 corresponding to $[M+H-H_2O]^+$ and $[C_8H_8N_3O]^+$ ions of TTX were detected in Multiple Reaction Monitoring mode. Preparation of calibration curve: A concentrated TTX solution was prepared gravimetrically and used fresh daily. Using this solution, seven calibration standards were prepared at 0.025, 0.050, 0.100, 0.200, 0.600, 0.800 and 1.01 µg/mL respectively. The linear regression showed a good linearity (R^2 = 0.997). Daughter ions ratio (DR) was estimated on 1.3379±0.2006. Calibration curve and parameters derived from calibration process are shown on Supplementary Material.

HPLC-HRMS

LC/HRMS analyses were performed in a LTQ-Orbitrap Discovery mass spectrometer coupled to an HPLC system Accela Thermo Scientific equipped with an electrospray ion source. Chromatographic separation was achieved using a 40.0 min isocratic elution on a TSKgel Amide-80 column (150 x 2.0 mm i.d., 5µm, Tosho, Tokyo Japan) maintained at 25 °C, mobile phase was comprised of $CH_3CO_2NH_4$ 16 mM/ CH_3CN (3:7) pH 5.5. Sample was dissolved on AcOH (1%). Injection volume (µl): 25. Elution pump flow: 0.2 ml/min. Scan Event: FTMS full scan: 65-450 at a resolution of 30,000. ESI ion source parameters were set as following: polarity positive; capillary temp (°C): 350. Capillary voltage (V): 26.00. Source voltage (KV): 4.50, and Full Scan Mode was used. Acquisition parameters conditions were set to our Orbitrap configuration in order to maximize analyte response and minimize as much as possible isobaric ion interference without significant different error and deviation on the measures.

Tandem HPLC-HRMS^2 spectrometry conditions

Tandem high resolution mass spectrometry was also used to detect TTX. Equipment and separation conditions were the same as in HPLC-HRMS, nevertheless in this experiment scan type chosen was *Selected Reaction Monitoring* (SRM). In this case, samples were previously manually-pass-through a Sep-Pak Plus (C18 Cartridges) Waters. MS conditions were: Parent Mass (*m/z*) 320.00, normalized Collision Energy (eV): 35.0, Acquisition Time (ms): 30.00 and mass range detected (*m/z*): 320.1 → 301.50-302.50 and 320.1 → 161.50-162.50, corresponding to [M+H-H$_2$O]$^+$ and [C$_8$H$_8$N$_3$O]$^+$ ions from TTX respectively. Resolution 30,000 and CID 35 %

Post-acquisition data processing

Post-acquisition treatments of LC-MS/MS data were applied following methodologies that were successfully employed in previous metabolite detections in extracts from natural sources.[178,277] Thus, Thermo Orbitrap files (*.raw) were processing manually by Xcalibur Thermo Fisher Scientific V3.0 and software package MZmine 2.21[278,279] that allows importing *.raw files, filtering data, baseline corrections, building a chromatogram for each mass detected, peak deconvolution and identification (using a formula predictor module and search over online data bases KEGG, MarinLit and PubChem).[280–282] Ion area calculation and linear regression analysis was carried out using Microsoft Excel 2013.

2.6.4 Results

Several specimens of *Diodon hystrix* were collected on Puerto la Unión, Republic of El Salvador in 2013. After processing samples, they were summited to MRM-MS/MS, LC-HPLC-HRMS and HRMS/MS following the workflow depicted in Figure 137. Mass of specimens and extracts are shown in **Table 27**. The fragment ions selected for quantification and confirmation ions were *m/z* 320.1 → 302.1 (corresponding to loss a molecule of water) and *m/z* 302.1 → 162.1 (corresponding to a loss of C$_8$H$_8$N$_3$O) that are in concordance with fragmentation patterns previously reported.[283]

MRM-MS/MS

The calibration curve used for TTX quantification attempt is shown in Supplementary Material (detection limit 6.2 ng/mL). The toxin was detected by comparison of the retention time (*R$_{time}$*) and MS/MS fragments of the sample to those of the standard according to daughter ion spectra previously reported (Figure 140).[284] Delta sample's and standard's retention time were calculated by using the following equation:

$$\Delta R_{time} = \left| R_{time\ of\ standard} - R_{time\ of\ sample} \right| \qquad \text{Equation 14}$$

Tetrodotoxin precursor ion mass was only detected in female gonads (FG) (R$_{time}$ = 7.38, Δ R$_{time}$ = 0.02 min, DR = 0.59) and in undefined gender muscle (MU) (R$_{time}$ = 7.49, Δ R$_{time}$ = 0.13, DR = 0.21), Δ R$_{time}$ was calculated using Equation 14.
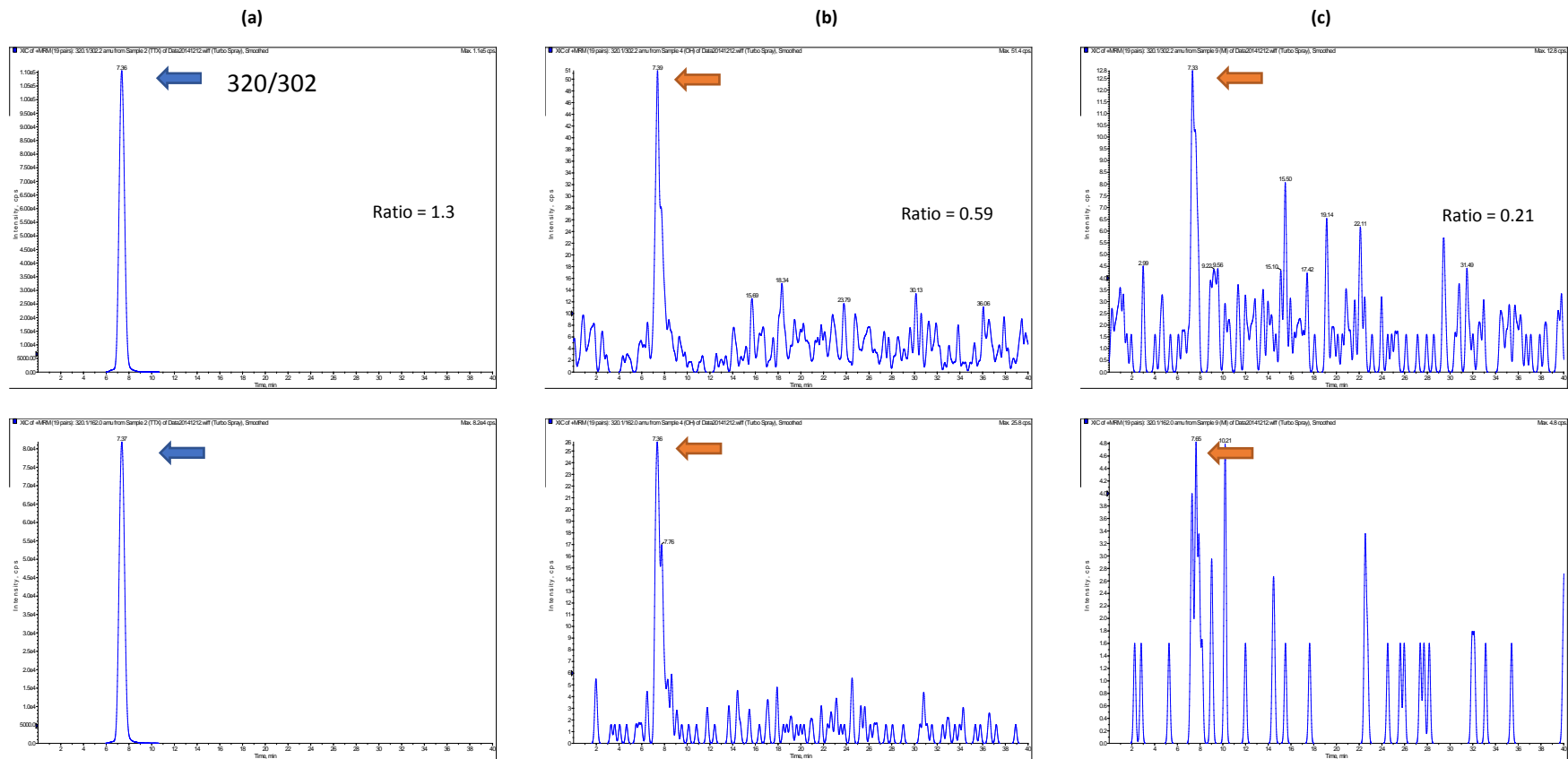
Figure 140. Chromatograms in MRM mode of TTX standard **(a),** female gonads sample **(b)** and muscle undefined **(c)** sample. Arrows show the transition; those on orange color show transitions on the samples. However, the expected ratio between the two quantifications ions (1.3) was not seen. (Upper row: $320 \rightarrow 302$ transition. Lower row: $320 \rightarrow 162$).

Tetrodotoxin could not be quantified using MRM-MS/MS, presumable because analyte concentration is below the quantification limits (0.0062 µg/mL). It is well known that daughter ions ratio is severely impacted by analyte concentration.

Ion transitions found in the samples of female gonads and undefined muscle (Figure *140*) matched with the standard. Nevertheless, daughter ions ratio found is not within the suggested ±30% (relative). Using this experimental was not possible to assure the presence of the analyte beyond a reasonable doubt (Table 28). For these reasons, other techniques were used in order to unequivocally identify the toxin's presence in *D. hyxtris.*

Table 28. Tetrodotoxin detection in *Diodon hystrix* using several techniques

Gender	Liver (g)	Gonads (g) (**)	Kidney (g)	Skin (g)	Muscle (g)
Female	ND	**MRM**	ND	**HPLC-HRFTMS**	ND
Male	**HPLC-HRFTMS**	ND	ND	ND	ND
Unknown	**LC HRMS²**	ND	ND	ND	**MRM**

ND Not detected

HPLC-HRMS

LC-HMRS was selected as a technique not only because it has been widely used on natural product detection and metabolites, [285,286] but also because it was recent successfully employed in TTX detection. [287]

Accurate mass measured (ADAM) is expressed as the average of the mass detected at three different peak positions in the extracted ion chromatogram (Figure 141). The mass accuracy is given as the difference between the theoretical and the measured values of the mass (Δ *m/z* ppm) (Equation 15)[288]

$$\Delta \, m/z = \left| \frac{m \, measured - m \, theoretical}{m \, theoretical} x 10^6 ppm \right| \qquad \text{Equation 15}$$

Natural isotope pattern used as additional information is a powerful tool to refine the number of possible candidates for natural product identification. This information is commonly presented as Relative Isotope Abundance (RIA) of carbon ^{12}C and $^{13}C_1{}^{12}C_{n-1}$ [288] (Equation 16). RIA was determined using Xcalibur software (Figure X1-SI and Table X1-SI). Isotopic ion abundance ratio error (RIA $_{error}$) did not exceed the maximum recommended value of |16%| for *full scan* mode ESI(+) on peaks with intensities between 1 x 10⁵ and 1 x 10⁶.[108,289]

$$RIA \, error \, (\%) = \left| 100x \frac{RIA_{exp} - RIA_{theo}}{RIA_{theo}} \right| \qquad \text{Equation 16}$$

LC-ESI(+)-HRMS of tetrodotoxin standard and representative *Diodon hystrix* sample (female skin) are displayed in Figure 141.
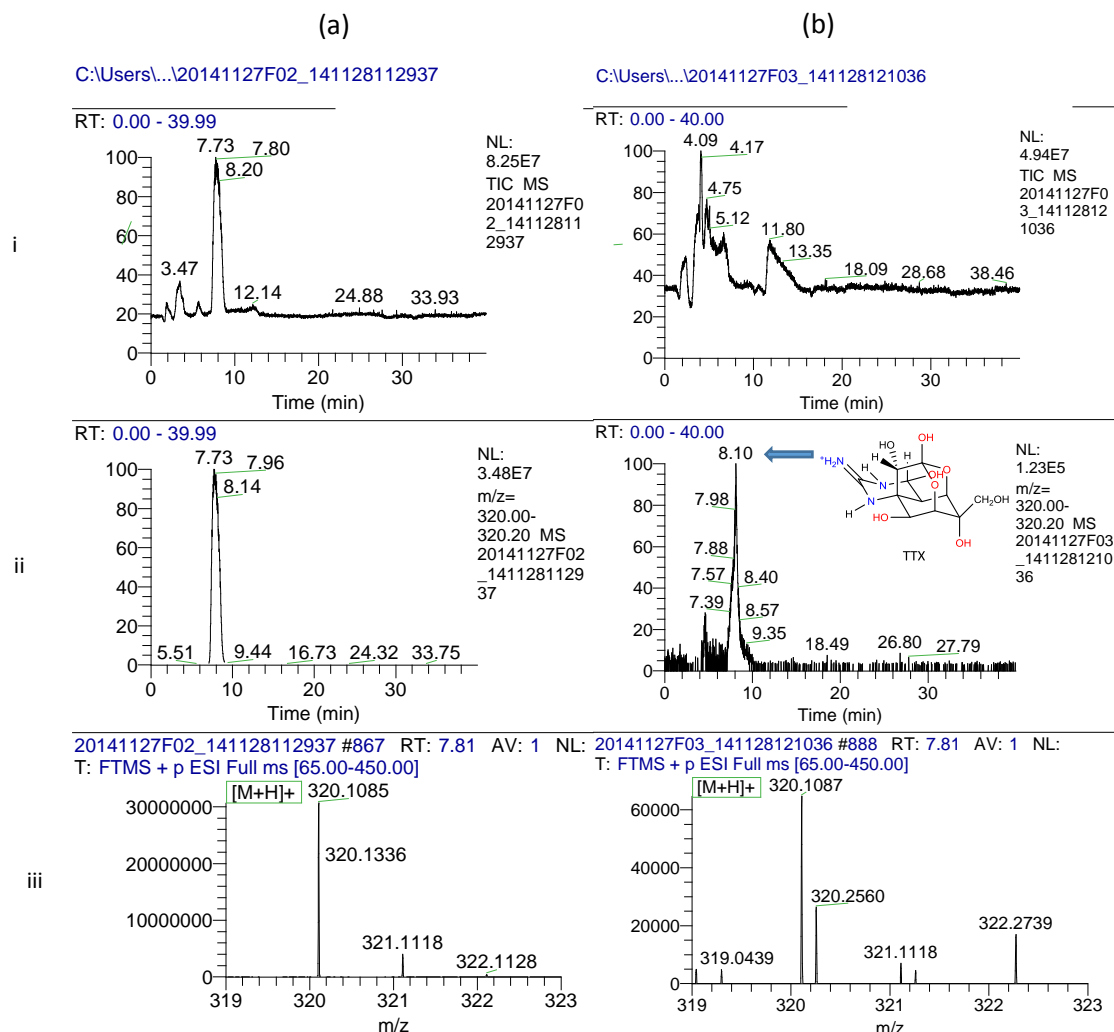
Figure 141. LC-ESI(+)-HRMS (SIM mode) of tetrodotoxin standard (**a**) and of extract from the female skin of *Diodon hystrix* (**b**). Total ion current (**i**), chromatogram extract mass range *m/z* 320.0-320.20 (**ii**) and high resolution mass spectra (**iii**) showing the presence of TTX in female skin sample (Δ m/z = 0.87 ppm, Δ R$_{time}$ = 0.4 min)

A compound that matched with the retention time and exact mass of TTX was found in two of the studied samples: female skin (FS) and male liver (ML). The Δ*m/z* ion ratio errors in this study were around 0.8 ppm (Table 29), which is accurate enough to calculate the possible molecular formulas for ions and molecules.[290] In that table the differences between accurate calculated mass and experimentally detected mass in ppm (Δ *m/z*) and the isotopic ion abundance ratio error (RIA $_{error}$) of M+1/M ($^{13}C_1/^{12}C$) are shown. Due to the sensitivity of this method, it is possible the detection of this isotopic ion with an appropriate intensity. Female skin sample was the only one that matched with the aforementioned conditions.

Table 29 Tetrodotoxin detection by HR-LC/MS in female skin sample of *Diodon hystrix*

TTX Standard solution									
Formula	R $_{time}$ (min)	CAM (Da)	DAM (Da)	ADAM (Da)	Δ m/z (ppm)	RIA theo (%)	RIA (%)	RIA exp (%)	|RIA error| (%)
$C_{11}H_{18}O_8N_3^+$	7.41	320.10884	320.10867	320.10857	0.84				
	7.80		320.10858						
	8.37		320.10846						
$C_{10}^{13}CH_{18}O_8N_3^+$	7.41	321.11220	321.11197	321.11191	0.90	11.9	12.80	12.46	4.7
	7.80		321.11191				12.36		
	8.37		321.11185				12.22		
$C_9^{13}C_2H_{18}O_8N_3^+$	7.41	322.11309	322.11295	322.11278	0.63	1.6	1.46	1.4	12.5
	7.80		322.11282				1.36		
	8.37		322.11258				1.36		
Female skin sample									
Formula	R $_{time}$ (min)	CAM (Da)	DAM (Da)	ADAM (Da)	Δ m/z ppm	RIA theo (%)	RIA (%)	RIA exp (%)	|RIA error| (%)
$C_{11}H_{18}O_8N_3^+$	7.67	320.10884	320.10867	320.10856	0.87				
	8.15		320.10852						
	8.37		320.10849						
$C_{10}^{13}CH_{18}O_8N_3^+$	7.67	321.11220	321.11160	321.11213	0.21	11.9	12.47	11.79	0.9
	8.15		321.11182				14.52		
	8.37		321.11298				8.37		

R time: Retention time in minutes. *CAM (Da):* Calculated accurate mass in Daltons. *DAM (Da):* Detected accurate mass in three different parts of the chromatogram peak in Daltons. *Δ m/z* Average of detected accurate mass in ppm. RIA theo *(%):* Relative isotopic abundance calculated. RIA (%): Relative isotope abundance detected. RIA exp (%): Average of relative isotope abundance detected. |RIA error (%)| Absolute value of the relative isotope abundance error. Calculations: RIA theo (%), was automatically calculated with ChemDraw V16 software, RIA exp (%), was automatically calculated by using a Xcalibur V 3 software. Δ *m/z* and |RIA exp (%)| was calculated by using Equations 2 and 3, respectively

The analysis displays a sharp peak at 8.10 min (ΔR_{time} = 0.37 min) for TTX in female skin (Figure 141) (Δ *m/z* = 1.25 ppm, absolute peak intensity 1.2 x 10^5) which fully overlap with the extracted ion chromatogram of the standard (Figure 142) and also RIA$_{error}$ was within the recommended maximum tolerance value of |16%| (Figure 143). Although any well-defined peak is showed in the chromatogram of male liver sample (ML) (Supplementary Material), there is an ion that seems TTX because its exact mass (Δ *m/z* = 1.25 ppm) and retention time (Δ R$_{time}$ = 0.08 min) matched with it. However, the presence of TTX on male liver (ML) sample was rule out because the RIA $_{error}$ was bigger than the maximum tolerance value aforementioned (Figure 143). This result was confirmed by MRM analysis (Table 28). This method allowed us to calculate the RIA$_{M+2/M}$ ($^{13}C_2$/^{12}C) of the standard (Table 29) but did not allow to calculate that value in our samples presumably due to the low analyte concentration. Moreover, any of the common adduct ions ([M+Na]$^+$, [M+K] $^+$, [M+ACN+Na]$^+$, [2M+Na]$^+$ and [M+H-H$_2$O]$^+$) were found in the mass spectra of the studied samples.
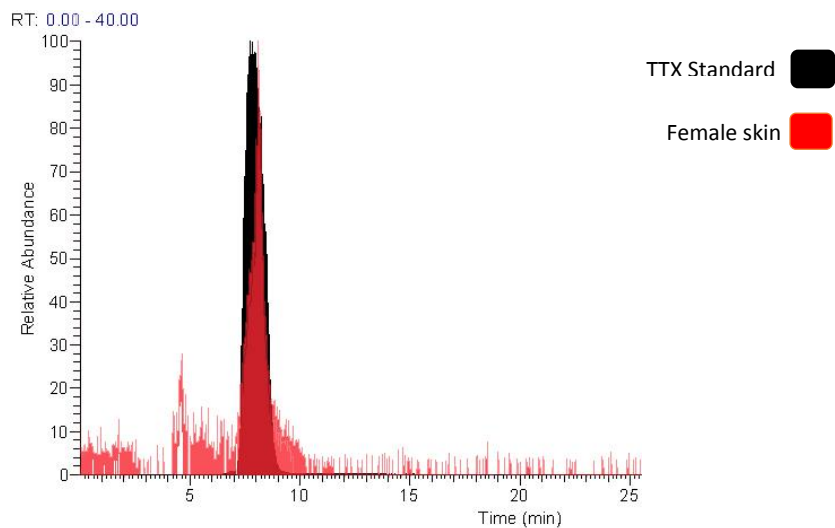
Figure 142. Overlapping of the LC-ESI(+)-HRMS extracted ion chromatogram of TTX standard (Black line) and Female Skin (Red line) under full scan
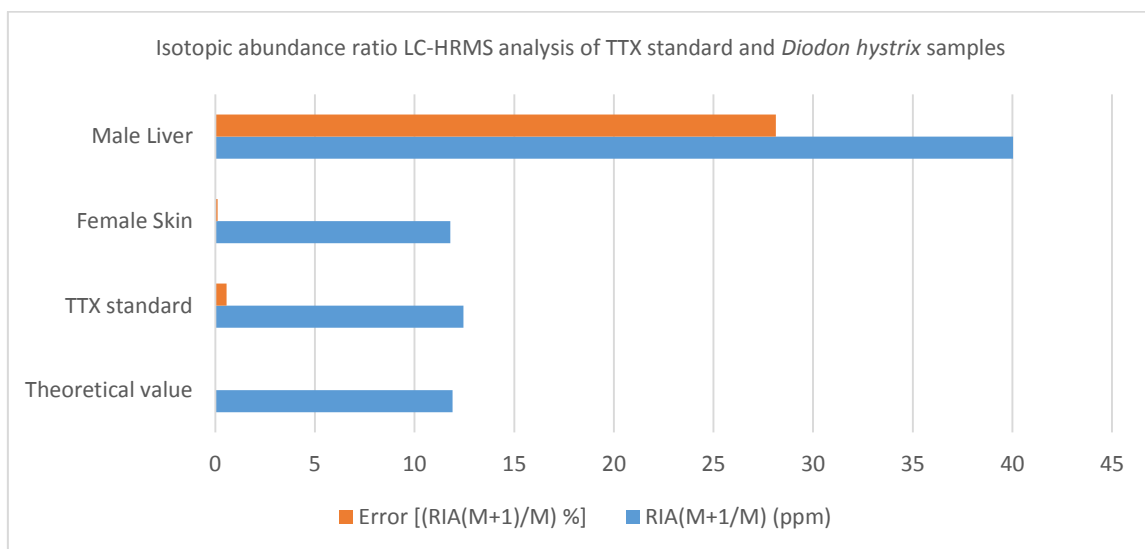
Figure 143. Isotopic ion abundance ratio (Blue) and isotopic ion abundance ratio error (Orange) using LTQ-Orbitrap on full scan mode.

LC HR MS^2 analysis

In order to ensure the presence of TTX, samples we analyzed by LC-high resolution (HR)-MS^2. A previous sample filtration step by using C18 Cartridges (Sep-Pak Plus of Waters) was carried out to remove any possible matrix interferences. TTX was used as standard to validate of the used method. TTX fragmentation was studied in the following samples from *D. hystrix*: Female skin, female gonads, male liver, female skin, undefined muscle and undefined liver. Parameters were set up by using a standard solution in order to have the best possible signal to noise ratio. TTX standard showed the expected two transitions very clearly (Figure 144, left column).

Molecular formulae and Ring Double Bond Equivalents (RBD) are very helpful tools when chemical structures are proposed. [291] They are generated in the Xcalibur 3.0 by using the exact mass function provided for the Orbitrap XL. Molecular formulae of the analyzed fragment ions matched to those of the reported in literature.[283] Two criteria were used for the selection of ions: they must be abundant during fragmentation and they must not be originated from the same part of the molecule under study. The only sample that showed the expected transitions for TTX was the undefined liver (UL) (Figure 144, right panel). Precursor ion at *m/z* 320 ($C_{11}H_{18}N_3O_8^+$, RBD = 4.5) gave the characteristic fragment ions at *m/z* 302 ($C_{11}H_{16}N_3O_7^+$, Δ *m/z* = 0.03 ppm, RBD = 5.5) and at m/z 162 ($C_8H_8N_3O^+$, Δ *m/z*: 3.64 ppm, RBD = 6.5). RBD value change from 4.5 to 5.5 for fragment at *m/z* 302 suggests the loss of a water molecule with an adjustment on the ring system that includes the formation of an extra 6 member ring [9-O-4-4a-8a] (Figure 145 middle). On the other hand, RBD value change from 5.5 to 6.5 for fragment *m/z* 162 suggests a mayor modification in the molecule that implies the break of several bonds with the formation of the structure displayed in Figure 145, right. The presence of TTX was also established in undefined liver sample on the basis on the experimental evidence collected from HR-MS^2 experiment (Table *28*)
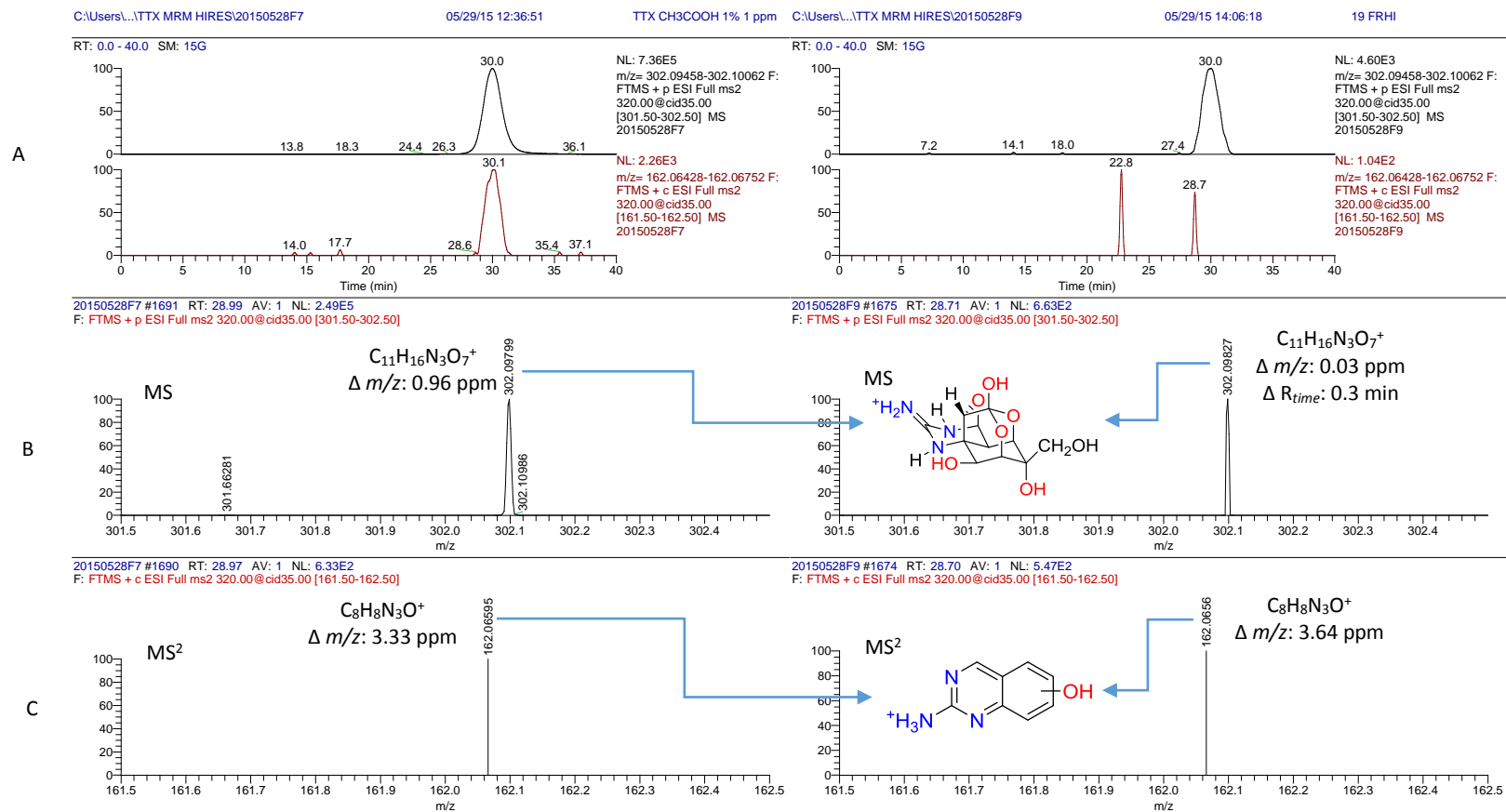
Figure 144. LC-ESI(+)-HRMS[2] of tetrodotoxin standard (Left column) and liver of undefined gender (UL) (Right column) of *Diodon hystrix*; obtained on a linear-trap quadruple-Orbitrap XL MS **(A –above)** Extracted ion chromatogram from *m/z* 320.00 → 302.09-302.1 **(A –below)** Extracted ion chromatogram from *m/z* 320.00 → 162.06. **(B -Right)** Fragmentation of the ion eluting at R$_{time}$ 28.8±0.1 min, shows the characteristics fragments at *m/z* 302.09828 m/z (Δ *m/z* = 0.03 ppm); which indicates the losing of a molecule of water on tetrodotoxin molecule **(C -Right)** Second fragmentation of the ion shows the characteristics fragments at *m/z* 162.06619 (Δ *m/z* = 3.64 ppm); which suggests the presents of the distinguishing group (5-8)-hydroxyquinazolin-2-amonium, commonly found in TTX fragmentation. LTQ-Orbitrap Discovery was operating with a resolution of 30000

TTX
Chemical Formula: $C_{11}H_{18}N_3O_8^+$
Exact Mass: 320.10884 Da

4,9-anhydro TTX
Chemical Formula: $C_{11}H_{16}N_3O_7^+$
Exact Mass: 302.09828 Da

(5-8)-hydroxyquinazolin-2-amonium
Chemical Formula: $C_8H_8N_3O^+$
Exact Mass: 162.06619 Da
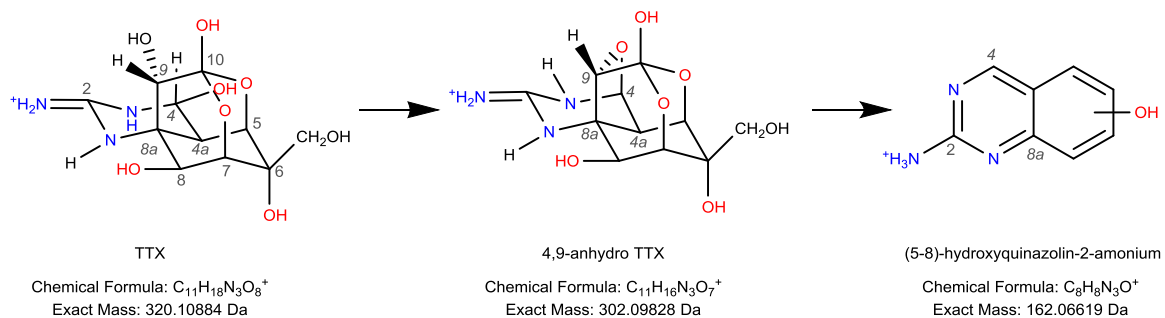
Figure 145. Chemical structures of TTX fragments generated on LTQ-Orbitrap XL, by MS^2 experiment

Data analysis by MZmine

Accurate mass is used as a robust tool to identity the presence of anilities in routine analysis. [278,291] Laboratories that wish to automatize natural products detection by LC-HRMS, should validate their data-analyzing-methodologies until proper software parameters are found. Since its introduction, MZmine has been successfully used in metabolomics and natural products dereplication over the years [292,293] and in combination with LTQ Orbitrap Hybrid Mass Spectrometer for data processing.[294,295] We do want to provide an optimized workflow using MZmine 2.3 for LC-HRMS data processing which is applicable for TTX detection. Software data-analyzing Workflow is shown in Figure 146 and parameters used are described below [278,296].
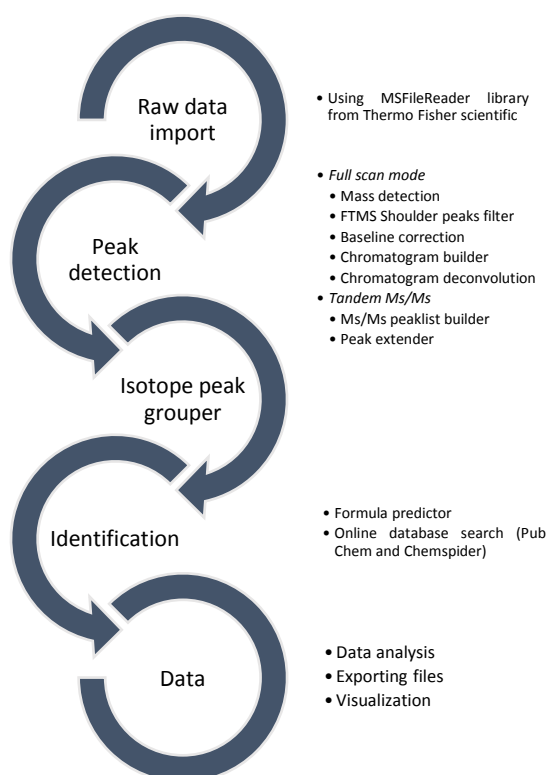
Figure 146. Data analysis workflow used on MZmine 2.3 for processing LC-HRMS files (*.raw) and dereplication of TTX

Orbitrap files from the samples were analyzed in automatized mode. A peak emerge after treating female skin Orbitrap data file with aforementioned workflow (Figure 146), which was attributed to the compound of interest. TTX was certainly identified in FS sample with the aid of existing high resolution MS, isotope pattern and RDB available on online databases records through connection supported by MZmine. MZmine 2 is an appropriate tool to automatic peak detection in LTQ Orbitrap files (*.Raw) routinely toxin detection.
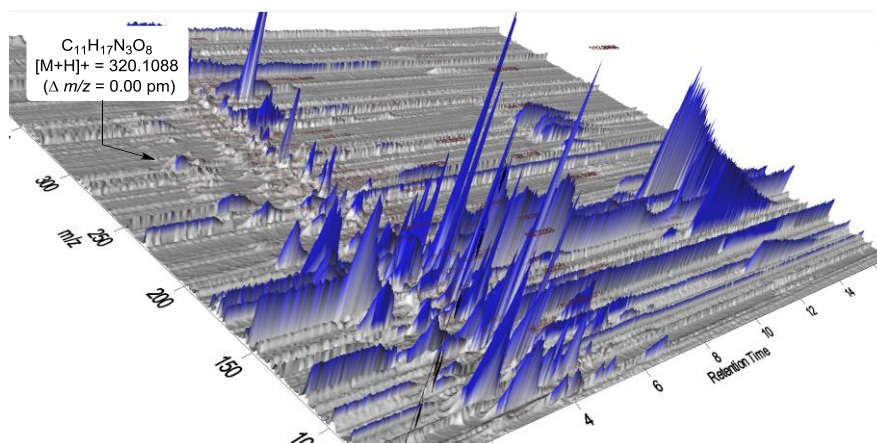
Figure 147. LC/HRMS (3D projection) of female skin sample from *Diodon hystrix*

2.6.5 Conclusions

LC-HRMS analysis of several specimens of *Diodon hystrix* (Porcupinefish) collected in El Salvador have demonstrated the presence of TTX (Table 28). Several techniques were used that includes MRM-MS/MS, LC-HRMS and LC-HRMS[2] along with a post-processing data using MZmine 2. Detection was validated using a commercially available TTX sample as standard and the values obtained were in agreement with the detection parameters described in SANTE 11945/2015. Although TTX has been detected in species of the *Diodon hystrix*, this is the first study of the detection of this toxin in fishes collected in El Salvador. The developed approach used here can be adapted to detect TTX from other marine sources such as bacteria and invertebrates with minimum changes.

References

1. Wirz, L. N. & Allison, J. R. Fitting alignment tensor components to experimental RDCs, CSAs and RQCs. *J. Biomol. NMR* **62,** 25–29 (2015).

2. Tripathy, C., Yan, A. K., Zhou, P. & Donald, B. R. Extracting Structural Information from Residual Chemical Shift Anisotropy: Analytic Solutions for Peptide Plane Orientations and Applications to Determine Protein Structure BT - Research in Computational Molecular Biology. in (eds. Deng, M., Jiang, R., Sun, F. & Zhang, X.) 271–284 (Springer Berlin Heidelberg, 2013).

3. Losonczi, J. A., Andrec, M., Fischer, M. W. F. & Prestegard, J. H. Order Matrix Analysis of Residual Dipolar Couplings Using Singular Value Decomposition. *J. Magn. Reson.* **138,** 334–342 (1999).

4. Hallwass, F. *et al.* Residual Chemical Shift Anisotropy (RCSA): A Tool for the Analysis of the Configuration of Small Molecules. *Angew. Chemie Int. Ed.* **50,** 9487–9490 (2011).

5. Smith, S. G. & Goodman, J. M. Assigning stereochemistry to single diastereoisomers by GIAO NMR calculation: The DP4 probability. *J. Am. Chem. Soc.* **132,** 12946–12959 (2010).

6. Bifulco, G., Bassarello, C. & Riccio, R. Calculations of NMR J-Coupling Values in the Determination of Relative Configuration in Organic Compounds.

7. Hellemann, E. & Gil, R. R. New Stretching Method for Aligning Gels: Its Application to the Measurement Residual Chemical Shift Anisotropies (RCSAs) without the Need for Isotropic Shift Correction. *Chem. – A Eur. J.* **24,** 3689–3693 (2018).

8. Isaacson, E. Numerical Recipes in C: The Art of Scientific Computing (William H. Press, Brian P. Flannery, Saul A. Teukolsky, and William T. Vetterling); Numerical Recipes: Example Book (C) (William T. Vetterling, Saul A. Teukolsky, William H. Press, and Brian P. Flannery). *SIAM Rev.* **31,** 142 (1989).

9. Navarro-Vázquez, A. MSpin-RDC. A program for the use of residual dipolar couplings for structure elucidation of small molecules. *Magn. Reson. Chem.* **50,** S73–S79 (2012).

10. Hallwass, F. *et al.* Measurement of residual chemical shift anisotropies in compressed polymethylmethacrylate gels. Automatic compensation of gel isotropic shift contribution. *Magn. Reson. Chem.* **56,** 321–328 (2018).

11. d'Auvergne, E. J. & Gooley, P. R. Optimisation of NMR dynamic models II. A new methodology for the dual optimisation of the model-free parameters and the Brownian rotational diffusion tensor. *J. Biomol. NMR* **40,** 121–133 (2008).

12. Sun, H. *et al.* Challenge of Large-Scale Motion for Residual Dipolar Coupling Based Analysis of Configuration: The Case of Fibrosterol Sulfate A. *J. Am. Chem. Soc.* **133,** 14629–14636 (2011).

13. Liu, L.-Y., Sun, H., Griesinger, C. & Liu, J.-K. The Use of a Combination of RDC and Chiroptical Spectroscopy for Determination of the Absolute Configuration of Fusariumin A from the Fungus Fusarium sp. *Nat. Prod. Bioprospect.* **6,** 41–48 (2016).

14. Schuetz, A. *et al.* Stereochemistry of sagittamide a from residual dipolar coupling enhanced NMR. *J. Am. Chem. Soc.* **129,** 15114–15115 (2007).

15.   R. Gil, R. *Structural analysis of rigid and flexible small organic molecules assisted by residual dipolar couplings*. *Planta Medica* **80,** (2014).

16.   Liu, Y. & Prestegard, J. H. A device for the measurement of residual chemical shift anisotropy and residual dipolar coupling in soluble and membrane-associated proteins. *J. Biomol. NMR* **47,** 249–258 (2010).

17.   Nath, N. *et al. Determination of configuration of small molecules from residual chemical shift anisotropy (RCSAs) at microgram levels CDCl 3 compatible Poly(methyl methacrylate)(PMMA) gel : Different alignment conditions could be induced by moving the piston of the New E*. (2016).

18.   Nath, Nilamoni; Fuentes-Monteverde, Juan Carlos; Regelin, Michael; Pech-Puch, Dawrin; Jiménez, Carlos; Rodríguez, J. G. C. Unequivocal determination of 3D molecular structures including relative configuration using proton residual chemical shift anisotropy. (2019).

19.   Cornilescu, G., Marquardt, J. L., Ottiger, M. & Bax, A. Validation of Protein Structure from Anisotropic Carbonyl Chemical Shifts in a Dilute Liquid Crystalline Phase. *J. Am. Chem. Soc.* **120,** 6836–6837 (1998).

20.   Timári, I. *et al.* Real-time broadband proton-homodecoupled CLIP/CLAP-HSQC for automated measurement of heteronuclear one-bond coupling constants. *RSC Adv.* **6,** 87848–87855 (2016).

21.   Thiele, C. M. & Bermel, W. Speeding up the measurement of one-bond scalar (1J) and residual dipolar couplings (1D) by using non-uniform sampling (NUS). *J. Magn. Reson.* **216,** 134–143 (2012).

22.   Nath, N. *et al.* Determination of Relative Configuration from Residual Chemical Shift Anisotropy. *J. Am. Chem. Soc.* **138,** 9548–9556 (2016).

23.   Marcó, N., Gil, R. R. & Parella, T. Isotropic/Anisotropic NMR Editing by Resolution-Enhanced NMR Spectroscopy. *ChemPhysChem* **19,** 1024–1029 (2018).

24.   Kiraly, P., Nilsson, M. & Morris, G. A. Practical aspects of real-time pure shift HSQC experiments. *Magn. Reson. Chem.* **56,** 993–1005 (2017).

25.   Foroozandeh, M. *et al.* Ultrahigh-Resolution NMR Spectroscopy. *Angew. Chemie Int. Ed.* **53,** 6990–6992 (2014).

26.   Foroozandeh, M., Morris, G. A. & Nilsson, M. PSYCHE Pure Shift NMR Spectroscopy. *Chem. – A Eur. J.* **24,** 13988–14000 (2018).

27.   Kiraly, P. *et al.* Real-time pure shift (15)N HSQC of proteins: a real improvement in resolution and sensitivity. *J. Biomol. Nmr* **62,** 43–52 (2015).

28.   Troche-Pesqueira, E., Anklin, C., Gil, R. R. & Navarro-Vázquez, A. Computer-Assisted 3D Structure Elucidation of Natural Products using Residual Dipolar Couplings. *Angew. Chemie Int. Ed.* **56,** 3660–3664 (2017).

29.   Agranat, I., Wainschtein, S. R. & Zusman, E. Z. The predicated demise of racemic new molecular entities is an exaggeration. *Nat. Rev. Drug Discov.* **11,** 972 (2012).

30.   Nicolaou, K. C. & Snyder, S. A. Chasing Molecules That Were Never There: Misassigned Natural Products and the Role of Chemical Synthesis in Modern Structure Elucidation. *Angew. Chemie Int. Ed.* **44,** 1012–1044 (2005).

31. Schmidt, M. *et al.* Determining the Absolute Configuration of (+)-Mefloquine HCl, the Side-Effect-Reducing Enantiomer of the Antimalaria Drug Lariam. *J. Am. Chem. Soc.* **134,** 3080–3083 (2012).

32. XIE, Z.-X., ZHANG, L.-Z., REN, X.-J., TANG, S.-Y. & LI, Y. Asymmetric Synthesis of (+)-(11R,12S)-Mefloquine Hydrochloride. *Chinese J. Chem.* **26,** 1272–1276 (2008).

33. Pattenden, G., Ashweek, N. J., Baker-Glenn, C. A. G., Walker, G. M. & Yee, J. G. K. Total Synthesis of (−)-Ulapualide A: The Danger of Overdependence on NMR Spectroscopy in Assignment of Stereochemistry. *Angew. Chemie Int. Ed.* **46,** 4359–4363 (2007).

34. Anet, F. A. L. & Bourn, A. J. R. Nuclear Magnetic Resonance Spectral Assignments from Nuclear Overhauser Effects1. *J. Am. Chem. Soc.* **87,** 5250–5251 (1965).

35. Haasnoot, C. A. G., de Leeuw, F. A. A. M. & Altona, C. The relationship between proton-proton NMR coupling constants and substituent electronegativities—I: An empirical generalization of the karplus equation. *Tetrahedron* **36,** 2783–2792 (1980).

36. Butts, C. P. *et al.* Interproton distance determinations by NOE - surprising accuracy and precision in a rigid organic molecule. *Org. Biomol. Chem.* **9,** 177–184 (2011).

37. Matsumori, N., Kaneno, D., Murata, M., Nakamura, H. & Tachibana, K. Stereochemical Determination of Acyclic Structures Based on Carbon–Proton Spin-Coupling Constants. A Method of Configuration Analysis for Natural Products. *J. Org. Chem.* **64,** 866–876 (1999).

38. Tjandra, N. & Bax, A. Direct Measurement of Distances and Angles in Biomolecules by NMR in a Dilute Liquid Crystalline Medium. *Science (80-.).* **278,** 1111 LP-1114 (1997).

39. Bax, A., Kontaxis, G. & Tjandra, N. in *Nuclear Magnetic Resonance of Biological Macromolecules - Part B* (eds. James, T. L., Dötsch, V. & Schmitz, U. B. T.-M. in E.) **339,** 127–174 (Academic Press, 2001).

40. Kummerlöwe, G. & Luy, B. in (ed. Webb, G. A. B. T.-A. R. on N. M. R. S.) **68,** 193–232 (Academic Press, 2009).

41. Thiele, C. M. *et al.* On the Treatment of Conformational Flexibility when Using Residual Dipolar Couplings for Structure Determination. *Angew. Chemie Int. Ed.* **48,** 6708–6712 (2009).

42. Schmid, M. B. *et al.* Residual Dipolar Couplings in Short Peptidic Foldamers: Combined Analyses of Backbone and Side-Chain Conformations and Evaluation of Structure Coordinates of Rigid Unnatural Amino Acids. *ChemBioChem* **10,** 440–444 (2009).

43. Gayathri, C., Tsarevsky, N. V. & Gil, R. R. Residual dipolar couplings (RDCs) analysis of small molecules made easy: Fast and tuneable alignment by reversible compression/relaxation of reusable PMMA gels. *Chem. - A Eur. J.* **16,** 3622–3626 (2010).

44. Trigo-Mouriño, P., Navarro-Vázquez, A., Ying, J., Gil, R. R. & Bax, A. Structural Discrimination in Small Molecules by Accurate Measurement of Long-Range Proton–Carbon NMR Residual Dipolar Couplings. *Angew. Chemie Int. Ed.* **50,** 7576–7580 (2011).

45. Kummerlöwe, G. *et al.* Variable angle NMR spectroscopy and its application to the measurement of residual chemical shift anisotropy. *J. Magn. Reson.* **209,** 19–30 (2011).

46. Liu, Y. *et al.* Unequivocal determination of complex molecular structures using anisotropic NMR measurements. *Science (80-.).* **356,** (2017).

47. Freudenberger, J. C., Spiteller, P., Bauer, R., Kessler, H. & Luy, B. Stretched Poly(dimethylsiloxane) Gels as NMR Alignment Media for Apolar and Weakly Polar Organic Solvents: An Ideal Tool for Measuring RDCs at Low Molecular Concentrations. *J. Am. Chem. Soc.* **126,** 14690–14691 (2004).

48. Meyer, N.-C. C., Krupp, A., Schmidts, V., Thiele, C. M. & Reggelin, M. Polyacetylenes as Enantiodifferentiating Alignment Media. *Angew. Chemie Int. Ed.* **51,** 8334–8338 (2012).

49. Czarniecka, K. & Samulski, E. T. Polypeptide Liquid Crystals: A Deuterium NMR Study. *Mol. Cryst. Liq. Cryst.* **63,** 205–214 (1981).

50. Gil-Silva, L. F., Santamaría-Fernández, R., Navarro-Vázquez, A. & Gil, R. R. Collection of NMR Scalar and Residual Dipolar Couplings Using a Single Experiment. *Chem. – A Eur. J.* **22,** 472–476 (2015).

51. Moskalenko, Y. E., Bagutski, V. & Thiele, C. M. Chemically synthesized and cross-linked PDMS as versatile alignment medium for organic compounds. *Chem. Commun.* **53,** 95–98 (2017).

52. Zong, W. *et al.* An Alignment Medium for Measuring Residual Dipolar Couplings in Pure DMSO: Liquid Crystals from Graphene Oxide Grafted with Polymer Brushes. *Angew. Chemie Int. Ed.* **55,** 3690–3693 (2016).

53. Leyendecker, M., Meyer, N.-C & Thiele, C. M. Development of New Supramolecular Lyotropic Liquid Crystals and Their Application as Alignment Media for Organic Compounds. *Angew. Chemie* **129,** 11629–11632 (2017).

54. Wolkenstein, K., Sun, H., Falk, H. & Griesinger, C. *Structure and Absolute Configuration of Jurassic Polyketide-Derived Spiroborate Pigments Obtained from Microgram Quantities*. *Journal of the American Chemical Society* **137,** (2015).

55. Chou, J. J., Gaemers, S., Howder, B., Louis, J. M. & Bax, A. A simple apparatus for generating stretched polyacrylamide gels, yielding uniform alignment of proteins and detergent micelles*. *J. Biomol. NMR* **21,** 377–382 (2001).

56. Liu, Y., Cohen, R. D., Gustafson, K. R., Martin, G. E. & Williamson, R. T. Enhanced measurement of residual chemical shift anisotropy for small molecule structure elucidation. *Chem. Commun.* **54,** 4254–4257 (2018).

57. Kramer, F., Deshmukh, M. V, Kessler, H. & Glaser, S. J. Residual dipolar coupling constants: An elementary derivation of key equations. *Concepts Magn. Reson. Part A* **21A,** 10–21 (2004).

58. Bifulco, G., Riccio, R., Martin, G. E., Buevich, A. V & Williamson, R. T. Quantum Chemical Calculations of 1JCC Coupling Constants for the Stereochemical Determination of Organic Compounds. *Org. Lett.* **15,** 654–657 (2013).

59. Frisch, M. J. *et al.* Gaussian 09, Revision B.01. *Gaussian 09, Revision B.01, Gaussian, Inc., Wallingford CT* (2009).

60. García, M. E., Woodruff, S. R., Hellemann, E., Tsarevsky, N. V & Gil, R. R. Di(ethylene glycol) methyl ether methacrylate (DEGMEMA)-derived gels align small organic molecules in methanol. *Magn. Reson. Chem.* **55,** 206–209 (2016).

61. Schrödinger. MacroModel. (2018).

62. Halgren, T. A. Merck molecular force field. I. Basis, form, scope, parameterization, and performance of MMFF94. *J. Comput. Chem.* **17,** 490–519 (2018).

63.   Gilbert, K. E. Pcmodel. (2014).

64.   Ramelow, U. S. & Pingili, S. Synthesis of Ethylene Glycol Dimethacrylate-Methyl Methacrylate Copolymers, Determination of their Reactivity Ratios, and a Study of Dopant and Temperature Effects on their Conductivities. *Polymers* **2,** (2010).

65.   Hatäda, K., Kitayama, T., Fujikawa, K., Ohta, K. & Yuki, H. *Studies on the Anionic Polymerization of Methyl Methacrylate Initiated with Butyllithium in Toluene by Using Perdeuterated Monomer*. *Polymer Bulletin* **1,** (1978).

66.   Hatada, K., Kitayama, T. & Masuda, E. Studies on the Radical Polymerization of Methyl Methacrylate in Bulk and in Benzene Using Totally Deuterated Monomer Technique. *Polym. J.* **18,** 395 (1986).

67.   Mathias, L. J. *et al.* Gel-state NMR investigation of crosslinked poly(methy1 methacrylate) incorporating 13C labeled ethylene glycol dimethacrylate. *Macromol. Symp.* **141,** 47–56 (2011).

68.   Min, K., Silberstein, M. & Aluru, N. R. Crosslinking PMMA: Molecular dynamics investigation of the shear response. *J. Polym. Sci. Part B Polym. Phys.* **52,** 444–449 (2013).

69.   Kimura, T., Kodaira, T. & Hamashima, M. Separation and Structure of Methyl Methacrylate Telomers Synthesized in the Presence of Bromotrichloromethane. *Polym. J.* **15,** 293 (1983).

70.   Hatada, K., Kitayama, T. & Yuki, H. Studies on the radical polymerization of methyl methacrylate using perdeuterated monomer. *Die Makromol. Chemie, Rapid Commun.* **1,** 51–56 (2018).

71.   ABE, Y. *et al.* The Total Synthesis of Santonin. *Proc. Jpn. Acad.* **30,** 116–118 (1954).

72.   Teles, Rubens R; França, José; Navarro-Vázquez, Armando; Hallwass, F. ATRIBUIÇÃO DA ESTEREOQUÍMICA DA α-SANTONINA ATRAVÉS DAS MEDIDAS DO ACOPLAMENTO DIPOLAR RESIDUAL. *Quim. Nova* **38,** 1345–1350 (2015).

73.   Ivanescu, B., Miron, A. & Corciova, A. Sesquiterpene Lactones from Artemisia Genus: Biological Activities and Methods of Analysis. *J. Anal. Methods Chem.* **2015,** 247685 (2015).

74.   Sakipova, Z. *et al.* Quantification of santonin in eight species of Artemisia from Kazakhstan by means of HPLC-UV: Method development and validation. *PLoS One* **12,** e0173714–e0173714 (2017).

75.   SHLLINGER, J. E. Anthelmintic Properties of Santonin. *J. Agric. Res.* **34,** 839–845 (1927).

76.   R. OLDHAM, R., M Wang, Y., van Eys, J. & P. CARTER, J. *Hemolytic Crisis in a Patient Treated With Santonin: Possible Santonin Poisoning*. *Southern medical journal* **64,** (1971).

77.   Discovery Studio. (2016).

78.   Adamo, C. & Barone, V. Toward reliable density functional methods without adjustable parameters: The PBE0 model. *J. Chem. Phys.* **110,** 6158–6170 (1999).

79.   Dunning, T. H. Gaussian basis sets for use in correlated molecular calculations. I. The atoms boron through neon and hydrogen. *J. Chem. Phys.* **90,** 1007–1023 (1989).

80.   Cheeseman, J. R., Trucks, G. W., Keith, T. A. & Frisch, M. J. A comparison of models for

calculating nuclear magnetic resonance shielding tensors. *J. Chem. Phys.* **104,** 5497–5509 (1996).

81. Scalmani, G. & Frisch, M. J. Continuous surface charge polarizable continuum models of solvation. I. General formalism. *J. Chem. Phys.* **132,** 114110 (2010).

82. Foroozandeh, M., Adams, R. W., Nilsson, M. & Morris, G. A. Ultrahigh-Resolution Total Correlation NMR Spectroscopy. *J. Am. Chem. Soc.* **136,** 11867–11869 (2014).

83. Marquardt, D. An Algorithm for Least-Squares Estimation of Nonlinear Parameters. *J. Soc. Ind. Appl. Math.* **11,** 431–441 (1963).

84. Cornilescu, G. & Bax, A. Measurement of Proton, Nitrogen, and Carbonyl Chemical Shielding Anisotropies in a Protein Dissolved in a Dilute Liquid Crystalline Phase. *J. Am. Chem. Soc.* **122,** 10143–10154 (2000).

85. Balboa, E. M. *et al.* Photodamage attenuation effect by a tetraprenyltoluquinol chromane meroterpenoid isolated from Sargassum muticum. *J. Photochem. Photobiol. B Biol.* **148,** 51–58 (2015).

86. Valls, R., Piovetti, L., Banaigst, B. & Praud, A. Secondary metabolites from Morocco brown algae of the genus Cystoseira. *Phytochemistry* **32,** 961–966 (1993).

87. Valls, R., Mesguiche, V., Piovetti, L., Prost, M. & Peiffer, G. Meroditerpenes from the brown alga Cystoseira amentacea var. stricta collected off the French mediterranean coast. *Phytochemistry* **41,** 1367–1371 (1996).

88. Cecilia Noguez, F. H. Good Computational Practice in the Assignment of Absolute Configurations by TDDFT Calculations of ECD Spectra. *Chirality* **26,** 553–562 (2014).

89. Brémond, É. *et al.* Benchmarking Density Functionals on Structural Parameters of Small-/Medium-Sized Organic Molecules. *J. Chem. Theory Comput.* **12,** 459–465 (2016).

90. Stewart, J. J. P. Optimization of parameters for semiempirical methods I. Method. *J. Comput. Chem.* **10,** 209–220 (2018).

91. Heyd, J. & Scuseria, G. E. Efficient hybrid density functional calculations in solids: Assessment of the Heyd–Scuseria–Ernzerhof screened Coulomb hybrid functional. *J. Chem. Phys.* **121,** 1187–1192 (2004).

92. Peverati, R. & Truhlar, D. G. Communication: A global hybrid generalized gradient approximation to the exchange-correlation functional that satisfies the second-order density-gradient constraint and has broad applicability in chemistry. *J. Chem. Phys.* **135,** 191102 (2011).

93. Weigend, F. & Ahlrichs, R. Balanced basis sets of split valence, triple zeta valence and quadruple zeta valence quality for H to Rn: Design and assessment of accuracy. *Phys. Chem. Chem. Phys.* **7,** 3297–305 (2005).

94. Kontaxis, G., Clore, G. M. & Bax, A. Evaluation of Cross-Correlation Effects and Measurement of One-Bond Couplings in Proteins with Short Transverse Relaxation Times. *J. Magn. Reson.* **143,** 184–196 (2000).

95. Rumsey, D. J. *Statistics For Dummies*. (Wiley Publishing, Inc., 2003).

96. Furrer, J., John, M., Kessler, H. & Luy, B. *J-Spectroscopy in the presence of residual dipolar couplings: Determination of one-bond coupling constants and scalable resolution*. *Journal of biomolecular NMR* **37,** (2007).

97. Thiele, C. M. Use of RDCs in rigid organic compounds and some practical considerations concerning alignment media. *Concepts Magn. Reson. Part A* **30A,** 65–80 (2007).

98. Griesinger, C., Meiler, J. & Peti, W. in (eds. Krishna, N. R. & Berliner, L. J.) 163–229 (Springer US, 2002). doi:10.1007/0-306-47936-2_7

99. Kakita, V. M. R., Rachineni, K. & Bharatam, J. Unambiguous determination of conformation and relative configuration of a multiple stereo-centre molecule Rifamycin-S by using scaled residual dipolar couplings: A case study. *J. Mol. Struct.* **1053,** 122–126 (2013).

100. Choy, W.-Y., Tollinger, M., Mueller, G. & E. Kay, L. *Direct structure refinement of high molecular weight proteins against residual dipolar couplings and carbonyl chemical shift changes upon alignment: An application to maltose binding protein. Journal of Biomolecular NMR* **21,** (2001).

101. COSSUTA, D. *et al.* EXTRACTION OF HYPERFORIN AND HYPERICIN FROM ST. JOHN'S WORT (HYPERICUM PERFORATUM L.) WITH DIFFERENT SOLVENTS. *J. Food Process Eng.* **35,** 222–235 (2011).

102. Wang, H. M. *et al.* Isolation and spectral study of 4-methyl-6,8-dihydroxy-7H-benz[de]anthracen-7-one. *Magn. Reson. Chem.* **41,** 301–303 (2003).

103. Wolkenstein, K., Schoefberger, W., Müller, N. & Oji, T. Proisocrinins A–F, Brominated Anthraquinone Pigments from the Stalked Crinoid Proisocrinus ruberrimus. *J. Nat. Prod.* **72,** 2036–2039 (2009).

104. Martin-Pastor, M., Canales-Mayordomo, A. & Jiménez-Barbero, J. NMR experiments for the measurement of proton–proton and carbon–carbon residual dipolar couplings in uniformly labelled oligosaccharides. *J. Biomol. NMR* **26,** 345–353 (2003).

105. Li, G.-W., Liu, H., Qiu, F., Wang, X.-J. & Lei, X.-X. Residual Dipolar Couplings in Structure Determination of Natural Products. *Nat. Products Bioprospect.* **8,** 279–295 (2018).

106. Marcó, N., Nolis, P., Gil, R. R. & Parella, T. 2JHH-resolved HSQC: Exclusive determination of geminal proton-proton coupling constants. *J. Magn. Reson.* **282,** 18–26 (2017).

107. Cecilia Noguez, F. H. SpecDis: Quantifying the Comparison of Calculated and Experimental Electronic Circular Dichroism Spectra. *Chirality* **26,** 553–562 (2014).

108. WATSON, J. T. O. D. S. An Introduction to Mass Spectrometry: Instrumentation, Applications and Strategies for Data Interpretation. 1–20 (2009).

109. Miertuš, S., Scrocco, E. & Tomasi, J. Electrostatic interaction of a solute with a continuum. A direct utilizaion of AB initio molecular potentials for the prevision of solvent effects. *Chem. Phys.* **55,** 117–129 (1981).

110. Adamo, C. & Barone, V. Exchange functionals with improved long-range behavior and adiabatic connection methods without adjustable parameters: The mPW and mPW1PW models. *J. Chem. Phys.* **108,** 664–675 (1998).

111. Foroozandeh, M., Adams, R. W., Nilsson, M. & Morris, G. A. Ultrahigh-Resolution Total Correlation NMR Spectroscopy. *J. Am. Chem. Soc.* **136,** 11867–11869 (2014).

112. Enthart, A., Freudenberger, J. C., Furrer, J., Kessler, H. & Luy, B. The CLIP/CLAP-HSQC: Pure absorptive spectra for the measurement of one-bond couplings. *J. Magn. Reson.* **192,** 314–322 (2008).

113. Efron, B. Bootstrap Methods: Another Look at the Jackknife. *Ann. Stat.* **7,** 1–26 (1979).

114. Sánchez-Pedregal, V. M., Santamaría-Fernández, R. & Navarro-Vázquez, A. Residual Dipolar Couplings of Freely Rotating Groups in Small Molecules. Stereochemical Assignment and Side-Chain Conformation of 8-Phenylmenthol. *Org. Lett.* **11,** 1471–1474 (2009).

115. Böttcher, B. & Thiele, C. M. Determining the Stereochemistry of Molecules from Residual Dipolar Couplings (RDCs). *eMagRes* (2012). doi:doi:10.1002/9780470034590.emrstm1194

116. Criddle, L. M. & Aacn, by. Rhabdomyolysis: Pathophysiology, Recognition, and Management Email alerts. **23,** (2003).

117. Bedry, R. *et al.* Wild-Mushroom Intoxication as a Cause of Rhabdomyolysis. *N. Engl. J. Med.* **345,** 798–802 (2001).

118. Laubner, G. & Mikulevičienė, G. A series of cases of rhabdomyolysis after ingestion of Tricholoma equestre. *Acta medica Litu.* **23,** 193–197 (2016).

119. Nieminen, P., Kärjä, V. & Mustonen, A.-M. Indications of hepatic and cardiac toxicity caused by subchronic Tricholoma flavovirens consumption. *Food Chem. Toxicol.* **46,** 781–786 (2008).

120. Fujii, K., Ikai, Y., Oka, H., Suzuki, M. & Harada, K. A Nonempirical Method Using LC/MS for Determination of the Absolute Configuration of Constituent Amino Acids in a Peptide: Combination of Marfey's Method with Mass Spectrometry and Its Practical Application. *Anal. Chem.* **69,** 5146–5151 (1997).

121. Wu, W. *et al.* Isolation and Structural Elucidation of Proline-Containing Cyclopentapeptides from an Endolichenic Xylaria sp. *J. Nat. Prod.* **74,** 1303–1308 (2011).

122. Krukau, A. V, Vydrov, O. A., Izmaylov, A. F. & Scuseria, G. E. Influence of the exchange screening parameter on the performance of screened hybrid functionals. *J. Chem. Phys.* **125,** 224106 (2006).

123. Chai, J.-D. & Head-Gordon, M. Long-range corrected hybrid density functionals with damped atom-atom dispersion corrections. *Phys. Chem. Chem. Phys.* **10,** 6615–6620 (2008).

124. Runge, E. & Gross, E. K. U. Density-Functional Theory for Time-Dependent Systems. *Phys. Rev. Lett.* **52,** 997–1000 (1984).

125. Schmider, H. L. & Becke, A. D. Optimized density functionals from the extended G2 test set. *J. Chem. Phys.* **108,** 9624–9631 (1998).

126. Yanai, T., Tew, D. P. & Handy, N. C. A new hybrid exchange–correlation functional using the Coulomb-attenuating method (CAM-B3LYP). *Chem. Phys. Lett.* **393,** 51–57 (2004).

127. Curtiss, L. A. *et al.* Extension of Gaussian-2 theory to molecules containing third-row atoms Ga–Kr. *J. Chem. Phys.* **103,** 6104–6113 (1995).

128. Mennucci, B. Polarizable continuum model. *Wiley Interdiscip. Rev. Comput. Mol. Sci.* **2,** 386–404 (2012).

129. Marques, M. A. L. & Gross, E. K. U. TIME-DEPENDENT DENSITY FUNCTIONAL THEORY. *Annu. Rev. Phys. Chem.* **55,** 427–455 (2004).

130. Gilbert, K. E. PC Model. (2014).

131. Barone, V. & Cossi, M. Quantum Calculation of Molecular Energies and Energy Gradients in Solution by a Conductor Solvent Model. *J. Phys. Chem. A* **102,** 1995–2001 (1998).

132. Cossi, M., Rega, N., Scalmani, G. & Barone, V. Energies, structures, and electronic properties of molecules in solution with the C-PCM solvation model. *J. Comput. Chem.* **24,** 669–681 (2003).

133. Paudel, L. *et al.* Simultaneously Enhancing Spectral Resolution and Sensitivity in Heteronuclear Correlation NMR Spectroscopy. *Angew. Chemie Int. Ed.* **52,** 11616–11619 (2013).

134. Lodewyk, M. W., Siebert, M. R. & Tantillo, D. J. Computational Prediction of 1H and 13C Chemical Shifts: A Useful Tool for Natural Product, Mechanistic, and Synthetic Organic Chemistry. *Chem. Rev. (Washington, DC, United States)* **112,** 1839–1862 (2012).

135. Kolmer, A., Edwards, L. J., Kuprov, I. & Thiele, C. M. Conformational analysis of small organic molecules using NOE and RDC data: A discussion of strychnine and α-methylene-γ-butyrolactone. *J. Magn. Reson.* **261,** 101–109 (2015).

136. Rodríguez, J. *et al.* Thelepamide: An Unprecedented Ketide-Amino Acid from Thelepus crispus, a Marine Annelid Worm. *Org. Lett.* **16,** 464–467 (2014).

137. Eckart, C. Some Studies Concerning Rotating Axes and Polyatomic Molecules. *Phys. Rev.* **47,** 552–558 (1935).

138. Sass, J. *et al.* Purple Membrane Induced Alignment of Biological Macromolecules in the Magnetic Field. *J. Am. Chem. Soc.* **121,** 2047–2055 (1999).

139. Procházková, E. *et al.* Uncovering Key Structural Features of an Enantioselective Peptide-Catalyzed Acylation Utilizing Advanced NMR Techniques. *Angew. Chemie Int. Ed.* **55,** 15754–15759 (2016).

140. Willoughby, P. H., Jansma, M. J. & Hoye, T. R. A guide to small-molecule structure assignment through computation of (1H and 13C) NMR chemical shifts. *Nat. Protoc.* **9,** 643 (2014).

141. J. Willmott, C. & Matsuura, K. *Advantages of the Mean Absolute Error (MAE) over the Root Mean Square Error (RMSE) in Assessing Average Model Performance*. *Climate Research* **30,** (2005).

142. Wolkenstein, K., Gross, J. H. & Falk, H. Boron-containing organic pigments from a Jurassic red alga. *Proc. Natl. Acad. Sci. U. S. A.* **107,** 19374–19378 (2010).

143. Schmidts, V. *et al.* RDC-Based Determination of the Relative Configuration of the Fungicidal Cyclopentenone 4,6-Diacetylhygrophorone A12. *J. Nat. Prod.* **76,** 839–844 (2013).

144. Timári, I. *et al.* Accurate determination of one-bond heteronuclear coupling constants with "pure shift" broadband proton-decoupled CLIP/CLAP-HSQC experiments. *J. Magn. Reson.* **239,** 130–138 (2014).

145. Ge, H. M. *et al.* Relative and Absolute Configuration of Vatiparol (1 mg): A Novel Anti-inflammatory Polyphenol. *Chem. – A Eur. J.* **18,** 5213–5221 (2012).

146. Shah, C. A., Rosario, G. X. & Sachdeva, G. Progesterone receptors : various forms and

functions in reproductive tissues. (2005).

147. Korde, S. S., Katoch, R., Udasi, R. A. & Trivedi, G. K. Total assignment of 1H and 13C NMR spectra of pregnenolone and progesterone haptens using 2D NMR spectroscopy. *Magn. Reson. Chem.* **37,** 594–597 (1999).

148. Kummerlöwe, G., Halbach, F., Laufer, B. & Luy, B. Precise Measurement of RDCs in Water and DMSO Based Gels Using a Silicone Rubber Tube for Tunable Stretching. 29–33 (2008).

149. Gil, R. R., Gayathri, C., Tsarevsky, N. V & Matyjaszewski, K. Stretched Poly(methyl methacrylate) Gel Aligns Small Organic Molecules in Chloroform. Stereochemical Analysis and Diastereotopic Proton NMR Assignment in Ludartin Using Residual Dipolar Couplings and 3J Coupling Constant Analysis. *J. Org. Chem.* **73,** 840–848 (2008).

150. Navarro-Vázquez, A., R. Gil, R. & Blinov, K. *Computer-Assisted 3D Structure Elucidation (CASE-3D) of Natural Products Combining Isotropic and Anisotropic NMR Parameters*. *Journal of Natural Products* **81,** (2018).

151. Sternberg, U. & Witter, R. Molecular dynamics simulations on PGLa using NMR orientational constraints. *J. Biomol. NMR* **63,** 265–274 (2015).

152. Erenler, R. *et al.* Bioassay-guided isolation, identification of compounds from Origanum rotundifolium and investigation of their antiproliferative and antioxidant activities. *Pharm. Biol.* **55,** 1646–1653 (2017).

153. Shams Eldin, S. M. *et al.* Bioactivity-Guided Isolation of Potential Antidiabetic and Antihyperlipidemic Compounds from Trigonella stellata. *J. Nat. Prod.* **81,** 1154–1161 (2018).

154. Levine, R. A. *et al.* Determination of Neurotoxic Acetogenins in Pawpaw (Asimina triloba) Fruit by LC-HRMS. *J. Agric. Food Chem.* **63,** 1053–1056 (2015).

155. Wang, J., Chow, W., Leung, D. & Chang, J. Application of Ultrahigh-Performance Liquid Chromatography and Electrospray Ionization Quadrupole Orbitrap High-Resolution Mass Spectrometry for Determination of 166 Pesticides in Fruits and Vegetables. *J. Agric. Food Chem.* **60,** 12088–12104 (2012).

156. Zhang, Q.-W., Lin, L.-G. & Ye, W.-C. Techniques for extraction and isolation of natural products: a comprehensive review. *Chin. Med.* **13,** 20 (2018).

157. Alexander, D. B. & Zuberer, D. A. Use of chrome azurol S reagents to evaluate siderophore production by rhizosphere bacteria. *Biol. Fertil. Soils* **12,** 39–45 (1991).

158. McCormack, P., Worsfold, P. J. & Gledhill, M. Separation and Detection of Siderophores Produced by Marine Bacterioplankton Using High-Performance Liquid Chromatography with Electrospray Ionization Mass Spectrometry. *Anal. Chem.* **75,** 2647–2652 (2003).

159. Gangadharan, S., Ghidelli, S. & Kamakaka, R. T. B. T.-M. in E. in *Chromatin and Chromatin Remodeling Enzymes, Part C* **377,** 234–254 (Academic Press, 2003).

160. Hagel, L. Gel-Filtration Chromatography. *Curr. Protoc. Mol. Biol.* **44,** 10.9.1-10.9.2 (2001).

161. Bucar, F., Wube, A. & Schmid, M. Natural product isolation – how to get from biological material to pure compounds. *Nat. Prod. Rep.* **30,** 525–545 (2013).

162. Andrade-Eiroa, A., Canle, M., Leroy-Cancellieri, V. & Cerdà, V. Solid-phase extraction of

organic compounds: A critical review (Part I). *TrAC Trends Anal. Chem.* **80,** 641–654 (2016).

163. ZHANG, L., YUAN, D.-X., FANG, K. & LIU, B.-M. Determination of Siderophores in Seawater by High Performance Liquid Chromatography-Tandem Mass Spectrometry Coupled with Solid Phase Extraction. *Chinese J. Anal. Chem.* **43,** 1285–1290 (2015).

164. Freeman, R. A. & Boyer, G. L. Solid phase extraction techniques for the isolation of siderophores from aquatic environments. *J. Plant Nutr.* **15,** 2263–2276 (1992).

165. McCarthy, M. D. & Bronk, D. A. in (eds. Capone, D. G., Bronk, D. A., Mulholland, M. R. & Carpenter, E. J. B. T.-N. in the M. E. (Second E.) 1219–1275 (Academic Press, 2008). doi:https://doi.org/10.1016/B978-0-12-372522-6.00028-1

166. Koelmel, J., Prasad, M. N. V, Velvizhi, G., Butti, S. K. & Mohan, S. V. in (eds. Prasad, M. N. V & Shih, K. B. T.-E. M. and W.) 339–390 (Academic Press, 2016). doi:https://doi.org/10.1016/B978-0-12-803837-6.00015-9

167. Aguilar, M.-I. in (ed. Aguilar, M.-I.) 9–22 (Springer New York, 2004). doi:10.1385/1-59259-742-4:9

168. Boone, C. & Adamec, J. in (eds. Ciborowski, P. & Silberring, J. B. T.-P. P. and A. C. (Second E.) 175–191 (Elsevier, 2016). doi:https://doi.org/10.1016/B978-0-444-63688-1.00010-0

169. Wolfender, J.-L. HPLC in Natural Product Analysis: The Detection Issue. *Planta Med* **75,** 719–734 (2009).

170. Brunnée, C. The ideal mass analyzer: Fact or fiction? *Int. J. Mass Spectrom. Ion Process.* **76,** 125–237 (1987).

171. Hu, Q. *et al.* The Orbitrap: a new mass spectrometer. *J. Mass Spectrom.* **40,** 430–443 (2005).

172. Bane, V. *et al.* LC-MS/MS method for the determination of tetrodotoxin (TTX) on a triple quadruple mass spectrometer. *Food Addit. Contam. Part A* **33,** 1728–1740 (2016).

173. Yost, R. A. & Enke, C. G. Triple quadrupole mass spectrometry for direct mixture analysis and structure elucidation. *Anal. Chem.* **51,** 1251–1264 (1979).

174. Yao, X., McShane, A. J. & Castillo, M. J. in (eds. Issaq, H. J. & Veenstra, T. D. B. T.-P. and M. A. to B. D.) 259–278 (Academic Press, 2013). doi:https://doi.org/10.1016/B978-0-12-394446-7.00017-0

175. Stone, J. in (eds. Nair, H. & Clarke, W. B. T.-M. S. for the C. L.) 37–62 (Academic Press, 2017). doi:https://doi.org/10.1016/B978-0-12-800871-3.00003-1

176. Price, N. D. *et al.* in (eds. Ginsburg, G. S. & Willard, H. F. B. T.-G. and P. M. (Second E.) 60–72 (Academic Press, 2013). doi:https://doi.org/10.1016/B978-0-12-382227-7.00005-7

177. Zubarev, R. A. & Makarov, A. Orbitrap Mass Spectrometry. *Anal. Chem.* **85,** 5288–5296 (2013).

178. Hoffmann, T., Krug, D., Hüttel, S. & Müller, R. Improving Natural Products Identification through Targeted LC- MS / MS in an Untargeted Secondary Metabolomics Workflow Improving Natural Products Identification through Targeted LC-MS / MS in an Untargeted Secondary Metabolomics Workflow. (2014). doi:10.1021/ac502805w

179. Wang, K., Lin, K., Huang, X. & Chen, M. A Simple and Fast Extraction Method for the Determination of Multiclass Antibiotics in Eggs Using LC-MS/MS. *J. Agric. Food Chem.* **65,** 5064–5073 (2017).

180. Wolfender, J.-L., Terreaux, C. & Hostettmann, K. The Importance Of LC-MS And LC-NMR In The Discovery Of New Lead Compounds From Plants. *Pharm. Biol.* **38,** 41–54 (2000).

181. Diogène, J. *et al.* Identification of ciguatoxins in a shark involved in a fatal food poisoning in the Indian Ocean. *Sci. Rep.* **7,** 8240 (2017).

182. Bose, U. *et al.* LC-MS-based metabolomics study of marine bacterial secondary metabolite and antibiotic production in Salinispora arenicola. *Mar. Drugs* **13,** 249–266 (2015).

183. Makarov, A. Electrostatic Axially Harmonic Orbital Trapping: A High-Performance Technique of Mass Analysis. *Anal. Chem.* **72,** 1156–1162 (2000).

184. Hardman, M. & Makarov, A. A. Interfacing the Orbitrap Mass Analyzer to an Electrospray Ion Source. *Anal. Chem.* **75,** 1699–1705 (2003).

185. Kellmann, M., Muenster, H., Zomer, P. & Mol, H. Full Scan MS in Comprehensive Qualitative and Quantitative Residue Analysis in Food and Feed Matrices: How Much Resolving Power is Required? *J. Am. Soc. Mass Spectrom.* **20,** 1464–1476 (2009).

186. Low, I. A. *et al.* Selected ion monitoring mass spectrometry: Parameters affecting quantitative determination. *Biomed. Mass Spectrom.* **12,** 633–637 (2018).

187. de Hoffmann, E. Tandem mass spectrometry: A primer. *J. Mass Spectrom.* **31,** 129–137 (2018).

188. Lange, V., Picotti, P., Domon, B. & Aebersold, R. Selected reaction monitoring for quantitative proteomics: a tutorial. *Mol. Syst. Biol.* **4,** 222 (2008).

189. Johnstone, T. C. & Nolan, E. M. Beyond iron: non-classical biological functions of bacterial siderophores. *Dalton Trans.* **44,** 6320–6339 (2015).

190. Comensoli, L., Bindschedler, S., Junier, P. & Joseph, E. in (eds. Sariaslani, S. & Gadd, G. M. B. T.-A. in A. M.) **98,** 31–60 (Academic Press, 2017).

191. Wilson, B. R., Bogdan, A. R., Miyazawa, M., Hashimoto, K. & Tsuji, Y. Siderophores in Iron Metabolism: From Mechanism to Therapy Potential. *Trends Mol. Med.* **22,** 1077–1090 (2016).

192. Saha, M. *et al.* Microbial siderophores and their potential applications: a review. *Environ. Sci. Pollut. Res.* **23,** 3984–3999 (2016).

193. Neilands, J. B. Siderophores: Structure and function of microbial iron transport compounds. *J. Biol. Chem.* **270,** 26723–26726 (1995).

194. Souto, A. *et al.* Structure and Biosynthetic Assembly of Piscibactin , a Siderophore from Photobacterium damselae subsp . piscicida , Predicted from Genome Analysis. *European J. Org. Chem.* 5693–5700 (2012). doi:10.1002/ejoc.201200818

195. Soengas, R. G. *et al.* Synthesis and biological activity of analogues of vanchrobactin, a siderophore from Vibrio anguillarum serotype O2. *Org. Biomol. Chem.* **6,** 1278–1287 (2008).

196. Balado, M., Osorio, C. R. & Lemos, M. L. FvtA is the receptor for the siderophore vanchrobactin in Vibrio anguillarum: utility as a route of entry for vanchrobactin

analogues. *Appl. Environ. Microbiol.* **75,** 2775–2783 (2009).

197. Sandy, M. *et al.* Vanchrobactin and anguibactin siderophores produced by Vibrio sp. DS40M4. *J. Nat. Prod.* **73,** 1038–1043 (2010).

198. Espada, A., Anta, C., Bragado, A., Rodríguez, J. & Jiménez, C. An approach to speed up the isolation of hydrophilic metabolites from natural sources at semipreparative level by using a hydrophilic–lipophilic balance/mixed-mode strong cation exchange–high-performance liquid chromatography/mass spectrometry system. *J. Chromatogr. A* **1218,** 1790–1794 (2011).

199. Boiteau, R. M. *et al.* Siderophore-based microbial adaptations to iron scarcity across the eastern Pacific Ocean. *Proc. Natl. Acad. Sci. U. S. A.* **113,** 14237–14242 (2016).

200. McMillan, D. G. G. *et al.* Acquisition of Iron by Alkaliphilic ≪em>Bacillus≪/em> Species. *Appl. Environ. Microbiol.* **76,** 6955 LP-6961 (2010).

201. Griffiths, G. L., Sigel, S. P., Payne, S. M. & Neilands, J. B. Vibriobactin, a siderophore from Vibrio cholerae. *J. Biol. Chem.* **259,** 383–385 (1984).

202. Osorio, C. R., Collins, M. D., Toranzo, A. E., Barja, J. L. & Romalde, J. L. 16S rRNA gene sequence analysis of Photobacterium damselae and nested PCR method for rapid detection of the causative agent of fish pasteurellosis. *Appl. Environ. Microbiol.* **65,** 2942–2946 (1999).

203. Romalde, J. L. Photobacterium damselae subsp. piscicida: an integrated view of a bacterial fish pathogen. *Int. Microbiol.* **5,** 3–9 (2002).

204. Aoki, T. *et al.* Complete Genome Sequence of Photobacterium damselae subsp. piscicida Strain OT-51443 Isolated from Yellowtail (Seriola quinqueradiata) in Japan. *Genome Announc.* **5,** e00404-17 (2017).

205. Tran, H. B., Lee, Y.-H., Guo, J.-J. & Cheng, T.-C. De novo transcriptome analysis of immune response on cobia (Rachycentron canadum) infected with Photobacterium damselae subsp. piscicida revealed inhibition of complement components and involvement of MyD88-independent pathway. *Fish Shellfish Immunol.* **77,** 120–130 (2018).

206. Segade, Y., Montaos, M. A., Rodríguez, J. & Jiménez, C. A Short Stereoselective Synthesis of Prepiscibactin Using a SmI2-Mediated Reformatsky Reaction and Zn2+-Induced Asymmetric Thiazolidine Formation. *Org. Lett.* **16,** 5820–5823 (2014).

207. Mouriño, S., Osorio, C. R. & Lemos, M. L. Characterization of Heme Uptake Cluster Genes in the Fish Pathogen ≪em>Vibrio anguillarum≪/em> *J. Bacteriol.* **186,** 6159 LP-6167 (2004).

208. Liang, S. *et al.* Immune response of turbot (Scophthalmus maximus L.) to a broad spectrum vaccine candidate, recombinant glyceraldehyde-3-phosphate dehydrogenase of Edwardsiella tarda. *Vet. Immunol. Immunopathol.* **150,** 198–205 (2012).

209. Edrees, A. *et al.* Construction and evaluation of type III secretion system mutants of the catfish pathogen Edwardsiella piscicida. *J. Fish Dis.* **41,** 805–816 (2018).

210. Beck, B. R. *et al.* A Lactococcus lactis BFE920 feed vaccine expressing a fusion protein composed of the OmpA and FlgD antigens from Edwardsiella tarda was significantly better at protecting olive flounder (Paralichthys olivaceus) from edwardsiellosis than

single antigen vac. *Fish Shellfish Immunol.* **68,** 19–28 (2017).

211. Yang, W. *et al.* An invasive and low virulent Edwardsiella tarda esrB mutant promising as live attenuated vaccine in aquaculture. *Appl. Microbiol. Biotechnol.* **99,** 1765–1777 (2015).

212. Louden, B. C., Haarmann, D. & Lynne, A. M. Use of Blue Agar CAS Assay for Siderophore Detection. *J. Microbiol. Biol. Educ.* **12,** 51–53 (2011).

213. Amin, S. A., Küpper, F. C., Green, D. H., Harris, W. R. & Carrano, C. J. Boron Binding by a Siderophore Isolated from Marine Bacteria Associated with the Toxic Dinoflagellate Gymnodinium catenatum. *J. Am. Chem. Soc.* **129,** 478–479 (2007).

214. Amin, S. A., Green, D. H., Küpper, F. C. & Carrano, C. J. Vibrioferrin, an Unusual Marine Siderophore: Iron Binding, Photochemistry, and Biological Implications. *Inorg. Chem.* **48,** 11451–11458 (2009).

215. Yamamoto, S., Okujo, N., Yoshida, T., Matsuura, S. & Shinoda, S. Structure and Iron Transport Activity of Vibrioferrin, a New Siderophore of *Vibrio parahaemolyticus*. *J. Biochem.* **115,** 868–874 (1994).

216. Funahashi, T. *et al.* Identification and characterization of pvuA, a gene encoding the ferric vibrioferrin receptor protein in Vibrio parahaemolyticus. *J. Bacteriol.* **184,** 936–946 (2002).

217. TAKEUCHI, Y., AKIYAMA, T. & HARAYAMA, T. Total Synthesis of the Siderophore Vibrioferrin. *Chem. Pharm. Bull. (Tokyo).* **47,** 459–460 (1999).

218. Chiu, T., Kao, L. & Chen, M. Antibiotic resistance and molecular typing of Photobacterium damselae subsp . damselae , isolated from seafood. (2013). doi:10.1111/jam.12104

219. Osorio, C. R. *et al.* A Transmissible Plasmid-Borne Pathogenicity Island Confers Piscibactin Biosynthesis in the Fish Pathogen Photobacterium damselae subsp . piscicida. *Appl. Environ. Microbiol.* **81,** 5867–5879 (2015).

220. Rivas, A. J., Labella, A. M., Borrego, J. J., Lemos, M. L. & Osorio, C. R. Evidence for horizontal gene transfer, gene duplication and genetic variation as driving forces of the diversity of haemolytic phenotypes in Photobacterium damselae subsp. damselae. (2014). doi:10.1111/1574-6968.12464

221. Schwyn, B. & Neilands, J. B. Universal chemical assay for the detection and determination of siderophores. *Anal. Biochem.* **160,** 47–56 (1987).

222. Chaves-Fonnegra, A. *et al.* Clionapyrrolidine A - A metabolite from the encrusting and excavating sponge Cliona tenuis that kills coral tissue upon contact. *J. Chem. Ecol.* **34,** 1565–1574 (2008).

223. Lindel, T. *et al.* Eleutherobin, a New Cytotoxin that Mimics Paclitaxel (Taxol) by Stabilizing Microtubules. *J. Am. Chem. Soc.* **119,** 8744–8745 (1997).

224. Pellati, F. & Benvenuti, S. Determination of ephedrine alkaloids in Ephedra natural products using HPLC on a pentafluorophenylpropyl stationary phase. *J. Pharm. Biomed. Anal.* **48,** 254–263 (2008).

225. Frawley, E. R. *et al.* Iron and citrate export by a major facilitator superfamily pump regulates metabolism and stress resistance in Salmonella Typhimurium. *Proc. Natl. Acad. Sci.* **110,** 12054 LP-12059 (2013).

226. Jones, A. M. & Wildermuth, M. C. The Phytopathogen Pseudomonas syringae pv. tomato DC3000 Has Three High-Affinity Iron-Scavenging Systems Functional under Iron Limitation Conditions but . *J. Bacteriol.* **193,** 2767 LP-2775 (2011).

227. Guerinot, M. L., Meidl, E. J. & Plessner, O. Citrate as a siderophore in Bradyrhizobium japonicum. *J. Bacteriol.* **172,** 3298 LP-3303 (1990).

228. Tanabe, T. *et al.* Identification and Characterization of Genes Required for Biosynthesis and Transport of the Siderophore Vibrioferrin in Vibrio parahaemolyticus *J. Bacteriol.* **185,** 6938 LP-6949 (2003).

229. Silva, A. M. N., Kong, X., Parkin, M. C., Cammack, R. & Hider, R. C. Iron(iii) citrate speciation in aqueous solution. *Dalt. Trans.* 8616–8625 (2009). doi:10.1039/B910970F

230. Bennett, B. D. *et al.* Absolute metabolite concentrations and implied enzyme active site occupancy in Escherichia coli. *Nat. Chem. Biol.* **5,** 593 (2009).

231. Pressler, U., Staudenmaier, H., Zimmermann, L. & Braun, V. Genetics of the iron dicitrate transport system of Escherichia coli. *J. Bacteriol.* **170,** 2716 LP-2724 (1988).

232. Mazoy, R. & Lemos, M. L. Iron-binding proteins and heme compounds as iron sources for Vibrio anguillarum. *Curr. Microbiol.* **23,** 221–226 (1991).

233. Fouz, B., Toranzo, A. E., Biosca, E. G., Mazoy, R. & Amaro, C. Role of iron in the pathogenicity of Vibrio damsela for fish and mammals. *FEMS Microbiol. Lett.* **121,** 181–188 (1994).

234. Mazoy, R., Botana, L. M. & Lemos, M. L. Iron uptake from ferric citrate by Vibrio anguillarum. *FEMS Microbiol. Lett.* **154,** 145–150 (1997).

235. Hider, R. C. & Kong, X. Chemistry and biology of siderophores. *Nat. Prod. Rep.* **27,** 637–657 (2010).

236. Romero, M. *et al.* In vitro quenching of fish pathogen Edwardsiella tarda AHL production using marine bacterium Tenacibaculum sp. strain 20J cell extracts . *Dis. Aquat. Organ.* **108,** 217–225 (2014).

237. Balado, M. *et al.* Two Catechol Siderophores, Acinetobactin and Amonabactin, Are Simultaneously Produced by Aeromonas salmonicida subsp. salmonicida Sharing Part of the Biosynthetic Pathway. *ACS Chem. Biol.* **10,** 2850–2860 (2015).

238. Prasain, J.-S. K. E.-J. K. in Ch. 21 (IntechOpen, 2012). doi:10.5772/32085

239. May, A. L., Eisenhauer, M. E., Coulston, K. S. & Campagna, S. R. Detection and Quantitation of Bacterial Acylhomoserine Lactone Quorum Sensing Molecules via Liquid Chromatography–Isotope Dilution Tandem Mass Spectrometry. *Anal. Chem.* **84,** 1243–1252 (2012).

240. Natrah, F. M. I., Defoirdt, T., Sorgeloos, P. & Bossier, P. Disruption of Bacterial Cell-to-Cell Communication by Marine Organisms and its Relevance to Aquaculture. *Mar. Biotechnol.* **13,** 109–126 (2011).

241. Vizcaino, M. I. *et al.* Antimicrobial Resistance of the Coral Pathogen Vibrio coralliilyticus and Caribbean Sister Phylotypes Isolated from a Diseased Octocoral. *Microb. Ecol.* **59,** 646–657 (2010).

242. Silvester, R., Alexander, D., George, M. & Abdulla, M. H. *Prevalence and multiple antibiotic resistance of Vibrio coralliilyticus, along the southwest coast of India. Current science* **112,** (2017).

243. Nguyen, T. V, Alfaro, A. C., Young, T., Ravi, S. & Merien, F. Metabolomics Study of Immune Responses of New Zealand Greenshell™ Mussels (Perna canaliculus) Infected with Pathogenic Vibrio sp. *Mar. Biotechnol.* **20,** 396–409 (2018).

244. Schreier, H. J. & Schott, E. J. Draft Genome Sequence of the Shellfish Bacterial Pathogen Vibrio sp. Strain B183. *Genome Announc.* **2,** e00914-14 (2014).

245. Cano-Gómez, A., Goulden, E. F., Owens, L. & Høj, L. Vibrio owensii sp. nov., isolated from cultured crustaceans in Australia. *FEMS Microbiol. Lett.* **302,** 175–181 (2010).

246. Beaz-Hidalgo, R. *et al.* Vibrio celticus sp. nov., a new Vibrio species belonging to the Splendidus clade with pathogenic potential for clams. *Syst. Appl. Microbiol.* **33,** 311–315 (2010).

247. Tarazona, E. *et al.* Multilocus sequence analysis of putative Vibrio mediterranei strains and description of Vibrio thalassae sp. nov. *Syst. Appl. Microbiol.* **37,** 320–328 (2014).

248. Llamas, I. *et al.* Quorum sensing in halophilic bacteria: detection of N-acyl-homoserine lactones in the exopolysaccharide-producing species of Halomonas. *Extremophiles* **9,** 333–341 (2005).

249. García-Aljaro, C., Vargas-Cespedes, G. J. & Blanch, A. R. Detection of acylated homoserine lactones produced by Vibrio spp. and related species isolated from water and aquatic organisms. *J. Appl. Microbiol.* **112,** 383–389 (2011).

250. Llamas, I., Keshavan, N. & González, J. E. Use of Sinorhizobium meliloti as an Indicator for Specific Detection of Long-Chain N-Acyl Homoserine Lactones. *Appl. Environ. Microbiol.* **70,** 3715 LP-3723 (2004).

251. Wang, J., Quan, C., Wang, X., Zhao, P. & Fan, S. Extraction, purification and identification of bacterial signal molecules based on N-acyl homoserine lactones. *Microb. Biotechnol.* **4,** 479–490 (2010).

252. Yotsu-Yamashita, M., Toennes, S. W. & Mebs, D. Tetrodotoxin in Asian newts (Salamandridae). *Toxicon* **134,** 14–17 (2017).

253. Stokes, A. N. *et al.* Confirmation and Distribution of Tetrodotoxin for the First Time in Terrestrial Invertebrates: Two Terrestrial Flatworm Species (Bipalium adventitium and Bipalium kewense). *PLoS One* **9,** e100718 (2014).

254. Wang, X.-J., Yu, R.-C., Luo, X., Zhou, M.-J. & Lin, X.-T. Toxin-screening and identification of bacteria isolated from highly toxic marine gastropod Nassarius semiplicatus. *Toxicon* **52,** 55–61 (2008).

255. Bane, V., Lehane, M., Dikshit, M., O'Riordan, A. & Furey, A. Tetrodotoxin: Chemistry, toxicity, source, distribution and detection. *Toxins (Basel).* **6,** 693–755 (2014).

256. Salvitti, L., Wood, S. A., Taylor, D. I., McNabb, P. & Cary, S. C. First identification of tetrodotoxin (TTX) in the flatworm Stylochoplana sp.; a source of TTX for the sea slug Pleurobranchaea maculata. *Toxicon* **95,** 23–29 (2015).

257. Narahashi, T. Pharmacology of tetrodotoxin. *J. Toxicol. Reviws* **20,** 67–84 (2001).

258. Mattias Eliasson, Stefan Rännar, Rasmus Madsen, Magdalena A. Donten, Emma Marsden-Edwards, Thomas Moritz, John P. Shockcor, Erik Johansson, and J. T. Strategy for Optimizing LC-MS Data Processing in Metabolomics: A Design of Experiments Approach. *Anal. Chem.* 6869–6876 (2012). doi:10.1016/j.ijpharm.2011.11.009

259. Noguchi, T. & Arakawa, O. Tetrodotoxin--distribution and accumulation in aquatic organisms, and cases of human intoxication. *Mar. Drugs* **6,** 220–242 (2008).

260. Lee, M. J. *et al.* A tetrodotoxin-producing Vibrio strain, LM-1, from the puffer fish Fugu vermicularis radiatus. *Appl. Environ. Microbiol.* **66,** 1698–1701 (2000).

261. Yu, V. C. H., Yu, P. H. F., Ho, K. C. & Lee, F. W. F. Isolation and identification of a new tetrodotoxin-producing bacterial species, Raoultella terrigena, from Hong Kong marine puffer fish Takifugu niphobles. *Mar. Drugs* **9,** 2384–2396 (2011).

262. Vermeij, G.J.; Zipser, E. The Diet of Diodon hystrix (Teleostei : Tetraodontiformes): Shell-crushing on Guam ' s Reefs. *Bish. Mus. Bull. Zool.* **175,** 169–175 (2015).

263. Ellis, J. R. Occurence of exotic fished in east Anglian waters: Porcupinefish Diodon hystrix and Piranha Pygocentrus sp. *Trans. Suffolk Nat. Soc.* **42,** 39–43 (2006).

264. Leis, J. M. Nomenclature and distribution of the species of the porcupinefish family Diodontidae (Pisces, Teleostei). *Mem. Museum Victoria* **63,** 77–90 (2006).

265. Davis, E. W. The ethnobiology of the Haitian zombi. *J. Ethnopharmacol.* **9,** 85–104 (1983).

266. Yasumoto, T. & Kao, C. Y. Tetrodotoxin and the Haitian zombie. *Toxicon* **24,** 747–749 (1986).

267. Sims, Joel Kevin; Ostman, D. C. Pufferfish Poisoning : Emergency Diagnosis and Management of Mild. *Ann. Emerg. Med.* **15,** 1094–1098 (1986).

268. Trevett, A. J., Mavo, B. & Warrell, D. A. Tetrodotoxic Poisoning from Ingestion of a Porcupine Fish (Diodon hystrix) in Papua New Guinea: Nerve Conduction Studies. *Am. J. Trop. Med. Hyg.* **56,** (1997).

269. van Gorcum, T. F., Janse, M., Leenders, M. E. C., de Vries, I. & Meulenbelt, J. Intoxication Following Minor Stabs from the Spines of a Porcupine Fish. *Clin. Toxicol.* **44,** 391–393 (2006).

270. Campbell, S., Harada, R. M., DeFelice, S. V, Bienfang, P. K. & Li, Q. X. Bacterial production of tetrodotoxin in the pufferfish Arothron hispidus. *Nat. Prod. Res.* **23,** 1630–1640 (2009).

271. Chulanetra, M. *et al.* Toxic marine puffer fish in Thailand seas and tetrodotoxin they contained. *Toxins (Basel).* **3,** 1249–1262 (2011).

272. Ayub, M. N. A., Mohamad, S. & Mohammad, O. *Distribution of Tetrodotoxin among Tissues of Pufferfish from Sabah and Sarawak Waters*. *Sains Malaysiana* **43,** (2014).

273. Chen, C.-Y. & Chou, H.-N. *Detection of Tetrodotoxin by High Performance Liquid Chromatography in Lined-Moon Shell and Puffer Fish*. *Acta Zool. Taiwan* **9,** (1998).

274. Sherwood, C. A. *et al.* Rapid optimization of MRM-MS instrument parameters by subtle alteration of precursor and product m/z targets. *J. Proteome Res.* **8,** 3746–3751 (2009).

275. Johnson, A. R. & Carlson, E. E. Collision-Induced Dissociation Mass Spectrometry: A Powerful Tool for Natural Product Structure Elucidation. *Anal. Chem.* **87,** 10668–10678

(2015).

276. Sleno, L. & Volmer, D. A. SPECIAL FEATURE : Ion activation methods for tandem mass spectrometry. *J. Mass Spectrom.* **39,** 1091–1112 (2004).

277. Macintyre, L. *et al. Metabolomic Tools for Secondary Metabolite Discovery from Marine Microbial Symbionts*. (2014). doi:10.3390/md12063416

278. Pluskal, T., Castillo, S., Villar-Briones, A. & Oresic, M. MZmine 2: modular framework for processing, visualizing, and analyzing mass spectrometry-based molecular profile data. *BMC Bioinformatics* **11,** 395 (2010).

279. Katajamaa, M., Miettinen, J. & Orešič, M. MZmine: Toolbox for processing and visualization of mass spectrometry based molecular profile data. *Bioinformatics* **22,** 634–636 (2006).

280. Chen, Y. *et al.* Assessment of data pre-processing methods for LC-MS/MS-based metabolomics of uterine cervix cancer. *Analyst* **138,** 2669–77 (2013).

281. Kanehisa, M., Sato, Y., Kawashima, M., Furumichi, M. & Tanabe, M. KEGG as a reference resource for gene and protein annotation. *Nucleic Acids Res.* **44,** D457–D462 (2016).

282. Kim, S. *et al.* PubChem Substance and Compound databases. **44,** 1202–1213 (2017).

283. Shoji, Y., Yotsu-Yamashita, M., Miyazawa, T. & Yasumoto, T. Electrospray ionization mass spectrometry of tetrodotoxin and its analogs: liquid chromatography/mass spectrometry, tandem mass spectrometry, and liquid chromatography/tandem mass spectrometry. *Anal. Biochem.* **290,** 10–17 (2001).

284. Chen, X. W. *et al.* Separation, identification and quantification of tetrodotoxin and its analogs by LC-MS without calibration of individual analogs. *Toxicon* **57,** 938–943 (2011).

285. Su, X., Lu, W. & Rabinowitz, J. D. Metabolite Spectral Accuracy on Orbitraps. *Anal. Chem.* **89,** 5940–5948 (2017).

286. Chervin, J. *et al.* Targeted Dereplication of Microbial Natural Products by High-Resolution MS and Predicted LC Retention Time. (2017). doi:10.1021/acs.jnatprod.6b01035

287. Bane, V., Brosnan, B., Barnes, P., Lehane, M. & Furey, A. High-resolution mass spectrometry analysis of tetrodotoxin (TTX) and its analogues in puffer fish and shellfish. *Food Addit. Contam. Part A. Chem. Anal. Control. Expo. Risk Assess.* **33,** 1468–89 (2016).

288. Weber, R. J. M., Southam, A. D., Sommer, U. & Viant, M. R. Characterization of Isotopic Abundance Measurements in High Resolution FT-ICR and Orbitrap Mass Spectra for Improved. *Anal. Chem.* **83,** 3737–3743 (2011).

289. Xu, Y. *et al.* Evaluation of accurate mass and relative isotopic abundance measurements in the LTQ-Orbitrap mass spectrometer for further metabolomics database building. *Anal. Chem.* **82,** 5490–5501 (2010).

290. Makarov, A. *et al.* Performance evaluation of a hybrid linear ion trap/orbitrap mass spectrometer. *Anal. Chem.* **78,** 2113–2120 (2006).

291. Kind, T. & Fiehn, O. Seven Golden Rules for heuristic filtering of molecular formulas obtained by accurate mass spectrometry. *BMC Bioinformatics* **8,** 105 (2007).

292. Chagas-Paula, D. A., Oliveira, T. B., Zhang, T., Edrada-Ebel, R. & Da Costa, F. B.

Prediction of anti-inflammatory plants and discovery of their biomarkers by machine learning algorithms and metabolomic studies. *Planta Med.* **81,** 450–458 (2015).

293. Omar, R. M. K. *et al.* Chemical characterisation of Nigerian red propolis and its biological activity against Trypanosoma Brucei. *Phytochem. Anal.* **27,** 107–115 (2016).

294. Najdekr, L. *et al.* Influence of mass resolving power in orbital ion-trap mass spectrometry-based metabolomics. *Anal. Chem.* acs.analchem.6b02319 (2016). doi:10.1021/acs.analchem.6b02319

295. Hu, M., Krauss, M., Brack, W. & Schulze, T. Optimization of LC-Orbitrap-HRMS acquisition and MZmine 2 data processing for nontarget screening of environmental samples using design of experiments. *Anal. Bioanal. Chem.* **408,** 7905–7915 (2016).

296. Gürdeniz, G., Kristensen, M., Skov, T. & Dragsted, L. O. The Effect of LC-MS Data Preprocessing Methods on the Selection of Plasma Biomarkers in Fed vs. Fasted Rats. *Metabolites* **2,** 77–99 (2012).

297. Sandoval, M. A. R. Extraction of Phorbol Esters (PEs) from Pinion cake using computationally-designed polymers as adsorbents for Solid ... Extraction of Phorbol Esters (PEs) from Pinion cake using computationally-designed polymers as adsorbents for Solid Phase Extractio. 1–56 (2017).